The background of the slide is a complex technical drawing of a multi-cavity circuit board assembly. The drawing is rendered in white lines on a dark blue background. It shows various components, including circular cavities, rectangular slots, and intricate wiring patterns. Several dimensions and specifications are visible, such as '2-56 UNC - 2B' in multiple locations, '49' indicating a width, and '1.57' indicating a height. The drawing is a detailed isometric or perspective view of the assembly, showing the internal structure and the arrangement of the cavities.

# Multi-Cavity Operations in Circuit Quantum Electrodynamics

Yvonne Y. Gao



# Multi-Cavity Operations in Circuit Quantum Electrodynamics

A Dissertation  
Presented to the Faculty of the Graduate School  
of  
Yale University  
in Candidacy for the Degree of  
Doctor of Philosophy

by Yvonne Y. Gao

Dissertation director: Robert J. Schoelkopf

May 2018

© 2018 by Yvonne Yuan Gao  
All rights reserved.

# Abstract

## Muti-Cavity Operations in Circuit Quantum Electrodynamics

Yvonne Y. Gao

2018

The eventual success of a quantum computer relies on our ability to robustly initialise, manipulate, and measure quantum bits, or qubits, in the presence of the inevitable occurrence of errors. This requires us to encode quantum information redundantly in systems that are suitable for Quantum Error Correction (QEC). One promising implementation is to use three dimensional (3D) superconducting microwave cavities coupled to one or more non-linear ancillae in the circuit quantum electrodynamics (cQED) framework. Such systems have the advantage of good intrinsic coherence properties and large Hilbert space, making them ideal for storing redundantly encoded quantum bits. Recent progress has demonstrated the universal control and realisation of QEC beyond the break-even point on a logical qubit encoded in a multi-photon state of a single cavity. This thesis presents the first experiments in implementing quantum operations between multi-photon states stored in two separate cavities. We first explore the ability to create complex two-mode entangled states and perform full characterisation in a novel multi-cavity architecture. Subsequently, we demonstrate the capability to implement conditional quantum gates between two cavity modes, assisted by a single ancilla. In addition, we develop a direct, tunable coupling between two spectrally separated cavities and use it to study complex multiphoton interference between stationary bosonic states. Combining this with robust single cavity controls, we construct a universal entangling gate between multi-photon states. The results presented in this thesis demonstrate the vast potential of 3D superconducting systems as robust, error-correctable quantum modules and the techniques developed constitute an important toolset towards realising universal quantum computing on error-corrected qubits.

# Table of contents

<b>Table of contents</b>	<b>i</b>
<b>List of Figures</b>	<b>iii</b>
<b>List of Tables</b>	<b>vi</b>
<b>Acknowledgements</b>	<b>1</b>
<b>1 Introduction</b>	<b>5</b>
1.1 A quantum bit . . . . .	6
1.2 Fragility of a quantum bit . . . . .	10
1.3 Towards operations on error-corrected logical qubits . . . . .	12
1.4 A précis of the chapters to come . . . . .	14
<b>2 Logical qubits in Circuit QED</b>	<b>17</b>
2.1 Quantum LC oscillators . . . . .	20
2.2 Adding non-linearity with the Josephson junction . . . . .	24
2.3 Combining transmons with harmonic oscillators . . . . .	27
2.4 Transmon readout and characterisation . . . . .	30
2.5 Control and measurement of a cavity state . . . . .	34
2.6 Cavity-based QEC schemes . . . . .	39
2.7 Toward operations on multiple logical qubits . . . . .	45
<b>3 Multi-cavity cQED architecture</b>	<b>47</b>
3.1 Design of multi-cavity devices . . . . .	48
3.2 Measurement of Hamiltonian parameters . . . . .	53
3.3 Characterisation of cavity coherence . . . . .	57
3.4 Extension to incorporate multiple ancillae . . . . .	61
3.5 Experimental configurations . . . . .	66
<b>4 Putting a Schrödinger cat in two boxes</b>	<b>73</b>
4.1 Deterministic state creation . . . . .	74
4.2 Joint parity measurement . . . . .	78
4.3 A bell pair of encoded qubits . . . . .	90
4.4 Understanding imperfections . . . . .	96
4.5 Discussion . . . . .	99

---

<b>5</b>	<b>A CNOT gate between two multi-photon qubits</b>	<b>101</b>
5.1	RF controlled sideband transitions . . . . .	102
5.2	Implementation of CNOT gate . . . . .	107
5.3	Analysis of gate fidelity . . . . .	113
5.4	Discussion . . . . .	115
<b>6</b>	<b>Programmable interference between two microwave quantum memories</b>	<b>117</b>
6.1	Bilinear coupling between two cavity modes . . . . .	119
6.2	Coherence of BS operations . . . . .	125
6.3	Bosonic interference and its applications in cQED . . . . .	130
6.4	Alternative drive configurations . . . . .	136
6.5	Discussion . . . . .	140
<b>7</b>	<b>Building a universal entangler in cQED</b>	<b>142</b>
7.1	The exponential-SWAP unitary operation . . . . .	143
7.2	eSWAP operation in single photon encoding . . . . .	146
7.3	Generating a two-mode cat state using eSWAP . . . . .	149
7.4	Discussion . . . . .	155
<b>8</b>	<b>Conclusion and future directions</b>	<b>158</b>
	<b>List of publications</b>	<b>164</b>
	<b>References</b>	<b>165</b>

# List of Figures

<b>Introduction</b>	<b>5</b>
1.1 Bloch sphere of a qubit . . . . .	7
1.2 A CNOT gate . . . . .	9
1.3 Classical vs quantum errors . . . . .	10
1.4 Effect of bit and phase flip errors on a Bloch sphere . . . . .	11
1.5 A roadmap for quantum computing . . . . .	13
<b>Logical qubits in Circuit QED</b>	<b>17</b>
2.1 Quantised harmonic oscillator . . . . .	21
2.2 Planar and 3D cavities . . . . .	23
2.3 An anharmonic quantum oscillator . . . . .	25
2.4 Readout histogram . . . . .	30
2.5 Qubit coherence measurements . . . . .	31
2.6 Manipulation of transmon $ f\rangle$ level . . . . .	32
2.7 Coherence measurements of transmon $ f\rangle$ level . . . . .	33
2.8 Ancilla spectroscopy as probe for cavity population . . . . .	34
2.9 Parity measurement . . . . .	36
2.10 Wigner representation of cavity state . . . . .	37
2.11 Example of an optimal control pulse . . . . .	38
2.12 7-Qubit Steane code . . . . .	40
2.13 The cat code cycle . . . . .	43
2.14 Binomial code Bloch sphere . . . . .	44
<b>Multi-cavity cQED architecture</b>	<b>47</b>
3.1 External details of the original double-cavity package . . . . .	48
3.2 Overview of the 3D architecture . . . . .	50
3.3 A Y-shaped transmon device . . . . .	51
3.4 Clamping of the transmon chip . . . . .	52
3.5 Characterization of transmon-cavity dispersive coupling . . . . .	54
3.6 Cross-Kerr coupling between Alice and Bob . . . . .	57
3.7 $T_1$ measurement of cavities . . . . .	58
3.8 $T_2$ measurement of cavities . . . . .	59
3.9 Cartoon of double cavity system with three ancillae . . . . .	61
3.10 Simultaneous Rabi experiment . . . . .	62

3.11	Field distribution in HFSS simulation . . . . .	64
3.12	RF and fridge configurations for entangled cat and CNOT experiment . . . . .	68
3.13	RF and fridge configurations for bosonic interference and eSWAP experiment . . . . .	71
<b>Putting a Schrödinger cat in two boxes</b>		<b>73</b>
4.1	qcMAP protocol to create two-mode cat . . . . .	76
4.2	Single cavity Wigner tomography . . . . .	79
4.3	Two experimental protocols for joint parity measurement . . . . .	82
4.4	Joint Wigner tomography . . . . .	86
4.5	Coherence of larger two-mode cat states . . . . .	88
4.6	Joint Wigner measurements in the Re-Im planes . . . . .	88
4.7	Decay of joint parity . . . . .	89
4.8	Direct fidelity estimation of a cat state . . . . .	91
4.9	Two-qubit Pauli correlators . . . . .	94
4.10	Bell signal of an odd two-mode cat state . . . . .	95
<b>A CNOT gate between two multi-photon qubits</b>		<b>101</b>
5.1	Four-wave mixing in a Josephson junction . . . . .	103
5.2	Drive sideband transition . . . . .	105
5.3	Drive sideband transition with multiple photons in the target cavity . . . . .	106
5.4	Protocol to implement CNOT using sideband drives . . . . .	108
5.5	Creation of Bell state with single-photon encoding . . . . .	109
5.6	Undesired coupling . . . . .	110
5.7	Example of reconstructed density matrices in Binomial encoding . . . . .	112
5.8	Entangled state generation in the Binomial encoding . . . . .	113
5.9	Characterisation of CNOT performance . . . . .	115
<b>Programmable interference between two microwave quantum memories</b>		<b>117</b>
6.1	RF-driven direct coupling between two cavities . . . . .	119
6.2	A three-level lambda system . . . . .	120
6.3	Stark shift due to drives . . . . .	123
6.4	Characterisation of bilinear coupling . . . . .	124
6.5	Examples of single photon oscillation measurements . . . . .	125
6.6	Extracted $\tau_1$ and $\tau_\phi$ . . . . .	127
6.7	Tunable coupling strength . . . . .	128
6.8	SWAP operation between two cavities . . . . .	129
6.9	HOM interference between two spectrally-separated cavity modes . . . . .	130
6.10	Statistics of bosonic interference . . . . .	131
6.11	Overlap measurement of two coherent states . . . . .	132
6.12	Cascaded microwave Mach-Zehnder interferometers . . . . .	134
6.13	Interference of multiphoton states . . . . .	135
6.14	Different frequency configurations of drives . . . . .	137
6.15	Drives above the nonlinear mode . . . . .	138
6.16	Drives symmetric around nonlinear mode . . . . .	139

---

<b>Building a universal entangler in cQED</b>	<b>142</b>
7.1 Proposed circuit to implement $U_{\text{eSWAP}}(\theta)$ . . . . .	144
7.2 Circuit to implement eSWAP unitary . . . . .	146
7.3 eSWAP in single photon encoding . . . . .	147
7.4 Joint Wigner measurement from correlated single Wigner functions . . . . .	150
7.5 $U_{\text{eSWAP}}(\theta = \frac{\pi}{4})$ on coherent states . . . . .	151
7.6 Coherent state under $U_{\text{BS}}$ . . . . .	153
7.7 Joint Pauli correlators after $U_{\text{eSWAP}}(\theta = \frac{\pi}{4})$ . . . . .	154
7.8 Joint Wigner function after eSWAP unitary . . . . .	155
<b>Conclusion and future directions</b>	<b>158</b>
8.1 Photograph of a quantum module consisting of 4 high-Q cavities . . . . .	160
8.2 Quad-rail encoding in cQED . . . . .	161

## List of Tables

<b>Multi-cavity cQED architecture</b>	<b>47</b>
3.1 Hamiltonian parameters of original design . . . . .	55
3.2 Coherence properties of double-cavity system . . . . .	60
3.3 Hamiltonian parameters of new system . . . . .	63
3.4 Simulated vs measured Hamiltonian parameters . . . . .	65
3.5 Coherence properties of double-cavity with three ancillae . . . . .	66
<b>Putting a Schrödinger cat in two boxes</b>	<b>73</b>
4.1 Contributions to the reduction of contrast in joint Wigner measurements . . . . .	98

## Acknowledgements

I owe many people my heart-felt gratitude for making my experience at Yale so extraordinary. Over the past six years, my colleagues on the 4th floor of Becton have generously offered me constant support and guidance. ANDREI PETRENKO was the first person I worked with at very beginning of my graduate studies. He introduced me to the machineries and the inner workings of the lab with incredible patience. His enthusiasm on the then nascent quantum error correction experiment was extremely contagious and inspiring. Majority of my Ph.D work has been done in collaboration with CHEN WANG. He taught me the art of protecting qubits from the evil environment through meticulous shielding and filtering. He also instilled in me the importance of always being attentive to the finest details in each experiment and never settling for any half-hearted conclusions. Working with Chen has been a truly enriching experience.

I am also greatly indebted to my all colleagues who took care of the maintenance of lab equipments. Their hard work is instrumental to success of our experiments. In particular, I would like to thank CHRIS AXLINE, KEVIN CHOU, and ANIRUDH NARLA for taming the fridges and its numerous dependencies. They have also often been the brave first responders when either man-made or natural disasters strike. I must also thank MICHAEL HATRIDGE, KATRINA SILVA, and NICK FRATTINI for providing not only the excellent quantum amplifiers but also for their patience in educating me on how to calibrate and operate them. Thanks to these stable and robust amplifiers, we are able to build increasingly complex experiments and obtain many beautiful Wigner plots. Additionally, I would like also express my appreciate to NISSIM OFEK for constructing the FPGA logical and PHIL REINHOLD for building the beautiful FPGA interface and rendering his programming ex-

pertise to facilitate many of my experiments.

The success of our experimental work also relies heavily on the outstanding achievements in developing more robust, easily integratable quantum components. Specially, I want to thank MATTHEW REAGOR and CHRIS AXLINE for pioneering the development of high-Q 3D cavities with integrated quasi-3D readout restructures. The design of the double-cavity devices that enabled the experiments discussed in this thesis would not have been possible without the foundational work they established. I also had a chance to work SERGE ROSENBLUM and BRIAN LESTER on my final experiments in the lab. Despite the steep learning curves and relatively demanding timeline, they are able to pick up the threads quickly and push the experiment forward. It is truly exciting to see new developments built upon my prior work.

I would like to express my deep gratitude to LUIGI FRUNZIO, who is unarguably the pillar of our team on the 4th floor. He provides the essential support that ensures the smooth day-to-day running of the lab. Luigi is also one of the most generous people I have encountered, always willingly to share his experience and provide invaluable advice to someone in need. His fun stories make fabrication trainings with him such a thoroughly enjoyable experience. I must also highlight the important roles played by GISELLE DEVITO, MARIA RAO, THERESA EVANGELISTE and NUCH GRAVES. Their diligent work shielded us from administrative quandaries that I would inevitably find myself in without their help.

I have been fortunate enough to work closely with Prof. LEONID GLAZMAN, Prof. LIANG JIANG and Prof. STEVE GIRVIN during my study at Yale. The scale and depth of their knowledge never cease to amaze me. Discussions with them are always immensely illuminating. They have helped me gain so much valuable insight into both the concepts that underpin my experimental work and the fascinating realm of quantum physics in general. I am also grateful for my external readers Prof. PETER RAKICH and Prof. DAVE SCHUSTER for taking their valuable time to read through this thesis and help me make it better.

My experience working with Prof. MICHEL DEVORET is truly unforgettable. His incredibly intuitive understanding of quantum mechanics and mesoscopic physics has helped

me see them from a different light and make interesting connections between different areas of the field. He is also a master of analogies, often able to provide the most apt and elegant descriptions of abstract concepts using simple phenomena from our daily lives.

Most importantly, I would like to thank my advisor, Prof. ROBERT SCHOELKOPF. I am immensely grateful that he has given me the opportunity to join this extraordinary team of people on the 4th floor. The open, collaborative research environment Rob and Michel created is such a creative haven where there is never a shortage of exciting new ideas. Rob has also taught me the importance of microwave hygiene and perils of ground loops. Through my interactions with Rob, I have also learnt how to consolidate ideas and present them in the most succinct yet impactful manner. His mentorship has not only allowed me to become a more competent researcher but also helped me grow as a person.

Finally, I would like to thank my mum, GUIYU, and my dad, HONGYI, for instilling in me a strong sense of optimism and adventure. Their love and encouragement have pushed me forward through all the ups and downs in my life. I am also thankful to my dear friend IVAN TAN, who has been such a pillar of strength that I know I could always count on. Last, but definitely not the least, I would like to thank STEVEN TOUZARD for being my best friend and partner during this wonderful journey; and my dog, LOU, for always being so happy to see me when I get back from work.

I have indeed been extremely fortunate to have these amazing people in my life. The accomplishment of my doctorate and this thesis would not have been possible without their unconditional love and support. Thank you all!



## Chapter 1

# Introduction

The idea of using the unique characteristics of quantum mechanics to perform computational tasks is first brought forth by Richard Feynman [1]. In his vision, a quantum computer will not only provide significant speed-ups over its classical counterparts but more crucially, will allow us to simulate quantum mechanical phenomena in nature that cannot be captured by classical machines. In less than three decades since Feynman's thought experiment, the field of quantum computing and quantum information science is abuzz with amazing new ideas and developments. The rapid progress both our understanding of the fundamental features of quantum mechanics and the ability to verify these concepts experimentally has made the realisation of a quantum computer closer than ever.

In order to fully comprehend the concepts of quantum computing, one must be willing to relinquish the familiar, and comforting, principles that govern the operations of a classical computer. This is because the inner workings of a quantum computer are fundamentally different from the usual *modus operandi* of computation in the classical world. In contrast to the deterministic nature of classical mechanics, the outcome of a quantum measurement is intrinsically probabilistic. Further, the 'spooky' effects of quantum mechanics, such as superposition and entanglement, are exploited as a feature rather than a bug. David Deutsch summed up these unusual characteristics and the resulting computational potential of a quantum computer using a concept he called 'quantum parallelism'. It highlights that a quantum machine could provide the ability to act on superpositions and therefore the global properties of a large system can be extracted efficiently with a single round of

computation. This gives a quantum computer superior computational power over its classical counterparts and makes it ideal for solving highly demanding problems such as factorisation and simulations involving a large ensemble of particles.

In this brief introductory chapter, I will touch on some of the most basic building blocks of a quantum computer. My goal is to provide a brief overview of some key ideas that have shaped the direction of my experimental work, rather than providing an extensive review of the field. We will look into three main topics: the properties of a quantum bit (section 1.1), the mechanisms that could degrade the quantum information (section 1.2), and the remedy against them (section 1.3). The discussion will then be followed by a synopsis of the forthcoming chapters in the rest of this thesis.

## 1.1 A quantum bit

Just as a *bit* is a fundamental concept of classical information, a quantum bit, or ‘qubit’ for short, is an elementary building block of quantum information and quantum computing. However, unlike its classical counterpart, a qubit has more than two possible states. A general state of a qubit can be described by its wavefunction,

$$|\psi\rangle = \alpha|0\rangle + \beta|1\rangle \tag{1.1}$$

where  $\alpha, \beta$  can be complex numbers and  $|\alpha|^2 + |\beta|^2 = 1$ . In other words, the state of a qubit is a vector in a two-dimensional complex vector space span by the basis states  $\{|0\rangle, |1\rangle\}$ . In fact, any pure state state can be represented by a state vector in this space. While  $|\psi\rangle$  contains the full information about a pure state, it is insufficient if we want to describe quantum systems in mixed states, which are statistical ensembles of several quantum states. Instead, we can use the density matrix,  $\rho$ , as a more general description of the quantum system. It is defined as

$$\rho = \sum_j p_j |\psi_j\rangle \langle \psi_j| \tag{1.2}$$

where the coefficient  $p_j$  is the probability of being in a state  $|\psi_j\rangle$ . The density matrix formalism offers a convenient tool to describe a general quantum system and its dynamics.

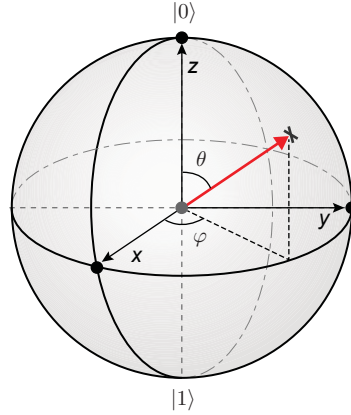


Figure 1.1: **The Bloch sphere representation of a qubit.** It allows a geometric interpretation of the qubit state which can be expressed by a complex vector on the sphere. It can be characterised by two numbers that corresponds to the equatorial and azimuthal angles,  $\theta$  and  $\varphi$

A qubit can be implemented in many different physical forms. In fact, any quantum state with two well-defined levels, such as the orientation of a nuclear spin in a magnetic field or the energy levels of an atom, can be used to realise a qubit. A useful geometrical representation for a two-level quantum systems is the Bloch sphere, as illustrated in Fig 1.1, where the two poles correspond to the two orthogonal basis states, denoted as  $|0\rangle$  and  $|1\rangle$ . Any arbitrary qubit state can be visualised as a point on this unit three-dimensional sphere defined by

$$|\psi\rangle = \cos \frac{\theta}{2} |0\rangle + e^{i\varphi} \sin \frac{\theta}{2} |1\rangle \quad (1.3)$$

where  $\theta, \varphi$  are real numbers. All pure states of two-level the system can be simple described as a point lying on the surface of the sphere, whereas the interior points correspond to the mixed states associated to the density operator  $\rho$ . One can, in principle, store an infinite amount of information within a single Bloch sphere. However, due to the quantum mechanical nature of the system, only a single bit of information about the state of the qubit can be obtained from each measurement.

We can fully control these quantum bits and their superpositions using quantum gates.

Since any single qubit state can be represented by a two-component complex vector on the Bloch sphere, we can also express the gates as simple  $2 \times 2$  Hermitian matrices ( $M = M^\dagger$ ). One particularly useful set of  $M$  is given by the Pauli matrices, which can be written as

$$\sigma_z = \begin{pmatrix} 1 & 0 \\ 0 & -1 \end{pmatrix}, \quad \sigma_x = \begin{pmatrix} 0 & 1 \\ 1 & 0 \end{pmatrix}, \quad \sigma_y = \begin{pmatrix} 0 & -i \\ i & 0 \end{pmatrix}, \quad \sigma_i = I = \begin{pmatrix} 1 & 0 \\ 0 & 1 \end{pmatrix} \quad (1.4)$$

We can visualise the action of these operations on the Bloch sphere of a qubit, where  $\sigma_{x,y,z}$  is simply a rotation by  $\pi$  about each respective axis. In other words,  $\sigma_z$  imparts a differential phase of  $\pi$  between  $|0\rangle$  and  $|1\rangle$  and  $\sigma_x$  flips their populations,  $\sigma_y$  performs both of these operations together, and  $\sigma_i$  is equivalent to the identity operation. They provide a complete set gates to perform arbitrary manipulations of a qubit.

The appeal of a quantum computing over classical systems becomes apparent when we bring together multiple quantum bits. Thanks to the ability of a single qubit to be in a superposition state, a two-qubit state can now exist in a superposition of  $2^N$ , ( $N = 2$ ) different states.

$$\begin{aligned} |\psi\rangle &= |\psi\rangle_{Q1} \otimes |\psi\rangle_{Q2} \\ &= \frac{1}{\sqrt{2}}(|0\rangle + |1\rangle) \otimes \frac{1}{\sqrt{2}}(|0\rangle + |1\rangle) \\ &= \frac{1}{2}(|00\rangle + |01\rangle + |10\rangle + |11\rangle) \end{aligned} \quad (1.5)$$

Taking advantage of the nature of quantum mechanics, a quantum computer is able to operate on all possible configurations of the state simultaneously. This feature is called quantum parallelism. With the help of clever transformations [2, 3], it allows us to extract the global property of the system efficiently with a single round of calculation. In other words, we can consider a system with  $N$  qubits as a function,  $f(x)$ , which contains  $2^N$  arguments. If we were to compute a complete table of the values of  $f(x)$  on a classical computer,  $2^N$  calculations are required. The problem quickly becomes intractable due to this hefty scaling. In contrast, a quantum computer, thanks to quantum parallelism, is

able to compute  $f(x)$  once and extract the global properties of the system. This allows the quantum computer to achieve exponential speed-ups and hence, significant boost of its computational power.

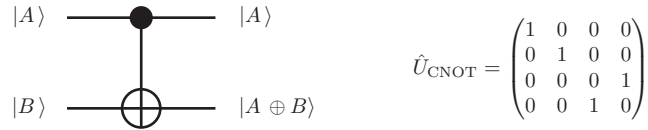


Figure 1.2: **A CNOT gate.** The circuit representation of a CNOT gate between A and B with its corresponding unitary matrix

Another uniquely quantum mechanical resource that can be harnessed for quantum computing is entanglement. When systems are entangled with one another, the resulting measurement correlations are stronger than the bounds set by classical physics. When such non-classical correlations exist among the parts of a system, we can no longer fully decipher the state of the system by dividing it up and studying the individual parts separately. An example of maximally entangled state of two qubits is defined as

$$|\phi^\pm\rangle = \frac{1}{\sqrt{2}}(|00\rangle \pm |11\rangle) \quad (1.6)$$

In such a state, local measurement of the first bit along any chosen axis yields a completely random outcome. This type of entangled state can be generated using the controlled-NOT (CNOT) gate. Similar to single qubit manipulations, the CNOT gate can be expressed as a unitary matrix  $U_{\text{CNOT}}$  (Fig 1.2). It is a transformation that flips the second (Target) bit if the first (Control) is ‘1’, and acts trivially if the first is ‘0’. Therefore, by initialising the Control in a superposition state, we can generate an entangled pair of qubits, which is often referred to as an EPR pair or a Bell state. Their highly non-classical correlations provide valuable resources for a wide range applications such as quantum teleportation and quantum key distribution.

## 1.2 Fragility of a quantum bit

Unique features of quantum mechanics such as superposition and entanglement allow a quantum computer to have superior computational potential over any classical machine. However, these very features also make quantum information much more fragile. Let us consider a simple comparison between a classical and quantum switch as shown in Fig 1.3. In a classical system, the state of a switch is determined by some control parameter (e.g. the applied voltage). Since a classical bit is only binary, i.e. it can take one of two possible outcomes, we can choose a threshold value to divide the response of the system to either ‘0’ or ‘1’. As a result, there is no direct one-to-one mapping between the value of the control parameter to the final state of the switch and hence, a small fluctuation in the control signal by  $\pm\epsilon$  does not lead to an incorrect response of the switch.

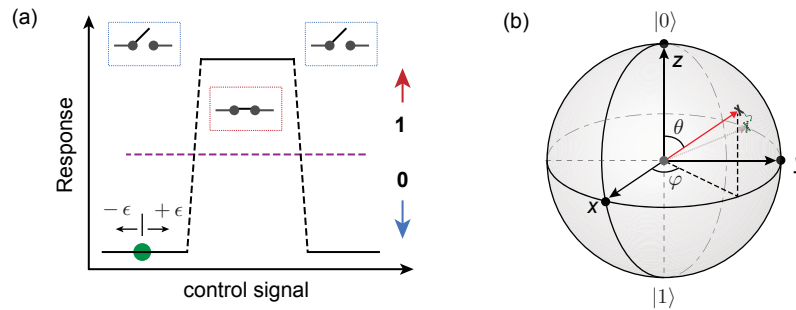


Figure 1.3: **Cartoon description of the different nature of classical and quantum errors.** (a) The state of a classical bit, such as whether a switch is open or closed, is governed by a control signal with a well-defined threshold (purple dashed line). Any value below the threshold counts as a ‘0’ and any value above it, a ‘1’. When a small amount of noise (error) with amplitude  $\epsilon$  occurs in the control signal, it will not affect the state value assigned. (b) In contrast to this, a quantum bit lives on the surface of a Bloch sphere and hence, its parameters are no longer discrete numbers. Any small amount of noise would affect the state of the qubit and corrupt the information it carries.

Physically, errors can occur in a quantum system due to either imperfect operations (unitary errors) on the state or environmental decoherence. The former is usually associated with incorrect knowledge of the full system dynamics. This results in errors in the unitary manipulations we perform on the qubits and causes the operation to deviate from

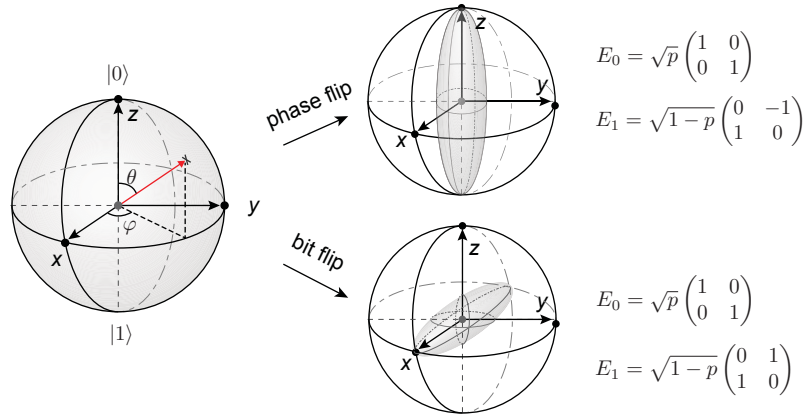


Figure 1.4: **Effects of two types of errors on a qubit.** A bit flip error causes the state of a qubit to be flipped from  $|0\rangle$  to  $|1\rangle$  (and vice versa) with probability  $1 - p$ . This causes a contraction of the Bloch sphere in the  $\hat{y} - \hat{z}$  plane, while leaving the  $x$ -axis unharmed. The phase flip error modifies the phase of the quantum superposition. This causes an contraction in the  $\hat{x} - \hat{y}$  plane while leaving the  $z$ -components intact

the intended unitary transformation. However, even if we can somehow achieve perfect knowledge of our quantum system, we still face the challenge of decoherence. It is generally defined as a process in which the environment continually measures the quantum system, collapsing it into one of its basis states. Despite our best efforts in isolating the delicate quantum information from its noisy environment, it always has some finite interaction with the outside world. There are three main types of decoherence mechanisms in a two-level system. Consider a state  $|\psi\rangle = c_0|g\rangle + c_1|e\rangle$ . It can experience amplitude damping, which can be thought of as a loss of excitation, at rate  $\Gamma_{\downarrow}$ . This is the undesired change of the qubit's state from  $|e\rangle$  to  $|g\rangle$  due to the an exchange of energy between the qubit and the environment which has an equilibrium population of  $n_{\text{th}}$ . The second type of decoherence is dephasing, occurring at the timescale  $T_{\phi}$ . It is a unique quantum error channel which leads to a modification of the phase relationship between  $c_0$  and  $c_1$  without any energy loss. Additionally, the upward transition from  $|g\rangle$  to  $|e\rangle$  at rate  $\Gamma_{\uparrow}$  will also degrade the coherence of the quantum state. Overall, these processes will cause the state of the qubit to decay exponentially in time,  $t$ , towards a thermal equilibrium with its environment and completely corrupt the quantum information. As a result of these decoherence processes, quantum information is subjected to two types of errors: bit flip and phase flip, as illustrated by the two

deformed Bloch spheres in Fig 1.4. We can quantify the associated time scales with a single decoherence time  $T_2$ , where  $1/T_2 = 1/2T_1 + 1/T_\phi$ , where  $1/T_1 = \Gamma_\uparrow + \Gamma_\downarrow$ . Finite  $T_2$  in most quantum systems poses a major limitation to quality of quantum gates and complexity of the operations. The investigation of the various mechanisms that causes qubit decoherence is an extensive research area on its own. While we will not go into the details of these topics, one must recognise that in order to design a robust quantum computer, we must overcome these decoherence penalties. This demands both better coherence properties of our quantum system as well as clever quantum error correction schemes that will eventually allow us to detect and rectify both unitary and naturally-occurring errors in the quantum computer.

### 1.3 Towards operations on error-corrected logical qubits

Despite the seemingly insurmountable challenge of preserving quantum information in presence of the above-mentioned error channels, there is still hope for the quantum computer! Sophisticated quantum error correction (QEC) schemes have been developed to combat both unitary errors and decoherence. Central to these algorithms is the familiar idea of redundancy, which is used to provide protection against bit flip errors in classical error correction. In the quantum regime, instead of putting quantum information in single a two-level system, henceforth referred to as a physical qubit, we can redundantly encode the same information in a higher dimensional Hilbert space. When such an encoded bit of information is exposed to the ravages of a noisy environment or actions of a flawed quantum gate, we can now exploit certain symmetry properties associated with the particular encoding to detect and correct errors and recover the information without any corruption. We define this type of quantum entity as a logical qubit. Regardless of the specific physical implementation, quantum computation must ultimately be carried out on these error-protected logical qubits rather than directly on two-level systems.

The ability to implement robust logical qubits is no doubt an important milestone in quantum computing and a culmination of the continual efforts in various other aspects. I find it very instructive to think about the requirements of a successful quantum computer

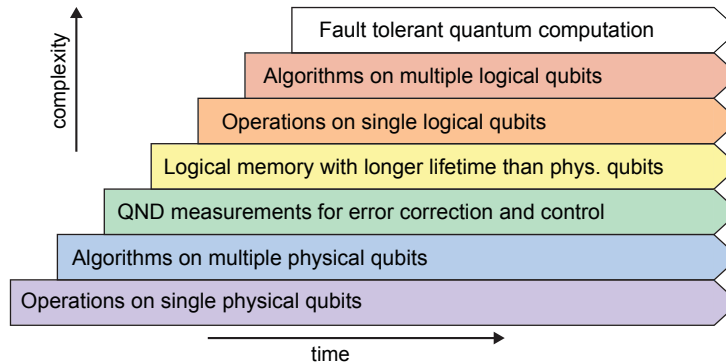


Figure 1.5: **A roadmap for quantum computing.** Figure reproduced from Ref. [4] describing the key stages in the development of robust quantum computation. While each advancement is built upon the mastery of the preceding steps, every individual component is a continuing task that needs to be perfected in parallel with the others.

as a set of overlapping and interconnecting stages (Fig 1.5) as discussed in Ref. [4]. The most fundamental requirement is the ability to have a robust physical qubit with sufficient coherence to allow its quantum state to be robustly manipulated and measured. Having established that, one must then control multiple physical qubits and implement high-quality quantum gates between them. Naturally, we must also be able to faithfully obtain the information without destroying it through the quantum non-demolition measurements. All of these steps are pivotal for the realisation of logical qubits which can be protected against quantum errors and have more robust performance than their uncorrected constituent parts. This is no easy feat but absolutely critical. The ability to attain this milestone will allow us to tackle the final hurdles of manipulating a collection of such logicals in order to achieve the eventual realisation of a robust quantum machine. Although many of these topics will not be discussed in detail in the scope of this writing, I must emphasise that the eventual success of our efforts will depend on continual research and improvements in each and every area mentioned above.

## 1.4 A précis of the chapters to come

The overarching theme of my Ph.D work is the development of essential tools required for implementing complex quantum operations on multiple logical qubits. This is very much motivated by the need for efficient quantum error correction as mentioned in introductory remarks above. In chapter two, I will describe the basics of our physical system, namely, superconducting circuit Quantum Electrodynamics (cQED) and aim to provide an overview of some of the exciting experimental progress made in this framework. In particular, I will introduce 3D superconducting cavities and highlight the reasons why it has become an increasingly attractive candidate for encoding quantum information. Needless to say, we will also devote time to discuss the Josephson junction and the transmon qubit, both are indispensable components for quantum operations in cQED. We will then proceed to discuss the control and measurement of single logical qubits encoded in cavities before ending chapter two with a brief discussion of how we can expand our information capacity by going to multi-cavity architectures.

In chapter three, I will elaborate on the idea of building a 3D multi-cavity structure where we can encode several logical qubits and implement operations amongst them using nonlinearities provided by transmon ancillae. I will describe in detail the design principles of the very first copy of a two-cavity system, bridged by a Y-shaped transmon which we call the ‘Ymon’. Following this, we will dwell into some techniques used to characterise this sample and highlight the its properties. In the last section of the chapter, we will introduce some of the upgrades introduced in the next generation of multi-cavity devices to facilitate the increasing complexity of the experiments. The devices described in this chapter form the cornerstone of all my major experimental works, which are discussed in the following four chapters.

Chapter four provides the details of the very first two-cavity experiment where we created and characterised a two-mode entangled cat state living in two spatially and spectrally separated boxes. In section 4.1, I will describe the entanglement generation between the two cavity modes via their dispersive interaction with the transmon ancilla. Following this, we

will explore the challenges of characterising the two-mode entangled cat state and how we can use additional levels in the transmon to perform joint Wigner measurements. In the final section of the chapter, I will show that this state is both an elegant demonstration of non-local mesoscopic entanglement and a useful resource for quantum information processing.

The next experiment carried out using this architecture goes beyond state creation and measurement; it aims to implement an entangling operation between multi-photon states stored in two separate cavities. This work is documented in chapter five, where I will start by describing an driven sideband transition that allows the transfer of excitation between a cavity and a transmon. In the subsequent section, I will explain how we combine this type of engineered interaction with the natural Hamiltonian to implement a CNOT gate between two cavity modes. Finally, we characterise the performance of this operation using quantum process tomography (QPT) as discussed in the section 5.3. In the concluding section of this chapter, I will have a discussion about the limitations of this implementation and how we can overcome them in future experiments.

Chapter six will present a different strategy to enable cavity-cavity interactions. I will describe the method used to directly couple two cavity modes without physically populating the excited levels of the transmon. We will study this type of engineered bilinear coupling in depth and quantify the imperfections present in our particular implementation. We will then proceed to show that this type of coupling alone can accomplish a variety of operations between two cavities such a 50:50 beamsplitter and a SWAP gate. Finally, we employ this type of coupling to implement a series of bosonic interference experiments between two detuned cavities using the 3D multi-cavity device.

In the final experiment, we will delve into the details of how we utilise this bilinear coupling to construct the exponential-SWAP (e-SWAP) unitary. It is a particularly useful operation because it provides a universal entangling capability between two bosonic modes. We will present a robust protocol to realise this unitary in cQED that suppresses the penalty of transmon  $T_1$  and  $T_2$  errors. I will then demonstrate this operation in action using different types of encodings. Last but not least, I will explore the future extensions of this experiment and some modifications to the system that would overcome some of the current limitations.

Finally, in the closing chapter, I aim to provide a holistic overview of my experiments and their relevance to our vision of modular quantum computer. I hope that the ideas and experimental progress documented in the preceding chapters of this thesis will inspire the readers to continue to push the frontiers of quantum computing with both great stoicism and optimism, and very importantly, have fun during the process.

## Chapter 2

# Logical qubits in Circuit QED

Over the past decade, quantum computing and quantum information science have gathered tremendous momentum from both academic and commercial research entities alike. With this comes the relentless progress in both the theoretical and experimental front, making such quantum machines no longer merely mathematical curiosities. In fact, the field has brought together a diverse, inter-disciplinary assembly of scientists and engineers who are working towards realising a robust and scalable quantum computer in various different physical systems. In general, any physical implementation of quantum information processing must satisfy a few basic prerequisites as outlined in [5]. These requirements include the ability to robustly represent quantum information and perform a universal set of unitary operations on them. Furthermore, we must also be able to both prepare fiducial initial states and faithfully measure the outcomes after quantum operations.

While many physical systems have shown outstanding capabilities in a particular aspect of these criteria, it remains a rather difficult balancing act to meet all the requirements. For example, optical photons, with their two orthogonal polarisations, are an attractive system to represent a quantum bit because they are chargeless particles that interact weakly with one another, as well as the environment. Consequently, they can also be easily transmitted over long distances with low loss in optical fibres, delayed with phase shifters, and combined using beamsplitters. However, the same properties that make photons appealing quantum systems also mean that it is highly challenging to both produce high-quality non-classical initial states and implement deterministic, non-linear operations between individual photons.

Such trade-offs are generally present in other physical implementations as well and the ability to achieve an optimised balance between these aspects is often key to designing an effective system for quantum computing.

The system that we focus on essentially consists of quantised superconducting electrical circuits where some non-linear elements, sometimes referred to as ‘artificial atoms’, interact with linear oscillators in the quantum regime. This general framework is referred to as circuit quantum electrodynamics (cQED) by analogy to cavity QED where photons interact with real atoms. cQED systems have an intrinsic advantage in achieving the balance between the above-mentioned aspects of quantum computing, which makes them ideal platform for quantum computing. Some of the merits of superconducting cQED implementations are highlighted here:

- **Ultra-low dissipation due to superconductivity.** Superconductors can carry electric signals without energy loss. This is a crucial condition for preservation of quantum coherence of this system.
- **Low noise as a result of low temperature.** Superconducting devices are generally operated at 10-20 mK inside commercially-built dilution refrigerators. At this temperature, the typical energy,  $kT$ , associated with thermal fluctuations is insignificant compare to the transition energy,  $\hbar\omega_{01}$  of a two-level system, usually designed to have  $\omega_{01} \sim 5$ -10 GHz. This ensures that any thermal occupation is negligible and the system can truly remain in its quantum ground state.
- **Availability of non-dissipative nonlinear element.** Quantum computing cannot be performed using purely linear components. In cQED devices, the nonlinearity is provided by Josephson tunnel junctions, which are non-dissipative quantum elements at the operating temperatures of superconducting devices. They are also relatively straightforward to fabricate and can be easily integrated with other superconducting structures.
- **Highly engineerable and lithographically defined Hamiltonians.** The exact parameters for each individual circuit can be simulated and optimised a priori to

produce the most suitable device for the intended task. The fabrication process is relatively fast and reliable, thanks to the highly mature electron-beam and photo lithography technologies. This makes it possible for us to achieve target system parameters with good precision.

- **Low noise classical controls.** Such systems are typically probed with microwave signals which have much more favourable noise properties compared to those associated with DC controls and better stability than most lasers.

Taking advantages of these favourable properties, superconducting cQED systems have shown outstanding progress in recent years and emerged as one of the most promising contenders for the realisation of robust quantum computation. Numerous breakthroughs, from the continual improvements of coherence properties to the rapid developments in high quality manipulations and characterisation of complex quantum states, have been demonstrated over the past decade.

The experiments covered in thesis are all carried out in the cQED playground with 3D superconducting systems and this chapter is dedicated to provide an overview of this framework. Since the physics of cQED have been discussed extensively in many excellent articles [6, 7, 8] and textbooks [9, 10, 11], I will not attempt to present an exhaustive account in this thesis. Rather, I will summarise the basic concepts with a focus on the specific knowledge necessary for understanding the experimental works described in the later chapters.

In section 2.1, I will start by describing one of the simplest cQED components: the quantum harmonic oscillator. We will outline the derivation of its quantised energy levels and briefly discuss the physical realisations of such quantum oscillators in superconducting systems. Then, in section 2.2, we will discuss the coupling of such linear modes to artificial atoms constructed using Josephson junctions. The specific type of artificial atom developed and most commonly studied in our team is the transmon [12]. It is the preferred nonlinear element in our systems for its good coherence properties and well-understood system Hamiltonian. Subsequently, section 2.3 will provide details about the Hamiltonian that described

the transmon-resonator system. In particular, we will consider the dispersive coupling which is responsible for the efficient readout of the transmon state and also allows us to implement conditional operations on a cavity state. In section 2.5, I will present the techniques used to manipulate and measure quantum information encoded in a cavity via its dispersive coupling to a transmon ancilla. We will conclude this chapter by discussing how we can use such systems to store quantum information in a manner that offers protection against errors in section 2.6.

## 2.1 Quantum LC oscillators

An LC oscillator, illustrated in Fig. 2.1(a), is one of the simplest circuit elements where the total energy of the system oscillates between the inductor and the capacitor. We can model the dynamics of such an oscillator by considering the Lagrangian in terms of the capacitor charge,  $Q$ , and inductor current,  $I$ :

$$\mathcal{L} = \frac{1}{2}LI^2 - \frac{1}{2}\frac{Q^2}{C} \quad (2.1)$$

In the lumped element limit where the physical size of the oscillator is much smaller than the wavelength of the electromagnetic waves at the frequency of the oscillator, we can assume that the current flow in the wires of the inductor does not build up charges anywhere except on the plates of the capacitor. Therefore, using charge conservation,  $I = \dot{Q}$ , we can write

$$\mathcal{L} = \frac{L}{2}\dot{Q}^2 - \frac{1}{2C}Q^2 \quad (2.2)$$

We now have reduced the system's dynamics to a single degree of freedom, which corresponds to the collective motion of all the electrons sloshing back and forth, charging and discharging the capacitor. Using Eq. 2.2, we derive the Euler-Lagrange equation of motion for the LC oscillator as

$$\ddot{Q} = -\omega^2 Q \quad (2.3)$$

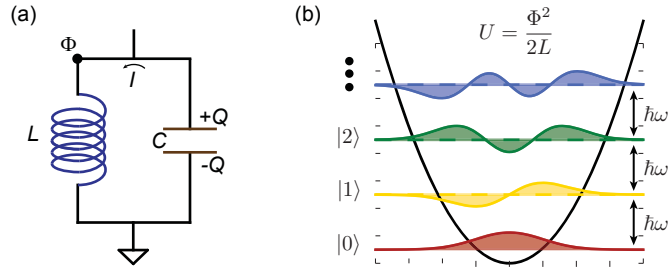


Figure 2.1: **Quantised harmonic oscillator** (a) A harmonic oscillator in the form of a resonant LC circuit, where  $L$  is the inductance  $C$  the capacitance and  $\Phi$  a time-dependent flux that is analogous to the position variable in a classical oscillator such as pendulum. Similarly, just the momentum is conjugate variable to position, the charge,  $Q$ , here is the conjugate to  $\Phi$ . (b) The equally-spaced energy levels of a quantised LC oscillator. The wavefunctions corresponding to the first four energy levels are sketched in red, yellow, green, and blue, respectively.

with  $\omega$  being the resonance frequency of the resonator given by  $\omega = 1/\sqrt{LC}$ . This is akin to the treatment of a simple system of mass on a spring where frequency of the oscillation,  $\omega$ , is only a function of the ‘mass’ ( $L$ ) and the ‘spring constant’ ( $1/C$ ).

Now we can write the Hamiltonian of the system as

$$H = \frac{\delta \mathcal{L}}{\delta \dot{Q}} \dot{Q} - \mathcal{L} = \frac{\Phi^2}{2L} + \frac{1}{2C} Q^2 \quad (2.4)$$

where  $\Phi = \frac{\delta \mathcal{L}}{\delta \dot{Q}}$ , is the node flux and the conjugate variable to  $Q$ . We can consider  $\Phi$  as the position coordinate of the system and  $Q$  the conjugate momentum, or vice versa. Following the usual treatment,  $\Phi$  and  $Q$  can be promoted to quantum operators by obeying the canonical commutation relation:

$$[\hat{\Phi}, \hat{Q}] = -i\hbar \quad (2.5)$$

and we can write the Hamiltonian of quantum LC oscillator:

$$\hat{H} = \hbar\omega(\hat{a}^\dagger \hat{a} + \frac{1}{2}) \quad (2.6)$$

with the raising and lowering operators  $\hat{a}^\dagger, \hat{a}$ :

$$\hat{a} = i \frac{1}{\sqrt{2L\hbar\omega}} \hat{\Phi} + \frac{1}{\sqrt{2C\hbar\omega}} \hat{Q} \quad (2.7)$$

$$\hat{a}^\dagger = -i \frac{1}{\sqrt{2L\hbar\omega}} \hat{\Phi} + \frac{1}{\sqrt{2C\hbar\omega}} \hat{Q} \quad (2.8)$$

This recovers the familiar dynamics of particle in a parabolic potential well and the wavefunction associated with each energy level describes the probability amplitudes that a particle can be found at certain positions within the well as sketched in Fig. 2.1(b). The energy eigenstates of the Hamiltonian,  $|n\rangle$ , are known as Fock states. Since  $(\hat{a}^\dagger)^m |n\rangle$  are also eigenstates for any integer  $m$ , there are infinite number of energy eigenstates with energies evenly separated by  $\hbar\omega$ .

We can also express the charge and phase operators in terms of  $\hat{a}, \hat{a}^\dagger$ :

$$\hat{\Phi} = \Phi_{\text{ZPF}}(\hat{a} + \hat{a}^\dagger) \quad (2.9)$$

$$\hat{Q} = -iQ_{\text{ZPF}}(\hat{a} - \hat{a}^\dagger) \quad (2.10)$$

where  $\Phi_{\text{ZPF}} = \sqrt{\hbar Z/2}, Q_{\text{ZPF}} = \sqrt{\hbar/2Z}$  are the zero-point fluctuations of the phase and charge of the oscillator's ground state, and  $Z = \sqrt{L/C}$  the characteristic impedance of the circuit. From this, we note that  $\Phi_{\text{ZPF}}$  and  $Q_{\text{ZPF}}$  are two conjugate variables that obey the Heisenberg's uncertainty relation.

This simple calculation reveals an interesting feature of the quantum LC oscillator: its fully quantum mechanical dynamics are shaped by two classical, macroscopic observables  $L$  and  $C$ . Both of these quantities can be designed and fabricated with good precision using standard lithographical or machining techniques. This entails that we now have at our disposal a fully quantum mechanical device whose characteristics can be engineered reliably and reproducibly. In particular, we can design the resonance frequency of the oscillator such that it can be cooled to its ground state,  $|0\rangle$ , at the operating temperatures of a commercial dilution refrigerator ( $T \sim 10$  mK) in order to suppress undesired population in the higher energy levels. This requirements puts a lower bound on the frequency given

by  $\omega/2\pi \gtrsim 5$  GHz for a vanishingly small population in  $|1\rangle$  suppressed by the Boltzmann factor  $e^{-\hbar\omega/k_B T} \simeq e^{-20}$ .

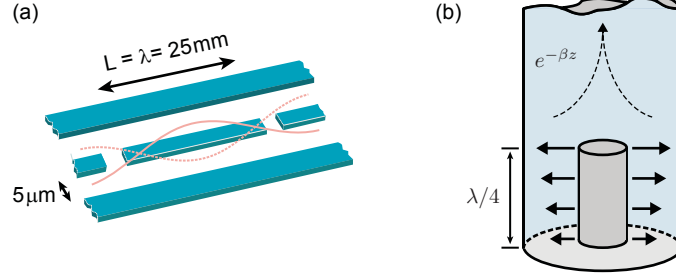


Figure 2.2: **Planar and 3D superconducting resonators** (a) Schematic illustration of a typical coplanar waveguide (CPW) resonator used in cQED. It consists of a superconducting wire evaporated on an insulating substrate with the ground planes on the same surface. The resonance frequency is determined by the length of the centre conductor and can be fabricated with high precision using standard lithographic methods. (b) Another physical implementation of such an LC oscillator in a 3D architecture where the energy resides primarily in vacuum, allowing superior coherence properties compared to planar structures.

There are many ways to realise a quantum LC oscillator in cQED. Broadly speaking, they can be constructed using any structure with well-defined electromagnetic modes such as transmission lines or cavities. Mathematically, a cavity can be treated as the continuum limit of a chain of the simple LC oscillators described above plus some additional resistive component reflect the losses present in the physical realisation. Two examples of quantum resonators commonly used in our experiments are illustrated in Fig. 2.2. The coplanar waveguide (CPW) resonator shown in Fig. 2.2(a) is composed of a centre conductor of length, ‘L’, width, ‘w’, separated by a gap, ‘g’, from the ground plane [13, 8]. These values are chosen to achieve a certain characteristic impedance, usually  $Z_0 = 50\Omega$ . The structure is patterned on a dielectric wafer with thin-film superconducting material, usually aluminium, deposited on the surface using either photo lithography or electron-beam lithography. It has been shown that the state-of-the-art CPW resonators can reach internal quality factors of  $Q_{\text{int}} \sim 10^6$  [14]. Such planar structures are compact and easy to fabricate, making them a staple in many cQED experiments. However, it is understood that their coherence will ultimately be limited by the material imperfections as most of the electric energy of such a resonator is stored in the substrate. To further prolong the lifetime of these resonators, it

is desirable to devise an alternative structure in which the electric energy of the resonator is predominantly stored in materials with low loss.

This leads us to a different design of quantum oscillators using 3D structures, in which the electric field resides primarily in vacuum, which is lossless. In Fig. 2.2(b), we highlight a particular design that has demonstrated outstanding coherence properties with  $Q_{\text{int}} \sim 10^8$ . In this design, a quarter-wave coaxial resonator is defined by short circuiting the inner and outer conductors of the coaxial transmission line at the bottom of the cylindrical structure and open circuiting the line at a distance  $\lambda/4$  away. The top of the centre conductor and the sidewalls of the cylinder form a waveguide with a cutoff frequency much higher than the resonance of the coaxial resonator in order to suppress energy dissipation. The quality factor is further enhanced by the lack of seams as the entire structure is machined out of a single block of high-purity (4N) aluminium. With these features, this type of 3D stub cavity has become an increasingly popular candidate for microwave quantum memories with storage times exceeding milliseconds [15]. They are in fact featured prominently in the experimental work discussed chapters 4 - 7.

## 2.2 Adding non-linearity with the Josephson junction

Having described the quantum mechanical properties of superconducting LC oscillators in the previous section, we now consider how they can be employed in quantum computation. Unfortunately, due to the degeneracy of their energy spectrum, such systems do not provide us a suitable two-level system to represent a quantum bit. In order to lift the degeneracy, we must introduce some form of non-linearity to the system without sacrificing the long storage times provided by these high-Q cavities.

This goal is accomplished by a remarkably simple and lossless quantum element called the Josephson junction [16, 17]. A cartoon of a junction is shown in Fig. 2.3(a). It consists of two superconducting islands separated by a thin insulating barrier. Although such a structure is made up of millions of electrons, we can represent their collective state by a single degree of freedom. This is because pairs of electrons, known as Cooper pairs, can be condensed into

a single collective ground state as we cool the device below the critical temperature of the superconductor. They can also coherently tunnel through the thin insulating barrier, which leads to a phase difference,  $\phi$ , between the macroscopic wavefunctions on each side of the barrier. This yields a new current-flux relationship described by the Josephson relation:

$$I(t) = I_c \sin \phi(t) \quad (2.11)$$

where  $I(t)$  is the tunneling supercurrent;  $\phi(t) = \Phi/\Phi_0$  the phase across the junction with  $\Phi_0 = h/2e$ . The characteristics of the junction is determined by  $I_c$ , which is the critical current of the superconductor and is usually set by the fabrication parameters of the junction. By replacing the linear inductor in a LC oscillator with the non-linear Josephson junction, we have essentially modified the quadratic potential of the linear oscillator to a cosine function as shown in Fig. 2.3b. This lifts the degeneracy between the different energy levels and therefore, making it possible for them to be addressed individually.

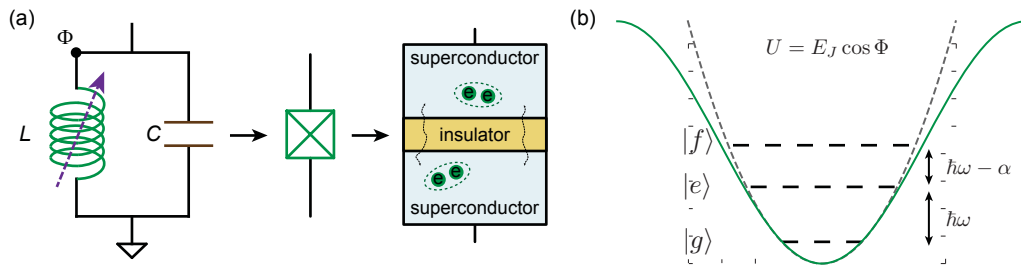


Figure 2.3: **An anharmonic quantum oscillator.** (a) A Josephson junction can be modeled as an oscillator with a non-linear inductance. Physically, this element (represented by the green box with a cross within) is composed of two superconductors separated by a thin insulating layer that allows the tunneling of electrons in pairs (Cooper pairs). When cooled far below the critical temperature of the superconductor, the tunneling events cause no significant dissipation, making the junction essentially a lossless non-linear inductor. (b) Due to the presence of the junction, the oscillator's potential is no longer quadratic (grey dashed line). Instead, it becomes a cosine function (green) of the node flux,  $\Phi$ . As a result, the degeneracy is lifted and the energy eigenstates can now be addressed individually

There are many different types of superconducting circuits which exploit the non-linearity that the Josephson junction offers. Traditionally, they employ either the flux [18, 19, 20], phase [21, 22] or charge [23, 24, 25] as the quantum degree of freedom. In the scope of

this work, we will focus on a particular type of Josephson junction based device called the transmon [26]. Its design was motivated by the need to suppress the sensitivity to charge noise which was a significant source of decoherence for superconducting charge qubits. The design of the transmon is simple: it is only composed of a single junction shunted by a large capacitance. Following the treatment in Ref. [26] and Ref. [27], we can describe the transmon circuit by the simple Hamiltonian:

$$\hat{H} = 4E_C(\hat{n} - n_0)^2 - E_J \cos \hat{\Phi} \quad (2.12)$$

where  $\hat{n}, \hat{\Phi}$  are the normalised operators for the charge and phase difference across the junction,  $n_0$  is the offset charge.  $E_C, E_J$  are design parameters that determine the key features of transmon. In particular, the transition frequency between the ground,  $|g\rangle$ , and first excited state,  $|e\rangle$ , scales as  $\omega_{ge} \sim \sqrt{8E_J E_C}$ . The charge noise refers to the fluctuations of  $n_0$ , which cause a change in the transition frequency of the circuit and induce dephasing. The protection against charge noise is achieved by choosing the parameters of the transmon such that  $1 \ll E_J/E_C < 10^4$ .

Another key parameter in the transmon design is its anharmonicity,  $\alpha$ . It is defined as the difference in transition energies of the a particular level,  $m$ , with its two neighbouring ones,  $m \pm 1$  (also referred to as absolute anharmonicity). From the exact diagonalisation of the transmon Hamiltonian in Ref. [26], we find that in the limit of large  $E_J/E_C$ , the anharmonicity simply scales with  $E_C$ :

$$\alpha = E_{m+1,m} - E_{m,m-1} \simeq -E_C \quad (2.13)$$

This indicates that as we increase  $E_J/E_C$  for reduced charge noise, we are also inadvertently lowering the anharmonicity of the transmon. A small anharmonicity undermines our ability to selectively address individual transitions with fast microwave controls. Fortunately, while the charge dispersion scales exponentially with  $E_J/E_C$ , the  $\alpha$  only scales polynomially. Therefore, in the transmon regime, it is possible to design devices with both good coherence times ( $\sim 50 - 100\mu s$ ) and large anharmonicity ( $\alpha \sim 200$  MHz) by choosing the appropriate

design parameters  $E_J$  and  $E_C$ .

All the relevant design parameters can be simulated accurately thanks to the simplicity of the transmon circuit. Another advantage of the transmon is its easy fabrication process, which involves well-established electron-beam and photo lithographic procedures. This makes it possible for us to engineer and fabricate precise device parameters that are optimised for the particular study. These favourable traits make the transmon a highly robust and versatile resource that is becoming the staple of many cQED experiments.

## 2.3 Combining transmons with harmonic oscillators

The two quantum systems introduced above, namely, superconducting cavities and transmons, are the two of the simplest and yet most crucial elements of cQED. We can engineer complex quantum structures by coupling them together in different configurations.

As an example, let us consider the case of a single transmon capacitively coupled to a simple resonator. The general Hamiltonian that describes such a system consists of the transmon Hamiltonian (Eq 2.12), that of the resonator (Eq 2.6), and a dipole coupling term that relates the voltage in the resonator, proportional to  $\hat{a}^\dagger + \hat{a}$ , to the charge of the transmon, proportional to  $\hat{n}$ . When the detuning between the two modes is far larger than their coupling strength, we can derive the familiar Hamiltonian in the dispersive coupling regime between an effective two-level system (transmon) and a superconducting resonator as detailed in many prior works [10, 28]:

$$\hat{H}_{\text{disp}}/\hbar = \omega \hat{a}^\dagger \hat{a} + (\omega_{\text{ge}} - \chi \hat{a}^\dagger \hat{a}) |e\rangle \langle e| - \frac{K}{2} \hat{a}^\dagger \hat{a}^\dagger \hat{a} \hat{a} \quad (2.14)$$

where  $\hat{a}$ ,  $\hat{a}^\dagger$  are the ladder operators of the resonator mode,  $\omega_r$  the resonator frequency,  $\chi$  the dispersive coupling, and  $K$  the inherited non-linearity of the resonator due to its coupling to the transmon.

However, the transmon is not simply a two-level system. Personally, I find it more intuitive to consider it as an anharmonic oscillator and its coupling to other modes as a hybridisation between the two modes. To treat the transmon as an anharmonic oscillator,

let us return to Eq. 2.12. We can expand the cosine and combine the quadratic terms such that it resembles the Hamiltonian of a harmonic oscillator (Eq. 2.6) with some higher order perturbations:

$$\hat{H} = 4E_C(\hat{n} - n_0)^2 + \frac{E_J}{2}\hat{\Phi}^2 - E_J \left\{ \cos \hat{\Phi} - \frac{\hat{\Phi}^2}{2} \right\} \quad (2.15)$$

Now we are able to diagonalise the quadratic parts to find the lowest order energy levels. Subsequently, we expand the argument of the cosine using Eq. 2.9 and write the higher order terms as:

$$\hat{H} = -E_J \left\{ \cos [\Phi_{\text{ZPF}}^b(\hat{B} + \hat{B}^\dagger)] - \frac{\hat{\Phi}^2}{2} \right\} \quad (2.16)$$

where  $\hat{B}, \hat{B}^\dagger$  are the ladder operators of the bare transmon mode.

Following this treatment, the coupling of a transmon to other modes can simply be considered as additional contributions to the flux. In a hybridised quantum system, excitations in other modes necessarily result in some current flow through the junction, which can be represented by a additional contributions to the argument of the cosine Hamiltonian. Therefore, in the case of a transmon coupled to a resonator in a Jaynes-Cummings interaction, we can write the re-diagonalised Hamiltonian of the system as:

$$\hat{H} = -E_J \left\{ \cos [\Phi_{\text{ZPF}}^b(\hat{b} + \hat{b}^\dagger) + \Phi_{\text{ZPF}}^a(\hat{a} + \hat{a}^\dagger)] - \frac{\hat{\Phi}^2}{2} \right\} \quad (2.17)$$

where  $\hat{a}$  and  $\hat{b}$  are the dressed operators associated with the resonator and transmon respectively. This is a particularly useful framework for systems where a single transmon is coupled to multiple resonator modes. Each additional linear mode can simply be modeled as additional components of the flux.

We can recover the more familiar form of the dispersive coupling Hamiltonian by Taylor expanding the full system Hamiltonian given by Eq. 2.17 in addition to the resonance frequencies associated with mode  $\hat{a}$  and  $\hat{b}$ . We then take the rotating wave approximation (RWA) [29] and keep all the non-rotating terms up to 4th order:

$$\hat{H}/\hbar \approx \omega_a \hat{a}^\dagger \hat{a} + \omega_b \hat{b}^\dagger \hat{b} - \chi_{ab} \hat{a}^\dagger \hat{a} \hat{b}^\dagger \hat{b} - \frac{K_b}{2} \hat{b}^\dagger \hat{b}^\dagger \hat{b} \hat{b} - \frac{K_a}{2} \hat{a}^\dagger \hat{a}^\dagger \hat{a} \hat{a} \quad (2.18)$$

where  $\omega_a$  and  $\omega_b$  are the modified resonance frequencies of the resonator and transmon respectively due to the non-linear coupling between them,  $\chi_{ab}$  denotes the dispersive coupling between the two modes,  $K_b$  is the anharmonicity of the transmon mode, also referred to as  $\alpha$ , and  $K_a$  is the anharmonicity of the resonator mode inherited from the transmon. In the limit of mode  $\hat{b}$  being a simple two-level system, Eq. 2.18 becomes Eq. 2.14.

Let us now have a closer look at each term in Eq. 2.18. First of all, the resonance frequencies of each mode are now ‘dressed’ due to mode hybridisation. The dressed frequencies can be accurately predicted using standard simulations and do not depend on the number excitations in other modes. Apart from this, the generally more important term is the state-dependent frequency shift. When operated in the strong dispersive regime, where  $\chi$  is much larger than the linewidth of the modes [13], the dispersive shift offers us a convenient tool to implement conditional operations between a transmon and a resonator mode. One example is the well-known dispersive readout where the frequency shift of a low-Q resonator is used to detect the state of the transmon [6, 7]. Conversely, we can also use the the same type of frequency shift to perform conditional gates [30] on a resonator mode controlled by the transmon state. The remaining terms are the anharmonicities associated with each mode. Typically, the transmon is the most non-linear element in the system with  $\alpha \sim 200$  MHz. The resonator that couples to it will inherit a small amount of non-linearity that roughly scales as  $K \sim \chi^2/\alpha \simeq 1 - 10$  kHz. This small inherited nonlinearity is sufficient to lift the degeneracy of energy levels in superconducting cavities and allow each transition to be addressed individually.

With these useful tools afforded by the Hamiltonian, we can couple a transmon to one or more resonators capacitively and perform quantum operations between them. Furthermore, by engineering the resonance frequencies and coupling strengths of each mode to the environment, we can achieve a separation of coherence times over 3 orders of magnitude between different components in the same system. For example, in a typical system, a transmon can simultaneously couple to a low-Q ( $Q \sim 1000$ ) resonator adapted for fast readout and a 3D high-Q cavity ( $Q \gtrsim 10^8$ ) that is ideal for information storage.

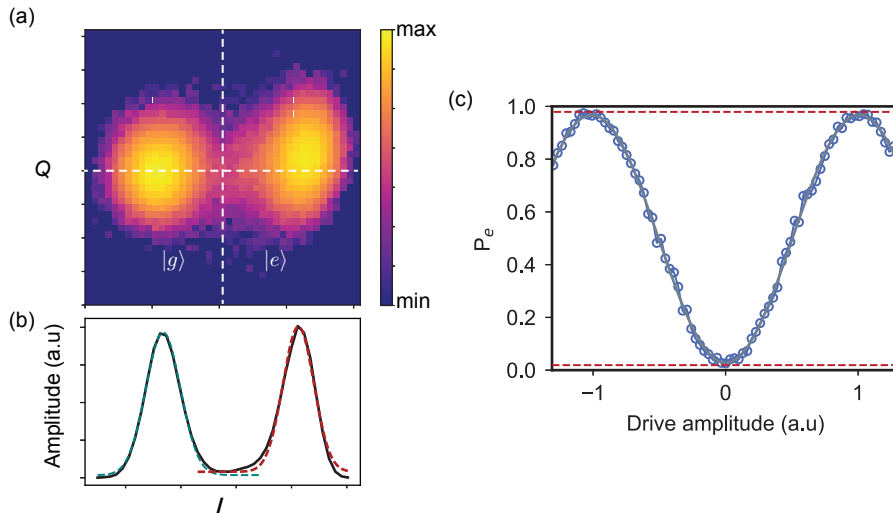


Figure 2.4: **Efficient readout of transmon state.** (a) An example of a 2D histogram showing the demodulated and integrated readout signal after quantum limited amplification through a JPC. The the in-phase ( $I$ ) and quadrature ( $Q$ ) values are an accumulation from 1000 shots on a logarithmic scale (base 2). We achieve a good discrimination between the transmon ground and excited state with a separation roughly 4 times the linewidth of their respective gaussian distribution. This allows accurate determination of transmon state from a single shot. (b) Projection of the accumulated readout signal to the  $I$ -axis. The two Gaussian peaks are well-separated with a small overlap  $\leq 0.1\%$ . (c) Rabi measurement of a transmon to determine the drive amplitude corresponding to a  $\pi$  and/or  $\pi/2$  pulses. The two red dashed lines show the Rabi contrast of  $\approx 96\%$  due to the non-zero excited state population. This can be improved with transmon cooling either through feedback or post-selection.

## 2.4 Transmon readout and characterisation

In this section, we will examine in more detail the capabilities of transmon-resonator systems provided by the dispersive Hamiltonian Eq. 2.18. We will first focus on the quantum non-demolition (QND) measurement of a transmon state using a low-Q superconducting resonator. This is extremely important since we often need to learn about the state of a transmon without destroying it. Under the strong dispersive Hamiltonian, the transition frequency of the resonator is dependent on the transmon state. Thus, by probing the transition frequency with a weak microwave drive, we can infer the state of qubit without perturbing it significantly.

An important consideration for this readout method to be effective is the relative rate at

which the information leaks out of the system ( $\kappa$ ) and the interaction strength ( $\chi$ ) between the transmon and the resonator. The lifetime ( $1/\kappa$ ) of the resonator can be controlled by simply varying its coupling to a transmission line. In a typical design, we can achieve a high-quality readout by optimising the design parameters such that  $\chi/\kappa \sim 1$ . Finally, we can further enhance the readout by amplifying the outgoing signal at the quantum limit using a Josephson parametric amplifier which can be either phase-sensitive (JBA) [31] or phase-preserving (JPC) [32]. With this, we can efficiently determine the state of a transmon in a single shot while preserving its quantum properties. A typical readout histogram with the transmon initialised in a superposition of  $|g\rangle$  and  $|e\rangle$  is shown in Fig. 2.4(a). Here, the transmitted signal from the resonator is shown in logarithmic scale. The two well-separated gaussian blobs correspond to the transmon in  $|g\rangle$  or  $|e\rangle$  respectively.

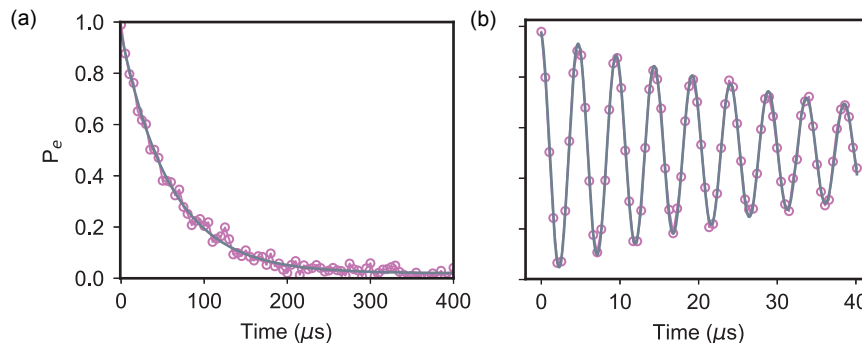


Figure 2.5: **Measurement of transmon  $T_1$  and  $T_2$**  (a)  $T_1$  measurement implemented by first exciting the transmon to  $|e\rangle$  and monitor its decay back to ground state after a variable delay time. A single exponential fit (grey) is used to extract the decay constant. For typical devices, we expect  $T_1 \sim 50 - 100 \mu\text{s}$ . (b) A Ramsey experiment to measure  $T_2$  of the transmon. The experimental sequence consists of two  $\pi/2$  pulses separated by a variable delay time. The envelope of the measured oscillations indicates the  $T_2$  and the its frequency provides us information on the detuning from the transmon  $|g\rangle - |e\rangle$  resonance frequency. In this case, we intentionally introduced a 200 kHz detuning to highlight this feature.

With the ability to efficiently and accurately determine the state of a transmon, we can now perform a series of simple measurements to determine the key parameters associated with the transmon mode. For example, we can implement a Rabi-flopping experiment to extract the power required to flip the transmon from  $|g\rangle$  to  $|e\rangle$  and vice versa. An example

of the Rabi experiment is shown in Fig. 2.4(c) where the state of the transmon oscillates as a function of the drive amplitude. The measured minima indicates the equilibrium thermal population of the transmon. In this case, the device has  $\leq 2\%$  excited state population, significantly higher than what the Boltzman statistics predict for the base temperature of the dilution refrigerator. The source of this thermal population is not yet known, but can sometimes be further suppressed through additional shielding and filtering. Practically, we prepare the ground state with high fidelity by performing an initial measurement of the transmon state and only proceed if the outcome is  $|g\rangle$ . We then characterise the coherence properties of the transmon in a series of time-domain measurements.

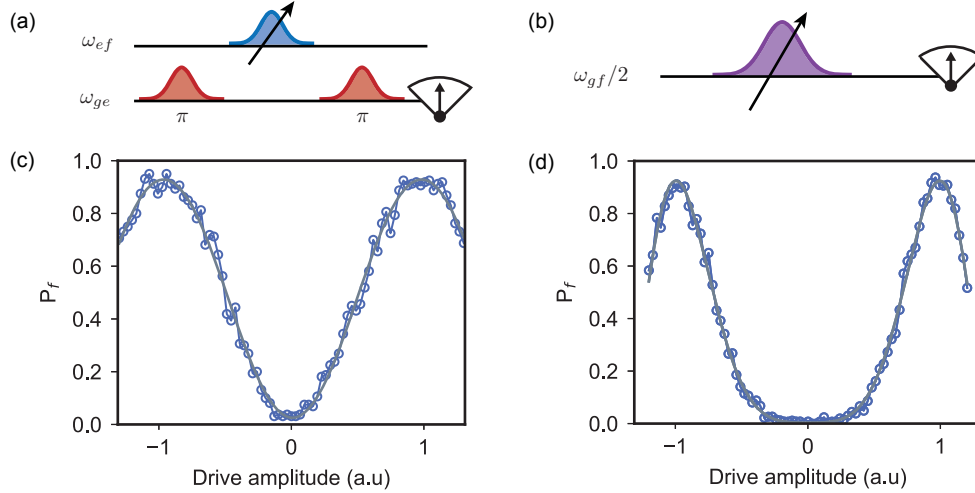


Figure 2.6: **Manipulation of transmon  $|f\rangle$  level.** (a) The protocol for manipulating the  $|e\rangle - |f\rangle$  transition of a transmon using a two-step procedure. The transmon is first fully flipped to  $|e\rangle$ . This followed by a pulse at  $\omega_{ef}$  with variable drive amplitude and a final  $\pi$  pulse at  $\omega_{ge}$  before the readout. (b) The sequence for implementing a direct transition between  $|g\rangle$  and  $|f\rangle$ . Since it is a two-photon process, the drive is typically much stronger than that of a regular  $\pi$  pulse. (c) The measured Rabi flops between  $|e\rangle$  and  $|f\rangle$  fitted to a sine function. (d). The measured Rabi between  $|g\rangle$  and  $|f\rangle$  fitted to a functional form  $y \propto \sin^2 2\pi f x^2$

Another useful feature of a transmon is the potential to use its third energy level for certain manipulations. Therefore, it would be useful to also calibrate the  $|f\rangle$  state properties. We show that since the  $|e\rangle \rightarrow |f\rangle$  transition occurs at a different frequency from that of  $|g\rangle \rightarrow |e\rangle$ , we can simply use the same techniques but with the drive frequency centred

around the  $|e\rangle - |f\rangle$  transition instead. For example, we can perform a  $\pi$  pulse between the  $|e\rangle$  and  $|f\rangle$  state of the transmon using the protocol described in Fig. 2.6(a). In fact, we can manipulate any superpositions of the transmon's  $|g\rangle$ ,  $|e\rangle$ , and  $|f\rangle$  levels. For example, we can directly flip the transmon from its ground state to  $|f\rangle$  by driving at the frequency  $\omega_{gf} \approx (\omega_{ge} + \omega_{ef})/2$ .

With the ability to Rabi flop the transmon between its first three energy levels, we can now probe the coherence time scales associated with the  $|f\rangle$  state. First, we can perform a  $T_1$  measurement to calibrate the relaxation rate of  $|f\rangle$ . This is done by first flipping the transmon to  $|f\rangle$  and then measure the probability of it having relaxed to either  $|g\rangle$  or  $|e\rangle$  after a variable delay time. An example of this measurement is shown in Fig. 2.7(a), where the probability of remaining in  $|f\rangle$  exponentially decays over time. From this, we extract a  $T_1^{ef} \approx 40\mu\text{s}$ , which is roughly half of the decay time of  $|e\rangle$ .

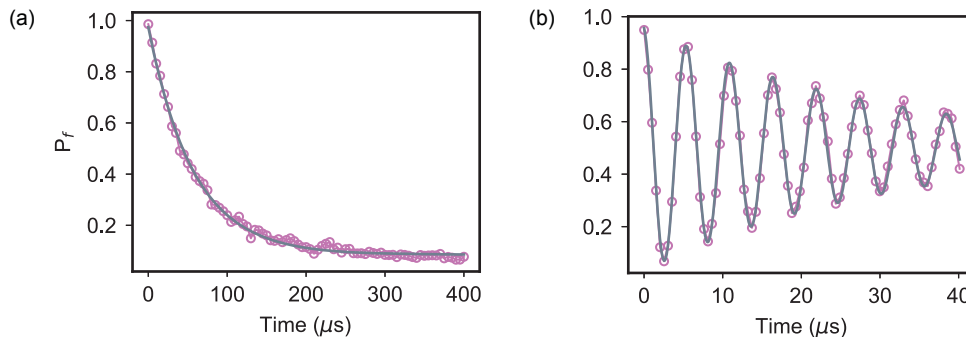


Figure 2.7: **Coherence measurements of transmon  $|f\rangle$  level.** (a)  $T_1$  measurement implemented by first exciting the transmon to  $|f\rangle$  and monitor its decay back to ground state after a variable delay time. A single exponential fit (grey) is used to extract the decay constant. For typical devices, we expect  $T_1^{ef} \sim 20 - 40\mu\text{s}$ , about half of that of the  $|e\rangle - |g\rangle$  relaxation time. (b) A Ramsey experiment to measure  $T_2^{ef}$  of the transmon. The measurement monitors coherence of the  $|e\rangle - |f\rangle$  superposition, which is typically half that of the  $|g\rangle - |e\rangle$  superposition.

In order to measure the decoherence of the  $|f\rangle$  state, we use a Ramsey interference experiment with the initial transmon state being  $(|e\rangle + |f\rangle)/\sqrt{2}$  and  $(|g\rangle + |f\rangle)/\sqrt{2}$  respectively. As expected,  $T_{2,ef}$  and  $T_{2,gf}$  are very similar and roughly half of that of  $T_{2,ge}$ . This goes to show that the transmon is an atom with at least three well-defined energy levels and we

can use any chosen pair of these energy levels to implement conditional operations on the cavity state. This additional degree of freedom that comes without any increased hardware requirements is highly advantageous. We will exploit it in the entangled cat experiment described in Chapter 4.

## 2.5 Control and measurement of a cavity state

Another component in our cQED toolbox is the transmon-controlled cavity state manipulation. We again exploit the dispersive coupling between the transmon and the cavity to perform non-linear operations on the cavity mode. We treat the effect of the coupling as a shift of the transmon's transition frequency dependent on the number of excitations present in the cavity. We use this frequency shift to individually address a specific energy level and perform a measurement of the cavity state using the transmon as a meter. A simple example is the number-splitting experiment where we can probe the population in each Fock state using a spectrally selective  $\pi$  pulse on the transmon (Fig. 2.8). However, this type of measurement does not reveal any phase information of the state stored in the cavity. To do so, we must develop new tomographic techniques that are more suitable for cavity states which occupy a much larger Hilbert space compared to the transmons.

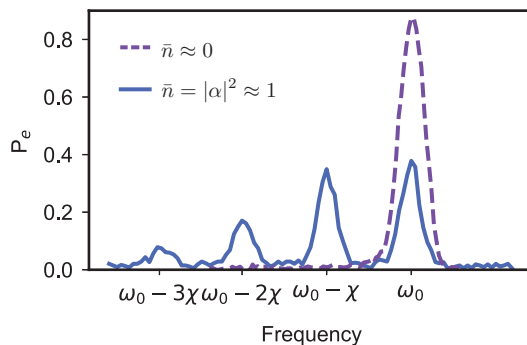


Figure 2.8: **Ancilla spectroscopy as probe for cavity population** Spectroscopy measurement of the transmon in presence of zero (violet) and one average (blue) photon in the cavity. Without any displacement, the cavity state is very close to being in vacuum, with a small residual photon population  $\leq 0.2\%$ . In presence of cavity photons, dispersive coupling shifts the  $|g\rangle \rightarrow |e\rangle$  transition frequency down by integer multiple of  $\chi$ , as shown by the blue trace

Due to the small inherited non-linearity, we cannot address single energy eigenstates (Fock states) of a cavity and cause level transitions between them with just a classical drive. Rather, we can only create coherent state of a certain amplitude and phase. Mathematically, we can describe a coherent state  $\alpha$  as a infinite superposition of Fock states weighted by a Poisson distribution:

$$|\alpha\rangle = e^{-|\alpha|^2/2} \sum_{n=0}^{\infty} \frac{\alpha^n}{\sqrt{n!}} |n\rangle \quad (2.19)$$

Conceptually, they are the most similar to a classical state such as that of a simple oscillating pendulum. Its state at any specific point in time has some instantaneous mean position and velocity that have minimal and symmetric uncertainties. The evolution of such states can be visualised as a periodic oscillation about a circular trajectory in the phase space with radius  $|\alpha|$ . We can characterise the action of a classical electromagnetic drive on the resonator by a displacement operator  $D(\alpha)$ :

$$\hat{D}(\alpha) = e^{\alpha^* \hat{a} - \alpha \hat{a}^\dagger} \quad (2.20)$$

where  $\alpha$  is the magnitude of the displacement in phase space. When acting on the vacuum, which is also a coherent state,  $\hat{D}(\alpha)$  displaces  $|0\rangle$  into a coherent state with amplitude  $\alpha$ .

A particularly useful and illustrative measurement of the cavity state is the Wigner function. It is defined as a quasi-probability distribution of a state,  $\rho$ , or the Fourier transform of the density matrix in the position coordinates. Therefore, the Wigner function contains the full information of a quantum state in a cavity.

However, a more convenient way to think about the Wigner function is through its relation to the parity operator of a system [33, 29]:

$$W(\beta) = \frac{2}{\pi} \text{Tr}[\hat{D}(\beta)^\dagger \rho \hat{D}(\beta) \hat{P}] \quad (2.21)$$

This relates the Wigner function to the expectation values of the photon number parity operator,  $\hat{P} = e^{i\pi \hat{a}^\dagger \hat{a}}$ , of a cavity state after it is displaced coherently with amplitude  $\beta$ . It contains complete information of the quantum state [34] and thus, we can reconstruct its density matrix using a Wigner tomogram [35] within a certain truncated Hilbert space. It

is also well adapted to display non-classical correlations present in the cavity state. In fact, we can assert that the presence of negativity a state's Wigner function is sufficient evidence for its non-classical nature.

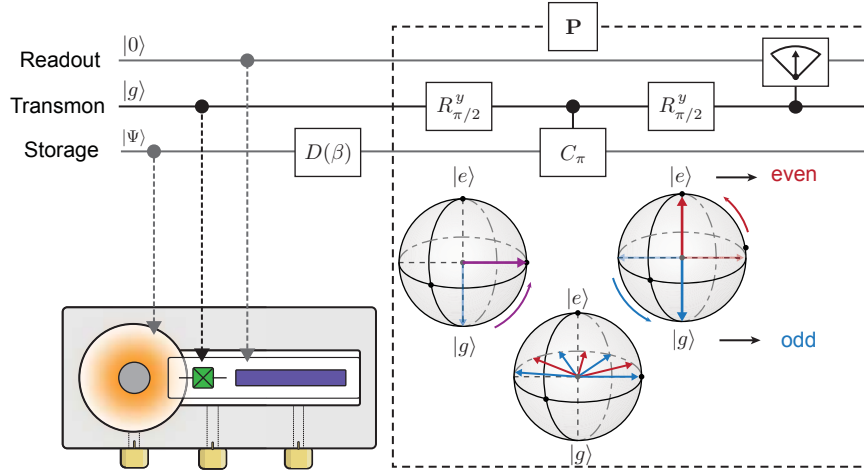


Figure 2.9: **Photon number parity measurement protocol.** The experimental protocol to measure the Wigner function of a cavity state in a typical module. It consists of a high-Q storage cavity (orange) coupled to a transmon (green), which is read out by a quasiplanar resonator (purple). All components are housed in a single high-purity aluminium package and couples to the microwave drives via SMA couplers (yellow). The protocol maps displaced parity onto the transmon state via two  $\pi/2$  pulses separated by a wait time  $\pi/\chi$ . The cartoon Bloch spheres indicate the precession of Bloch vectors at different times.

The connection between the photon number parity and Wigner function is a very powerful tool for cQED systems because we can measure the parity of a cavity state rather easily via its dispersive coupling with a transmon. Eigenstates of parity operator are simply states of cavity with only even- or odd-numbered Fock states are present,

$$\hat{P} |\text{even}\rangle = + |\text{even}\rangle \quad (2.22)$$

$$\hat{P} |\text{odd}\rangle = - |\text{odd}\rangle \quad (2.23)$$

with eigenvalues  $\pm 1$ . By measuring the Wigner function, or the parity at various points in the phase space, we are able to fully characterise a cavity state without directly probing the exact photon number occupations and their relative phases.

Experimentally, a parity measurement is implemented by a simple Ramsey pulse sequence on the transmon as depicted in Fig.2.9(a). Starting with a  $\pi/2$  pulse that brings the transmon to a superposition of  $|g\rangle$  and  $|e\rangle$ , we simply let the system evolve for a time corresponding to  $\pi/\chi$  before performing another  $\pi/2$ . During the evolution, the cavity and transmon becomes entangled at a rate  $\chi$ , resulting in a precession of each Fock state  $|n\rangle$  around the Bloch sphere at rate proportional to  $n\chi$ . This essentially performs controlled-phase gate on each cavity photon conditioned on the transmon state, described by  $C_\pi = \hat{I} \otimes |g\rangle\langle g| + e^{-i\pi\hat{n}} \otimes |e\rangle\langle e|$ . Therefore, at the time  $\pi/\chi$ , all even photon states would acquire a phase  $2n\pi$  while the odd states acquire  $(2N + 1)\pi$ , pointing them along opposite directions on the equator of the Bloch sphere. Finally, the second  $\pi/2$  pulse maps the parity information onto either the ground and excited state of the transmon respectively. Combing this measurement with the displacement operation, we can now perform Wigner tomography to fully characterise a cavity state.

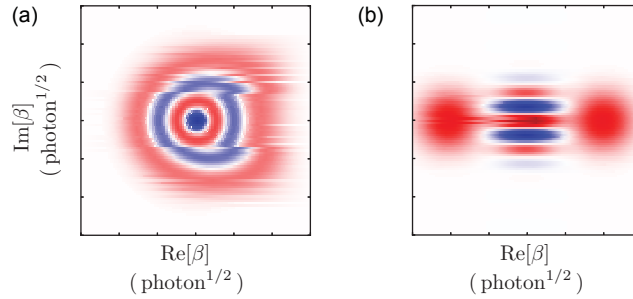


Figure 2.10: **Wigner representation of a cavity state.** (a) Simulated Wigner function of a Fock state  $|n\rangle = 3$ . It has value -1 at the origin since  $|n\rangle = 3$  is an odd parity state. Its radial symmetrical arises from the lack of a well-defined phase for single Fock states. (b) Simulated Wigner function of a cat state which is an even superposition of two coherent state  $|\psi\rangle = (|\alpha\rangle + |-\alpha\rangle)/\mathcal{N}$ , with  $\alpha = 2$ . The fringes indicate the phase coherence of the superposition.

Another powerful feature of the dispersive coupling is that a single transmon is sufficient to prepare any quantum states in a superconducting cavity and perform universal control on it. This is accomplished by considering a full model of the time-dependent drift Hamiltonian in the presence of classical control fields. It has been demonstrated [36] that for our cavity-transmon system, numerical optimisation procedures can reliably solve the inversion problem

of finding the control fields to implement an intended operation. In our case, the Gradient Ascent Pulse Engineering (GRAPE) [37] method is used to efficiently compute the control pulses,  $\epsilon(t)$ . We also impose a set of amplitude and derivative (bandwidth) penalties in the optimisation routine in order to make that the solutions are limited to what our DACs can physically implement.

The optimised control signals are implemented through full in-phase/quadrature (IQ) modulated microwave fields centred on the transmon (cavity) frequencies. Using this method, we achieve a universal set of controls on multi-photon states in a superconducting cavity as shown in Ref.[36]. In the scope of this work, we simply use such numerically optimised controls to create initial states. An example is shown in Fig.2.11. Here, we start with the cavity in vacuum and transmon in its ground state. We apply the computed pulse sequence via the coupling pins to the two modes simultaneously. This brings us to the desired state of a coherent superposition of  $|0\rangle$  and  $|2\rangle$  while bringing the transmon back to its ground state. In most case, the duration necessary to perform an operation scales with  $1/\chi$  and the fidelity of these sequences are ultimately limited by the coherence times of the transmon ancillae.

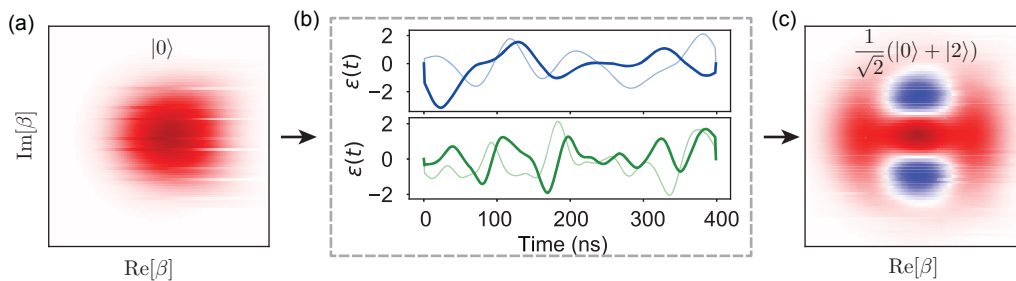


Figure 2.11: **Example of an OCT pulse.** An sample of the optimal control pulse that implements a non-trivial state transfer from vacuum (a) to a superposition of Fock states (c). The operation is accomplished by the numerically optimised control signals on both the transmon (green) and cavity (blue) modes. The transmon is driven to its excited state during the sequence but ends in the ground state at the end of the operation.

Putting these capabilities together, we assemble a simple cavity-transmon system in which we control and measure cavity states using a transmon ancilla whose state is extracted efficiently via a another resonator. A typical design is shown in Fig. 2.9 where we couple a

standard transmon (green) to a long-lived stub cavity (orange) where quantum information can be coherently stored, as well as a low-Q quasi-planar resonator (purple) fabricated on the same sapphire chip for fast readout [38]. It is a simple yet versatile quantum system that provides a robust platform for a wide range of possibility in cQED experiments. Most importantly, it inspires a different paradigm of hardware efficient quantum error correction schemes.

## 2.6 Cavity-based QEC schemes

As discussed in the introductory remarks, quantum information is fragile and it is prone to both bit-flip and phase-flips errors. However, the fundamental concepts of quantum mechanics render the familiar classical error correction techniques ineffective. Therefore, in order to eventually be able to perform faithful quantum computation, we must develop more sophisticated quantum error correction (QEC) schemes that respect the features of quantum mechanics. Ultimately, quantum algorithms must be performed on components that can be made robust against errors due to decoherence and imperfection operations. At this point, I would like to remind the reader an important distinction of *physical* vs *logical* qubits. A physical qubit is simply a quantum object with two well-defined states. It could be a single transmon, a electron spin or the first two levels of a slightly anharmonic resonator. On the other hand, a logical qubit is a register or a system where a quantum bit is redundantly encoded. It must possess a symmetry property that can be used to detect and correct errors.

So how can we construct logical qubits using available technologies in our cQED toolbox? There are a few key considerations. First, the physical system that we choose to redundantly encode the information must have relatively favourable coherence properties. The next question is how one can achieve redundant encoding in an efficient manner. In the more traditional approach to QEC schemes, a logical qubit is often composed of a collection of physical qubits. The simplest code is the three-qubit bit flip code where the logical states  $|0\rangle_0 = |000\rangle$  and  $|1\rangle_0 = |111\rangle$ . The error syndromes are measured by mapping the parities of the logical state onto two ancillae. While this is sufficient to detect and correct a single

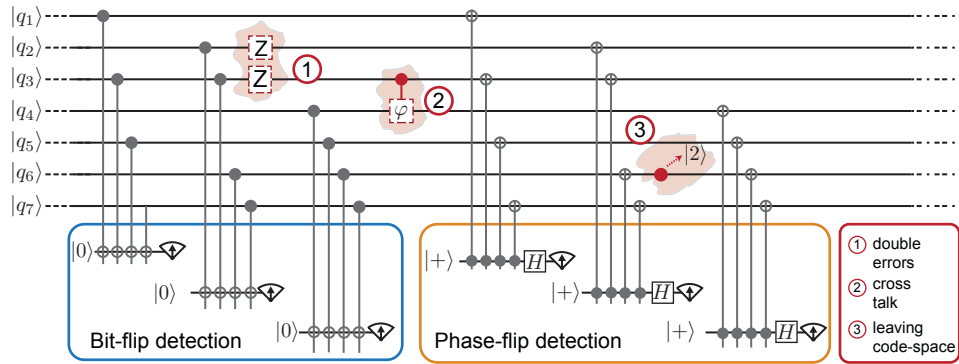


Figure 2.12: **7-Qubit error correction code.** The Steane code is a first order code is capable of correcting both phase and bit flip errors in one of the seven physical qubits within one round of QEC. This requires a series controlled-NOT (CNOT) operations to map joint parities of multiple qubits onto a number of ancillae, which are read out to determine if any of the 7 physical qubits experienced an error. On top of the staggering complexity, there are also a variety of different failure modes, a few of which are illustrated in red.

bit flip error, it fails when two of the physical qubits are flipped and is not capable of detecting phase flips without introducing further redundancy. In order to correct both bit and phase flip errors, we can expand the code space to incorporate 7 physical bits for the logical encoding such as in the Steane code (Fig.2.12). It consists of 7 two-level systems as the logical qubit and a further 6 ancillae for syndrome measurements for a single round of QEC. Despite the significant overhead required, it can only handle errors on a single physical qubit within the code space per round. The large number of physical qubits needed also introduces additional decoherence penalties that leads to seven-fold increase in the logical error rate. Despite the improvements in qubit coherence and the increasingly more robust two-qubit operations demonstrated in recent cQED experiments, it still remains a daunting task to implement such QEC schemes due to the highly penalising hardware overhead and operational complexity.

Many previous works have demonstrated some elements of QEC in cQED systems [39, 40, 41, 42] as well as on other platforms such as NMR [43, 44], ions [45, 46], and photons [47, 48]. However, these experiments have yet been able to shown an extension of the lifetimes of the quantum information in presence of naturally-occurring errors. In fact, the lifetime of the logical bit is usually worse compared to a simple, uncorrectable encoding using the most

coherent physical components in the system. This is because by using a collection of two-level systems to redundantly represent a quantum bit, the system now is susceptible to new error channels and an enhanced rate of decoherence. Although such imperfections can be corrected, it inevitably requires additional physical qubits and drastically increases the complexity. This poses a daunting task for experimentalists due to the colossal amount of hardware overhead required for such operations

Is there an alternative approach to QEC that is more tractable and less resource-intensive? It would be highly desirable to construct logical qubits in systems where we can harness a larger Hilbert space without imposing too much hardware overhead. One particular quantum system that has this capability is the harmonic oscillator, where an infinite number of energy levels are permitted within a single structure. This led to the development of a QEC scheme that exploits the large Hilbert space of superconducting cavities instead. In this framework, we can utilise the higher energy levels of the same cavity to redundantly encode a quantum bit.

The cavity-based approach is a powerful tactic for QEC, offering potential protection against various imperfections, including dephasing, loss of excitation, and thermal heating, etc. The advantage of this strategy is two-fold. Firstly, coherence times for 3D superconducting cavities have exceeded that of transmons by two orders of magnitude. This effectively reduces the rate of decoherence induced errors. Secondly, we can expand information capacity without an insurmountable hardware requirement by using the large size of a cavity's Hilbert space. Furthermore, it has been demonstrated that a logical qubit encoded in a single cavity has only one dominant type error [49, 15], namely, single photon loss. Therefore, we can essentially achieve redundant encoding in cavities without increasing the error channels that the quantum bit is exposed to. In the long run, this scheme also makes it more tractable to scale up to systems with multiple logical qubits as shown in the experiments described later in this writing.

The governing strategy for constructing such cavity-based bosonic codes is to provide a symmetry property that can track the occurrence of single photon jumps. Mathematically, a loss of excitation in a resonator is equivalent to the application of the lowering operation,

$\hat{a}$ , on the cavity field. Conveniently, another consequence associated with this is the change of the photon number parity:

$$\hat{a}|\text{even}\rangle = |\text{odd}\rangle, \quad \hat{a}|\text{odd}\rangle = |\text{even}\rangle \quad (2.24)$$

This makes the parity of a cavity state a natural syndrome for the dominant error channel. Additionally, coherent states are an attractive option for a logical encoding since they are eigenstates of  $\hat{a}$ . Further, the overlap between two coherent states is suppressed exponentially in the difference of their amplitudes. As a result, we can get two almost orthogonal basis states to encode a quantum bit by simply choosing two sufficiently large coherence states. For example, one possible choice is the ‘two-legged cat’ states where

$$|0\rangle_L = |C_\alpha^+\rangle = \frac{1}{\sqrt{2}}(|\alpha\rangle + |-\alpha\rangle) \quad (2.25)$$

$$|1\rangle_L = |C_\alpha^-\rangle = \frac{1}{\sqrt{2}}(|\alpha\rangle - |-\alpha\rangle) \quad (2.26)$$

The two basis states are also even (+) and odd (-) eigenstates of the number parity operator:  $\langle C_\alpha^\pm | \hat{P} | C_\alpha^\pm \rangle = \pm 1$ . This can be effectively measured as a syndrome using the Ramsey-type experiment discussed in the previous section. However, not all states on the Bloch sphere in this encoding have well-defined parity. For example, the state that lies along the logical  $Y$  axis is cat with no parity,  $|0\rangle_L + i|1\rangle_L = |\alpha\rangle + i|-\alpha\rangle$ , and hence does not possess a measurable symmetry property to indicate the occurrence of an error.

To overcome this shortcoming, we can tap into a larger part of the cavity’s Hilbert space such that all individual basis states are eigenstates of the parity operator. This is commonly referred to as the ‘four-legged’ cat code where the logical space is span by superpositions of the ‘two-legged’ cats along the real and imaginary axes in the phase space:

$$|0\rangle_L = |C_\alpha^\pm\rangle = \mathcal{N}_\alpha^\pm(|\alpha\rangle \pm |-\alpha\rangle); \quad |1\rangle_L = |C_{i\alpha}^\pm\rangle = \mathcal{N}_\alpha^\pm(|i\alpha\rangle \pm |-i\alpha\rangle) \quad (2.27)$$

where  $\mathcal{N}_\alpha^\pm = 1/\sqrt{2(1 \pm \exp(-2|\alpha|^2))}$  and  $\mathcal{N}_\alpha^\pm \rightarrow 1/\sqrt{2}$  for large  $\alpha$ . In order to preserve sufficient orthogonality, we must choose  $|\alpha|^2 \gtrsim 2$ . It has been shown that using this encoding,

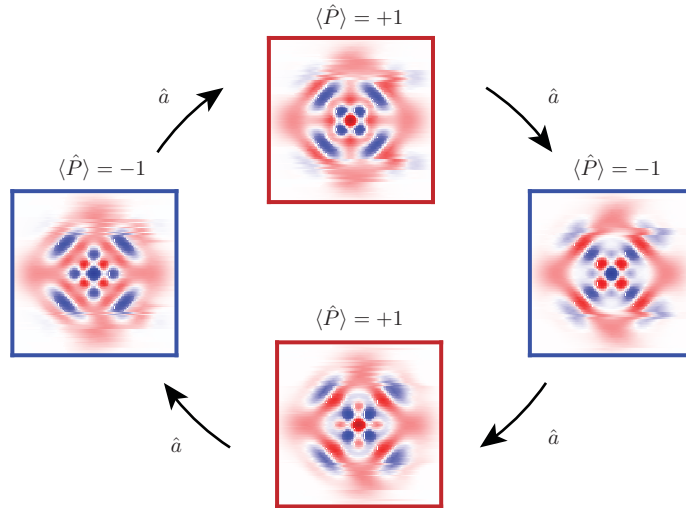


Figure 2.13: **The cycle depicting a code word in the ‘four-legged’ cat encoding undergoing four successive photon jump events.** The initial state is an even superposition of  $|C_\alpha^+\rangle, |C_{i\alpha}^+\rangle$ . Its parity switches after each photon loss and the original state is recovered after the 4th event. Between the stochastic applications of  $\hat{a}$ , the cat states also deterministically decay towards vacuum (not shown here).

we can now directly use parity as the error syndrome corresponding to single photon loss, which is the dominant error channel for a logical qubit stored in a cavity [50]. We can illustrate this symmetry by considering the action of  $\hat{a}$  on a logical state:

$$c_0|C_\alpha^+\rangle + c_1|C_{i\alpha}^+\rangle \xrightarrow{\hat{a}} c_0|C_\alpha^-\rangle + ic_1|C_{i\alpha}^-\rangle \xrightarrow{\hat{a}} c_0|C_\alpha^+\rangle - c_1|C_{i\alpha}^+\rangle \quad (2.28)$$

This implies that each photon loss event effectively leads to a  $\pi/2$  rotation about the logical  $Z$  axis, with the recovery of the initial logical state after 4 jumps. In other words, we have discretised the continuous error due to decoherence. Therefore, by monitoring the parity through single-shot measurements and repeatedly updating our knowledge of the cavity state we keep track of the stochastic evolution of the logical qubit. Equipped with this knowledge, we now have the capability to account for the errors and hence maintain the coherence of the logical states beyond the coherence times of the best physical components in the system as shown in Ref.[49]. This is a powerful scheme that has demonstrated the ability to protect the coherence of the logical qubit against the dominant naturally occurring error. It can, in

principal, also be corrected for dephasing errors [50].

One of the trade-offs for using continuous variable encoding schemes is the non-orthogonality of the basis states. Photon loss from the cavities causes the coherent states to decay towards vacuum and increases their overlaps. In direct competition to this effect is the increased rate of energy loss at  $\bar{n}\kappa$  from the cavity at larger photon numbers. Taking both of these constraints into account, we choose  $\alpha \approx 2$  for most of the operations described in this work. At this amplitude, the non-orthogonality is suppressed exponentially by  $4|\alpha|^2$  such that  $|\langle\alpha|i\alpha\rangle|^2 < 10^{-3}$ .

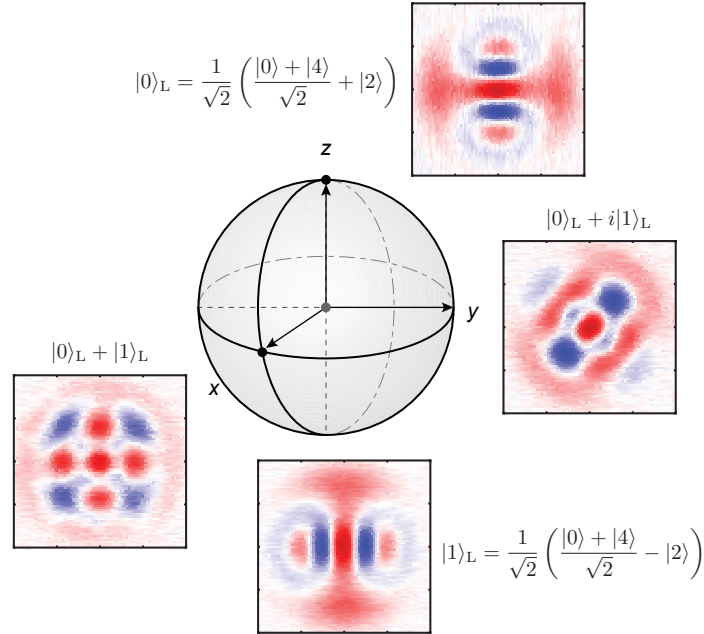


Figure 2.14: **Logical Bloch sphere in the Binomial encoding.** The logical  $|0\rangle$  and  $|1\rangle$  are simply superpositions of even photon number Fock states. All code words have the same mean photon number. A photon loss event results in a change of parity, which can be detected as the error syndrome. The four Wigners are measurements on four of the basis states prepared using OCT pulses

Another possible choice of bosonic encoding uses discrete variables, i.e Fock state, instead of coherent states. As discussed in Ref. [51], we can use a finite superposition of Fock state to construct code words that offers protection against both dephasing and amplitude damping. One particular example is the binomial code where even Fock state superpositions, weighted

with binomial coefficients, are used to encode a logical qubit:

$$|0\rangle_L = \frac{1}{\sqrt{2}} \left( \frac{|0\rangle + |4\rangle}{\sqrt{2}} + |2\rangle \right); \quad |1\rangle_L = \frac{1}{\sqrt{2}} \left( \frac{|0\rangle + |4\rangle}{\sqrt{2}} - |2\rangle \right) \quad (2.29)$$

As shown in Fig. 2.14, the logical Bloch sphere under this encoding is spanned by even superpositions of Fock states with the same mean photon number. Similar to the cat code, a photon loss even brings the logical code words to a subspace of odd photon numbers, which is orthogonal to the even manifold. Further, with the same mean photon number in each code word, an error does not impose any asymmetry in the logical Bloch sphere.

The advantage of this encoding scheme is that it operates in a restricted Hilbert space. Therefore, it can be less demanding to prepare and implement unitary operations on these code words compared to cat states. Additionally, the smaller mean photon number required in this code also alleviates the complications due to higher order non-linearities in the system. We can prepare these states using OCT pulses [36] and measure their Wigner functions with high fidelity. In light of these advantages, this particular encoding is frequently adopted in experimental works described in the later chapters.

## 2.7 Toward operations on multiple logical qubits

Using such bosonic encodings, we can now construct a logical qubit in a superconducting cavity and use the transmon as an ancilla to assist the manipulation and measurement of the cavity state. Rapid progress has been made in this cavity-based scheme. In 2016, Ofek and Petrenko et al. demonstrated for the first time the extension of a logical qubit's lifetime beyond the coherence times of the best physical component in the system [49]. Subsequently, both theoretical and experimental advancements have been shown in the high-fidelity control of a single logical qubit [36, 52, 53] in similar 3D cQED architectures. Going beyond systems with a single logical qubit is both a natural scientific progression from these remarkable achievements and an important component in realising robust algorithms on multipartite quantum systems.

We can approach the challenge of scaling up to more logical qubits in a modular ar-

---

chitecture. In this framework, individual quantum systems are combined into a complex quantum network. We can envision that each module will consist of single or several logical qubits which can be error-corrected and debugged easily individually. In the world of superconducting circuits, we can construct these modules using superconducting cavities and transmons, where logical qubits can be encoded in the large Hilbert space of cavities and controlled via the nonlinearity provided by the transmon ancillae. Within each module, we must also have the ability to implement robust quantum operations between logical qubits. This requires an architecture consisting of several high-Q cavities. Furthermore, we need to expand our cQED toolbox and develop techniques to introduce non-linear interactions between them while maintaining minimal always-on couplings. In the following chapter, we will discuss the design considerations and the characterisation of a double-cavity sample built for this purpose. Together with the capabilities to connect individual cQED modules to one another, which have been shown in recent works [54, 55], the increased complexity in each module would allow us to realise a scalable network of quantum systems.

## Chapter 3

# Multi-cavity cQED architecture

Rapid progress in controlling individual quantum systems over the past twenty years [56, 57] has opened up a wide range of possibilities of quantum information processing. Potential applications ranging from universal quantum computation to long-distance quantum communication share the central theme of exploiting quantum superpositions within a large Hilbert space. Additionally, cat states, which span a Hilbert space whose dimension grows linearly with the number of photons, have been proven to be an attractive candidate for redundantly encoding quantum information in an error-correctable manner [58, 50, 49]. Superconducting cavities coupled to transmon ancillae provide us a system with large Hilbert space that can be controlled and characterised efficiently. Moreover, with the recent improvement in the coherence properties of superconducting cavities, we can now store quantum information coherently for milliseconds [15]. Therefore, it is highly advantageous for us to expand the information capacity of cQED systems by designing a scalable architecture consisting of multiple long-lived superconducting cavities.

In this chapter, I will discuss the design and characterisation of multi-cavity devices that have been developed at Yale over the past three years. In section 3.1, I will present in detail the design of the first double-cavity system. In this minimalist design, the two-cavities are controlled and characterised using a single transmon ancilla. Their Hamiltonian parameters are calibrated and presented in section 3.2. Subsequently, we show in section 3.3 that such a device exhibits excellent coherence properties. Here, I also will describe the typical system Hamiltonian parameters and highlight the key design considerations for this type of devices.

In section 3.4, I will present a second generation design which allows the addition of more ancillary modes when necessary. The modification aims to provide more robust single-cavity control and measurement capabilities. These systems are the playground where all the games of multi-cavity operations described in chapters 4-7 take place.

### 3.1 Design of multi-cavity devices

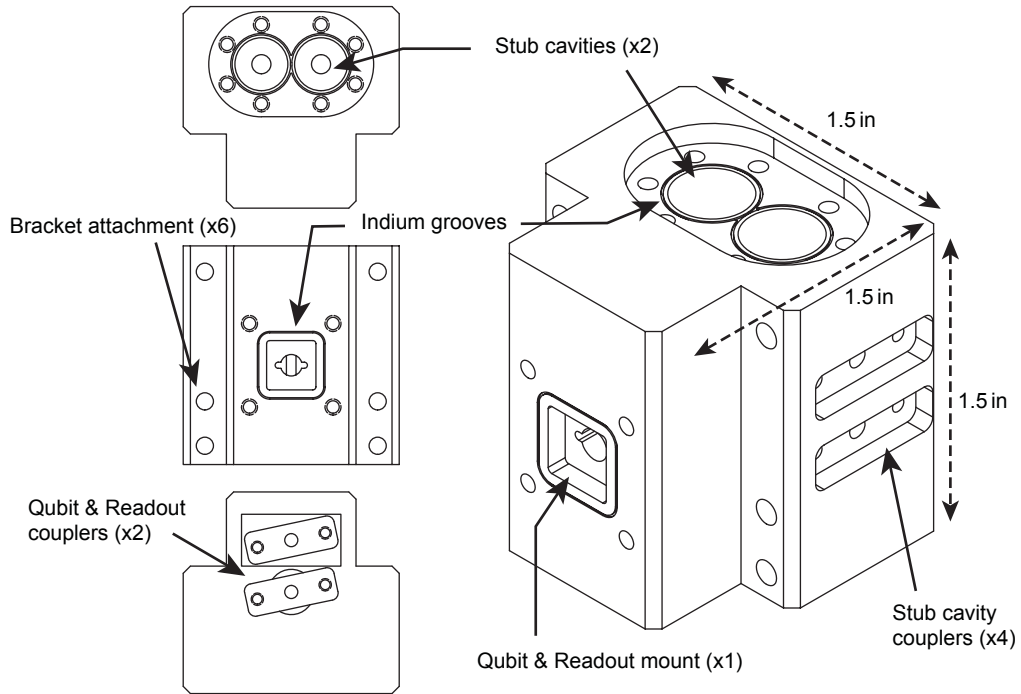


Figure 3.1: **External details of the double-cavity system.** The device consists of two 3D stub cavities that simultaneously couple to a Y-shaped transmon housed in the tunnel with its antenna protruding into each cavity. The tunnel has up to two SMA connectors that provide coupling to the transmon and its  $\lambda/2$  readout resonator. Each stub cavity also has two SMA couplers, intended for cavity drives as well as direct readout if necessary. A top lid is fastened with both screws and an indium seal to ensure light-tightness. The whole structure can be mounted on regular copper brackets with 6 screws, providing direct thermalisation of the device.

The first multi-cavity system borrows many key ingredients from recent experimental progress on the improvement of cavity coherence times [59] as well as integrated packages for 3D cQED devices [38]. Each of the two cavities are considered as a 3D version of a  $\lambda/4$  transmission line resonator between a centre stub 3.2 mm in diameter and a cylindrical wall

(outer conductor) 9.5 mm in diameter. The heights of the stubs determine the respective resonance frequencies of the stub cavities. The large volume to surface ratio of this structure ensures that the electric field resides predominantly in vacuum to reduce the loss in the imperfect surface.

Experimentally, we primarily use the fundamental mode of these coaxial cavities. It is important to ensure that the higher order resonances are sufficiently far from any other components in the system. Because the cavity is a  $\lambda/4$  resonator, the frequency of the next TEM harmonic is simply given by  $3\lambda/4$ . In a typical design, the fundamental mode is placed around 5 GHz. Therefore, the next mode is far detuned from it by  $\sim 10$  GHz, which gives the cavity a very clean spectrum and ensures that the undesired coupling of higher order modes to the other components are insignificant.

For the purpose of our experiments, it is key to ensure minimal direct inter-cavity coupling. Therefore, the two modes are typically spectrally separated by  $\gtrsim 1$  GHz. This corresponds to a difference in the heights of the centre stubs of  $\sim 0.8$  inches. Both cavities continue for  $\gtrsim 1$  inch above the top of the stubs to provide a  $\gtrsim e^{-10}$  attenuation of the E-field at the respective resonance frequencies. Microwave control signals are evanescently coupled to these cavities via a coaxial pin coupler through a hole in the sidewall. The coupling strength is simply controlled by the length of the pin, which is typically chosen such that they are extremely under-coupled. These parameters can be accurately simulated a priori and optimised to ensure high quality factors.

The device is typically machined out of high purity aluminium (4N). However, there usually are various imperfections on the inner surfaces of the cavities and tunnels in this structure due to the machining process. In order to achieve millisecond lifetimes consistently, we must chemically treat the surfaces such that the machining damages and residual mechanical grease are thoroughly removed. For this device, the whole package is chemically etched by about 80  $\mu\text{m}$  over a 4 hour period. The etch rate and quality depends on the flow rate across each surface. Due to the aspect ratio of the tunnel in this design, it is important to ensure that there is sufficient flow through the structure so that the inner walls of the tunnel can be adequately etched.

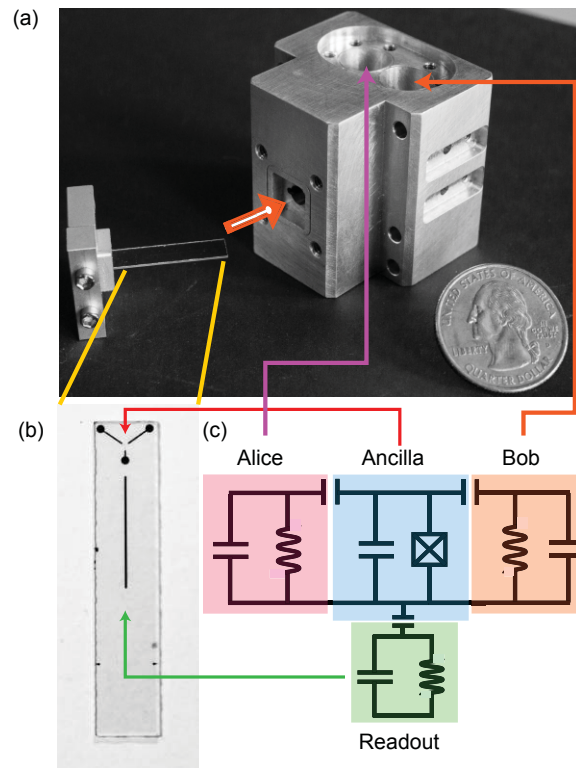


Figure 3.2: **Overview of the 3D architecture.** (a) A photograph of the full assembly of the device used in the entangled cat experiment. The machined aluminium package contains two coaxial stub cavities. A sapphire chip hosting the transmon ancilla is inserted through a tunnel. The extra strip of aluminium patterned on the same chip as the transmon forms a strip line resonator the tunnel walls. (b) A photograph of the Y-shape transmon deposited on a sapphire chip. (c) A schematic depicting the effective circuit of the cQED systems with three LC oscillators capacitively coupled to a single artificial atom (transmon)

Nonlinearity is introduced to the system by coupling a transmon device to both cavities. It is inserted through an elliptical tunnel opened from the outside towards the middle wall between the two cavities, therefore, creating a three way intersection between the tunnel and the two stub cavities. The vertical position of the tunnel is chosen to maximise the coupling to the high-Q cavities. Typically, the transmon is positioned to be near the top of the stubs where the electric field is maximal. This type of transmon, now often referred to as the ‘Y-mon’, contains a standard Josephson junction connected to three antenna pads in order to provide simultaneous coupling to multiple modes (Fig. 3.3(a)). The device is patterned on a  $5.5 \text{ mm} \times 27.5 \text{ mm}$  chip, which is diced from a  $430 \mu\text{m}$  thick c-plane sapphire wafer after fabrication. The Al/AlO<sub>x</sub>/Al junction is fabricated using the bridge-free process, which

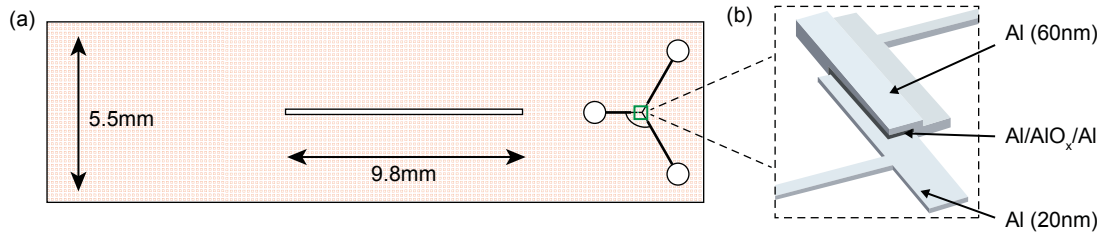


Figure 3.3: **The Y-shaped transmon containing a bridge-free Josephson junction.** (a) A Y-shaped transmon device fabricated on a sapphire substrate together with a quasi-planar resonator for independent readout. The circular pads provide the capacitive coupling to the other modes. This chip protrudes into the double-cavity device, allowing simultaneous coupling to both high-Q cavities. (b) Cartoon of a Josephson junction fabricated using the bridge-free technique. Two layers of thin-film Al are separated by an insulating barrier formed by aluminium oxide.

uses electron-beam lithography and the standard shadow-mask evaporation. A cartoon of the junction area is depicted in Fig. 3.3(b), where two layers of thin-film Al are evaporated with an oxide layer in between. The oxidation is done in a controlled environment which is calibrated to achieve the desired resistance-area (RA) product. The resonance frequency of this mode is determined by the design parameters  $E_C$  and  $E_J$ . In practice,  $E_J$  is inferred from room temperature resistance of the device which can be easily measured.  $E_C$  must be simulated numerically for each particular type of transmon design. In this geometry, the circular pads are the dominant contributions to  $E_C$  and provide the capacitive couplings to other modes. Their size and position are determined via HFSS simulations in order to achieve the desired frequency and coupling strength. The pads are connected to the junction by leads which are roughly  $100\ \mu\text{m} \times 600\ \mu\text{m}$ . Furthermore, we have also avoided excessively narrow features in the design, especially in the near junction area, in order to prevent quasiparticle induced relaxation. It has been shown [60] that quasiparticles can limit the  $T_1$  of transmons if they are not evacuated quickly. They can decay either through recombination with another quasiparticle, or single particle processes such as trapping by a vortex. It is generally more favourable to have large features with equal aspect-ratios to facilitate the evacuation of quasiparticles. Additionally, the exact dimensions of design are also optimised to reduce the surface participation, which has been shown to be a leading

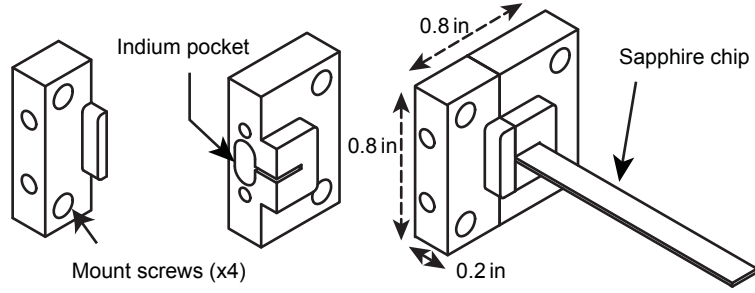


Figure 3.4: **Schematic of the clamps used to affix a sapphire chip to the double-cavity device.** The two halves are bolted together with the chip secured in between with indium wires placed in the Indium pocket. The clamps are made out of 6061 aluminium. The design can be easily adapted to work with chips of different dimensions.

source of loss for transmons [61] fabricated on dielectric substrates.

Another strip of aluminium is also deposited during the same process on the sapphire chip. This metal strip and wall of the tunnel form a planar-3D hybrid  $\lambda/2$  resonator, capacitively coupled to the Y-mon. The resonance frequency of this mode is determined by the length of the aluminium trace and its capacitance to the sidewalls of the tunnel. The dispersive coupling strength is controlled by distance between the Y-mon pad and the planar structure.

The coupling of each mode to the classical drives is done via a copper pin affixed to a SMA connector. The length of the pin and the position of the coupler determine the coupling strength for each mode. Alice and Bob are very weakly coupled to the outside world, with coupling  $Q$ 's  $\gtrsim 100 \times 10^6$ . The transmon drive is also weakly coupled to to ensure relatively good coherence times of the ancilla. We strongly couple the readout resonator mode to a transmission line to provide fast readout for the transmon state without limiting the transmon's quality factor. We can typically achieve a ratio  $\gtrsim 100$  between the  $Q$ 's by optimising the position of the coupling pin according to the field structure of the device.

The chip is mechanically held at one end with an aluminium fixture with an indium seal to ensure secure fastening of the chip. This design is based on the previous work done by M. Reagor. The clamps are made out of regular instead of high purity aluminium so that the screws can be tightened sufficiently without deforming the features. The chip is held

on one end by mechanically bolting together the two halves of the clamp, with additional indium wires to ensure that it is firmly held in place. Typically, a mounting mark is also patterned on the chip to indicate the desired lateral placement of the chip. The clamps are then attached to the main package with four screws and a gasket of 10 mil diameter indium wire in between the contact. The indium gasket aims to both enhance the light-tightness as well as the mechanical stability of the contact.

The full system is simulated in HFSS and the parameters are extracted from the simulation using standard Black Box Quantisation (BBQ) method described in Ref. [62]. In the next section, I will discuss the measurement of the realised Hamiltonian parameters of such a device which is used in two subsequent entangled cat and CNOT experiments described in Chapter 4 and 5 respectively.

## 3.2 Measurement of Hamiltonian parameters

There are four modes involved in such a system: two 3D cavities, a transmon ancilla, and a readout resonator. The transmon is an LC oscillator with much larger anharmonicity compared with the other modes, and is treated explicitly as a three-level artificial atom in this case. The reason for this treatment will become apparent in the subsequent chapters. Using well-established BBQ protocols, the other cavity/resonator modes are modeled as near-harmonic oscillators with weak nonlinearity inherited from their coupling to the Josephson junction.

The full system Hamiltonian can then be written in the following form up to the fourth

order in the coupling of the resonators to the transmon:

$$\begin{aligned}
H/\hbar = & \omega_A(a^\dagger a + \frac{1}{2}) + \omega_B(b^\dagger b + \frac{1}{2}) + \omega_R(r^\dagger r + \frac{1}{2}) + \omega_{ge}|e\rangle\langle e| + (\omega_{ge} + \omega_{ef})|f\rangle\langle f| \\
& - \chi_A^{ge} a^\dagger a |e\rangle\langle e| - (\chi_A^{ge} + \chi_A^{ef}) a^\dagger a |f\rangle\langle f| - \chi_B^{ge} b^\dagger b |e\rangle\langle e| - (\chi_B^{ge} + \chi_B^{ef}) b^\dagger b |f\rangle\langle f| \\
& - \chi_R^{ge} r^\dagger r |e\rangle\langle e| - (\chi_R^{ge} + \chi_R^{ef}) r^\dagger r |f\rangle\langle f| \\
& - \frac{K_A}{2} a^\dagger a^\dagger a a - \frac{K_B}{2} b^\dagger b^\dagger b b - \frac{K_R}{2} r^\dagger r^\dagger r r \\
& - K_{AB} a^\dagger a b^\dagger b - K_{AR} a^\dagger a r^\dagger r - K_{BR} b^\dagger b r^\dagger r
\end{aligned} \tag{3.1}$$

The first row represents the excitation energy of all the modes, explicitly including the transmon anharmonicity of  $\omega_{ge} - \omega_{ef} = 115.17$  MHz. The next two rows are second order terms ( $\sim 1$  MHz) representing the dispersive interactions ( $\chi$ 's) between the transmon and each of the three resonators. The last two rows are the fourth order terms ( $\sim 10$  kHz), including the self-Kerr energies ( $K_A, K_B, K_R$ ) of the resonators and the cross-Kerr interactions between any pairs of resonators ( $K_{AB}, K_{AR}, K_{BR}$ ). All Hamiltonian parameters of our device are listed in Table 3.1.

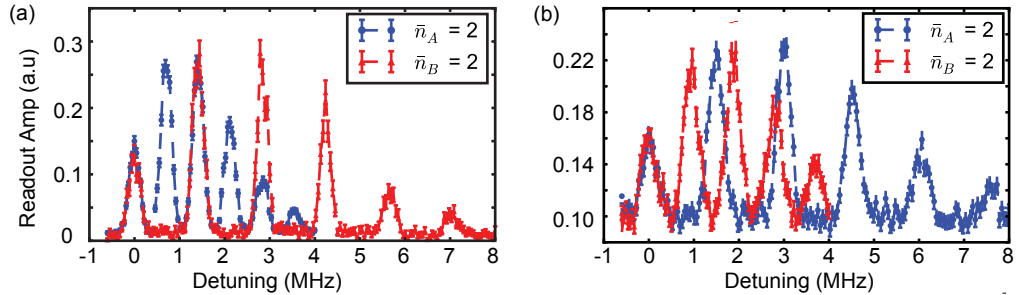


Figure 3.5: **Characterization of transmon-cavity dispersive coupling** (a) Photon-number-splitting of the transmon  $|g\rangle-|e\rangle$  transition frequency for a coherent state in Alice (blue) or Bob (red). The vertical axis represents the probability of exciting the  $|g\rangle-|e\rangle$  transition with a microwave tone at a frequency marked by the horizontal axis. (b) Photon-number-splitting of the transmon  $|e\rangle-|f\rangle$  transition frequency for a coherent state in Alice (blue) or Bob (red)

The key Hamiltonian terms that enable both the single and joint manipulation of the cavities are the dispersive shifts  $\chi_A^{ge}, \chi_A^{ef}, \chi_B^{ge}, \chi_B^{ef}$ . Since the readout resonator is always kept in the vacuum state until a final measurement is needed, its Hamiltonian terms do not

affect the quantum control and quantum state evolution in this experiment. The fourth-order Hamiltonian terms of Alice and Bob give a minor contribution to the infidelity of the experiment.

The dispersive frequency shifts ( $\chi$ 's) are measured both in the time domain by a Ramsey-type qubit state revival experiment as described in Ref. [63] and in the frequency domain by spectroscopy techniques, shown in Fig. 3.5. Although the transmon couples to both cavities simultaneously, its dispersive shifts to them differ sufficiently for us to be able spectrally distinguish photons from each cavity. Furthermore, for any single cavity characterisation routine, we can neglect the other mode by ensuring that it remains in the vacuum state throughout the measurement. Here, we simply require a spectrally selective  $\pi$  pulse whose full width at half maximum (FWHM) is narrower than that of the dispersive coupling [13]. This allows us to distinguish the transmon resonance peaks corresponding to different photon number states in the cavity. We use the same technique to calibrate  $\chi_{A,B}^{ef}$  as well. Instead of applying the selective  $\pi$  pulse on the  $|g\rangle - |e\rangle$  transition, we simply tune its frequency to be close to that of the  $|e\rangle - |f\rangle$  transition as shown in Fig. 3.5(b). The precision of this type of spectroscopy measurements is limited by the spectral width of the selective pulses, which in turn, is ultimately governed by the coherence times of the transmon. In this particular case, the transmon coherence is sufficient for us to perform a highly selective pulse.

	Frequency $\omega/2\pi$	Nonlinear Alice	interactions Bob	versus: Readout
$ e\rangle \rightarrow  g\rangle$	4.87805 GHz	0.71 MHz	1.41 MHz	1.74 MHz
$ f\rangle \rightarrow  e\rangle$	4.76288 GHz	1.54 MHz	0.93 MHz	1.63 MHz
Alice	4.2196612 GHz	0.83 kHz	-9 kHz	5 kHz
Bob	5.4467677 GHz	-9 kHz	5.6 kHz	12 kHz
Readout	7.6970 GHz	5 kHz	12 kHz	7 kHz

Table 3.1: **Hamiltonian parameters.** Measured Hamiltonian parameters of all cQED components, including the transmon ancilla, the two cavity resonators (Alice and Bob) and the readout resonator. The measured parameters include all transition frequencies ( $\omega/2\pi$ ), dispersive shifts between each resonator and each transmon transition ( $\chi/2\pi$ ), the self-Kerr of Alice ( $K_A/2\pi$ ) and Bob ( $K_B/2\pi$ ), and the cross-Kerr interaction between Alice and Bob ( $K_{AB}/2\pi$ ). The Kerr parameters and  $\chi^{ef}$  associated with the readout resonator are theoretical estimates based on the other measured parameters.

It is also worth noting that the Y-shaped transmon here has a relatively small anharmonicity with  $\alpha/2\pi \approx 115$  MHz. This arises from the choice of the transmon frequency and its special geometry. Because of the need to simultaneously couple to both cavities, the transmon is spectrally positioned to be in between the frequencies of Alice and Bob, with roughly equal detuning from each of them. Further, the length of the leads and size of the pads are chosen to provide sufficient capacitive coupling to the cavities. This results in a larger overall capacitance in the device. Thus, the anharmonicity is typically lower in this type of Y-shaped transmon compared to standard designs with only two antenna pads. This puts the device in a more favourable regime of the charge-noise dispersion but reduces the spectral selectivity in transmon manipulation pulses. In this case, the fastest  $|g\rangle \rightarrow |e\rangle$   $\pi$  pulse we could perform without significantly driving the  $|e\rangle \rightarrow |f\rangle$  transition has a standard deviation  $\sigma = 8$  ns. Apart from this trade-off, the coherence properties of such a device are comparable to the state-of-the-art transmons.

The self-Kerr terms ( $K_A$  and  $K_B$ ) induce distortion of the Gaussian probability distribution of the coherent state components of the cat state, and will cause state collapse and revival at long time scales [35]. There are a few different techniques for measuring the Kerr nonlinearity. Thanks to the good coherence times of the cavities, it is possible to perform a highly selective pulse and measure the frequency of each photon number peak with  $\sim 1$  kHz precision. But more efficiently, we can translate this inherited nonlinearity into a frequency shift of the system dependent of the different photon numbers in the cavity. This can be probed using a Ramsey-type experiment.

The cross-Kerr interaction  $K_{AB}$  induces spontaneous entanglement/disentanglement between Alice and Bob over long time scales. This type of undesired always-on coupling causes unintended interactions between two modes during idle times, which could limit the on-off ratio of any gate we hope to engineer between Alice and Bob. To calibrate it, we consider the cross-Kerr coupling as a frequency shift of one cavity that depends on the photon number present in the other. Therefore, it can be calibrated in a similar fashion using Ramsey experiments. The measurement of cross-Kerr between Alice and Bob is shown in Fig. 3.6. We observe a shift of the revival time on Alice as a result of a higher photon population in

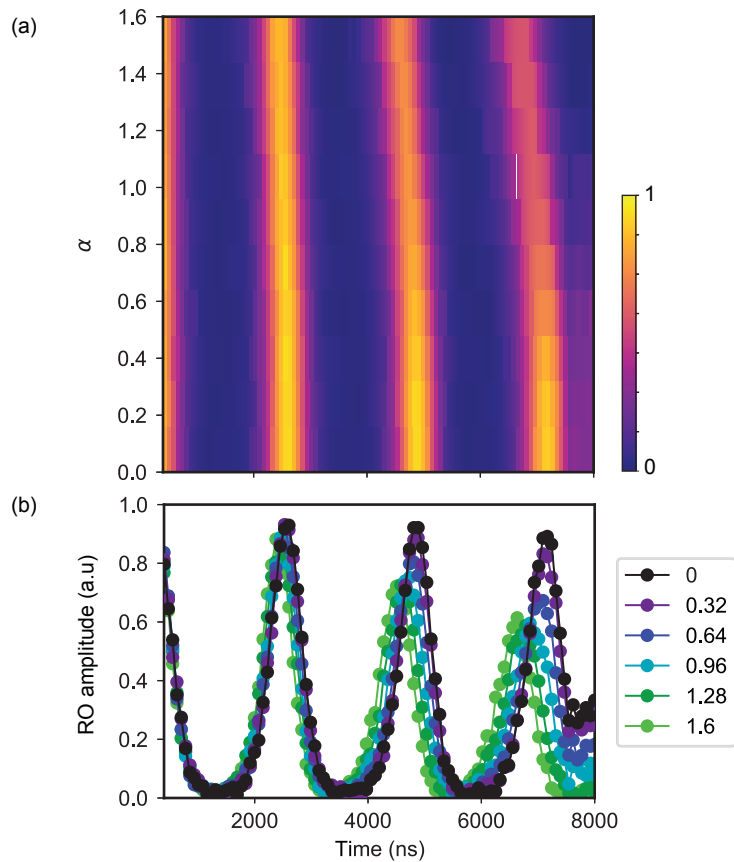


Figure 3.6: **Cross-Kerr coupling between Alice and Bob** (a) Measurement of Ramsey revival with  $\alpha_0 = 1$  in Bob as a function of time and the photon numbers in Alice,  $\alpha$ . A shift in the frequency of Bob is observed as larger  $\alpha$ . (b) 1D cut for several different displacements in Alice. The fitted revival time allow us to infer a cross-Kerr coupling on of 8 - 10 kHz.

Bob. The amount of the shift gives us  $K_{AB}$  of this system, which is  $\sim 9$  kHz. In general, it is beneficial to minimise this coupling by maintaining a large spectral separation between Alice and Bob.

### 3.3 Characterisation of cavity coherence

In order for this type of multi-cavity design to be relevant to future cQED experiments, we must be able to realise the non-linear couplings described above while maintaining the excellent coherent properties of the cavities. To demonstrate this, we measure the energy relaxation time,  $T_1$ , of the cavities by observing the decay of a coherent state in the cavity.

In this experiment, we first displace the cavity state by a coherent state  $|\alpha_0|^2 \gg 1$  and probe the probability of it being in vacuum after a variable delay time. This is measured by a spectrally selective  $\pi$  pulse that only excites the transmon if the cavity has relaxed back to vacuum. The sequence is presented in Fig. 3.7(a). The energy decay can be visualised in the phase space in a cartoon shown in Fig. 3.7(b) and has the following functional form:

$$P_e(t) \propto e^{-|\alpha_0|^2 \exp(-\kappa t)} \quad (3.2)$$

where  $\kappa$  is the characteristic decay constant associated with the energy relaxation of the cavity state. In the sample, the two cavities have  $\kappa/2\pi \sim 200$  Hz, corresponding to a lifetime  $T_1 \sim 2$  ms (Fig. 3.7(c)).

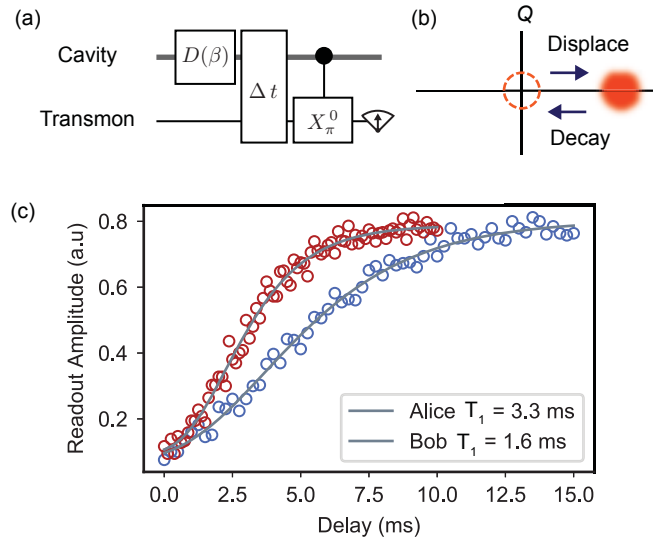


Figure 3.7:  $T_1$  measurement of cavities (a) Experimental protocol for measuring the cavity  $T_1$ . It consists of a large displacement of the cavity state followed by a variable delay. The final state is probed using a selective  $\pi$  pulse on the transmon conditioned on having zero photon in the cavity. (b) Phase space representation of the experiment which monitors the probability of a displaced coherent state relaxing back to vacuum after a certain delay. (c) The measured decay of coherent states in Alice and Bob respectively. The data (open circles) are fitted to Eq. 3.2 to give the cavity  $T_1$ .

Apart from having a low photon loss rate, the cavities must also be able to preserve the phase coherence of the quantum state in order for it to be a suitable memory to store superposition states. Similar to the case of two-level systems, we can characterise this

property using a Ramsey-type experiment and extract the decoherence time,  $T_2$ . To do so, we first prepare the cavity in a superposition of  $|0\rangle$  and  $|1\rangle$  Fock states using either SNAP or OCT pulses. Subsequently, we allow the system to evolve for a variable amount of time before probing the cavity state [15]. The result of such a measurement is shown in Fig. 3.8.

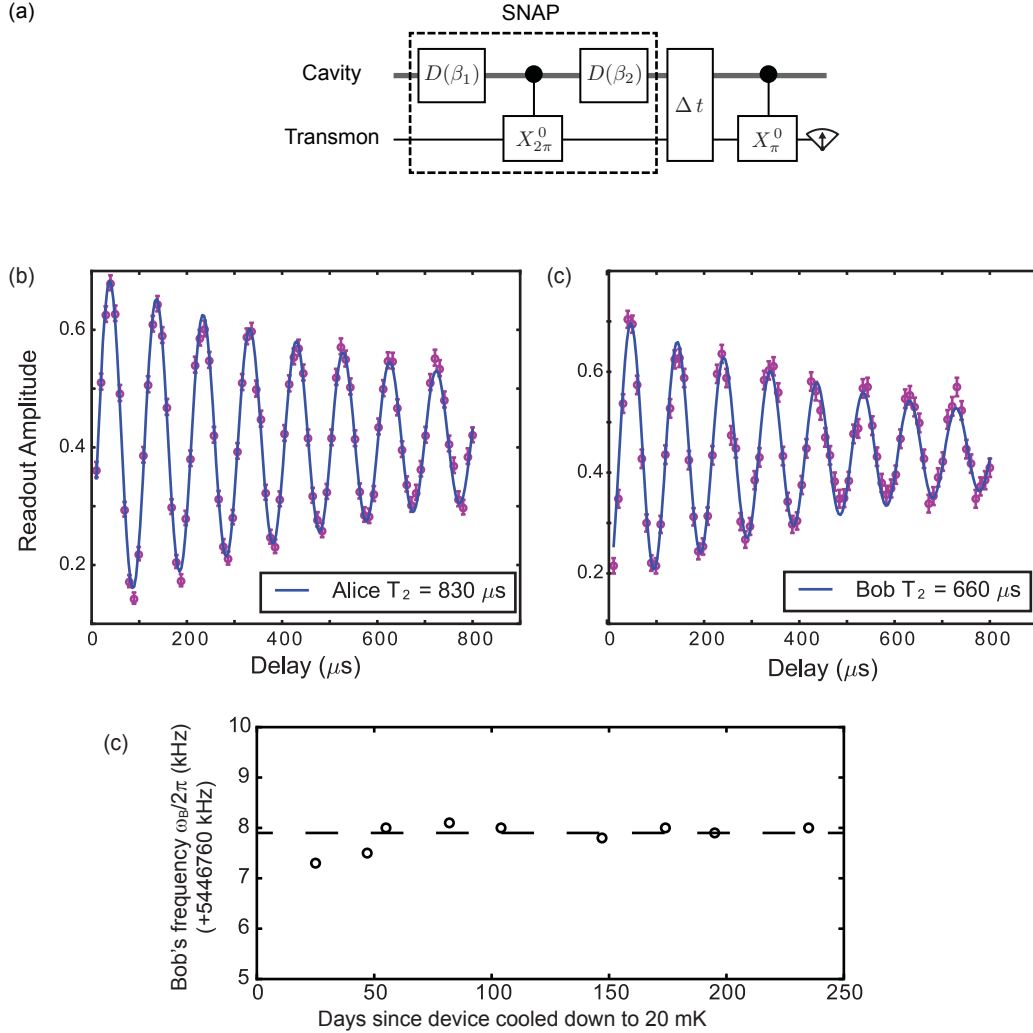


Figure 3.8:  $T_2$  measurement of cavities. (a) Experimental protocol for cavity  $T_2$  measurement. We use the SNAP [64, 15] sequence to prepare the superposition state  $|\psi\rangle = \frac{1}{\sqrt{2}}(|0\rangle + |1\rangle)$  (b), (c) Ramsey interference experiments of  $\frac{1}{\sqrt{2}}(|0\rangle + |1\rangle)$  in Alice and Bob, which determines their  $T_2$ . (d) Cavity resonance frequency of Bob extracted from Ramsey interference experiments done over the course of eight months. The data indicate remarkable long-term frequency stability of the 3D cavities.

This type of interference experiment, as described in Ref. [15], faithfully extracts the  $T_2$

without being affected by high-order nonlinearities. Together with the measurement of the cavity  $T_1$ , we find the cavity pure dephasing time  $T_\phi = 1/(\frac{1}{T_2} - \frac{1}{2T_1}) = 1.1 \pm 0.2$  ms for Alice and  $0.9 \pm 0.2$  ms for Bob.

The dephasing times are fully explained by the frequency shifts of the cavities due to the thermal excitation of the transmon ancilla [15]. The rate of the  $|g\rangle \rightarrow |e\rangle$  transition of the transmon,  $\Gamma_\uparrow$ , can be determined from its  $T_1$  and thermal population of the  $|e\rangle$  state,  $P_e$ :  $\Gamma_\uparrow = P_e/T_1 = 7.5\%/(70 \mu\text{s}) = 1/(0.9 \text{ ms})$ . The sources causing this type of upward transition are not yet well-known but it can sometimes be suppressed through careful shielding and filtering.

In addition, the cavity Ramsey experiment also allows the extraction of the precise resonance frequency of the cavity ( $\sim 1$  kHz). In the measurements shown in Fig. 3.8(b) and (c), an intentional detuning (10 kHz) is introduced in software. This allows us to fit the oscillation frequency and extract small deviations from the resonance frequency. Over the course of 8 months while the device was continuously operated at 20 mK, we observed no slow drift of cavity frequency exceeding its linewidth ( $\approx 200$  Hz) as shown Fig. 3.8(d).

	$T_1$	$T_2$	$P_e$
Alice	2.2-3.3 ms	0.8-1.1 ms	1-2%
Bob	1.2-1.7 ms	0.6-0.8 ms	2-3%
Ancilla $ e\rangle$	65-75 $\mu\text{s}$	30-45 $\mu\text{s}$	7.5%
Ancilla $ f\rangle$	26-32 $\mu\text{s}$	12-24 $\mu\text{s}$ <sup>a</sup>	0.5%
Readout	260-290 ns	N/A	<0.2%

Table 3.2: **Coherence properties of double-cavity system.** Energy relaxation time ( $T_1$ ), Ramsey coherence time ( $T_2$ ), coherence time with Hahn echo ( $T_{2E}$ ), and thermal population of the excited state ( $P_e$ ) of all components when applicable.

<sup>a</sup> $T_2=11-19 \mu\text{s}$  for  $|f\rangle$  vs.  $|g\rangle$

The coherence properties of the cavities are summarised in Table 3.2. Both cavities have coherences on par with the best single cavity system in similar designs. This demonstrates that such multi-cavity architecture can be constructed without adversely affecting the stability or the coherence properties individual high-Q cavities. Therefore, such systems provide a robust and attractive platform for storing and manipulating multiple bosonic logical qubits.

### 3.4 Extension to incorporate multiple ancillae

The design introduced in the beginning of this chapter provides a highly versatile systems for many different multi-cavity studies. With its single transmon, we already have universal control on both Alice and Bob, in theory. However, it does pose certain challenges when it comes to preparing more complex states and doing tomography on them. Therefore, we would like to build on this existing design to allow more experimental flexibility. The next generation of double-cavity device is shown in Fig. 3.9. In this system, additional ancillary modes, accompanied by their respectively on-chip readout resonators, are introduced to each stub cavity. This is accomplished simply by incorporating two more tunnels that protrudes into each of the stub cavities respectively. Since each additional transmons only couple to a single storage cavity, they assume a more traditional form with only two antenna pads. As a result, the substrate is not narrow and can be attached to the package using the a slightly modified version of the clamping fixture described in Fig. 3.4.

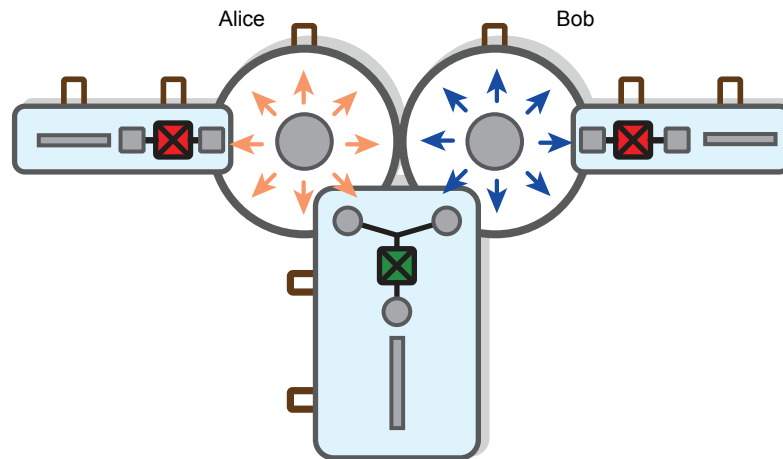


Figure 3.9: **Cartoon of a modified double-cavity cQED system.** The device consists of two high-Q cavities, 3 transmon ancillae and their respective readout resonators. Such a configuration provides more flexibility in both the individual and joint control of Alice and Bob.

This modification, albeit straightforward in implementation, does require some careful optimisation. First, by introducing additional non-linear elements into the system, each stub cavity now inherits Kerr nonlinearities from two transmons. This could become a serious

complication for experiments that involve high photon number occupations in the cavity modes. As a rule of thumb, the inherited nonlinearity scales as  $K \sim \chi^2/\alpha$ . Therefore, for the two side transmons, it is beneficial to choose a relatively large anharmonicity while remain protected against charge noise. In this case,  $\alpha \sim 200$  MHz appears fairly optimal. We also ensure that the  $\chi$  between each transmon to the cavity is limited to  $\sim 1$  MHz, which is sufficient to offer efficient cavity control and measurement while still allowing us to keep the  $K \lesssim 10$  kHz.

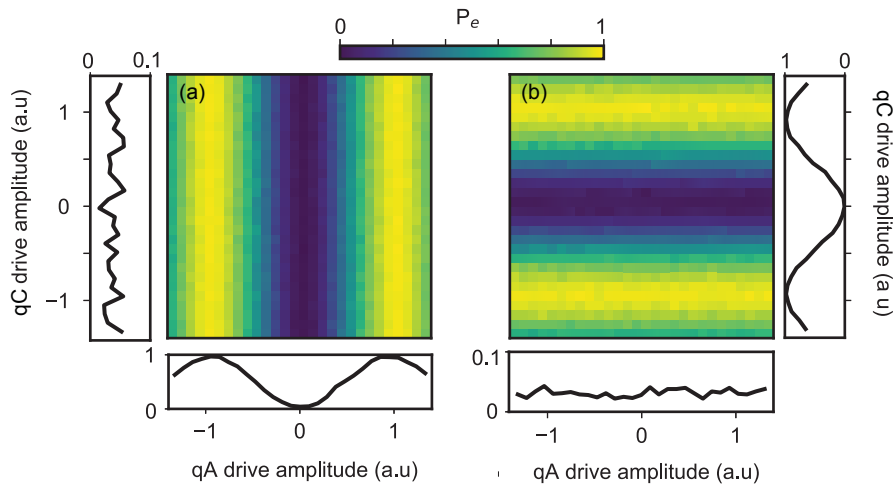


Figure 3.10: **Simultaneous Rabi experiment.** (a) Measurement of qA while we sweep the drive amplitudes on both qA and qC. The 1D projections show that the marginals along each axis. (b) The same measurement performed on qC while sweeping the drive amplitudes. The data show that the Rabi frequency of each qubit has negligible dependence on the state of the other mode.

The second key consideration is the spectral distribution of all the components in the system. It is crucial to minimise unwanted cross-coupling between the modes so that we can address them precisely and independently. In particular, we want to ensure centre and side ancillae do not couple to each other. This is achieved by optimising both their respective frequencies as well as their coupling to the cavity mode. We can confirm that the two transmon modes have negligible cross talk by performing a two mode Rabi experiment between two transmons, qA and qC. We drive them with variable amplitude simultaneously and perform readout on both in a two-dimensional measurement (Fig. 3.10). The data show

that the state of qA has very little impact on the Rabi frequency of qC and vice versa. This verifies that the two transmons do not have any measurable direct coupling.

We choose to position the three readout resonators at frequencies above all the other modes, between 7.5 GHz and 8.1 GHz. Due to the filtering process of the transmon and cavity modes between them, there is no measurable coupling between these independent readouts despite their spectral proximity. The output from each resonator is connected to a JPC, which allows efficient readout with high fidelity in a single shot. This provides the capability to perform both individual and joint readouts across all three output modes. Such devices are used in the bosonic interference study (Chapter 6) and entangling gate experiment (Chapter 7). Typical parameters for this type of devices are given in Table 3.3. Here, the parameters associated with transmon  $|f\rangle$  level are omitted since they are not exploited in the experiment that this sample is designed for.

	Frequency $\omega/2\pi$	Nonlinear Alice	interactions: Bob	qA	qB	qC
Alice	5.4821 GHz	4 kHz	( $\sim 1$ kHz)	0.77 MHz	N.A	0.27 MHz
Bob	6.5631 GHz	( $\sim 1$ kHz)	2 kHz	N. A	1.24 MHz	0.36 MHz
q(A)	4.4423 GHz	0.32 MHz	( $\sim 0$ kHz)	176 MHz	N.A	$\lesssim 1$ kHz
q(B)	4.7931 GHz	( $\sim 0$ kHz)	1.24 MHz	N.A	182 MHz	$\lesssim 1$ kHz
q(C)	6.0512 GHz	0.27 MHz	0.36 MHz	N.A	$\lesssim 1$ kHz	74 MHz
RO(A)	7.7245 GHz	(4 kHz)	( $\sim 0$ kHz)	1.2 MHz	N.A	( $\sim 0$ )
RO(B)	7.7219 GHz	( $\sim 0$ kHz)	4 kHz	N.A	0.8 MHz	( $\sim 0$ )
RO(C)	8.0627 GHz	( $\sim 0$ kHz)	( $\sim 0$ kHz)	N.A	N.A	1 MHz

Table 3.3: **Hamiltonian parameters of new system.** Values that are within a parenthesis are estimated/simulated parameters. Some non-linear couplings, such as  $\chi$  between qA and Bob, are omitted because they are too small to be simulated.

Despite the increased complexity in the system, we can still quite reliably simulate and predict its key Hamiltonian parameters as shown in the comparison in Table 3.4. With multiple non-linear elements in the device, the simulation process becomes considerably slower. To get around this, we take advantage of the weak coupling between the transmons and break the simulation into three independent parts. We first simulate each individual cavity and the transmon ancilla it couples to independently. It is important to note that

while we do not consider the second transmon mode that each cavity couples to, we must include the sapphire chip that contains the transmon. This is because the intrusion of the chip causes quite a significant shift in the cavity frequencies. Based on the single cavity and single transmon simulations, we can get a fairly accurate prediction on the resonance frequencies of each modes and the anharmonicities of the ancillae. We then simulate the centre system which consists of a Y-mon dispersively coupled to both Alice and Bob to get the parameters associated with qC. An example of this simulation is shown in Fig. 3.11 where we only consider one of the side transmons. The field distribution from this mode is well-confined to the single cavity it couples to and have negligible overlap with the mode of the other components in the system.

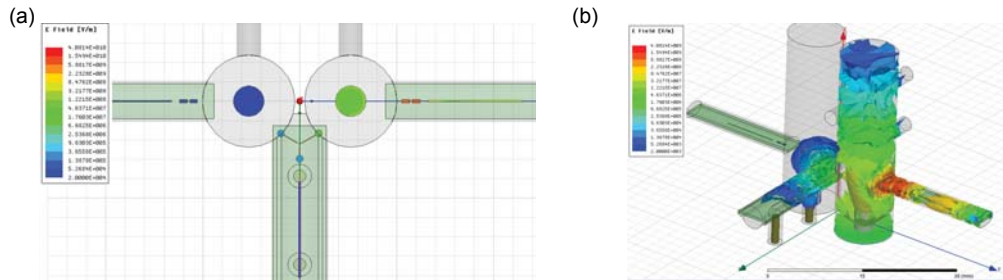


Figure 3.11: **Field distribution in HFSS simulation.** The device consists of two high-Q cavities, 3 transmon ancillae and their respective readout resonators are simulated in the HFSS eigenmode solver. The resulting field on each component due to the Josephson junction in the transmon on the right hand side is plotted. We observe highly localised field concentrated around the transmon with little excursion into other modes in the system.

The full simulation of the two cavity, three transmon system is very computationally demanding. It is carried out once to provide a comparison to the simplified procedure. As shown in Table 3.4, the predictions obtained from both simulation procedures show good agreement with the measured values. The dispersive couplings seem to show the largest discrepancies. This can be attributed to the variations in the chip position relative to the cavities due to imprecisions in the mounting. Since the chips are designed to protrude into the cavities near the maxima of the electric field, a small change in its position can lead to a significant deviation from the intended coupling strength. Based on our simulations, the discrepancy of  $\chi$  between qA and Alice can be accounted for by a 100  $\mu\text{m}$  lateral shift in

	Simulated (single JJ)	Simulated (full system)	Measured
$\omega_{ge}/2\pi$ (qA)	4.472 GHz	4.562 GHz	4.4423 GHz
$\omega_{ge}/2\pi$ (qB)	4.983 GHz	4.998 GHz	4.7931 GHz
$\omega_{ge}/2\pi$ (qC)	5.914 GHz	5.962 GHz	6.051 GHz
$\alpha/2\pi$ (qA)	175 MHz	172 MHz	178 MHz
$\alpha/2\pi$ (qB)	177 MHz	181 MHz	182 MHz
$\alpha/2\pi$ (qC)	75.7 MHz	79.4 MHz	74 MHz
Alice	5.471 GHz	5.424 GHz	5.482 GHz
$\chi_A^{qA}/2\pi$	0.98 MHz	0.75 MHz	0.76 MHz
$\chi_A^{qC}/2\pi$	0.166 MHz	0.248 MHz	0.28 MHz
Bob	6.550 GHz	6.575 GHz	6.5631 GHz
$\chi_B^{qB}/2\pi$	1.19 MHz	1.32 MHz	1.24 MHz
$\chi_B^{qC}/2\pi$	0.249 MHz	0.295 MHz	0.36 MHz

Table 3.4: **Simulated vs measured Hamiltonian parameters** Comparison between the predicted Hamiltonian parameters from a combination of three single-junction simulations, the full system simulation and the measured values. The two types of simulations give very close predictions. Both are consistent with the measured values.

the chip position.

We use the same characterisation techniques described earlier to measure the Hamiltonian parameters and the coherence properties for each mode in this type of systems. We summarise the results for a typical device in this architecture in Table 3.5.

In this particular system, the  $T_2$  of the three transmons seem to show rather drastic fluctuations. We attribute this to the mechanical vibrations that introduce low frequency noise to the device and lead a degradation of the transmons' frequency stability. We attempted to ameliorate this effect by enhancing the stability of the clamping. In particular, we fully affix the chip to the clamps using both stycast and indium seals. A handful of samples in this configuration have been cooled down in the same 3D package and characterised. The result seems to show that such a modification could improve the frequency stability of the transmon over the course of a few thermal cycles. Three out of the five devices measured showed significant improvements in their  $T_2$  from  $\sim 15 \mu\text{s}$  to  $\sim 40 \mu\text{s}$ . However, more systematic investigations are needed before a conclusive statement can be made.

It is also worth noting that the coherence times of Alice and Bob in this sample are

slightly inferior compared to the previous device. This could be due to the presence of two transmons in each cavity mode, introducing additional reverse-purcell limit on the cavity  $T_1$ . Furthermore, the dephasing due to upward transitions of the transmons will also be more severe since due to cavity's coupling to a second ancilla. Additionally, the vibration issues that degrade the transmon's  $T_2$  could also lead to a fluctuation of the cavity's frequencies due to the vibration of the sapphire chip. Depending on the frequency of the vibration, it could result in a deterioration of cavity's dephasing time scale.

	$T_1$	$T_2$	$T_{2E}$	$P_e$
Ancilla qA	65-75 $\mu$ s	15-45 $\mu$ s	60-80 $\mu$ s	3%
Ancilla qB	60-80 $\mu$ s	10-30 $\mu$ s	40-70 $\mu$ s	1.5%
Ancilla qC	20-40 $\mu$ s	10-30 $\mu$ s	20-35 $\mu$ s	0.5%
Alice	0.5-1 ms	0.4-0.6 ms	N/A	<1%
Bob	0.5-1 ms	0.4-0.6 ms	N/A	<1%
RO (A)	300-600 ns	N/A	N/A	<0.2%
RO (B)	500-800 ns	N/A	N/A	<0.2%
RO (A)	1000-1200 ns	N/A	N/A	<0.2%

Table 3.5: **Coherence properties of double-cavity with three ancillae.** Energy relaxation time ( $T_1$ ), Ramsey coherence time ( $T_2$ ), coherence time with Hahn echo ( $T_{2E}$ ), and thermal population of the excited state ( $P_e$ ) of all components when applicable. RO refers to the planar readout resonators for each ancilla.

### 3.5 Experimental configurations

In this section, we will discuss the cryogenic configurations and room temperature microwave control chains used for the subsequent experiments. These are crucial aspects that must be handled with careful considerations in order to create a stable, coherent quantum system. Here, we show two examples of the controls lines from room temperature to a double-cavity sample mounted on the base plate of the dilution refrigerator.

Shown in Fig. 3.12 is the set-up employed in the very first double-cavity experiment in 2015. Due to the limited availability of field-programmable gate array (FPGA) cards at that moment, we decided to use a combination of a single FPGA card and a Tektronix 5014C Arbitrary Waveform Generator (AWG) to provide the IQ controls for the experiment. The

AWG IQ outputs are triggered by a digital marker signal from the FPGA. The waveforms are pre-loaded to the AWG with the appropriate delay times corresponding to when a pulse is played from the FPGA card. While this configuration is perfectly capable of implementing the control sequences required for the experiment, the lack of easy synchronisation and fast feedback capabilities made it difficult to extend beyond this simple system with only 4 modes.

The configuration described in Fig. 3.13 is used to control our new device that contains more than one transmon ancillae. Due to the need to simultaneously control multiple IQ channels and fast feedback, we upgraded our system so that four FPGA cards are used to provide both the ADCs and DACs necessary for the experiment. The IF signals generated by the FPGA, ran at 500 mega sample in our experiments, passes through a 370 MHz commercial low-pass filter (Minicircuits BLP-300+) to eliminate high frequency noise. Subsequently, the signals are attenuated by 6-10 dB before passing through the double-balanced mixers from Marki Microwaves. The attenuations reduce DAC power ( $\sim 0.5$  V peak-to-peak) to be below the 1dB compression point of the mixer. Furthermore, this also attenuates any added noises from the DAC and allows us to access a greater dynamic range. The modulated signals from the mixer are subsequently amplified by low-noise amplifier (ZVA-183+) with a gain of roughly 25 dBm around our operation frequencies.

In the experiments described in chapters 5, 6, and 7, RF pumps are used to engineer new Hamiltonian terms in the system. For this type of drives, special amplification chains are set up in order to supply sufficient RF power. We use a minicircuit amplifier (ZVE-8G+) which has a large gain of 35 dB and relatively low noise figure of 4 dB. This is then filtered with commercial bandpass filters to reduce the spectral width of the input signal to reduce the power dissipation in the fridge. All amplified input signals also pass through a RF switch before going into the fridge. The switches are triggered by digital markers from the FPGA cards and have a fast switching time of  $\sim 10$  ns. This ensures that no RF power is transmitted into the fridge during idle times and suppress spurious thermal populations in the system.

Microwave control tones, together with added noise from the room temperature amplifi-



between 8-12 GHz as well as a home-made broadband Eccosorb filter which is filled with an infrared-absorbing material capable of exponentially suppressing the noise at and beyond the IR frequencies. All filters are clamped either directly or via a copper braid to the base plate to ensure good thermalisation.

Apart from careful shielding from thermal and RF noise, we must also protect the system against stray magnetic field. In one of my earlier experiments [60], it has been shown that when cooled in an effective magnetic field of 200 mG, a transmon's  $T_1$  and  $T_2$  could be reduced appreciably due to vortex-flow loss. Therefore, we house the sample in a Cryoperm shield to protect it from the magnetic fields of other RF components. Additionally, we must also make sure that all components inside the shield (screws, RF connectors, and cables etc) are made from non-magnetic materials. It is also becoming a common practice to include an additional Eccosorb filter in the Cryoperm shield, directly before the coupling port to the device. Measurements on a few samples tested with and without this additional filter seem to indicate that its presence strongly correlates with the low thermal population of transmons. All input lines are set up in this configuration, except an optional line that is attenuated by only 10 dB attenuation at base. It is used to drive multi-photon conversion processes necessary for the experiments described in chapter 6 and 7. This line is shown in purple on the wiring diagram (Fig. 3.13) and it is typically combined at base with the regular input line to that particular mode through a directional coupler with 6 dB additional attenuation. In addition, the 10 dB attenuation is provided by a special reflective attenuator that does not dissipate energy at base. This allows us to send a larger amount of microwave power into the system without causing excessive heating.

The outgoing signal from the device must also be attenuated and amplified appropriately to ensure clean, stable readout. Loss is very important since the signal from the measurement typically only consists of a few photons. We pass the signal through a single Eccosorb filter, located inside the Cryoperm, and a low-loss K&L filter. This typically incurs a 1-2 dB insertion loss on the signal before it passes through two cryogenic circulators (QuinStar) which provide  $\sim 20$  dB of isolation with an additional 0.3 dB loss. The signal is routed by the two circulators to the JPC which is typically tuned to operate at 20 dB again and a bandwidth

of 4-8 MHz. The amplified microwave signals then pass through two isolators to prevent unwanted reflection into the system. Subsequently, they travel along a superconducting coaxial cable from the base plate to the 4K stage where they are further amplified by a wideband HEMT amplifier before exiting the fridge to the room temperature interferometry.

This signal, now containing the information about the qubit state, is mixed with a local oscillator (LO) tone to an intermediate frequency (IF) of 50 MHz in a heterodyne detection chain. Since the FPGA cards have both DAC's and ADC's built in, we can perform a simple readout process using a single LO. This is achieved by splitting the output of the LO generator, now set at 50 MHz below the resonant frequency of the readout resonator, and performing single-sideband modulation on half of it using the FPGA. This passes through into the experiment and the returning signal is mixed with the unmodulated half of the LO output. As a result, the final signal recorded by the FPGA is demodulated in the same frame as the original modulation, making it insensitive to any added phase noise in the measurement process.

Using this type of room temperature configuration, we have the capability to efficiently modulate and demodulate RF signals over a large number of IQ channels. This is crucial for the success of the experiment as we work towards harnessing an increasing number of quantum components. Thanks to the clever logic developed by N. Ofek in our lab and the hardware developments in better FPGAs, we are able to robustly control two cavities, three transmons and three independent readouts in our most recent experiment.

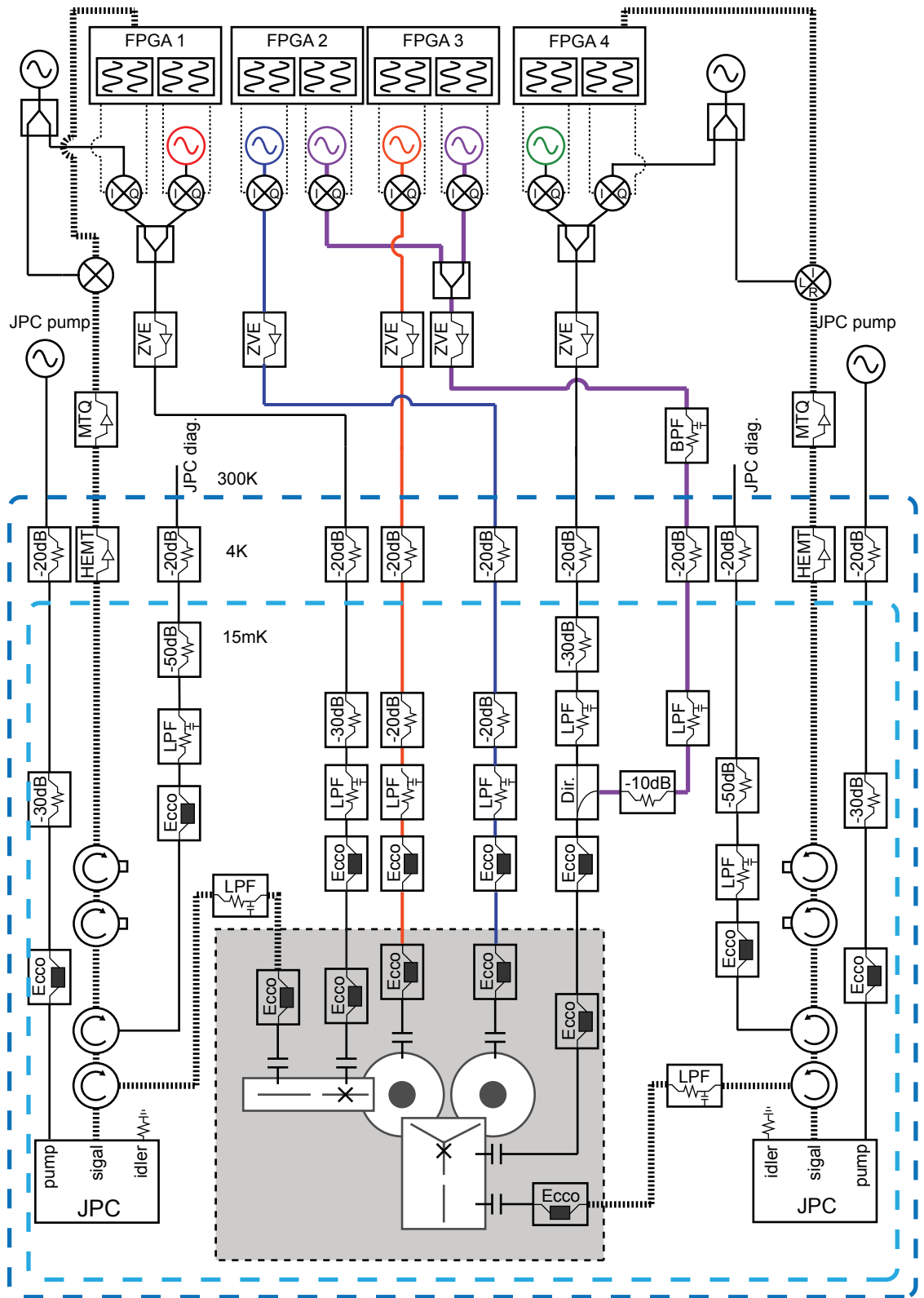


Figure 3.13: RF and fridge configurations for bosonic interference and eSWAP experiment. Input lines for only two transmon ancillae are included here due to space constraints.



## Chapter 4

### Putting a Schrödinger cat in two boxes

Since the birth of quantum mechanics, its many seemingly paradoxical predictions have piqued the interest of many experts and laypeople alike. Amongst these enigmas is the famous Schrödinger's *gedankenexperiment* of an unfortunate cat inside a closed box being simultaneously dead and alive. It highlights the peculiar consequences of extending the concept of superposition to macroscopically distinguishable objects. Over the years, exploiting quantum superpositions within a large Hilbert space has been a common theme for many experimental efforts aimed at probing the quantum-classical boundary. Also, such superpositions of "macroscopically-distinguishable" states that are far apart in phase space can be a valuable resource for the redundantly encoding of quantum information. The canonical example of such a state is the superpositions of coherent states of a harmonic oscillator, i.e.  $\mathcal{N}(|\alpha\rangle + |-\alpha\rangle)$  with  $\mathcal{N} \approx 1/\sqrt{2}$  at large  $|\alpha|$ , commonly referred to as "cat states". The two components correspond to distinct quasi-classical wave-packets with well-defined average amplitude and phase.

While we are able to explain Schrödinger's 'paradox' theoretically with increasing confidence, such exotic states are still hard to realise physically. This is because the superposition is highly delicate. Its non-classical correlations can be washed out easily as it inevitably gets in contact with the environment, which continually measures the state and projects it onto either dead ( $|\alpha\rangle$ ) or alive ( $|-\alpha\rangle$ ). Thanks to the rapid scientific and technological advancements over the recent decades, the coherence properties of quantum systems have improved by leaps and bounds. As a result, such cat states are no longer mere thought experiments.

They have been realised with single-mode optical photons [65] and microwave fields [56, 66]. These results offer more than just confirmation of the fundamental theories of quantum mechanics; they are also increasingly being recognised as key ingredients for new quantum technologies [67].

Existing cQED systems have demonstrated capabilities of creating and characterising single mode cat states with up to about 100 photons [63]. However, as the cat state occupies higher levels in the cavity, they are increasingly susceptible to decoherence effects, thus, limiting the accessible Hilbert space suitable for robust storage of quantum information. An alternative to expanding the available Hilbert space without sacrificing the coherence properties is to exploit several cavity modes simultaneously. The idea of creating a multi-mode cat state that lives in more than one harmonic oscillators has been conceived in early days of CQED [34] but experimental demonstrations have remained a challenge.

In this chapter, I will describe the first experimental realisation of a two-mode entangled cat state living in two superconducting cavities. We use the double-cavity system shown in Fig. 3.1 in this experiment, where two cavities, Alice and Bob, dispersively couple to a single transmon ancilla. I will start by introducing the protocol used to deterministically create a two-mode cat state using such a system in section 4.1. Subsequently, in section 4.2, we will examine the joint Wigner measurement and demonstrate full characterisation of the entangled state using the single transmon ancilla. Specifically, I will highlight the usage of the third level of transmon to achieve this efficiently without sacrificing the versatility of the system. Section 4.3, I will show that such two-mode cat states are equivalent to a bell-pair of qubits encoded in the coherent state basis. We will discuss the measurement of the two-qubit Pauli operators using joint parity mapping and also perform a simple Bell test to demonstrate that state we have created is indeed highly entangled.

## 4.1 Deterministic state creation

In our double-cavity cQED system, the transmon provides all the necessary non-linearity to implement a full set of controls over the cavity states. The two cavities, Alice and

Bob, are detuned from one another by  $\gtrsim 1$  GHz. This strongly suppresses their intrinsic coupling and hence, the entanglement between Alice and Bob can only be achieved through their respective interactions with the ancilla. It has been proposed [68], and experimentally demonstrated [63], that we can directly map the transmon state onto a superposition of two quasiorthogonal coherent states of a single resonator. We can also deterministically create a two-mode cat state of microwave fields in two superconducting cavities using the same technique, typically referred to as qcMAP. In this case, we must first create a three-way entanglement between the ancilla and both cavities using their strong dispersive interaction with the Y-mon. Subsequently, we can disentangle the ancilla from the cavities, leaving them in the two-mode entangled state,  $|\psi_{\pm}\rangle$ :

$$|\psi_{\pm}\rangle = \mathcal{N}(|\alpha\rangle_A|\alpha\rangle_B \pm |-\alpha\rangle_A|-\alpha\rangle_B) \quad (4.1)$$

where  $|\pm\alpha\rangle_A$  and  $|\pm\alpha\rangle_B$  are coherent states of two microwave eigenmodes (Alice and Bob) at different frequencies, whose amplitudes are chosen to be equal for simplicity. Each mode predominantly localised in one of the two cavities that are weakly connected. Despite a non-zero (but small) spatial overlap of the two modes, we will refer for convenience to the state of each mode as the state of the individual cavity. Quantum superpositions of the form  $|\psi_{\pm}\rangle$  have been previously realised in the optical domain [69] but were limited to small and non-orthogonal coherent states ( $|\alpha|^2 = 0.65$ ). For larger  $|\alpha|$  (*i.e.*  $|\alpha|^2 \gtrsim 2$ ),  $|\psi_{\pm}\rangle$  can be considered a single cat state living in two boxes whose superposed components are coherent states in a hybridised mode involving both Alice and Bob. Alternatively, in the more natural eigenmode basis,  $|\psi_{\pm}\rangle$  has been known as the entangled coherent states in theoretical studies [70], and may also be understood as two single-cavity cat states that are entangled with each other.

The qcMAP protocol [68] consists of a series of conditional operations between the transmon and each cavity, as shown in Fig. 4.1. In this particular protocol, the key operation is one that realises a three-way entanglement,  $D_{2\alpha}^g$ . It is an effective displacement by  $2\alpha$  conditional on the transmon being in its ground state. Under this gate, we can

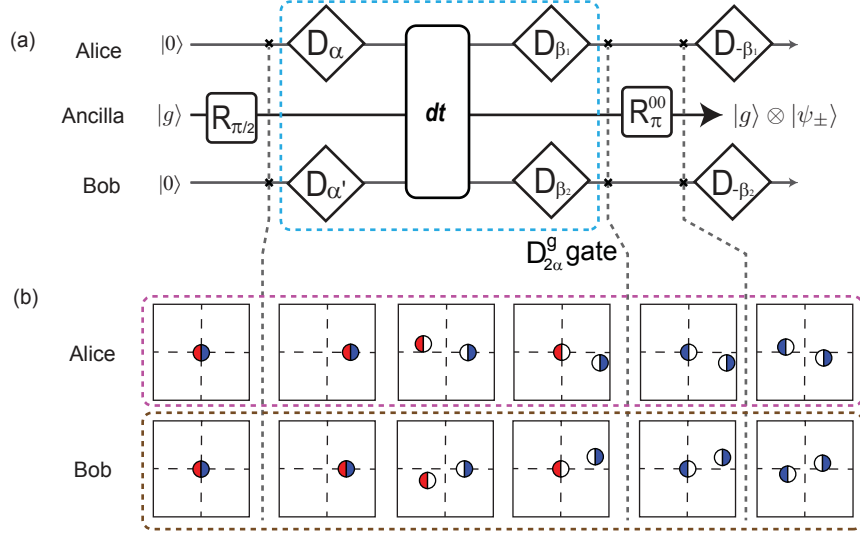


Figure 4.1: **qcMAP Protocol for deterministic creation of two-mode cat state.** (a) Pulse sequence for state creation, written in a general form that accommodates different photon numbers in each cavity. (b) Cartoon depicting the state evolution of Alice and Bob in their respective IQ planes. Blue and red indicate the cavity photon probability distribution associated with the ancilla  $|g\rangle$  and  $|e\rangle$  respectively. The rotation of the phase space during the protocol can be accounted by an independently calibrated rotation of the tomography angle such that the final state lies on the real axis in both Alice and Bob.

fully entangle the transmon excitation with both of the cavity states simultaneously, i.e.  $\frac{1}{2}(|g\rangle + |e\rangle)|0\rangle_A|0\rangle_B \rightarrow \mathcal{N}(|g\rangle|0\rangle_A|0\rangle_B + |e\rangle|2\alpha\rangle_A|2\alpha\rangle_B)$ . In principle, this operation can be implemented directly using sufficiently spectrally selective cavity drives ( $\text{FWHM} \ll \chi_i^{ge}$ ,  $i = A, B$ ). However, this requires an extremely long pulse duration, leading to more imperfections arising from transmon decoherence and Kerr effects. Therefore, we choose to implement this three-way entangling operation using two unconditional displacements separated by a wait time  $\Delta t$ , which can be independently calibrated. During this time, the cavities states both accumulate a conditional phase  $\phi_i = \chi_i^{ge} \Delta t$ , as described by this following unitary:

$$U(\Delta t) = \hat{I}_A \otimes \hat{I}_B \otimes |g\rangle\langle g| + e^{i\phi_A \hat{a}^\dagger \hat{a}} \otimes e^{i\phi_B \hat{b}^\dagger \hat{b}} \otimes |e\rangle\langle e| \quad (4.2)$$

We can visualise this process in the IQ plane of each cavity mode as shown in Fig. 4.1. The Gaussian blobs describe the photon probability distribution in the rotating frame which stays stationary when the ancilla is  $|g\rangle$  but starts rotating at an angular velocity  $\propto \chi_i$  when

the ancilla is excited. Therefore, when we prepare the transmon in a superposition state  $\frac{1}{\sqrt{2}}(|g\rangle + |e\rangle)$ , the initial coherent state is split with equal probability to accumulate a phase of zero or  $\phi_i$ . Hence, this effectively implements the conditional displacement operation,  $D_{2\alpha}^g$ . Subsequently, the transmon is disentangled from the cavities by a  $\pi$ -rotation conditional on both cavities being in vacuum. A final displacement then brings the cavities into the two-mode cat state. As shown in the cartoon, the final state may lie along a different axis in the IQ plane of each cavity. This is due to a deterministic phase accumulation over the preparation sequence which can be calibrated independently. We account for it by a introducing a rotation of the tomography axis in software such that the state in each cavity lie along either the real or imaginary axis.

Overall, all the operations required in this implementation are fast compared to the decoherence time scales and can be independently calibrated with good precision. A simple simulation that takes into account the decoherence in both the ancilla and the two cavities during this protocol indicates that the it is possible to create a two-mode cat state with high fidelity ( $\gtrsim 95\%$ ) in our system.

It is important to note that while we chose to express the state in the form Eq. 4.1, it can also be viewed as a larger cat state residing in a hybridised mode denoted by  $\hat{c}^\dagger = \frac{1}{\sqrt{2}}(\hat{a}^\dagger + \hat{b}^\dagger)$ :

$$|\psi_{\pm}\rangle = \mathcal{N}|\sqrt{2}(|\alpha\rangle_C \pm \sqrt{2}|\alpha\rangle_C) \quad (4.3)$$

In this basis, it is easy to see that we create single-mode cat state in Alice (or Bob) in the same system by simply omitting all the pulses on Bob (or Alice) and keep it in vacuum. Furthermore, it is also straightforward to create a two-mode cat in the basis  $\frac{1}{\sqrt{2}}(\hat{a}^\dagger + \hat{b}^\dagger)$  as it only requires a reversal of the displacements in either Alice or Bob. In fact, we can generate such states in an arbitrary basis spanned by two modes. It has been shown that with individual classical drives on each cavity and the transmon ancilla, it is sufficient to implement universal control of such two-cavity systems [51].

## 4.2 Joint parity measurement

After the creation of the two-mode cat, we now probe the state of each cavity using the standard Wigner tomography,  $W_i(\beta_i) = \frac{2}{\pi} \text{Tr}[\rho D_{\beta_i} P_i D_{\beta_i}^\dagger]$  ( $i=A$  or  $B$ ) [71, 72]. The Wigner function is a standard method to fully determine the quantum state of a single continuous-variable system, which represents the quasi-probability distribution of photons in the quadrature space defined by  $\text{Re}(\beta)$ - $\text{Im}(\beta)$ . It is measured using the established techniques described in section 2.5. Our measured individual Wigner functions,  $W_A$  and  $W_B$ , for a two-mode cat state  $|\psi_-\rangle$  with  $\alpha = 1.92$  are shown in Fig. 4.2. We observe that the quantum state of Alice or Bob on its own is a statistical mixture of two clearly-separated coherent states. The absence of the interference fringes indicates that there is no coherence between the two coherent state components. In other words, each cavity does not contain a regular (single-mode) cat state, which would contain characteristic fringes in the Wigner function [63]. This is not surprising; rather it is a unique signature of an entangled state. We can consider the single-cavity Wigner tomography as a partial trace operation on the two-mode entanglement state which eases the coherence and leaves both modes in a statistical mixture. In fact, we can generalise this property and state that it is sufficient [73] to prove the presence of entanglement by showing that each subsystem ( $\rho_A$  and  $\rho_B$ ) is less pure than the full system ( $\rho_{AB}$ ), i.e

$$\text{Tr}(\rho_A^2) < \text{Tr}(\rho_{AB}^2); \quad \text{Tr}(\rho_B^2) < \text{Tr}(\rho_{AB}^2) \quad (4.4)$$

In this case, it is obvious from the measured Wigner function of each cavity that the subsystems are fully mixed. This already hints that we have indeed created an entangled state between two modes. In order to faithfully and quantitatively characterise such an entangled cat state, we must implement joint Wigner tomography such that the non-classical correlations between the two modes can be directly demonstrated.

Just as a cat state is an eigenstate of the parity operator, this particular two-mode cat state is an eigenstate of the joint photon number parity operator  $P_J$ :

$$P_J = P_A P_B = e^{i\pi a^\dagger a} e^{i\pi b^\dagger b} = e^{i\pi(n_A + n_B)} \quad (4.5)$$

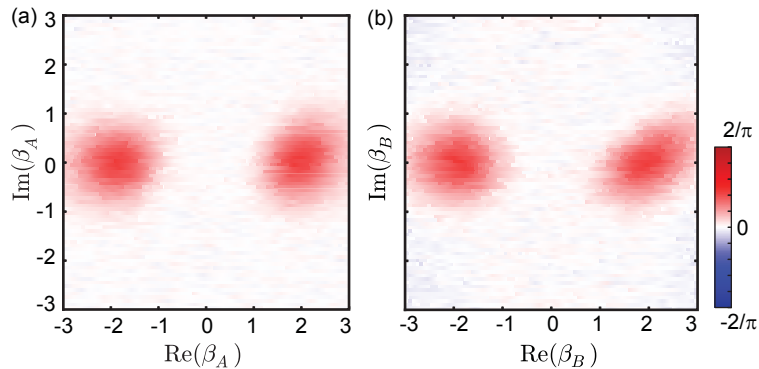


Figure 4.2: **Wigner tomography of individual cavities.** Measured single-cavity scaled Wigner function of (a) Alice ( $\frac{\pi}{2}W_A(\beta_A)$ ) and (b) Bob ( $\frac{\pi}{2}W_B(\beta_B)$ ) respectively for the two-mode cats state  $|\psi_-\rangle$ , each plotted in the complex plane of  $\text{Re}(\beta_i)$  and  $\text{Im}(\beta_i)$  ( $i=A$  or  $B$ ). For either cavity, no interference fringes are observed in its Wigner function, indicating a statistical mixture of two coherent states, as opposed to a single-cavity cat state, after tracing out the quantum state of the other cavity. The distortion of the coherent states is due to Kerr nonlinearity in the cavities. The photon number parity within each cavity is close to 0, reflected by the value of respective Wigner functions near the origin.

where  $\hat{a}(\hat{a}^\dagger)$  and  $\hat{b}(\hat{b}^\dagger)$  are the annihilation (creation) operators of photons in Alice and Bob, and  $P_A$  and  $P_B$  are the photon number parity operators in individual cavities. Remarkably,  $|\psi_+\rangle$  (or  $|\psi_-\rangle$ ) has definitively an even (or odd) number of photons in the two cavities combined, while the photon number parity in each cavity separately is maximally uncertain. This again echoes the observation of the mixed state in the individual Wigner measurements shown in earlier. In order to faithfully characterise the state, we must perform a joint parity measurement which only learns about the parity of the total number of photons in both Alice and Bob. Additionally, photon loss in either of the cavities, which tend to be the dominant error mechanisms in such systems, translates into a change of the joint parity. Therefore quantum non-demolition measurements of the joint parity operators not only illustrate the highly non-classical properties of the state, but also are instrumental for quantum error correction in general.

Before I proceed to discuss the details of measuring the joint parity, let us first briefly review the underlying principle of the single parity measurement of a single cavity [33, 71]. Such measurements use a dispersively coupled ancilla [71, 74] to impart a conditional cavity phase shift [66],  $C_\phi = \mathbb{I} \otimes |g\rangle\langle g| + e^{i\phi a^\dagger a} \otimes |e\rangle\langle e|$ , of  $\phi = \pi$  and therefore allow the cavity states

with even or odd photon numbers to be mapped to  $|g\rangle$  or  $|e\rangle$  of the qubit for subsequent readout. By extension, in our multi-cavity architecture, measuring the joint photon number parity requires  $C_\pi$  in both Alice and Bob, which is difficult to achieve simultaneously with existing techniques [74] unless  $\chi_A^{ge} = \chi_B^{ge}$ . In this case, in a wait time  $\Delta t = \pi/\chi_A^{ge} (= \pi/\chi_B^{ge})$ , we get:

$$\begin{aligned} U(\pi/\chi_i^{ge}) &= C_\pi^A C_\pi^B \\ &= \mathbb{I} \otimes |g\rangle\langle g| + \hat{P}_A \hat{P}_B \otimes |e\rangle\langle e| \end{aligned} \quad (4.6)$$

This  $\chi$ -matching can be realised in hardware with a precise set of design parameters. However, it is often extremely challenging to satisfy this requirement in presence of fluctuations in fabrication conditions. Without strictly identical  $\chi_A^{ge}$  and  $\chi_B^{ge}$ , the phase accumulation in one cavity is faster than the other, and it is in general not possible to realise parity operators in both cavities simultaneously using this simple protocol. Moreover, for a general two-cavity quantum state, this sequence can not measure a single-cavity parity operator ( $\hat{P}_A$  or  $\hat{P}_B$ ) due to inevitable entanglement between the ancilla and the photons in the other cavity during the process and therefore, limit the controllability of the system.

We overcome this challenge and avoid the stringent requirements on Hamiltonian parameters by exploiting the  $|f\rangle$  level of the transmon. As we have shown in section 3.3, the  $|f\rangle$  level of the transmon has perfectly satisfactory coherence properties and can be easily controlled using standard pulses. Therefore, we simply use the third transmon level as an additional degree of freedom to engineer an effective  $\chi$  that is matched. This method is most helpful when the  $|e\rangle \rightarrow |g\rangle$  transition of the ancilla shows stronger interaction with Bob ( $\chi_B^{ge} > \chi_A^{ge}$ ), while the  $|f\rangle \rightarrow |e\rangle$  transition shows stronger interaction with Alice ( $\chi_A^{ef} > \chi_B^{ef}$ ). This is physically realised by engineering the ancilla frequency to lie between those of the two cavities, *i.e.*  $\omega_A < \omega_{ef} < \omega_{ge} < \omega_B$ . Considering the quantum state with two cavities and three ancilla levels in general, the unitary evolution for any wait time  $\Delta t$

is:

$$\begin{aligned}
U(\Delta t) = & \mathbb{I}_A \otimes \mathbb{I}_B \otimes |g\rangle\langle g| + e^{i\phi_A \hat{a}^\dagger \hat{a}} \otimes e^{i\phi_B \hat{b}^\dagger \hat{b}} \otimes |e\rangle\langle e| \\
& + e^{i\phi'_A \hat{a}^\dagger \hat{a}} \otimes e^{i\phi'_B \hat{b}^\dagger \hat{b}} \otimes |f\rangle\langle f|
\end{aligned} \tag{4.7}$$

where

$$\begin{aligned}
\phi_A &= \chi_A^{ge} \Delta t, & \phi_B &= \chi_B^{ge} \Delta t \\
\phi'_A &= \chi_A^{gf} \Delta t, & \phi'_B &= \chi_B^{gf} \Delta t
\end{aligned} \tag{4.8}$$

where  $\chi_A^{gf} \equiv \chi_A^{ge} + \chi_A^{ef}$  and  $\chi_B^{gf} \equiv \chi_B^{ge} + \chi_B^{ef}$ . Therefore, the two cavities simultaneously can acquire conditional phases in their coherent state components at relative rates that differ for  $|e\rangle$  and  $|f\rangle$ . In light of this, we can now manipulate the ancilla in different superposition states among the three levels to concatenate conditional phase gates associated with  $\chi_i^{ge}$ ,  $\chi_i^{ef}$ , and  $\chi_i^{eg}$  with arbitrary weights. This additional degree of freedom not only allows for joint parity measurement  $P_J$  (applying  $C_\pi$  to both cavities), but also enables parity measurement of each cavity  $P_A$  or  $P_B$  individually without affecting the other (applying  $C_\pi$  and  $C_{2\pi}$  to the two cavities respectively).

Two possible pulse sequences for such  $\hat{P}_J$  measurement using three ancilla levels are shown in Fig. 4.3. In the first case, we exploit the  $|g\rangle - |f\rangle$  superposition of the ancilla to realise the joint measurement. For a given two-cavity quantum state  $\Psi_{AB}$ , we first use a  $R_{\pi/2}^{ge}$  rotation to prepare the ancilla in  $\frac{1}{\sqrt{2}}(|g\rangle + |e\rangle)$ . Then a wait time  $\Delta t_1$  imparts phases  $\phi_{A1} = \chi_A^{ge} \Delta t_1$  and  $\phi_{B1} = \chi_B^{ge} \Delta t_1$  to the two cavities for the  $|e\rangle$  component of the state:

$$\begin{aligned}
& \Psi_{AB} \otimes \frac{1}{\sqrt{2}}(|g\rangle + |e\rangle) \\
& \Rightarrow \frac{1}{\sqrt{2}} [\Psi_{AB} \otimes |g\rangle + e^{i\phi_{A1} \hat{a}^\dagger \hat{a}} e^{i\phi_{B1} \hat{b}^\dagger \hat{b}} \Psi_{AB} \otimes |e\rangle]
\end{aligned} \tag{4.9}$$

Next, the  $|e\rangle$  component in this intermediate state is converted to  $|f\rangle$  by a  $\pi$  rotation in the  $|e\rangle$ - $|f\rangle$  space,  $R_\pi^{ef}$ . Subsequently a second wait time  $\Delta t_2$  leads to a second simultaneous

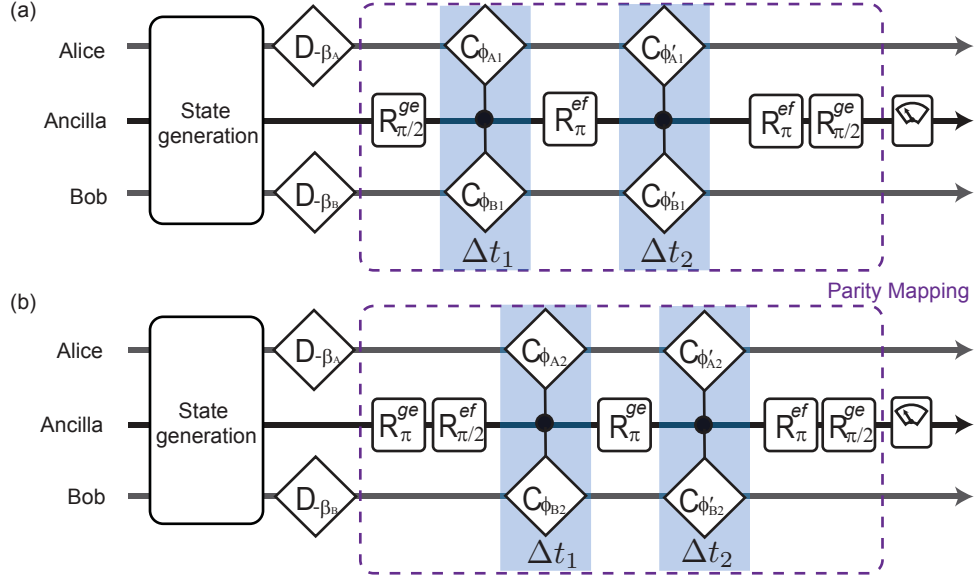


Figure 4.3: **Two experimental protocols for joint parity measurement**. (a) Pulse sequence for using the  $|g\rangle - |f\rangle$  supersposition to map joint photon number parity of Alice and Bob to the ancilla.  $D_{\beta}$  represents a displacement of cavity state by amplitude  $\beta$ . The additional of superscript indicates that the displacement operation is conditional on a certain transmon state.  $R_{\theta}^{ge}$  or  $R_{\theta}^{ef}$  represents an ancilla rotation by angle  $\theta$  in the  $|g\rangle - |e\rangle$  or  $|e\rangle - |f\rangle$  Bloch sphere.  $R_{\pi}^{00}$  is a  $\pi$ -rotation on  $|g\rangle - |e\rangle$  conditional on both cavities in the vacuum state. The conditional phase gates are realised by the wait time  $\Delta t_1$  and  $\Delta t_2$  while the ancilla is in a superposition state. Here  $\phi_A = \chi_A^{ge} \Delta t$ ,  $\phi_B = \chi_B^{ge} \Delta t$ ,  $\phi'_A = \chi_A^{gf} \Delta t$ ,  $\phi'_B = \chi_B^{gf} \Delta t$ . (b) An alternative parity measurement sequence involving the  $|e\rangle - |f\rangle$  superposition of the ancilla, where  $\phi_A = \chi_A^{ef} \Delta t$ ,  $\phi_B = \chi_B^{ef} \Delta t$  instead. We use  $\Delta t_1 = 28$  ns, and  $\Delta t_2 = 168$  ns for  $\hat{P}_J$  measurements presented in Fig. S10. This method reduces the parity mapping phase error at the cost of more ancilla pulse errors.

conditional phase gate, imparting phases  $\phi_{A2} = \chi_A^{gf} \Delta t_2$  and  $\phi_{B2} = \chi_B^{gf} \Delta t_2$  to the two cavities for the now  $|f\rangle$  component of the state:

$$\begin{aligned} & \frac{1}{\sqrt{2}} [\Psi_{AB} \otimes |g\rangle + e^{i\phi_{A1}} \hat{a}^\dagger \hat{a} e^{i\phi_{B1}} \hat{b}^\dagger \hat{b} \Psi_{AB} \otimes |f\rangle] \Rightarrow \\ & \frac{1}{\sqrt{2}} [\Psi_{AB} \otimes |g\rangle + e^{i(\phi_{A1} + \phi_{A2})} \hat{a}^\dagger \hat{a} e^{i(\phi_{B1} + \phi_{B2})} \hat{a}^\dagger \hat{a} \Psi_{AB} \otimes |f\rangle] \end{aligned} \quad (4.10)$$

The  $|f\rangle$  component is then converted back to  $|e\rangle$  by another  $R_{\pi}^{ef}$  pulse. If we can find  $\Delta t_1$

and  $\Delta t_2$  so that:

$$\begin{aligned}\phi_{A1} + \phi_{A2} &= \chi_A^{ge} \Delta t_1 + \chi_A^{gf} \Delta t_2 = \pi \\ \phi_{B1} + \phi_{B2} &= \chi_B^{ge} \Delta t_1 + \chi_B^{gf} \Delta t_2 = \pi\end{aligned}\quad (4.11)$$

the obtained quantum state is:

$$|\Psi\rangle_{\text{final}} = \frac{1}{\sqrt{2}} [\Psi_{AB} \otimes |g\rangle + \hat{P}_J \Psi_{AB} \otimes |e\rangle] \quad (4.12)$$

effectively realising the simultaneous controlled  $\pi$ -phase gate ( $C_\pi^A C_\pi^B$ ) in Eq. 4.6. Finally a  $R_{\pi/2}^{ge}$  pulse completes the projection of joint parity to the ancilla  $|g\rangle, |e\rangle$  levels, ready for readout through the readout resonator.

The condition for finding non-negative solutions for  $\Delta t_1$  and  $\Delta t_2$  in Eq 4.11 is that  $\chi_A^{ge} - \chi_B^{ge}$  and  $\chi_A^{gf} - \chi_B^{gf}$  have opposite signs. In essence, the cavity that acquires phase slower than the other at  $|e\rangle$  due to smaller  $\chi_i^{ge}$  is allowed to catch up at  $|f\rangle$  using its larger  $\chi_i^{gf}$ . It should be noted that such relative relation of the  $\chi$ 's is just a practically preferred condition rather than an absolute mathematical requirement. This is because parity mapping can be achieved whenever both cavities acquire a conditional phase of  $\pi$  modulo  $2\pi$ . It is always possible to allow extra multiples of  $2\pi$  phases applied to the cavity with stronger dispersive coupling to the ancilla, although it increases the total gate time and incurs more decoherence. The essential ingredient in engineering the  $\hat{P}_J$  operator is the extra tuning parameter  $\Delta t_2$  (in addition to  $\Delta t_1$ ) that allows two equations such as Eq 4.11 to be simultaneously satisfied.

This extra degree of freedom also enables measurement of the photon number parity of a single cavity,  $\hat{P}_A$  or  $\hat{P}_B$ , for an arbitrary two-cavity quantum state. This is realised with the same control sequences (Fig. 4.3A), choosing wait times such that one cavity acquires a conditional  $\pi$  phase (modulo  $2\pi$ ) while the other acquires 0 phase (modulo  $2\pi$ ). For example,

to measure  $\hat{P}_A$  we use  $\Delta t_1$  and  $\Delta t_2$  satisfying:

$$\begin{aligned}\phi_{A1} + \phi_{A2} &= \chi_A^{ge} \Delta t_1 + \chi_A^{gf} \Delta t_2 = \pi \pmod{2\pi} \\ \phi_{B1} + \phi_{B2} &= \chi_B^{ge} \Delta t_1 + \chi_B^{gf} \Delta t_2 = 0 \pmod{2\pi}\end{aligned}\quad (4.13)$$

Fig 4.3(b) shows an alternative version of joint parity mapping protocol, which uses more ancilla operations, but is better adapted to a larger parameter space of  $\chi$ 's. In this protocol, the ancilla spends time at the  $|e\rangle$ - $|f\rangle$  superposition so that conditional phases proportional to  $\chi_i^{ef}$  are applied to the cavities. To achieve joint parity mapping, the two time intervals  $\Delta t_1$  and  $\Delta t_2$  should satisfy:

$$\begin{aligned}\phi_{A1} + \phi_{A2} &= \chi_A^{ef} \Delta t_1 + \chi_A^{gf} \Delta t_2 = \pi \pmod{2\pi} \\ \phi_{B1} + \phi_{B2} &= \chi_B^{ef} \Delta t_1 + \chi_B^{gf} \Delta t_2 = \pi \pmod{2\pi}\end{aligned}\quad (4.14)$$

which avoids the use of extra  $2\pi$  phases to  $\chi_A^{ef} - \chi_B^{ef}$  has opposite sign versus  $\chi_A^{gf} - \chi_B^{gf}$ .

Experimentally, choices of the parity mapping sequence and gate times involve trade-offs in various aspects such as pulse speed/bandwidth and coherence time. We have measured joint parity (and subsequently Wigner functions) using both protocols. For the sequence of Fig 4.3(a),  $\Delta t_1 = 0$ ,  $\Delta t_2 = 184$  ns was experimentally implemented. For the sequence of Fig 4.3(b),  $\Delta t_1 = 28$  ns,  $\Delta t_2 = 168$  ns was used. The actual effective wait time was longer due to the non-zero duration (16 ns) of each ancilla rotation. Also, small deviations from the ideal timing is introduced due to 4 ns resolution of the FPGA output. The first protocol, with this choice of wait times, does not yield the exact  $\pi$  phases required for exact parity mapping (We estimate  $\phi_{A1} + \phi_{A2} = 0.97\pi$  and  $\phi_{B1} + \phi_{B2} = 1.03\pi$ ).

These phase errors lead to an estimated infidelity of the joint parity measurement of about 3% for the two-cavity states in this study. Exact phases can be achieved with longer wait times so that  $\phi_{A1} + \phi_{A2} = 3\pi$  and  $\phi_{B1} + \phi_{B2} = 5\pi$ , but the infidelity due to decoherence and high-order Hamiltonian terms outweighs the benefits. In principle, the second protocol that achieves exact  $\pi$  phases at relatively short total gate time should be more advantageous.

However, using the second protocol, we observe visibly identical results of joint Wigner tomography of the two-mode cat states with fidelity nearly equal to the first protocol. This is attributed to the extra infidelity from the more complicated ancilla rotations involved in the second protocol, due to pulse bandwidth limitations and unwanted ancilla population mixing. Details of the different contributions to the reduced contrast are provided in the section 4.4.

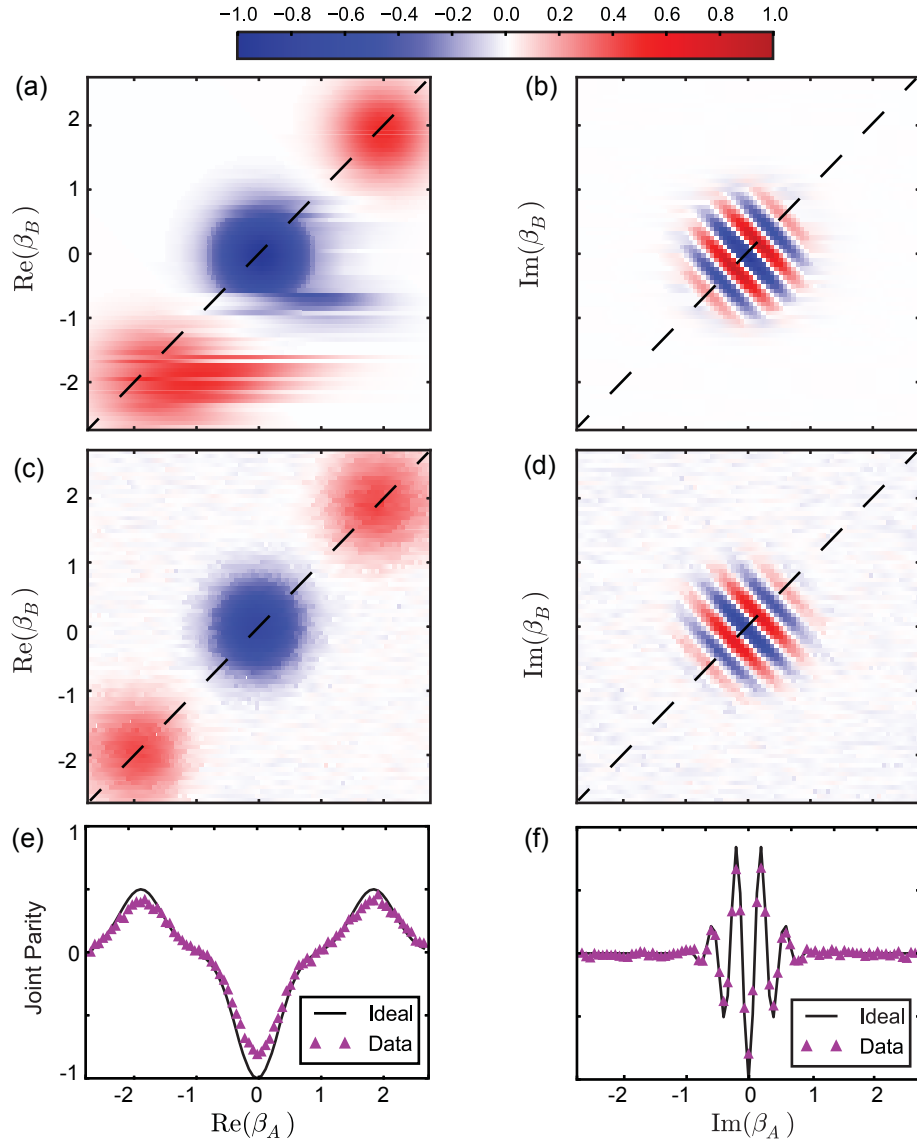


Figure 4.4: **Scaled joint Wigner tomography** (a, b) Two-dimensional plane-cut along (a) axes  $\text{Re}(\beta_A)\text{-Re}(\beta_B)$  and (b) axes  $\text{Im}(\beta_A)\text{-Im}(\beta_B)$  of the calculated 4D scaled joint Wigner function  $\langle P_J(\beta_A, \beta_B) \rangle$  of the ideal odd-parity two-mode cat state  $|\psi_-\rangle$  with  $\alpha = 1.92$ . The red features in (A) represent the probability distribution of the two coherent states components. The central blue feature in (A) and fringes in (B) demonstrate quantum interference between the two components. (c,d) The corresponding  $\text{Re}(\beta_A)\text{-Re}(\beta_B)$  and  $\text{Im}(\beta_A)\text{-Im}(\beta_B)$  plane-cuts of the measured joint Wigner function of  $|\psi_-\rangle$ , to be compared with the ideal results in (A) and (B) respectively. Data are taken in a  $81 \times 81$  grid, where every point represents an average of about 2000 binary joint parity measurements. (e) Diagonal line-cuts of the data shown in (A) and (C), corresponding to 1D plots of the calculated (black) and measured (red) scaled joint Wigner function along  $\text{Re}(\beta_A) = \text{Re}(\beta_B)$  with  $\text{Im}(\beta_A) = \text{Im}(\beta_B) = 0$ . (f) Diagonal line-cuts of the data shown in (B) and (D), corresponding to 1D plots of the calculated (black) and measured (red) scaled joint Wigner function along  $\text{Im}(\beta_A) = \text{Im}(\beta_B)$  with  $\text{Re}(\beta_A) = \text{Re}(\beta_B) = 0$ .

$W_J$  is a function in the four-dimensional (4D) phase space, whose value at each point  $(\text{Re}(\beta_A), \text{Im}(\beta_A), \text{Re}(\beta_B), \text{Im}(\beta_B))$ , after rescaling by  $\pi^2/4$ , is equal to the expectation value of the joint parity after independent displacements in Alice and Bob [75].

$$\begin{aligned} W_J(\beta_A, \beta_B) &= \frac{4}{\pi^2} \langle P_J(\beta_A, \beta_B) \rangle \\ &= \frac{4}{\pi^2} \text{Tr}[\rho D_{\beta_A} D_{\beta_B} P_J D_{\beta_B}^\dagger D_{\beta_A}^\dagger] \end{aligned} \quad (4.15)$$

For simplicity, we will therefore use the scaled joint Wigner function, or “displaced joint parity”  $\langle P_J(\beta_A, \beta_B) \rangle$  to represent the cavity state.  $\langle P_J \rangle$  at any given point  $(\beta_A, \beta_B)$  is directly measured by averaging single-shot readout outcomes and takes values between -1 and +1. To illustrate the core features in this 4D Wigner function of the state  $|\psi_-\rangle$ , we show its two-dimensional (2D) cuts along the  $\text{Re}(\beta_A)$ - $\text{Re}(\beta_B)$  plane and  $\text{Im}(\beta_A)$ - $\text{Im}(\beta_B)$  plane for both the calculated ideal state (Fig 4.4(a), (b), also see Ref [75]) and the measured data Fig 4.4(c), (d). The Wigner function contains two positively-valued Gaussian hyperspheres representing the probability distribution of the two coherent-state components, and an interference structure around the origin with strong negativity corresponding to an odd joint parity state, as expected. Excellent agreement is achieved between measurement and theory, with the raw data showing an overall 81% contrast of the ideal Wigner function. Comprehensive measurements of  $\langle P_J \rangle$  in the entire 4D parameter space further allow us to reconstruct the density matrix of the quantum state, which shows a total fidelity of also about 81% against the ideal  $|\psi_-\rangle$  state. The actual state fidelity may be significantly higher if various errors associated with tomography are removed. We will have a more detailed discussion about the sources of imperfections in section 4.4.

We can also measure the joint Wigner function along other planes. For example, we present the data obtained for the  $\text{Re}(\beta_A)$ - $\text{Im}(\beta_A)$  and  $\text{Re}(\beta_B)$ - $\text{Im}(\beta_B)$  planes in Fig. 4.6. The measurement indicates, not surprisingly, that only interference fringes are present on these planes, consistently with the results shown in Fig 4.4. Single cavity Wigner tomography is also performed using the protocol of Fig 4.3(a), with  $\Delta t_1 = 688$  ns,  $\Delta t_2 = 0$  for  $\hat{P}_A$ , and  $\Delta t_1 = 660$  ns,  $\Delta t_2 = 204$  ns for  $\hat{P}_B$ . Moreover, for  $\hat{P}_A$  measurement the  $R_\pi^{ef}$  pulses were

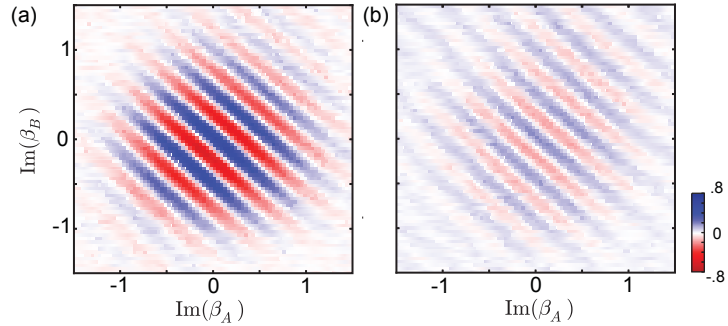


Figure 4.5: **Coherence of larger two-mode cat states.** Measured fringes in the  $\text{Im}(\beta_A) - \text{Im}(\beta_B)$  plane for two-mode cat states with photon numbers being (a)  $\alpha_A = 2.7, \alpha_B = 3.1$  and  $\alpha_A = 3.0, \alpha_B = 3.3$ .

skipped, taking advantage of the fact that  $\chi_B^{ge} \approx 2\chi_A^{ge}$ .

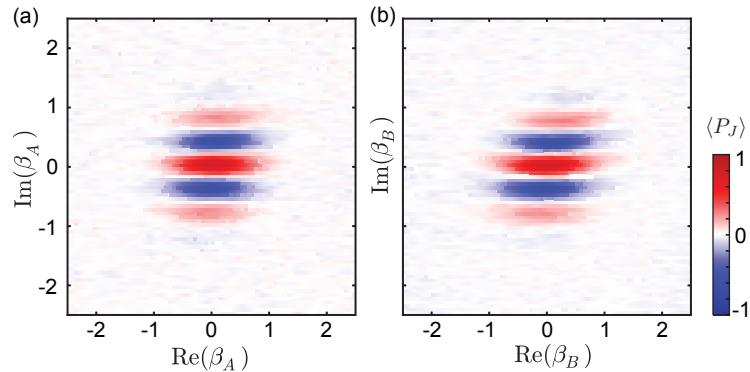


Figure 4.6: **Joint Wigner function of the two-mode cat state along single cavity I-Q planes.** Measured fringes in the  $\text{Im}(\beta_A) - \text{Im}(\beta_B)$  plane for two-mode cat states with photon numbers being (a)  $\alpha_A = 2.7, \alpha_B = 3.1$  and  $\alpha_A = 3.0, \alpha_B = 3.3$ .

Both the state creation and tomography method described so far can in principle be applicable to arbitrary photon numbers in the two cavities. We briefly measured the coherence features that lie in the  $\text{Im}(\beta_A) - \text{Im}(\beta_B)$  plane of the joint Wigner functions of two-mode cat states with larger and differing number of photons. The number of fringes increases with the total photon number, proportional to  $\sqrt{\alpha_A^2 + \alpha_B^2}$ . The largest state we measured (Fig. 4.5(b)) contains roughly 80 photons across the two cavities. While the interference patterns remain intact, the contrast of the measured joint Wigner function decreases quite significantly with increasing photon numbers. This corresponds to the increase in the non-idealities of joint parity measurement due to both stronger decoherence as well as

imperfections in ancilla rotations due to limited bandwidth.

Furthermore, we can also monitor the joint parity of the two-mode cat in the time domain to shine light on the decoherence time scales of the state after it has been created. Using a simple model that takes into account of both the photon loss rate of the two superconducting cavities, we can describe the decay of joint parity by

$$P_J(t) = P_J(t=0)\exp[-2\alpha^2(2 - e^{-t/\tau_A} - e^{-t/\tau_B})] \quad (4.16)$$

This model is only applicable when the total photon number is far from zero as all the photons decay from the cavities, joint parity will eventually approach +1. Since the initial decay is twice the photon loss rate, it is informative to consider a characteristic time scale during a span much shorter than the cavity lifetimes such that the photon populations in each cavity remains nominally constant.

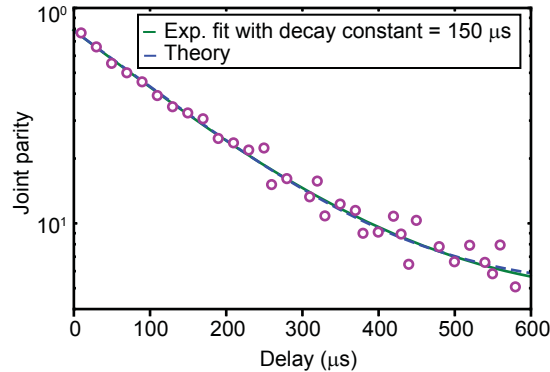


Figure 4.7: **Decay of joint parity.** The measured joint parity as a function of variable delay time after state creation. Green curve is a fit to a simple exponential function, which yields a time constant of 150  $\mu\text{s}$ . Blue dashed line shows the plot according to the theoretical model described in Eq. 4.16

For an even two-mode cat, we observe a decay time about 150  $\mu\text{s}$  with  $\alpha = 1.92$  using a simple single exponential fit. This is consistent with the average photon number over a duration of 600  $\mu\text{s}$  after state creation given the independently measured cavity lifetimes of  $\tau_A = 2.6$  ms and  $\tau_B = 1.5$  ms. This time scale is on par with, if not slightly superior to, the relaxation times of the state-of-the-art transmons. The result strongly echoes our motivation to use superconducting cavities to coherently store quantum information.

This particular measurement is not sensitive to other decoherence mechanisms such as the dephasing of the cat state due to a transmon thermal jump. However, given the thermal population of the device ( $\leq 8\%$ ) and its  $T_1$ , this dephasing time is  $\sim 1\text{ms}$ , which far exceeds the loss of joint parity due to photon loss. Therefore, it is not currently the limiting timescale and we believe it can be further improved with better thermalisation of the device to suppress the transmon thermal population.

### 4.3 A bell pair of encoded qubits

Compared with other reported quantum states of two harmonic oscillators, a striking property of the two-mode cat state is that its underlying compositions are highly distinguishable. Two-mode squeezed states [76, 77, 78, 79] have shown strong entanglement, but are Gaussian states without the Wigner negativity and the phase space separation as in a cat state. The “ $N00N$ ” state, an entangled state in the discrete Fock state basis, typically requires quantum operations of  $N$  photons one by one and so far has been realised with up to 5 photons [80, 81]. The two components of the cat state in Fig. 3 have a phase space separation of  $|\alpha - (-\alpha)| = \sqrt{15}$  in each cavity, giving an action distance of  $\sqrt{30}$  in the 4D phase space, or a cat size [72] of 30 photons. Our technique in principle allows the generation of two-mode cat states with arbitrary size using the same operation. So far we have measured cat sizes of up to 80 photons, and more macroscopic states can be achieved by implementing numerically optimised control pulses [37] and engineering more favourable Hamiltonian parameters.

Compared with single-cavity quantum states, the addition of the second cavity mode increases the quantum information capacity significantly. Despite the modest mean photon numbers, a full tomography of the two-mode cat state (partly shown in Fig. 3) requires a Hilbert space of at least 100 dimensions to be described (capturing 99% of the population), comparable to a 6 or 7 qubit GHZ state.

Our conservatively estimated quantum state fidelity is comparable to that reported for an 8-qubit GHZ state in trapped ions [82] and the largest GHZ state in superconducting circuits [40] (5 qubits). In addition, a great advantage of continuous-variable quantum control

is illustrated by our hardware-efficient quantum state tomography protocol that covers an enormous Hilbert space by simply varying two complex variables of cavity displacements.

An important motivation for creating multi-cavity cat states is to implement a promising paradigm towards fault-tolerant quantum computation [83, 50], where information is redundantly encoded in the coherent state basis [63]. Another advantage of this coherence-state based encoding is that we can perform a highly efficient tomography without accumulating a large grid of displaced parity measurements. In fact, it has been shown that 4 values of a cavity's the Wigner function is sufficient to reconstruct the state [84], an example of direct fidelity estimation (DFE) [85, 86].

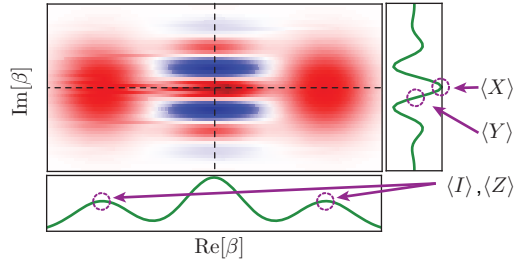


Figure 4.8: **Direct fidelity estimation of a cat state** Instead of performing full Wigner tomography, we can restrict ourselves to the encoded space and reconstruct the full density matrix of a cat state from 4 independent measurements. The Pauli set can be directly mapped to the displaced parity measurements.

In this context, our experiment realises an architecture of two encoded qubits entangled with each other. The two-mode cat state can be considered as a two-qubit Bell state  $\frac{1}{\sqrt{2}}(|0\rangle|0\rangle \pm |1\rangle|1\rangle)$ , where the quasi-orthogonal coherent states  $|\pm\alpha\rangle$  in each of the two cavities represent  $|0\rangle$  and  $|1\rangle$  of a logical qubit. In this encoding, the single-qubit Pauli operators can be written as:

$$\begin{aligned}
 X_j &\approx |-\alpha\rangle_j \langle \alpha|_j + |\alpha\rangle_j \langle -\alpha|_j \\
 Y_j &\approx i|-\alpha\rangle_j \langle \alpha|_j - i|\alpha\rangle_j \langle -\alpha|_j \\
 Z_j &\approx |\alpha\rangle_j \langle \alpha|_j - |-\alpha\rangle_j \langle -\alpha|_j \\
 I_j &\approx |\alpha\rangle_j \langle \alpha|_j + |-\alpha\rangle_j \langle -\alpha|_j
 \end{aligned} \tag{4.17}$$

For a cat state with sufficiently large  $\alpha$  ( $\langle |\alpha| - \alpha \rangle \ll 1$ ), we can directly map the encoded state observables to the cavity observables, which are the displaced parity operators of a cavity ( $\hat{P}_j(\beta) \equiv \hat{D}_{\beta_j} \hat{P}_j D_{\beta_j}^\dagger$ ):

$$\begin{aligned}
X_j &\approx \hat{P}_j(0) \\
Y_j &\approx \hat{P}_j\left(\frac{i\pi}{8\alpha}\right) \\
Z_j &\approx \hat{P}_j(\alpha) - \hat{P}_j(-\alpha) \\
I_j &\approx \hat{P}_j(\alpha) + \hat{P}_j(-\alpha)
\end{aligned} \tag{4.18}$$

The approximate sign is to reflect the non-zero overlap between the coherent states. Based on this, we can simply perform four independent parity measurements after the appropriate displacement in order to extract the set of Pauli operations  $\{I, X, Y, Z\}$ . As shown in Fig. 4.8, the observables  $I$  and  $Z$  require a comparison between two different measurements at the centre of each blob, while the observables  $X$  and  $Y$  are simply a single parity measurement after a particular displacement. We can directly extend this analysis to the two-mode cat and use it to implement an efficient tomography of the state in the two-qubit encoded states.

Based on this, the 16 two-qubit observables are products of single-qubit Pauli operators, and can all be expressed in the form of displaced joint parities. Since operators in different cavities commute,

$$\hat{P}_A(\beta_A) \hat{P}_B(\beta_B) = \hat{D}_{\beta_A} \hat{D}_{\beta_B} \hat{P}_J D_{\beta_A}^\dagger D_{\beta_B}^\dagger \equiv \hat{P}_J(\beta_A, \beta_B) \tag{4.19}$$

With this, we can fully characterise the Pauli operators using 16 independent measurements of displaced joint parity in the 4D phase space. This provides a direct, single-shot measurement of the expectation value of each two-qubit correlators and hence, another way to estimate the fidelity of the entangled state. Using the above-mentioned mapping, we can

map out the 16 two-qubit Pauli correlators as:

$$\begin{aligned}
I_A I_B &= \hat{P}_J(\alpha, \alpha) + \hat{P}_J(\alpha, -\alpha) + \hat{P}_J(-\alpha, \alpha) + \hat{P}_J(-\alpha, -\alpha) \\
I_A X_B &= \hat{P}_J(\alpha, 0) + \hat{P}_J(-\alpha, 0) \\
I_A Y_B &= \hat{P}_J(\alpha, \frac{i\pi}{8\alpha}) + \hat{P}_J(-\alpha, \frac{i\pi}{8\alpha}) \\
I_A Z_B &= \hat{P}_J(\alpha, \alpha) - \hat{P}_J(\alpha, -\alpha) + \hat{P}_J(-\alpha, \alpha) - \hat{P}_J(-\alpha, -\alpha) \\
X_A I_B &= \hat{P}_J(0, \alpha) + \hat{P}_J(0, -\alpha) \\
Y_A I_B &= \hat{P}_J(\frac{i\pi}{8\alpha}, \alpha) + \hat{P}_J(\frac{i\pi}{8\alpha}, -\alpha) \\
Z_A I_B &= \hat{P}_J(\alpha, \alpha) + \hat{P}_J(\alpha, -\alpha) - \hat{P}_J(-\alpha, \alpha) - \hat{P}_J(-\alpha, -\alpha) \\
X_A X_B &= \hat{P}_J(0, 0) \\
X_A Y_B &= \hat{P}_J(0, \frac{i\pi}{8\alpha}) \\
X_A Z_B &= \hat{P}_J(0, \alpha) - \hat{P}_J(0, -\alpha) \\
Y_A X_B &= \hat{P}_J(\frac{i\pi}{8\alpha}, 0) \\
Y_A Y_B &= \hat{P}_J(\frac{i\pi}{8\alpha}, \frac{i\pi}{8\alpha}) \\
Y_A Z_B &= \hat{P}_J(\frac{i\pi}{8\alpha}, \alpha) - \hat{P}_J(\frac{i\pi}{8\alpha}, -\alpha) \\
Z_A X_B &= \hat{P}_J(\alpha, 0) - \hat{P}_J(-\alpha, 0) \\
Z_A Y_B &= \hat{P}_J(\alpha, \frac{i\pi}{8\alpha}) - \hat{P}_J(-\alpha, \frac{i\pi}{8\alpha}) \\
Z_A Z_B &= \hat{P}_J(\alpha, \alpha) - \hat{P}_J(\alpha, -\alpha) - \hat{P}_J(-\alpha, \alpha) + \hat{P}_J(-\alpha, -\alpha)
\end{aligned} \tag{4.20}$$

Therefore, for any two-qubit state encoded in this subspace, we can perform efficient tomography without extensive measurement of the joint Wigner function. The encoded two-qubit tomography of a state  $|\psi_+\rangle$  with  $\alpha = 1.92$  is shown in Fig. ??, providing a direct fidelity estimation [86] of  $\frac{1}{4}(\langle II \rangle + \langle XX \rangle - \langle YY \rangle + \langle ZZ \rangle) = 78\%$  against the ideal Bell state, surpassing the 50% bound for classical correlation. The two-qubit tomography suggests that errors within the encoded space are quite small. The reduced contrast compared to the ideal

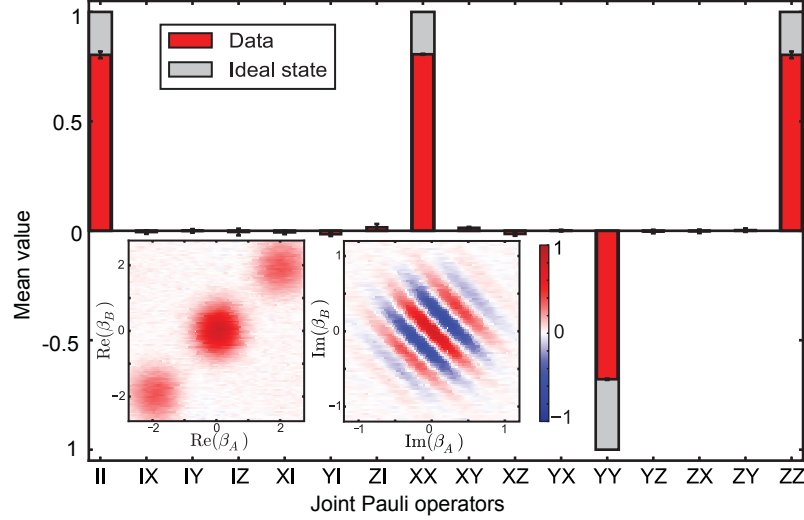


Figure 4.9: **Two-qubit Pauli correlators.** Red bars show tomography of two logical qubits encoded in the coherent state basis of two cavities, with the prepared state being an even-parity two-mode cat state,  $|\psi_+\rangle$  with  $\alpha = 1.92$ . Gray bars represent the ideal state. Insets show the  $\text{Re}(\beta_A)$ - $\text{Re}(\beta_B)$  and  $\text{Im}(\beta_A)$ - $\text{Im}(\beta_B)$  plane-cuts of the measured scaled joint Wigner function of the same state. The measured identity operator differs from 1 as a result of the parity measurement infidelity and leakage out of the code space.

state is mostly due to infidelity of the joint parity measurement and leakage out of the code space (due to higher-order Hamiltonian terms).

To further demonstrate this, we implement a more direct assessment similar to the Bell test. The two-mode cat state is a quantum mechanical system consisting of two continuous-variable subsystems. In general, for two continuous-variable systems, the correlation between their individual parities after independent displacements has a classical upper bound, which can be described by a CHSH-type Bell's inequality using the formulation proposed in Ref. [87] and discussed in Ref. [75]. Arbitrarily choosing two test displacements  $\beta_A, \beta'_A$  in Alice and two test displacements  $\beta_B, \beta'_B$  in Bob, the Bell signal  $\mathcal{B}$  can be constructed from parity correlations after all four combinations of displacements in the two cavities:

$$\begin{aligned} \mathcal{B} = & |\langle \hat{P}_A(\beta_A) \hat{P}_B(\beta_B) \rangle + \langle \hat{P}_A(\beta'_A) \hat{P}_B(\beta_B) \rangle \\ & + \langle \hat{P}_A(\beta_A) \hat{P}_B(\beta'_B) \rangle - \langle \hat{P}_A(\beta'_A) \hat{P}_B(\beta'_B) \rangle| \leq 2 \end{aligned} \quad (4.21)$$

where  $\hat{P}_i(\beta) \equiv \hat{D}_{\beta_i} \hat{P}_i D_{\beta_i}^\dagger$  ( $i = A, B$ ) is the displaced parity operator. Here measuring parity

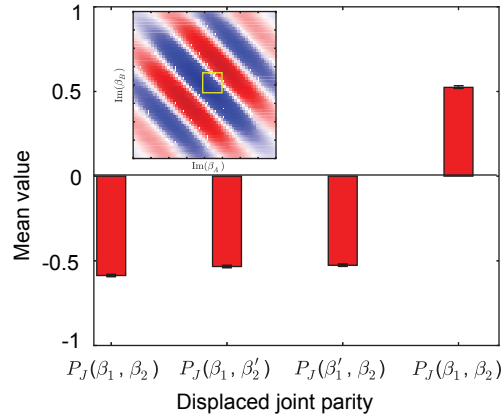


Figure 4.10: **Bell signal of an odd two-mode cat state.** Red bars show the amplitude of scaled joint Wigner function at the selected sampling points in the phase space defined by the imaginary amplitudes of  $\beta_A, \beta_B$ . Inset shows the location of the chosen sampling points in phase space

after different displacements is analogous to measuring  $\sigma_z$  of a spin- $\frac{1}{2}$  system after different rotations.

Equivalently, this Bell signal is represented by the values of joint Wigner function (or displaced joint parity) at the four vertices of a rectangle:

$$\mathcal{B} = \frac{\pi^2}{4} \left| W_J(\beta_A, \beta_B) + W_J(\beta'_A, \beta_B) + W_J(\beta_A, \beta'_B) - W_J(\beta'_A, \beta'_B) \right| \leq 2 \quad (4.22)$$

For a quantum state with entanglement between the two subsystems, this Bell's inequality can be violated. For near-optimal violation, we choose a square in the  $\text{Im}(\beta_A)\text{-Im}(\beta_B)$  plane with prominent interference fringes. The square is positioned to have three of the vertices close to the minimum of the central negative fringe and one in the vicinity of the maximum of the adjacent positive fringe, using  $\beta_A = \beta_B = -i\pi/(16\beta) = -0.102$  and  $\beta'_A = \beta'_B = 3i\pi/(16\beta) = 0.307$  (Fig. 5.5). Given these sampling points, the measured amplitude gives a Bell signal  $\mathcal{B} = 2.17 \pm 0.01$ , surpassing the classical threshold by more than 10 standard deviations. This indicates the non-classical nature of the two-mode cat state and the presence of quantum correlations between the two modes. This also demonstrates the robustness of our experimental technique in both the creation of the quantum mechanical

two-mode cat state as well as the joint parity measurement procedure. Without complete spatial separation and fully independent readout of the two modes, the violation should be considered a demonstration of the fidelity of the entanglement and the measurement rather than a true test of non-locality. Nevertheless, various schemes exist to further separate the two modes such as converting the cavity fields into itinerant microwave signals and/or optical photons [88].

## 4.4 Understanding imperfections

Although features of the measured joint Wigner function on the Re-Re and Im-Im planes can be compared to that of the ideal state for a qualitative gauge of the quality of the two-mode cat state, a full density matrix reconstruction would be required to rigorously evaluate the quantum state fidelity. The reconstruction requires a sufficiently large data set of  $W_J(\beta_k^{(A)}, \beta_k^{(B)})$ ,  $k \in (1, \dots, N_{\text{disp}})$  at  $N_{\text{disp}}$  unique displacements in the 4D phase space. The measured joint Wigner function at each of these points is simply a measurement of the scaled displaced joint parity

$$W_J(\rho, \beta_k^{(A)}, \beta_k^{(B)}) = \frac{4}{\pi^2} \text{Tr}[\rho D_k \hat{P}_J D_k] \quad (4.23)$$

where  $D_k = D_A(\beta_k^A) D_B(\beta_k^B)$ . This measurement, albeit lengthy, can be done easily using methods described in section 4.2.

In order to find the density matrix  $\rho$  from the measured set of  $W_J$ , we must find a matrix that relates the two such that  $\rho$  can be reconstructed from  $W_J$  by a simple matrix inversion. To establish this relation, we can write down  $\rho$  in the Fock state basis, truncated to some maximum photon number  $N_{\text{cutoff}}$ :

$$\rho = \sum_{i,j,k,l=1}^{N_{\text{cutoff}}} \rho_{ijkl} |ij\rangle \langle kl| \quad (4.24)$$

Next, we use the linearity of  $W_J$  in  $\rho$  to identify the contributions from each of its

components

$$\begin{aligned}
W_J(\rho, \beta_k^{(A)}, \beta_k^{(B)}) &= \frac{4}{\pi^2} \text{Tr}[\rho D_k \hat{P}_A \hat{P}_B D_k] \\
&= \frac{4}{\pi^2} \sum_{i,j,m,n} \rho_{i,j,m,n} \langle mn | \rho D_k \hat{P}_A \hat{P}_B D_k^\dagger | ij \rangle \\
&= \frac{4}{\pi^2} \sum_{i,j,m,n} \rho_{i,j,m,n} K_{mi}(\beta_k^{(A)}) K_{nj}(\beta_k^{(B)})
\end{aligned} \tag{4.25}$$

Now the matrix elements  $K_{mn}(\beta) \equiv \langle m | D(\beta) \hat{P} D(\beta)^\dagger | n \rangle$  are computed using the same method developed for standard Wigner state tomography [89]. In short, we find

$$K_{mn}(\beta) = e^{-|\beta|^2} (-1)^m (2\beta)^{n-m} \sqrt{\frac{m!}{n!}} L_m^{n-m}(\beta) \tag{4.26}$$

where  $L_m^{n-m}$  is a generalised Laguerre polynomial.

Now we compute independently each  $K_{mn}(\beta)$  and use them to reconstruct the density matrix from the measured joint Wigners. In order to ensure that the derived  $\rho$  has real eigenvalues and unity trace, we construct an optimisation problem to find  $\rho_{\text{ML}}$  that maximises the likelihood of agreeing with the measured data with the constraint that  $\text{Tr}(\rho) = 1$ . As an example, let us consider the state  $|\psi_+\rangle$  with  $\bar{n} = |\alpha|^2 \approx 3.7$ . In order to solve the optimisation problem, we must first determine an appropriate truncation based on the expected state. In this case, we choose to use  $N_{\text{cutoff}} = 12$ , which truncates  $\leq 0.1\%$  of the photons accordingly to Poisson statistics. This results in a system dimension of  $d = N_{\text{cutoff}}^2 = 144$  and therefore  $d^2 = 20736$  real parameters in  $\rho$ . This makes the computation rather demanding, but can be implemented with some clever routines such as the Broyden-Fletcher-Goldfarb-Shanno (BFGS) algorithm.

After performing the reconstruction, we find that the largest pure state that overlaps with the ideal state is given by the largest eigenvalue  $\lambda_{\text{max}}(\rho) \approx 0.824$ , with a purity  $\text{Tr}(\rho^2) = 0.68$ . The highest fidelity for the state of the specific form  $|\psi\rangle = |\alpha, \alpha\rangle + |-\alpha, -\alpha\rangle$  with  $\alpha = 1.905$  is  $\mathcal{F} = \langle \psi | \rho | \psi \rangle = 0.803$ . This is consistent with the fidelity inferred from the peak contrast of the joint parity measurement ( $\mathcal{F} \approx 0.81$ ). Small perturbations on the relative size and phase

	Assessment	Estimated infidelity
ancilla initialisation	$\sim 0.5\%$ probability not in $ g\rangle$	$\sim 1\%$
cavity initialisation	$\sim 0.5\%$ probability not in $ 0\rangle_A 0\rangle_B$	$\sim 1\%$
readout infidelity	1.0-1.5% error rate	2.5%
ancilla decoherence in state creation	$ g\rangle- e\rangle$ superposition for $0.65 \mu\text{s}$	2.2%
pulse error in state creation	imperfect spectral selectivity of $R_\pi^{00}$	$\sim 1\%$
ancilla decoherence in parity map	$ g\rangle- e\rangle$ & $ g\rangle- f\rangle$ superposition for $0.25 \mu\text{s}$	2.2%
timing (phase) error in parity map	$\pm 3\%$ phase error in $C_\pi^A$ and $C_\pi^B$	$\sim 3\%$
pulse error in parity map	population mixing in $ g\rangle- e\rangle- f\rangle$ rotations	$\sim 5\%$
photon loss in two cavities	3.7-7.3 photons in each cavity for $0.9 \mu\text{s}$	0.9%
Total		$\sim 19\%$

Table 4.1: **Contributions to the reduction of contrast in joint Wigner measurements.** The loss of contrast in the measured joint parity of the two-mode cat state,  $|\psi_\pm\rangle$  ( $\alpha = 1.92$ ), can be accounted for by these error channels. The estimated contribution is either measured in control experiments or inferred from simulations.

of the two coherent state components do not cause any insignificant variation of this state fidelity. Our reconstruction also finds that the joint parity of the largest eigenvector is 0.97 and that of the next few eigenvectors to be small and positive. This indicates that single-photon loss, which causes a change of joint parity from even to odd, is not the dominant error mechanism impacting the fidelity of the state preparation. In order to understand the different contributions to the state fidelity, we make a detailed error budget for both state generation and tomography.

The factors causing imperfections in the measured state can mostly be estimated directly from system parameters and tested in independent control experiments. The limited coherent times of the transmon and the cavities account for about 5% given the total time required to prepare and measure the two-mode cat state. Readout errors, calibrated to be roughly 1%, result in a 2% reduction in the measured joint parity since two rounds of readout are performed for each measurement. Moreover, we infer from the Rabi oscillations of the ancilla that there is a 2% chance of it starting from the wrong state despite the initialisation process. Additionally, further imperfections can arise from the joint parity measurement. This is primarily a result of incorrect mapping of the joint parity to the transmon state. For example, slight miscalibrations of  $\Delta t_1, \Delta t_2$  can lead to a discrepancy in the accumulated phase by  $\pm 3\%$ .

Another source of non-ideality is from the limited bandwidth of the transmon drives. In

order to correctly map the joint parity to the transmon state, we must implement rotations that are blind to the photon numbers of the cavities. This requires the Gaussian pulses to have sufficiently large spectral width ( $\text{FWHM} \gg \chi N_{\text{cutoff}}$ ). On the flip side, a broadband pulse causes a spectral overlap with the higher level transitions of the transmon. Constrained by these two conflicting requirements, we choose to use a pulse with  $\sigma = 2\pi \times 40$  MHz (16 ns pulse duration) as a compromise. Furthermore, we implement derivative removal via adiabatic gate (DRAG) [90] corrections on the transmon  $|g\rangle - |e\rangle$  rotation pulses to correct for the undesired effects of the  $|f\rangle$  level. However, our joint parity measurement requires high fidelity manipulations in the  $|e\rangle - |f\rangle$  manifold, often in presence of both  $|g\rangle$  and  $|h\rangle$ . Full correction protocols for such operations have not yet been proposed. The detailed break-down of the known sources of errors are presented in Table 4.1, with roughly 6% coming from the state creation and 13% from the measurement. This is consistent with our measurement of  $|0\rangle_A|0\rangle_B$  using the same joint parity mapping sequence, which yields a peak contrast of roughly 88%.

It is worth noting that there is not a dominant source of error. In order to improve the overall contrast, we must improve our system both in hardware and software. In particular, better precision in the microwave control sequence, and more sophisticated pulses on the ancilla would allow us to perform more robust joint parity measurements in the presence of large photon populations. The continual improvement of the transmon and cavity coherence is also indispensable.

## 4.5 Discussion

In this chapter, we have presented the first experimental realisation of a Schrödinger cat state that lives in two cavities. This two-mode cat is not only a beautiful manifestation of superposition and entanglement between macroscopically distinguishable, quasi-classical states [70], but also a highly valuable resource for new technologies such as quantum metrology [91], quantum networks, and teleportation [92].

The results described here are also powerful demonstrations of our ability to perform

high-fidelity quantum control over large two-cavity Hilbert space. This is a crucial ingredient for continuous-variable quantum computing schemes. The measurement of joint photon number parity of multiple harmonic modes is QND in nature and can be a useful tool in cavity-based quantum error correction schemes. It would also facilitate concurrent remote entanglement generation [93] in the modular architecture.

This experiment is also a verification that our cavity-transmon systems can be scaled to include multiple high-Q modes without sacrificing coherence or controllability. The scope of this work focuses on the creation of complex quantum states and joint tomography of two cavity modes. It paves the way towards performing quantum gates between states encoded in multiple superconducting cavities, which are investigated with the subsequent experiments. Finally, results from this work offer valuable insight for the design and optimisation of the next generation of multi-cavity quantum devices.

## Chapter 5

# A CNOT gate between two multi-photon qubits

In traditional approaches to quantum error correction, bits of quantum information are redundantly encoded in a register of two-level systems [94, 95]. Over the past years, elements of quantum error correction have been implemented in a variety of platforms, ranging from nuclear spins [43], photons [48] and atoms [96], to crystal defects [46] and superconducting devices [41, 49, 40]. However, for performing actual algorithms with an error-protected device, it is necessary not only to create and manipulate separate logical qubits, but also to perform entangling quantum gates between them. To date, a gate between logical qubits has yet been demonstrated, in part due to the large number of operations required for implementing such a gate. For example, in the Steane code [95, 97], which protects against bit and phase flip errors, a standard logical CNOT gate would consist of seven pairwise CNOT gates between two seven-qubit registers [5]. Previous experiments have demonstrated an effective gate between two-qubit registers that are protected against correlated dephasing [98]. In that case, an entangling gate could be implemented using just a single pairwise CNOT gate between the registers.

We choose to pursue a different strategy by encoding qubits in the higher-dimensional Hilbert space of a single harmonic oscillator [99], or more concretely in multi-photon states of a microwave cavity mode [50, 68]. This approach has the advantage of having photon loss as the single dominant error channel, with photon-number parity as the associated error syndrome. Codes whose basis states have definite parity, such as the Schrödinger cat code [63] or the binomial kitten code [51], can then be used to actively protect quantum

information against this error [74, 49]. In the previous chapter, we have presented in first experiment that prepares an entangled state between two modes [100] in a double-cavity cQED architecture. Now, we aim to implement a quantum gate between two multi-photon qubits in the same architecture. In contrast to gates between two-level systems, which can be coupled by a linear element such as a cavity bus [101], harmonic oscillators can non-trivially interact only if they are coupled by a nonlinear ancillary element. However, the requirement for fast interaction between the cavities without inheriting large undesired nonlinearities and decoherence from the ancilla, presents a challenge to the cavity-based approach to quantum error correction.

In the chapter, I will discuss the proof-of-principle experiment to demonstrate an engineered entangling gate between two cavity states in the same double-cavity system discussed previously. In section 5.1, I will provide the details of how we can enable cavity-cavity interactions using driven operations without establishing appreciable coupling between the two modes. Subsequently, we will look into how we can use this type of frequency-converting process to perform an effective conditional gate between multi-photon states stored in the two cavities. Next, I will discuss how we can quantify the gate performance using quantum process tomography and repeated gate applications. Finally, I will provide some concluding remarks on the merits and limitations of this type of inter-cavity operation.

## 5.1 RF controlled sideband transitions

In the discussions so far, we have only been using the transmon as a non-linear element to prepare, manipulate and read out cavity states. Here, we will exploit not just its properties as a two-level artificial atom, but also tap into the intrinsic four-wave mixing capabilities of the Josephson junction. In essence, the entangling operation relies on two distinct types of nonlinearity interactions. The first is the naturally occurring dispersive interaction, which can be understood as a rotation of the cavity phase space conditioned on the ancilla state. Here, we consider the ancilla ground and second excited states  $|g\rangle$  and  $|f\rangle$  only, since the first excited state  $|e\rangle$  is ideally not populated during the gate operation. In this case, the

effective Hamiltonian is

$$\hat{H}_{\text{disp}}/\hbar = -\tilde{\chi}_T \hat{a}_T^\dagger \hat{a}_T |f\rangle\langle f| - \tilde{\chi}_C \hat{a}_C^\dagger \hat{a}_C |f\rangle\langle f|, \quad (5.1)$$

where  $\hat{a}_{C(T)}$  is the control (target) annihilation operator. This is a simplification of Eq. 2.16, where the transmon ancilla is treated as a three-level atom. As a result of this interaction, the target (control) cavity phase space rotates at  $\tilde{\chi}_{T(C)}/2\pi = 1.9$  MHz (3.3 MHz) when the ancilla is in  $|f\rangle$ , but remains unchanged when the ancilla is in  $|g\rangle$ .

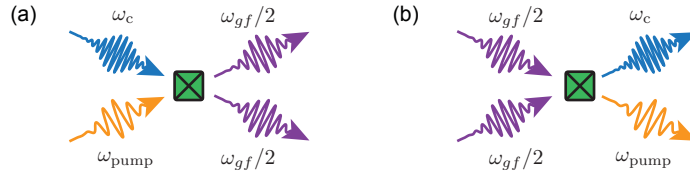


Figure 5.1: **Four-wave mixing process that enables a non-linear coupling between the ancilla and the control cavity.** (a) Process that extracts a photon from the control cavity and doubly excites the ancilla with the absorption of a pump photon. (b) The reverse process that brings the ancilla back to its ground state and transfers a photon back to the control cavity with the emission of a pump photon.

The second type of nonlinearity interaction is a frequency-converting coupling enabled through four-wave-mixing. Following the general framework for a single cavity-transmon system, we can write down the Hamiltonian for this particular system:

$$\hat{H}_J = -E_J \cos \left[ \phi_q (\hat{q} + \hat{q}^\dagger + \xi(t) + \xi^*(t)) + \phi_C (\hat{a}_C + \hat{a}_C^\dagger) + \phi_T (\hat{a}_T + \hat{a}_T^\dagger) \right] \quad (5.2)$$

where  $E_J/\hbar = 21$  GHz is the Josephson energy of the ancilla;  $\hat{q}, \hat{a}_C, \hat{a}_T$  are annihilation operator associated with the transmon ancilla, control, and target cavity mode respectively, and  $\phi_k$  ( $k = q, C, T$ ) are the normalised zero point fluctuation across the junction due to each mode.  $\xi(t) \approx \frac{g(t)}{\Delta}$  corresponds to the displacement of the ancilla mode in the presence of a pump tone with strength  $g(t)$  and detuning  $\Delta$  from its resonance. In the limit that the flux through the junction is small, this Hamiltonian can be approximated by the fourth order expansion of the cosine function. Therefore, different four-wave mixing processes can be

enabled by choosing appropriate pump frequencies, allowing previously non-resonant terms to be accessible. In this particular application, our aim is to engineer an interaction between the control cavity and the ancilla that allows energy exchange. This is commonly referred to as a sideband transition described by:

$$\hat{H}_{\text{SB}} = -\frac{1}{2}E_J\phi_q^3\phi_C\xi(t) \left[ \hat{a}_C\hat{q}^\dagger\hat{q}^\dagger + \hat{a}_C^\dagger\hat{q}\hat{q} \right] \quad (5.3)$$

This transition is enabled with a pump tone that satisfies the frequency matching condition  $\omega_p = \omega_{gf} - \omega_C - (n_C - 1)\tilde{\chi}_C$ , with  $\omega_{gf}/2\pi = 9.46$  GHz the ancilla  $|g\rangle - |f\rangle$  transition,  $n_C$  the number of control photons, and  $\tilde{\chi}_C$  the effective dispersive coupling between the ancilla and the control cavity. The process can in general be made insensitive to  $n_C$  if the coupling rate is much faster  $(n_C - 1)\tilde{\chi}_C$ . Through this interaction, we achieve an exchange of a single photon from the control cavity and two excitations from the ancilla in presence of a single pump photon. A cartoon depicting the two reciprocal mixing processes is shown in Fig 5.1. Here, the RF drive initiates a process that extracts a photon from the control cavity and populates the  $|f\rangle$  level of the ancilla while simultaneously enables the reverse operation. Therefore, when the  $|f\rangle$  state is occupied, the photon can be transferred back to the control cavity (with a deterministic phase change) accompanied by the emission of a pump photon.

It is important to note that this process relies on the junction being a good four-wave mixer. In other words, we must ensure  $|\xi|\phi_q \ll 1$  so that the cosine expansion remains valid. The pump strength can be calibrated independently through Stark shift measurements on the ancilla  $|g\rangle \rightarrow |e\rangle$  transition, which scales as  $-E_J\phi^4|\xi|^2$ . The zero point fluctuations associated with each mode can be inferred from other system parameters like the anharmonicity and Kerr. For the particular configuration used in this experiment, we use a pump strength of  $\xi \sim 0.5$ , which predicts a single photon oscillation rate of  $\Omega_C \sim 2\pi \times 8\text{MHz}$ . By exploiting two excitations from the transmon, this Hamiltonian allows a relatively fast nonlinear interaction. This is because the ancilla mode, being the most non-linear one, has the largest contribution to the junction's zero point flux fluctuation ( $\phi_q \approx 0.32 \gg \phi_C, \xi$ ).

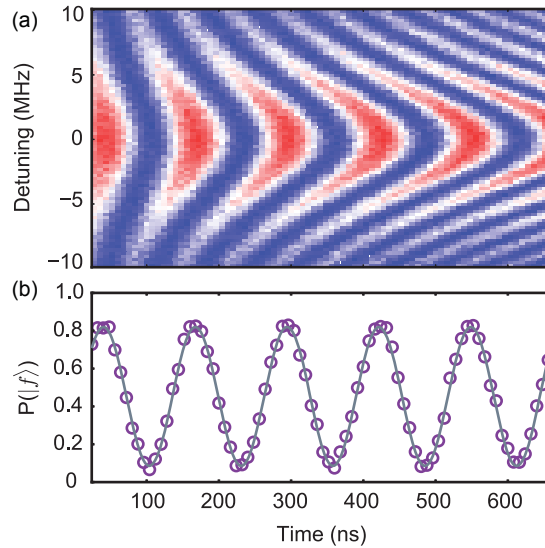


Figure 5.2: **Drive sideband transition.** (a) Measurement of the pumped sideband transition as a function of pump frequency and duration. The z-axis is an indication of the ancilla population. The resonant pump frequency deviates from the calculated frequency matching condition due to small amounts of AC Stark shifts on each mode in presence of the pump tone. The ancilla is initialised in its  $|f\rangle$  state. (b) 1D cut along the time axis to show the periodic oscillations of the ancilla population from  $|g\rangle$  to  $|f\rangle$ . The fitted frequency,  $f = 7.85\text{MHz}$  corresponds to the effective coupling strength of the pumped interaction.

The resultant interaction, described by the effective Hamiltonian

$$\hat{H}_{\text{sb}}/\hbar = \frac{\Omega_C(t)}{2} \left( \hat{a}_C |f\rangle\langle g| + \hat{a}_C^\dagger |g\rangle\langle f| \right), \quad (5.4)$$

leads to sideband oscillations[102] between the states  $|n_C, g\rangle$  and  $|n_C - 1, f\rangle$  [103, 104, 105]. The rate of this oscillation is measured directly by monitoring the population of the ancilla  $|f\rangle$  population in presence of the pump and a single control cavity photon. In Fig. 5.2, we vary both the frequency of the pump near the predicted value according to the frequency matching condition, and the duration of the tone with system initialised in  $|1\rangle_C|0\rangle_T|g\rangle$ . The data reveal that the actual resonance condition differs slightly from the theoretical prediction. This is attributed to the Stark shifts incurred on each mode in presence of the strong pump. Moreover, in the time domain we observe the periodic  $|g\rangle - |f\rangle$  oscillations as expected from Eq. 5.4. We quantify the rate the oscillation by fitting the 1D cut along the time axis to a decaying sinusoid and this yields  $\Omega = 2\pi \times 7.85\text{ MHz}$ , consistent with the

theoretical prediction.

This type of driven sideband transition is in principle compatible with different photon numbers in both the control and target cavities. It is useful to keep in mind that this interaction speed can be enhanced by a factor  $\sqrt{n_C}$ , where  $n_C$  is the population of the control cavity. When multiple photons are present in the target cavity, the sideband transition is in competition with the always-on dispersive coupling between the cavity and the ancilla.

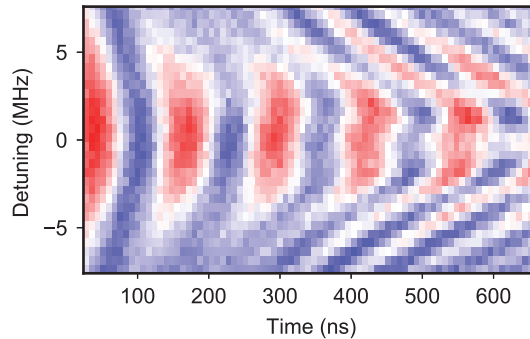


Figure 5.3: **Drive sideband transition with multiple photons in the target cavity** Measurement of the pumped sideband transition as a function of pump frequency and duration. Due to the dispersive shift between the target cavity and the ancilla, the resonance frequency is now shifted by an amount  $\propto n\chi_{gf}^T$  for each photon number state present.

We illustrate the effect of having multiple excitations in the target cavity in Fig. 5.3. Here, we measure same  $|g\rangle - |f\rangle$  oscillations as a function of pump duration and frequency, with the target cavity initialised in a kitten state  $\mathcal{N}(|0\rangle + |2\rangle + |4\rangle)$ . As a result of the different photon number states present in the target cavity, the  $|g\rangle - |f\rangle$  transition frequency is shifted by different amount of  $\propto n\chi_{gf}^T$ . Consequently, the resonance condition for the sideband drive is now split as shown by the distorted chevron peaks in Fig. 5.3. In this case, the sideband transition rate is comparable to the spread in the resonance frequencies and therefore, we can still implement operation by centering the pump frequency in the middle of the three resonance conditions. This does, however, introduce some additional imperfections and causes the oscillations to have slightly reduced contrast. In order to make the operation truly independently of the target state, we can either increase the pump strength such that the engineered sideband transition is much faster than the spread of frequencies due to  $\chi$ ,

or design a protocol to turn off the dispersive coupling during the sideband transition. Both would require certain modifications of the existing hardware and were not explored in this experiment. However, they are being actively investigated by other members of the lab as we continue to improve our ability to engineer fast and coherent non-linear operations between high-Q modes.

## 5.2 Implementation of CNOT gate

Let us look at how the driven sideband transition is utilised to perform an effective conditional operation between the two cavity modes. The basic mechanism behind the gate is to make the cavities interact sequentially with the ancilla, enabling an effective nonlinear interaction between the cavities without requiring a significant direct cavity-cavity coupling. This method is similar to the one used in a recent experiment on a gate between single optical photons [106].

We start by preparing the desired initial state using optimal control pulses on the ancilla and on the cavity [107, 36] simultaneously. The gate sequence is then performed in three steps. First, we apply the sideband pump tone for a time  $\pi/(\sqrt{2}\Omega_C)$ , exciting the ancilla from  $|g\rangle$  to  $|f\rangle$  conditioned on the control being in  $|1_L\rangle_C$  with  $\Omega_C$  being the pumped transition rate. We then turn off the pump for a time  $\delta t$ , which corresponds  $\pi/\tilde{\chi}$ , where  $\tilde{\chi}$  is the effective dispersive coupling between the ancilla and the target cavity in presence of the pump. During this wait time, the ancilla dispersively interacts with the target cavity, rotating its phase space by a  $\pi$ -phase. This essentially implements a logical  $\pi$ -pulse that flips  $|0_L\rangle_T$  into  $|1_L\rangle_T$  and vice versa, conditioned on the ancilla being in  $|f\rangle$ . We then apply the sideband pump pulse a second time to disentangle the ancilla from the cavities, thereby effectively achieving a CNOT gate between the two cavities. Finally, we use the ancilla to perform joint Wigner tomography on the two-cavity state [100, 33], from which we reconstruct the density matrix.

To demonstrate the action of the gate, we first use the simplest possible encoding compatible with the protocol, i.e using  $\{|0\rangle, |1\rangle\}$  encoding for both the control and target cavity. In this basis, the gate is accomplished by first applying the pump tone for 128 ns, which

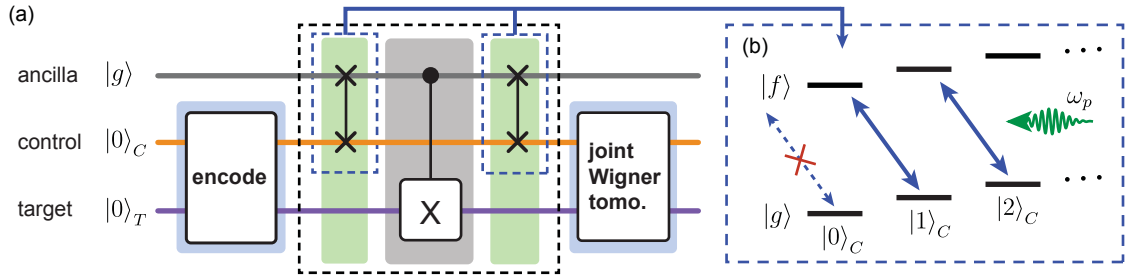


Figure 5.4: **Protocol to implement CNOT using sideband drives.** (a) The full experimental pulse sequence to perform the operation. It starts with the preparation of the desired initial states using OCT pulses. It is important to ensure that the ancilla is left in its ground state at the end of the state preparation pulse. The gate (black dashed box) itself consists of two entangling operations between the ancilla and the Control (blue dashed boxes), interleaved by a CNOT gate between the ancilla and target. The final state after the gate is characterised via joint Wigner measurements [100]. (b) The schematic level diagram illustrating the RF driven sideband transition between the ancilla and Control that realises an entangling process between them. A single photon from the control cavity, together with one from the RF pump, doubly excites the ancilla from its ground to  $|f\rangle$  level (solid blue lines). However, when no photons are present in the system, the ancilla transition becomes forbidden and the pump has no impact on the system.

fully converts a control photon and drive photon to double excitations of the ancilla. If the ancilla is excited to  $|f\rangle$ , the dispersive interaction between the target and the ancilla imparts a  $\pi$ -phase to the target cavity state in  $\sim 212$  ns. This is then followed by another 128 ns pump pulse to restore the control cavity state and disentangle the ancilla from the cavity modes. In total, the gate time is 468 ns, corresponding to  $\leq 4\%$  of the coherence time of the ancilla. While this encoding cannot be used for either error detection or error correction, it fully capitalises on the good coherence times of the cavities and provides an intuitive illustration of the operation.

The hallmark of a CNOT gate is its ability to entangle two initially separable systems. As a demonstration of this capability, we apply the gate to  $|\psi_{\text{in}}\rangle = (|0\rangle_C + |1\rangle_C) \otimes |0\rangle_T$ . Ideally, this should result in a logical Bell state  $|\psi_{\text{ideal}}\rangle = |0\rangle_C|0\rangle_T + |1\rangle_C|1\rangle_T$ . Using the raw measured Wigner function, we reconstruct the output density matrix  $\rho_{\text{meas}}$ . The real part of the density matrix is shown in Fig. 5.5. It shows excellent qualitative agreement with the ideal output state. The imaginary components are omitted here since they are very close to zero as expected and hence contain no significant information. From these results, we deduce

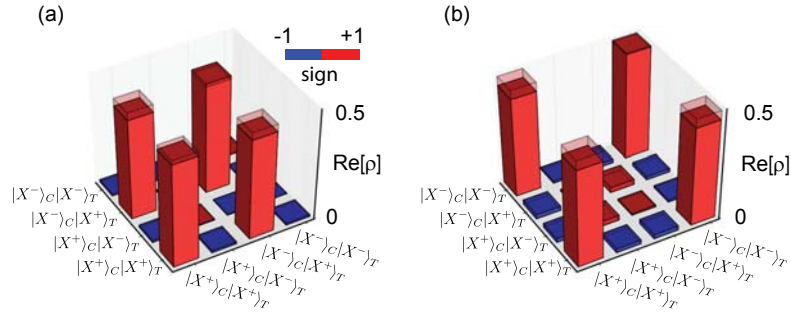


Figure 5.5: **Generation of an entangled Bell pair in the single-photon encoding.** Real parts of the reconstructed density matrix (solid bars) of (a), the initial separable state  $(|0\rangle_C + |1\rangle_C) \otimes (|0\rangle_T + |1\rangle_T)$ , and (b), the final state after the CNOT operation which is an entangled state  $|0\rangle_C(|0\rangle_T + |0\rangle_T) + |1\rangle_C(|0\rangle_T + |0\rangle_T)$ . The results are shown the basis  $|X^\pm\rangle$  for clarity. The ideal states are shown in transparent bars. The imaginary components are omitted as they are indistinguishable from noise and contain no meaningful information about the state

a state fidelity in the single photon encoding of  $F_{\text{Bell}} \equiv \langle \psi_{\text{ideal}} | \rho_{\text{meas}} | \psi_{\text{ideal}} \rangle = (95 \pm 2)\%$ . This is within the measurement uncertainty of the input state fidelity  $F_{\text{in}} = (97 \pm 2)\%$ . Based on these observations, we infer that the operation itself is fairly close to ideal, with its imperfections causing a slight reduction in the Bell state fidelity. However, the details of these nonidealities are obscured by imperfections in state preparation and joint Wigner measurement.

Another important figure of merit for an entangling gate is the ability to turn off the interaction, to prevent unwanted entanglement between the cavities. In practice, the cross-Kerr interaction between the cavities, described by the Hamiltonian  $\hat{H}_{CT}/\hbar = \chi_{CT} \hat{a}_C^\dagger \hat{a}_C \hat{a}_T^\dagger a_T$ , induces entanglement even when the gate operation is not applied. We use the Bell state in the single-photon encoding to demonstrate the on-off ratio of this entangling operation. This is essentially a competition between the engineered gate and the natural cross-talk between Alice and Bob. When starting with a Bell state, the cross-Kerr interaction first disentangles, and then re-entangles the two cavities. To examine this effect, we parametrise the amount of entanglement present in the system by its concurrence [108] and monitor it over a variable delay time. We show in Fig. 5.6, the decay of concurrence for an entangled state (blue) created by the engineered CNOT operation and a separable state (red). As expected, the cavity dephasing times of  $\sim 500 \mu\text{s}$  leads to a gradual overall loss of entanglement in

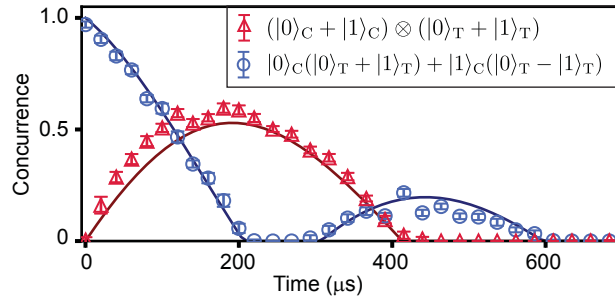


Figure 5.6: **Undesired entanglement induced by the coupling ancilla.** Concurrence vs. wait time for an initially separable state (red) using single-photon encoding, and for an initial Bell state (blue) obtained by applying the gate to the separable state. The presence of the cross-Kerr interaction between the two cavities is responsible for the observed oscillatory behavior, whereas dephasing due to thermal excitations in the ancilla results in a gradual decay of the entanglement. By fitting simulations (solid black curves) to the measured data, we determine a cross-Kerr interaction rate of  $\chi_{CT}/2\pi=2$  kHz.

both cases. From the measured curves, we infer a cross-Kerr interaction rate of  $\chi_{CT}/2\pi=2$  kHz. However, the residual entanglement rate for the multi-photon encoding is increased to  $\Omega_{\text{res}} = n_C \bar{n}_T \chi_{CT} = 2\pi \times 8$  kHz, where  $\bar{n}_T = 2$  is the average number of photons in the target cavity. We can therefore infer the on/off ratio of the entangling rate, defined by the ratio of the times to generate maximal entanglement without and with gate application, to be  $\pi/(\Omega_{\text{res}} t_g) \sim 300$ .

A crucial advantage of this implementation of CNOT is that it is by design compatible with more complex bosonic states. To highlight its potential, we extend the operation to two multi-photon states that are compatible with error detection and error correction. In this experiment, we choose a basis of even-parity Fock states

$$|0_L\rangle_C = |0\rangle_C, \quad |1_L\rangle_C = |2\rangle_C \quad (5.5)$$

for the control cavity, and Schrödinger kitten states [51]

$$|0_L/1_L\rangle_T = \frac{1}{\sqrt{2}} \left( \frac{|0\rangle_T + |4\rangle_T}{\sqrt{2}} \pm |2\rangle_T \right) \quad (5.6)$$

for the target cavity (henceforth omitting normalization). These encodings allows error detection of a photon loss event in both cavities, as well as error correction in the target

cavity as discussed in Ref. [51].

To implement the entangling gate between the two modes in this encoding, we simply use the same CNOT protocol introduced earlier for the single Fock state encoding with minor adaptations. The two types of nonlinear interactions necessary for the implementation, namely, the pumped ancilla-control coupling and the ancilla-target dispersive coupling, can both be photon-number independent. It is straightforward to see that the dispersive Hamiltonian allows conditional rotation of the target cavity's phase space regardless of its encoding. For these particular code words (Eq. 5.6), a flip between  $|0_L\rangle$  and  $|1_L\rangle$  is simply a rotation of the phase-space by  $\pi$ .

The sideband transition, as we have mentioned in the previous section, can also be made photon-number insensitive if the coupling is strong, or spectrally broad, to remain unselective to all the dispersively shifted photon number peaks. In this case, the pump transition occurs at  $\Omega_C/2\pi = 7.85$  MHz when the control cavity contains a single photon. In this encoding, the control is prepared in the Fock state  $|2\rangle$ . This provides bosonic enhancement to the pumped sideband transition, allowing a stronger ancilla-control coupling with  $\Omega'_C/2\pi = \sqrt{2} \times 7.85 = 11.2$  MHz, which is large compare to the spread in the transmon frequencies. Therefore, we can indeed drive the sideband transition in this multi-photon encoding.

Now, we modify the gate protocol to work with this new multi-photon encoding. First, in light of the bosonic enhancement in the sideband transition, we apply for the pump tones for a shorter period of 64 ns. If the control is in  $|0_L\rangle_C = |2\rangle$ , a photon will be extracted together with a pump photon, doubly exciting the ancilla to  $|f\rangle$ . The ancilla now dispersively interacts with the target cavity, bringing it from  $|0_L\rangle_T$  to  $|1_L\rangle_T$  or vice versa by imparting a  $\pi/2$  phase. This process takes roughly 100 ns. Subsequently, we apply the pump tones again for 45 ns to disentangle the ancilla. This completes the operation with a total gate time of  $t_g \sim 190$  ns. The shorter gate time is favourable since its performance is ultimately limited by the ratio of  $t_g$  to the coherence time of the ancilla. We will have a more in-depth discussion of this point in the later section.

In order to demonstrate the action of the gate between multi-photon states, we first use it on a simple example,  $|\psi\rangle = |1_L\rangle_C \otimes |0_L\rangle_T$ , where both the initial and final states are

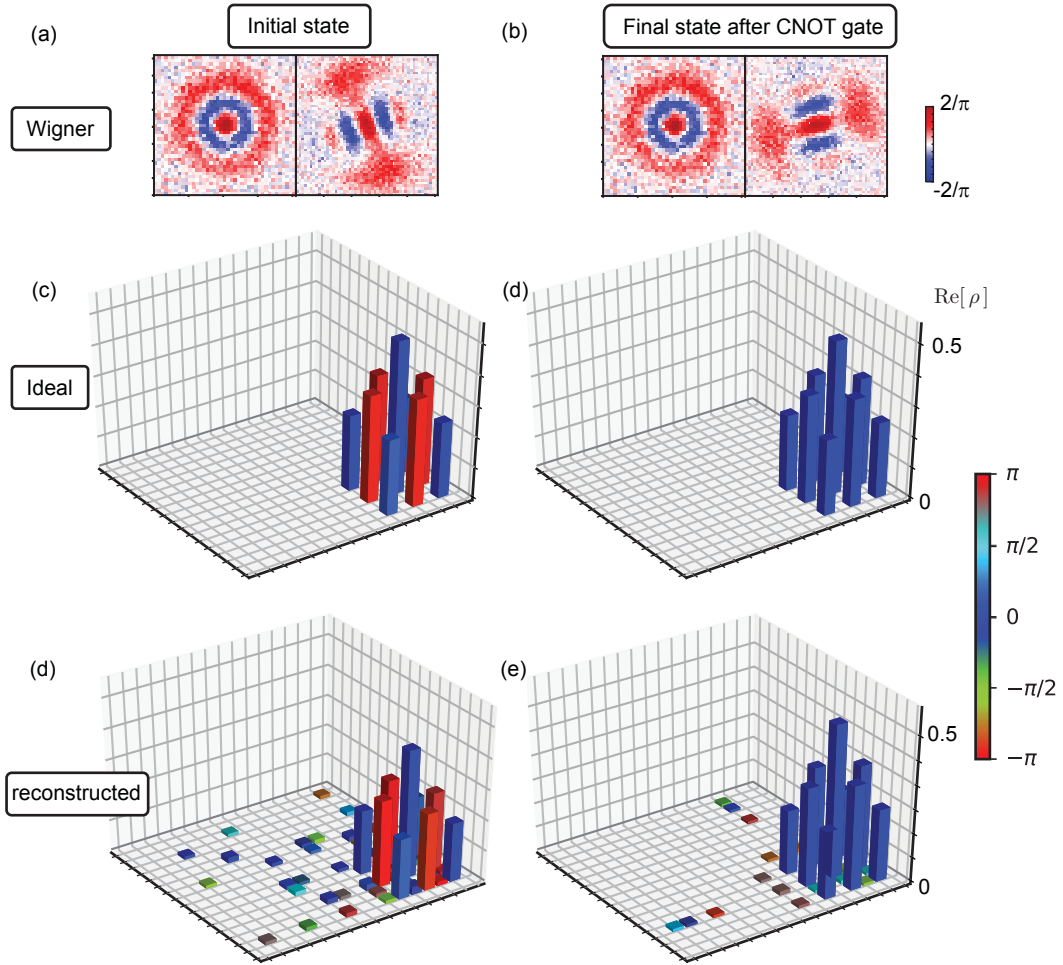


Figure 5.7: **Example of reconstructed density matrices in Binomial encoding** The CNOT gate is applied to the initial state  $|1_L\rangle_C \otimes |0_L\rangle_T$ . (a) The initial and final Wigners of the control and target cavity. (c), (d) The ideal density matrices of the initial and final joint-cavity states. (e), (f) The density matrices reconstructed from joint Wigner tomography.

separable. This allows us to directly characterise the initial and final states using single cavity Wigner measurements as shown in Fig. 5.7(a) and (b). The data indicate that after the operation, the control cavity remains in  $|1_L\rangle_C$  while the target state has been rotated by  $\pi$ , which indicates a flip between  $|0_L\rangle_T$  to  $|1_L\rangle_T$ . We also perform joint Wigner tomography and reconstruct the full density matrices of the state using the same method described in section 4.4. Our result, presented in Fig. 5.7(e) and (f), show that the reconstructed density matrix are in a good agreement with the ideal states. Further, we can also carry out the same experiment as in the single photon case to demonstrate the ability of the gate to

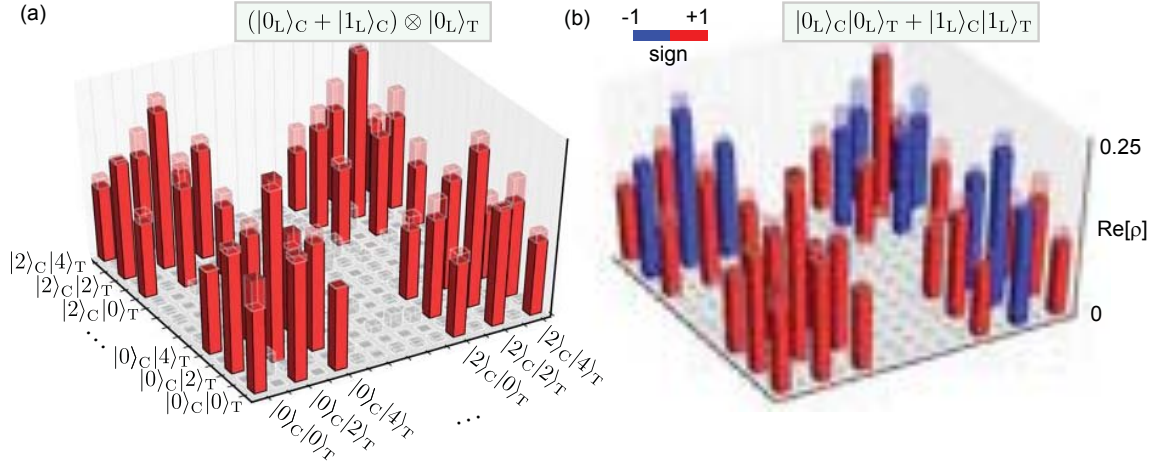


Figure 5.8: **Entangled state generation in the Binomial encoding.** (a) The reconstructed density matrix for the separable state  $(|0\rangle_C + |2\rangle_C) \otimes \left(\frac{|0\rangle_T + |4\rangle_T}{\sqrt{2}} + |2\rangle_T\right)$ . (b) The reconstructed density matrix of the state after the CNOT. We use a truncated Hilbert space for the reconstruction, with maximum 3 and 5 photons in the control and target respectively. The absence of higher excitations are confirmed via other control experiments. The imaginary parts are omitted since they are indistinguishable from noise. The density matrix corresponding to the ideal initial and final states are shown in transparent bars

entangle two multi-photon states. The final entangled state, shown in Fig 5.8, exhibits good agreement with the ideal Bell state. The state fidelity are calculated in the same manner as for the single photon encoding and yields a fidelity of  $(90 \pm 2)\%$ . Although this seems lower than the single photon case, we can deduce that the imperfections are mainly due to the more complex state preparation pulses and the joint Wigner tomography. This can be verified by the  $(92 \pm 2)\%$  state fidelity extracted from the input state. We will discuss in a bit more detail about the sources of imperfections in the operation.

### 5.3 Analysis of gate fidelity

To fully characterize the CNOT gate, we next perform quantum process tomography[58] (QPT). We achieve this by applying the gate to sixteen logical input states that together span the entire code space. By performing quantum state tomography on the resulting output states we can reconstruct the quantum process  $\epsilon(\rho_{\text{in}})$ , which captures the action of the gate on an arbitrary input state  $\rho_{\text{in}}$ .

The results are expanded in a basis of two-qubit generalized Pauli operators  $E_i$  on the code space as  $\epsilon(\rho_{\text{in}}) = \sum_{m,n=0}^{15} \chi_{m,n} E_m \rho_{\text{in}} E_n$ , where  $\chi$  is the process matrix. Using the measured  $\chi$  (Fig 5.9), we determine a process fidelity of  $F_{\text{CNOT}} \equiv \text{Tr} \{ \chi_{\text{ideal}} \chi \} = (89 \pm 2) \%$  for the binomial encoding. We estimate the effect of non-ideal state preparation and measurement by performing QPT on the process consisting of encoding and measurement only, yielding a fidelity with the identity operator of  $F_{\text{identity}} = (92 \pm 2) \%$ . The same procedure is carried out for the Fock encoding as well. The results indicate a very similar process fidelity. For the following discussion, we will focus on the Binomial encoding since it is more relevant for the future application of this operation on fully error-correctable logical states.

To more accurately determine the performance of the gate and highlight specific error mechanisms, we apply it repeatedly to various input states (Fig. 4b). We then measure how the state fidelity decreases with the number of gate applications. A first observation is that no appreciable degradation in state fidelity occurs when the control qubit is in  $|0_L\rangle_C$ . Indeed, the control cavity contains no photon in this case, and as a result the ancilla remains in its ground state at all times. When the initial two-cavity state is  $|1_L\rangle_C |X_L^-\rangle_T$  (introducing  $|X_L^\pm\rangle \equiv (|0_L\rangle \pm |1_L\rangle)$  and  $|Y_L^\pm\rangle \equiv (|0_L\rangle \pm i|1_L\rangle)$ ), corresponding to  $|2\rangle_C |2\rangle_T$  in the Fock-state basis, the ancilla does get excited to the  $|f\rangle$ -state, and we measure a small decay in fidelity of  $(0.6 \pm 0.3)\%$  per gate application. This is consistent with the ancilla decay time from  $|f\rangle$  to  $|e\rangle$ , measured to be  $40 \mu\text{s}$ . While the qubit is irreversibly lost when a decay occurs, the final ancilla state is outside the code space, and therefore this is a detectable error. If the control qubit is initially in a superposition state, the first sideband pump pulse will entangle the control cavity with the ancilla, making the state prone to both ancilla decay and dephasing ( $T_2^f = 17 \mu\text{s}$ ). For example, for  $|X_L^+\rangle_C |X_L^-\rangle_T$ , we measure a decay in fidelity of  $(0.9 \pm 0.2)\%$  per gate. When the target cavity state is not rotationally invariant (i.e. not a Fock state), we observe larger decay rates ( $(2.0 \pm 0.3)\%$  for  $|1_L\rangle_C |0_L/1_L\rangle_T$ , and  $(2.1 \pm 0.2)\%$  for  $|Y_L^+\rangle_C |Y_L^+\rangle_T$ ). While an accurate determination of the gate fidelity would require randomised benchmarking [109], the data presented in Fig. 5.9(b) are sufficient to indicate an average degradation in state fidelity of approximately 1% per gate application, close to the  $\sim 0.5\%$  limit set by ancilla decoherence.

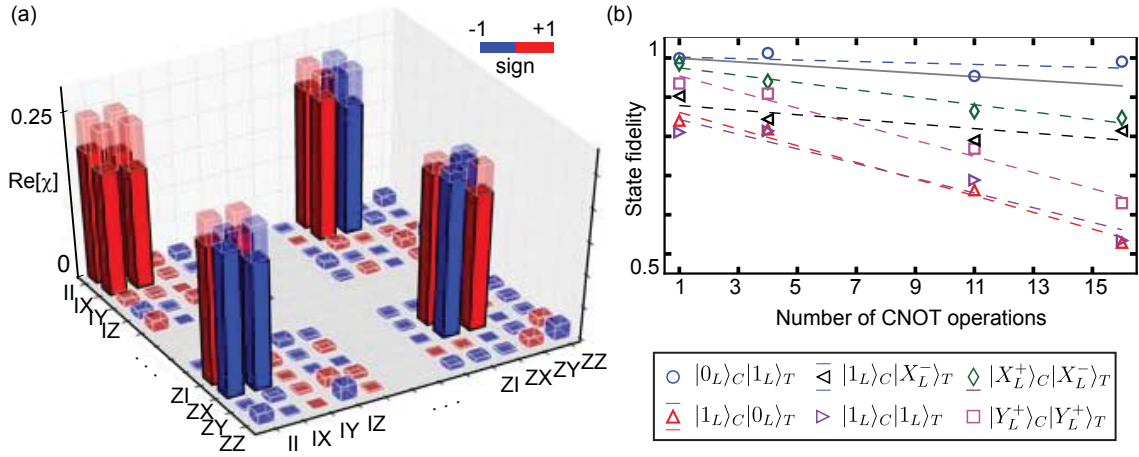


Figure 5.9: **Characterization of the CNOT gate.** **a**, Quantum process tomography. The solid (transparent) bars represent the measured (ideal) elements of the process matrix  $\chi$ . The corresponding process fidelity is  $F_{\text{CNOT}} = (89 \pm 2) \%$ . For clarity, only the corners of the process matrix are presented. State fidelity under repeated gate applications for various input states, chosen to highlight different error mechanisms of the gate (the dashed lines are linear fits). The solid gray line depicts the simulated average slope of state fidelity imposed by ancilla decoherence.

## 5.4 Discussion

In this chapter, we reviewed the experimental demonstration of a CNOT gate between two multi-photon qubits encoded in two high-Q ( $T_1 \sim 0.002$  s) superconducting cavities. This implementation uses a single ancilla transmon, driven by off-resonant RF pump pulses, to provide the strong nonlinear interaction for the operation. We have shown the ability to generate high-fidelity multi-photon Bell state in two different bosonic encodings using the gate. Further, we also perform quantum process tomography of the operation, and use repeated gate application to quantify imperfections in the operation. Our results show that the decoherence of the ancilla limits the number of coherent CNOT operations to  $\sim 10^2$ , bringing this gate within the regime required for practical quantum operations [110, 111]. In addition, we also measure the undesired entangling rate between the cavities during idle times, and infer a high on/off ratio of the entangling rate [112, 113] of  $\sim 300$ . This figure of merit is important since undesired cross-talk is often a major hurdle when trying to scale up to a larger number of qubits.

However, there are a few downsides associated with this particular technique to imple-

ment the entangling gate. First, by directly using the ancilla excited states, the system experiences an excursion out of the code space during the protocol. As a result, neither the parity nor the joint parity of the system is preserved. This makes it incompatible with existing error-tracking and error correction protocols that use parity (or joint parity) as the dominant error syndrome. Further, since the cavity states are fully entangled with the ancilla  $|f\rangle$  level during the gate, the encoded quantum bit is exposed to both energy relaxation and dephasing errors of the ancilla. While a relaxation event can be detected, dephasing of the ancilla causes an uncorrectable error to the encoded state. Lastly, this technique is only compatible with a certain type of encoding. For example, a more generalised form of the Binomial code with basis states  $|0_L\rangle = \frac{1}{\sqrt{2}}(\frac{\sqrt{3}|0\rangle+|8\rangle}{2} + |2\rangle)$  and  $|1_L\rangle = \frac{1}{\sqrt{2}}(\frac{\sqrt{3}|0\rangle+|8\rangle}{2} - |2\rangle)$  can be used for both the control and target encoding. This provides error-correction capabilities but the presence of higher photon numbers subjects the system to more non-idealities due to higher order Hamiltonian terms. More crucially, the sideband transition must be efficiently fast to address all photon number states in the control cavity. This requires stronger pumps which can in turn result in adverse effects due to more significant heating and the probability of driving other unwanted transitions.

Going forward, it is desirable to design protocols that directly couple the two cavity states and preserve the code space during the operation. Ideally, it gate should be performed without physically populating any excited levels of the ancilla, or in other words, ancilla-cavity entanglement should be avoided or minimised during the operation. With this in mind, let us now move on to the next chapter in which I will explore a different implementation of an entangling gate between cavities that has the potential to meet these requirements.

## Chapter 6

# Programmable interference between two microwave quantum memories

We have established that superconducting cavities, with their excellent coherence properties and large available Hilbert space, are a great resource for redundantly encoding quantum information. The information is stored in the form of multi-photon states with a certain symmetric property that can be exploited as the error syndrome. The success of a quantum computing scheme that builds on a network of such logical qubits encoded in superconducting cavities relies on the ability to switch on and off robust, tunable couplings between them. Furthermore, such a coupling will also provide us the capability to study complex bosonic interactions between multi-photon states stored in the cavities. In particular, it would be interesting to engineer inter-cavity couplings that could implement quantum interference experiments between these stationary photons.

Interference experiments are one of the simplest probes into many of the riveting facets of quantum mechanics, from wave-particle duality to non-classical correlations. The seminal work by Hong, Ou, and Mandel (HOM) is an elegant manifestation of two-particle quantum interference arising from bosonic quantum statistics [114]. In their experiment, two photons incident on a 50:50 beamsplitter always exit in pairs from the same, albeit random, output port. Central to such interference experiments is the unitary operation  $\hat{U}_{\text{BS}} = \exp[i\frac{\pi}{4}(\hat{a}\hat{b}^\dagger + \hat{a}^\dagger\hat{b})]$ . For propagating particles, this is simply realized with a 50:50 beamsplitter, but more generally, it can be implemented by engineering a time-dependent

coupling of the form  $\hat{H}_{\text{int}}(t)/\hbar = g(t)\hat{a}\hat{b}^\dagger + g^*(t)\hat{a}^\dagger\hat{b}$ . Recent experiments have demonstrated this type of coupling in different physical systems, enabling interference of both bosonic and fermionic particles [115, 116, 117, 118]. These results have shed light on the concept of entanglement [119, 120] and enabled fundamental tests of quantum mechanics like the violation of Bell's inequalities [121]. They also have profound technological implications, with new applications in areas such as quantum metrology [122], simulation [123], and information processing [124, 125].

Our cQED systems have been proposed as a promising platform to study bosonic interference and implementation of scalable boson sampling [126]. So far, interference between harmonic oscillator modes has been demonstrated in cQED using flux tunable elements [127, 128, 129]. However, such systems tend to suffer from the unfavorable coherence properties, limiting the complexity of the experiment to single photons. We can overcome this by using the 3D multi-cavity architecture introduced in Chapter 3, where complex bosonic states can be stored coherently in superconducting cavities. In this chapter, we will focus on a series of quantum interference experiments performed on such a device.

In section 6.1, I will introduce the frequency-converting, bilinear coupling that effectively implements a beamsplitter (BS) operation between two cavity modes. Subsequently, we will examine sources of imperfections present in such an operation in section 6.2. We will also study the effects of the microwave drives on the system and discuss the key considerations in determining the optimal configurations. From there, we will highlight three sets of interference experiments using this engineered BS in section 6.3. These results serve to demonstrate how the cQED implementation can be applied to boson sampling and linear optical quantum computing (LOQC). Finally, in section 6.4, we will consider the several alternative drive configurations we have tested during this experiment and discuss the potential limitations of this type of driven interactions.

## 6.1 Bilinear coupling between two cavity modes

In the previous chapter, we have discussed that a non-linear cavity-cavity coupling can be achieved by allowing them to sequentially interacting with the transmon ancilla. Although this method enables fast interactions, it necessarily populates the higher excited levels of the ancilla. Here, we aim to explore an alternative method to engineer a coupling between Alice and Bob while allowing the ancilla to remain in its ground state.

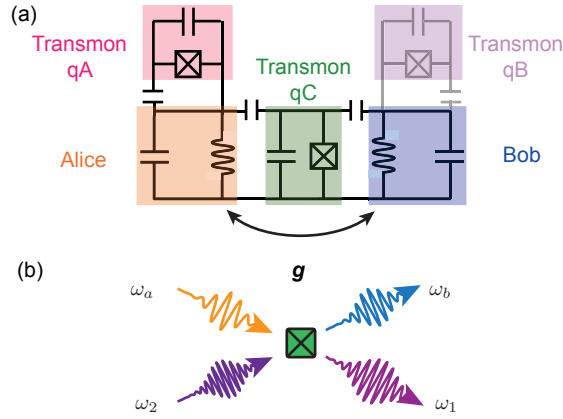


Figure 6.1: **RF driven direct coupling between two cavities.** Effective circuit of the cQED system consisting of two 3D stub cavities (Alice and Bob), three transmon ancillae, and their respective readout resonators. The centre Ymon (green) allows nonlinear coupling between Alice and Bob without incurring a large direct, always-on coupling. The driven bilinear coupling mediated by the transmon is analogous to the tunnel coupling between particles trapped in two separate potential wells. The two transmons on the side are optional but are introduced here to provide more flexible single-cavity control and tomography capabilities.

This is accomplished by driving the Josephson junction at frequencies that allow direct conversion between Alice and Bob without spectrally overlapping with any ancilla transitions. In particular, we introduce a robust and tunable coupling of the form  $\hat{H}_{\text{int}}$  using the four-wave mixing capability of qC. Physically, this allows direct energy transfer between Alice and Bob in spite of their frequency difference. Hence, we have the capability to design the two cavities with a large detuning  $\gtrsim 1$  GHz to suppress undesired cross-talk while still be able to turn on a bilinear coupling. This type of coupling has been shown between a memory and a propagating mode [130] to enable the on-demand generation of complex itinerant

quantum states. Here, we engineer such a coupling between two long-lived memory modes, Alice and Bob. This coupling allows us to perform a variety of different operations between bosonic states stored in Alice and Bob. In particular, we will realise the unitary operation  $U(\theta) = \exp[-\frac{i}{\hbar} \int_0^T H_{\text{int}}(t) dt]$  while only virtually populating the excited levels of qC.

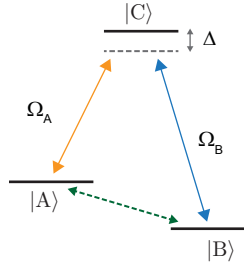


Figure 6.2: **A three-level lambda system.** A schematic showing a simple Lambda system where a coupling between  $|A\rangle$  and  $|B\rangle$  can be achieved by driving two separate transitions to a third level  $|C\rangle$  from  $|A\rangle$  and  $|B\rangle$  respectively. When they are driven off-resonantly, the population in  $|C\rangle$  can be suppressed by  $\sim (\Omega/\Delta)^2$ .

This type of driven transitions that do not physically populate the higher levels of the transmon provides a variety of advantages. Most importantly, it eliminates errors due to transmon decoherence, which tends to be far less favourable than that of 3D superconducting cavities. We can gain some insight into such a process by considering a simple three level  $\Lambda$ -system depicted in Fig. 6.2. The effective coupling between  $|A\rangle$  and  $|B\rangle$  can be established via the transitions between  $|A\rangle - |C\rangle$  and  $|B\rangle - |A\rangle$ , which are driven off resonantly with a detuning  $\Delta$ . In such a configuration, the effective coupling scales as  $\sim \sqrt{\Omega_A \Omega_B}$  with an occupation of state  $|C\rangle$  is given by  $(\Omega/\Delta)^2$ . In the regime where  $\Omega/\Delta \ll 1$ , we can say that the process only virtually involves  $|C\rangle$ , and therefore, inherits negligible properties from this state. The case of the driven bilinear coupling involves more than three levels and is conceptually more complex than this simple picture portrayed here. Theoretical works are underway to model this process in a similar framework [131].

Another way to approach the problem is to consider the cosine treatment of the Hamiltonian. Similar to the methods used in [132], the full Hamiltonian describing the system

consisting of Alice, Bob, qC, and two RF drive tones on qC is written as

$$\begin{aligned} \hat{H}/\hbar = & \tilde{\omega}_a \hat{a}^\dagger \hat{a} + \tilde{\omega}_b \hat{b}^\dagger \hat{b} + \tilde{\omega}_c \hat{c}^\dagger \hat{c} - \frac{E_J}{\hbar} (\cos \hat{\varphi} + \hat{\varphi}^2) \\ & + 2\text{Re}[\epsilon_1 e^{-i\omega_1 t} + \epsilon_2 e^{-i\omega_2 t}] (\hat{c}^\dagger + \hat{c}) \end{aligned} \quad (6.1)$$

where  $\tilde{\omega}_k$  is the bare frequency of each mode and  $\hat{\varphi}$  is the flux across the junction, which can be decomposed into a linear combination of the phase across each mode:

$$\hat{\varphi} = \sum_{k=a,b,c} \phi_k (\hat{k}^\dagger + \hat{k}) \quad (6.2)$$

This Hamiltonian captures the behavior of the system when irradiated by two drives with complex amplitude  $\epsilon_1$  and  $\epsilon_2$ , and frequencies  $\omega_1, \omega_2$ , respectively. In our particular configuration, the drive tones are predominantly coupled to qC.

We eliminate the fastest time scales corresponding to the resonance frequencies of each mode using the following unitary transformation

$$\hat{U} = e^{-i\omega_{ge} t \hat{c}^\dagger \hat{c}} e^{-i\omega_a t \hat{a}^\dagger \hat{a}} e^{-i\omega_b t \hat{b}^\dagger \hat{b}} \quad (6.3)$$

Then we make a displacement transformation for qC such that  $\hat{c} \rightarrow \hat{c} + \xi_1 e^{-i\omega_1 t} + \xi_2 e^{-i\omega_2 t}$ . In this new frame, we express the amplitudes of the drives,  $\xi_{1(2)}$ , as a function of the amplitudes of the drive tones and their respective detunings from the  $|g\rangle - |e\rangle$  transition frequency of qC,  $\omega_{ge}$ :

$$\xi_{1(2)} = -\frac{i\epsilon_{1(2)}}{(i\tilde{\kappa} + i(\omega_{ge} - \omega_{1(2)}))} \quad (6.4)$$

where  $\tilde{\kappa}$  is the effective decay rate of the mode to which the drives couple to primarily. In this case, it is the decay associated with qC, which is at least an order of magnitude smaller than the coupling rates associated with the driven interaction. Now we simplify the Hamiltonian to

$$\hat{H}/\hbar = -E_J \cos(\phi_a(\hat{a} + \hat{a}^\dagger) + \phi_b(\hat{b} + \hat{b}^\dagger) + \phi_c(\hat{c} + \hat{c}^\dagger + \xi_1 + \xi_1^* + \xi_2 + \xi_2^*)) \quad (6.5)$$

From this, we derive the effective Hamiltonian,  $H_{\text{int}}$ , discussed in the main text by expanding the Hamiltonian in the new frame to the 4th order and perform the standard rotating wave approximations (RWA). As the frequency matching condition is satisfied when  $\omega_2 - \omega_1 = \omega_b - \omega_a$ , the only 4th order, non-rotating terms are:

$$\hat{H} = \hat{H}_{ss}^{1(2)} + \hat{H}_{\text{Kerr}} + \hat{H}_{\text{int}} \quad (6.6)$$

$$\hat{H}_{\text{int}} = -E_J \phi_c^2 \phi_a \phi_b (\xi_1 \xi_2^* \hat{a}^\dagger \hat{b} + \xi_1^* \xi_2 \hat{a} \hat{b}^\dagger) \quad (6.7)$$

$$\hat{H}_{ss}^{1(2)} = -E_J \phi_c^4 |\xi_{1(2)}|^2 \hat{c}^\dagger \hat{c} = -2\alpha |\xi_{1(2)}|^2 \hat{c}^\dagger \hat{c} \quad (6.8)$$

$$\hat{H}_{\text{Kerr}} = - \sum_{k=a,b,c} \frac{E_J \phi_k^4}{4} \hat{k}^\dagger \hat{k}^\dagger \hat{k} \hat{k} - E_J \phi_a^2 \phi_b^2 \hat{a}^\dagger \hat{a}^\dagger \hat{b} \hat{b} \quad (6.9)$$

$$- E_J \phi_a^2 \phi_c^2 \hat{a}^\dagger \hat{a}^\dagger \hat{c} \hat{c} - E_J \phi_b^2 \phi_c^2 \hat{b}^\dagger \hat{b}^\dagger \hat{c} \hat{c} \quad (6.10)$$

where  $H_{\text{int}}$  is the desired interaction term.  $\hat{H}_{\text{Kerr}}$  describes the self-Kerr and cross-Kerr coupling terms [62], which do not depend on the microwave drives. They are calibrated independently using methods developed in Ref. [35]. Finally,  $H_{ss}^{1(2)}$  captures the Stark shift of the resonance frequency of qC ( $\tilde{\omega}_c$ ) in the presence of each RF drive. It is also worth noting that the drives are applied adiabatically with a smooth ring-up and ring down time of  $\sim 100$  ns to ensure that no additional spectral components are present in the drive tones.

We further simplify  $\hat{H}_{\text{int}}$  and express it as a function of system parameters that we measure independently, i.e.

$$\hat{H}_{\text{int}} = -E_J \phi_a \phi_b \phi_c^2 \left( \xi_1 \xi_2^* \hat{a} \hat{b}^\dagger + \xi_1^* \xi_2 \hat{a}^\dagger \hat{b} \right) = g(t) \hat{a} \hat{b}^\dagger + g^*(t) \hat{a}^\dagger \hat{b} \quad (6.11)$$

$$g(t) = E_J \phi_a \phi_b \phi_c^2 \xi_1(t) \xi_2^*(t) = \sqrt{\chi_{ac} \chi_{bc}} \xi_1(t) \xi_2^*(t) \quad (6.12)$$

where the effective coupling strength is  $g_{\text{eff}} = \sqrt{\chi_{ac} \chi_{bc}} |\xi_1| |\xi_2|$ . The dispersive couplings are calibrated using standard Ramsey or number-splitting experiments (section 2.3) and the strength of each drive tone  $|\xi_{1,2}|$  can be calibrated independently by measuring the Stark shift of the resonance frequency of qC.

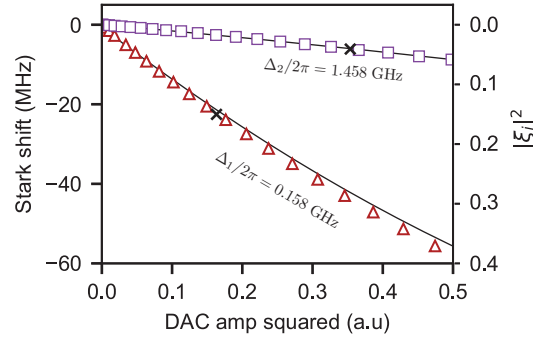


Figure 6.3: **Stark shift due to drives.** The measured Stark shifts on qC in the presence of each drive are shown in open face markers. The solid line is a fit including 6th order terms from the cosine expansion. This provides an independent calibration of the drive strength, shown in the second vertical axis (right). The black cross indicates the typical drive strength used in this series of experiments

To do so, let us re-write the stark shift in terms of  $\alpha$  and the drive strength  $\xi_k$ :

$$\Delta_k = -2\alpha|\xi_k|^2 \quad (6.13)$$

Both  $\alpha$  and the  $\Delta_k$  can be measured accurately using simple spectroscopy experiments. Therefore, we now have an independent calibration for each individual  $\xi_k$ . In Fig. 6.3, the measured Stark shift for each drive tone is presented as a function of the input DAC power. Both drives are positioned above the transition frequency of qC with drive 1 (red triangles) having a much smaller detuning compared to drive 2 (violet squares). As a result, drive 2 causes a much smaller Stark shift which is well-described by a linear dependence on power. In contrast, the drive tone at  $\omega_1$ , due to its spectral proximity to the qC frequency, leads to a greater frequency shift for nominally the same input power. It also exhibits fairly obvious deviations from the linear dependence as predicted by the model. Rather, a quadratic dependence on power is necessary to describe the behaviour. This arises from the 6th order expansion of the cosine Hamiltonian, which is no longer negligible at large  $\xi$ .

In order to demonstrate the action of  $\hat{H}_{\text{int}}$ , we first implement it on the simplest case with only a single excitation in Alice and Bob. The general technique used in our investigation is described by the pulse sequence in Fig. 6.4(a). To begin with, we initialise the memories

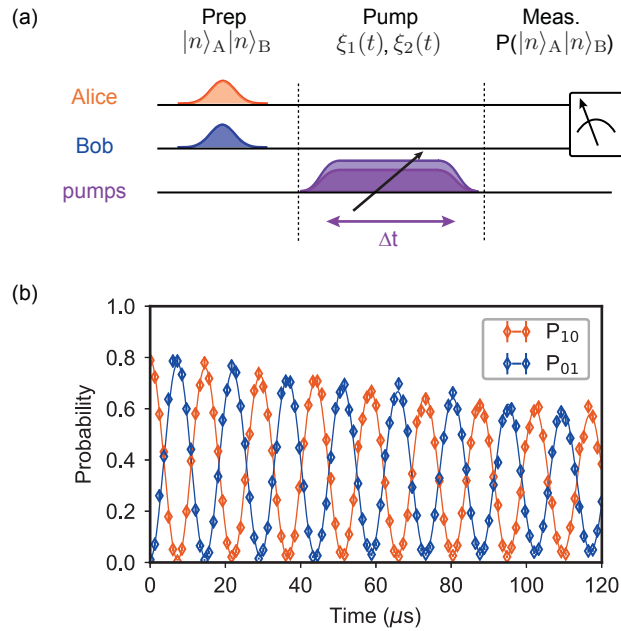


Figure 6.4: **Characterisation of bilinear coupling.** (a) Pulse sequence used to characterise the engineered bilinear interaction. The experiment starts with the preparation of desired initial states using single cavity drives. Subsequently two drive tones are introduced to initiate the four-wave mixing process that provides the frequency-converting coupling between Alice and Bob. The system evolves in presence of the drives with a variable amount time before we probe the joint photon population distribution in Alice and Bob using transmon C as the metre. (b) Example of the measured oscillations of a single photon from Alice to Bob at a particular drive strength. Data are shown in circles and solid line is a fit to the functional form  $P = Ae^{-t/\tau_1} [1 + e^{-t/\tau_\phi} \sin(2\pi t f_0 + \phi_0)]$ , with  $\tau_1$  the single photon lifetime and  $\tau_\phi$  the dephasing time of the cavity mode, and  $f_0$  the frequency of the oscillation.

in  $|1\rangle_A |0\rangle_B$  using numerically optimised pulses, as described in [36] while ensuring that qC remains in its ground state. We then apply the drive tones, tuned to satisfy the frequency-matching condition, for a variable amount of time before measuring the joint population distribution in the two memories using a photon-number selective  $\pi$  pulse on qC. This allows us to monitor the evolution of the single photon as it coherently oscillates between A and B over the duration of the drives.

We show here in Fig. 6.4(b) the behaviour of a single excitation undergoing the interaction at a coupling strength  $g/2\pi = 34$  kHz with  $|\xi_1 \xi_2| \approx 0.1$ . We observe coherent oscillations of the photon between Alice and Bob as the system evolves under the engineered unitary

operaton. By varying the duration of the drives, we can achieve a few different types of useful operations between the two memories. We define  $\theta = \int_0^T g(t)dt$  as the effective mixing angle of the process. It is fully tunable by varying the duration of the two microwave drives. For  $\theta = \frac{\pi}{2} \pmod{\pi}$ , the unitary performs a SWAP operation that exchanges the states between the two memories, while for  $\theta = \pi/4 \pmod{\pi/2}$  it corresponds to a 50:50 BS operation ( $\hat{U}_{\text{BS}}$ ). Since  $g(t)$  is fully tunable parameter and can be made fast compared to the natural direct coupling ( $\lesssim 1$  kHz) between Alice and Bob, these operations can be implemented with a large on-off ratio. Furthermore, we observe that the oscillations persist far beyond the transmon  $T_1$  ( $\simeq 50 \mu\text{s}$ ) and the decay timescale is consistent with the natural photon loss rate in Alice (Bob) with time constant  $\tau \simeq 400 \mu\text{s}$  in the absence of the coupling. This demonstrates that at this amplitude, the microwave drives themselves do not introduce any significant decoherence to the system.

## 6.2 Coherence of BS operations

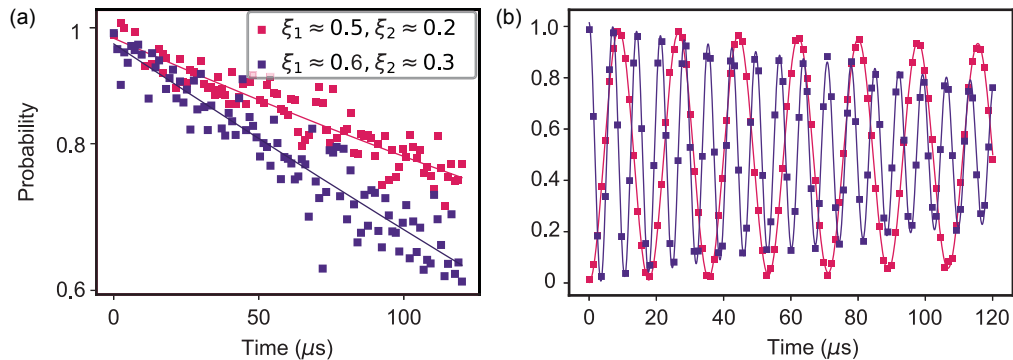


Figure 6.5: **Decoherence of single photon oscillation.** (a) The envelope given  $P = P_{01} + P_{10}$  for two different effective drive powers. The decay of the envelopes corresponds to photon loss from the system and allows us to extract a decay constant for a single photon living between Alice and Bob. The data exhibit linear behaviour on the Log scale, indicating that the the single photon decay from the system can be described by a single exponential. (b) The measured single photon oscillations after removing the effects of photon loss by dividing the raw data with the envelopes at each drive power. This provides indication of the single photon dephasing time which is well described by a decaying sinusoidal fit (solid lines).

We assess the fidelity of the BS operation by analyzing the decoherence time associated

with the evolution of a single excitation under  $\hat{U}_\theta$ . There are two mechanisms which can decoherence in the single photon evolution, namely, photon loss from the memories, at rate  $\tau_1$ , and dephasing process that prohibits the photon from constructively interfering with itself, at rate  $\tau_\phi$ . To estimate the effective photon loss rate, we sum the measure  $P_{10}$  and  $P_{01}$ . This yields the envelope which describes the decay of the probability of having a single photon in the system. The time constant of this exponential decay is the effective  $\tau_1$  of the single photon living between the two memories, as shown in Fig. 6.5(a). We then divide the measured  $P_{10}$  by this envelope to extract the pure dephasing time from a decaying sinusoidal function (Fig. 6.5(b)). For the more weakly driven process (red), we extract an effective  $\tau_1 \simeq 400 \mu\text{s}$  and  $\tau_\phi \simeq 800 \mu\text{s}$  at the effective drive strength  $\xi_1 \xi_2 \simeq 0.1$ . Combining these, we infer an effective decoherence time  $T_2 = 400 \mu\text{s}$  for the operation. This is consistent with the intrinsic coherence times of Alice and Bob, indicating that the engineered BS operation does not introduce additional sources of decoherence. However, we clearly observe a deterioration of both  $\tau_1$  and  $\tau_\phi$  when we operate the drives at a higher power (dark purple).

Another metric that indicates the coherence of the operation is the qC excited state population due to the drives in addition to its equilibrium thermal population of  $\lesssim 1\%$ . Appreciably higher population can arise from the increasing direct participation of the transmon mode as well as direct heating of the microwave components due to the large incoming drive power. When this occurs, the damage to our system is two fold. First, since qC is also used as a metre to monitor the photon number distributions in Alice and Bob, an elevated excited state population causes wrong readings in the measurement. Furthermore, the undesired  $|g\rangle \rightarrow |e\rangle$  transition also results in additional dephasing of the cavity states, introducing further imperfections in the operation. In practice, we can mitigate this effect by implementing a simple post-selection process that only considers the data if qC is measured in its ground state after the operation.

We present these nonidealities of the engineered operation at different drive powers in Fig. 6.6. Naively, one might think that the fixed coupling to the environment and the associated imperfections become less important as operation speeds up. However, as the coupling strength increases so does the participation of the transmon excited levels, which

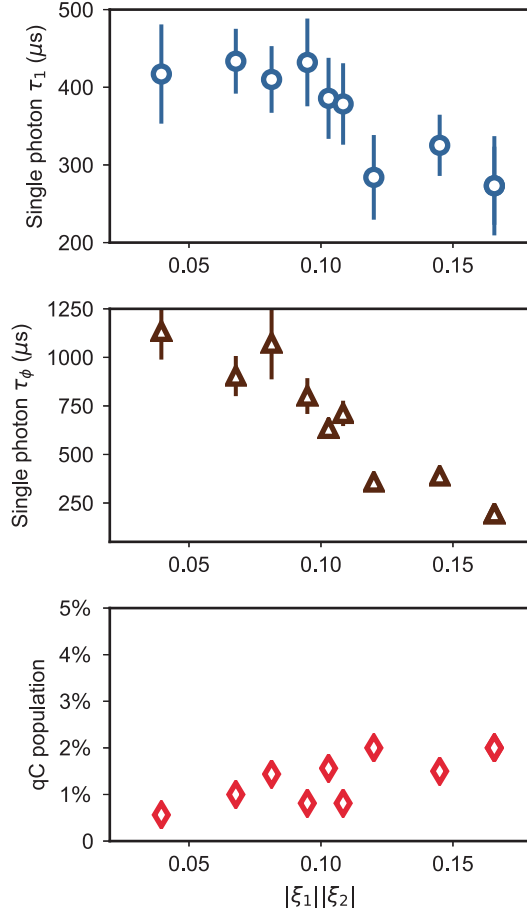


Figure 6.6: **Extracted  $\tau_1$  and  $\tau_\phi$ .** (a), (b) Extracted  $\tau_1$  and  $\tau_\phi$  for a range of effective drive powers  $|\xi_1||\xi_2|$  starting with the system in  $|1\rangle_A|0\rangle_B$ . (c) The independently measured excited state population of qC after a drive duration corresponding to a single BS operation.

are measured independently after each BS. We observe that the probability of qC departing from its ground state  $1 - P_g$  increases from 0.6% to 2% as we increase the drive strengths. We observe both an apparent reduction in the readout contrast as well as faster decoherence during  $\hat{U}_{\text{BS}}$ . The former can be mitigated by performing post-selection: data are discarded if qC does not remain in  $|g\rangle$  after the operation. This ensures that qC is a faithful metre for the joint photon population of Alice and Bob. We attribute the degradation of the coherence to the greater participation of qC. This causes the system to inherit less favorable coherence times from qC during the operation.

Additionally, we extract the coupling coefficient,  $g_{\text{eff}}$ , for a particular drive configuration

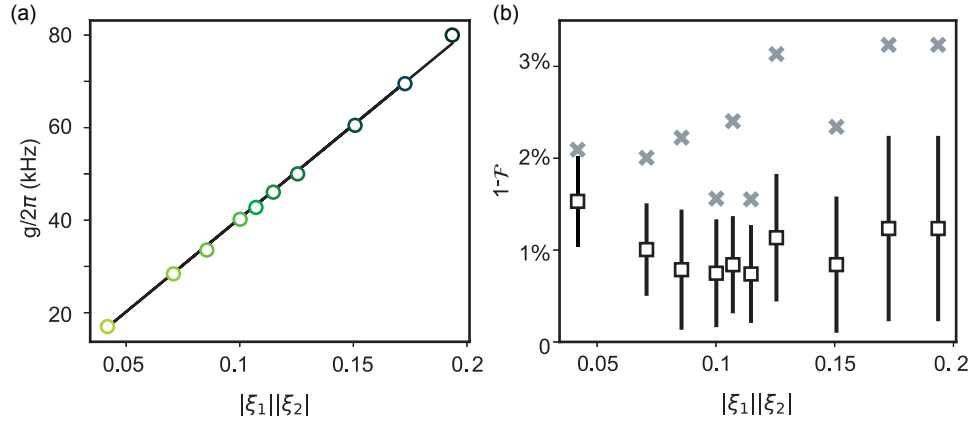


Figure 6.7: **Tunability of bilinear coupling.** (a) The coupling strength of the engineered bilinear coupling as a function of effective drive powers extracted from single photon dynamics (green circles). The solid black line is the theoretical prediction given the drive powers and the system parameters,  $\chi_{ac}, \chi_{bc}$ . (b) The infidelity of a single BS operation computed by comparing the driven coupling rate to the decoherence rate of the system. Black squares are extracted from data after post-selecting on the transmon remaining in its ground state after the operation and grey crosses are computed without post-selection.

from the frequency of the decaying sinusoidal. The coupling strength is fully tunable and we show that it scales linearly with the effective drive powers as shown in Fig. 6.7(a), consistent with that predicted by a simple model that uses the 4th order expansion of the cosine Hamiltonian. However, as the drive powers increase, we start to deviate from the prediction due to the increasing effects of higher order terms. Using these measured coupling coefficients and the extracted decoherence time scales shown in Fig. 6.6(a), we compute a measure of the infidelity for each drive power defined as

$$1 - \mathcal{F} = \tau_{\text{BS}}/T_{\text{BS}} \quad (6.14)$$

where  $T_{\text{BS}}$  is the operation time required to implement an effective BS and  $1/\tau_{\text{BS}} = 1/2\tau_1 + 1/\tau_\phi$  is the decoherence time of a single photon undergoing the process. Combining the faster operations and the penalty of increased qC participation, the overall infidelity ends up roughly constant over different drive powers as shown in Fig. 6.7(b). At the chosen operation power, we show that the BS operation has an infidelity of  $(99 \pm 0.5)\%$ . When post-selection on qC is not implemented, we do observe an increase of infidelity as the

coupling becomes stronger. This, however, is most likely to be a result of mistakes in the measurement due to the incorrect initial state of our metre, qC.

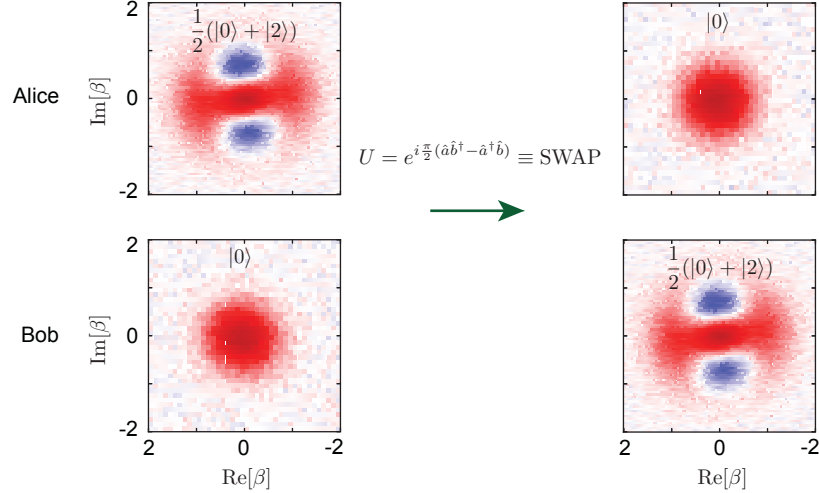


Figure 6.8: **SWAP operation between two cavities.** The bilinear coupling is tuned to implement a SWAP operation between Alice and Bob. In this example, we transfer a small kitten state from Alice to Bob, which is initialised in vacuum. The raw Wigner functions are shown for each mode, before and after the operation. By computing the overlap with the ideal states, we extract a transfer fidelity of  $98 \pm 1\%$ .

Finally, we illustrate the phase coherence of the operation by preparing Alice in a superposition state and then turn on the coupling. In particular, we implement a full transfer of the state in Alice to Bob by choosing a drive duration corresponding to  $\theta = \pi/2$  radians, which effectively performs a SWAP gate between Alice and Bob. As shown in Fig. 6.8, the system is initialised in the state  $\frac{1}{2}(|0\rangle + |2\rangle)_A \otimes |0\rangle_B$ . It then evolves under the bilinear coupling Hamiltonian for  $6\ \mu\text{s}$ , which is twice of what is required for a single BS operation. We then perform Wigner tomography on each cavity using their respective transmon ancilla. We find that Alice is now in vacuum while Bob contains the superposition state, with the same relative phase between the two Fock states. Visually, the operation allows excellent preservation of the coherence of the initial states. More quantitatively, we compute the state fidelities of the initial and final state using the measured Wigner functions. From this, we infer an infidelity of  $\sim 2.5\%$  for the SWAP operation, which roughly doubles that of the BS because it takes twice as long to implement. This demonstrates that the engineered

unitary is capable of preserving the phase coherence of quantum superpositions and is fully compatible with highly non-classical states.

### 6.3 Bosonic interference and its applications in cQED

In this section, we will now employ the engineered BS operation to study bosonic interference between two stationary photons stored in Alice and Bob. Importantly, we exploit the frequency-converting capability of the BS to enable such experiments between photons that are far detuned from each other.

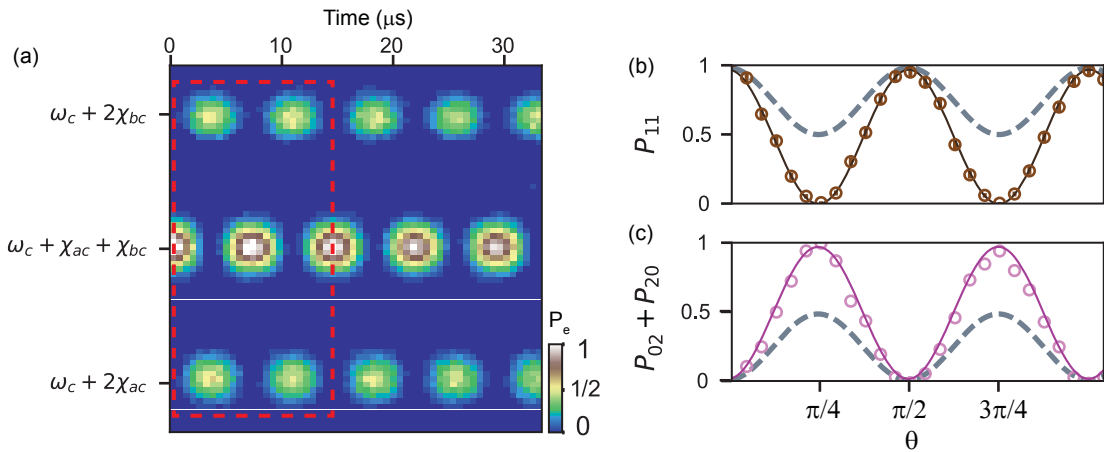


Figure 6.9: **HOM interference between two spectrally-separated cavity modes using the frequency-converting BS.** (a) Measurement of the joint photon number distribution of Alice and Bob as a function of drive duration using qC as the probe. The vertical axis indicates the probability of successfully exciting qC conditioned with a spectrally narrow pulse. The three frequencies at which this occurs correspond to the dispersively shifted resonance of qC with state  $|0\rangle_A|2\rangle_B$ ,  $|2\rangle_A|0\rangle_B$ , and  $|1\rangle_A|1\rangle_B$  respectively. 1D cuts along the time axis are shown in (b) and (c) for the region inside the red box. In (b), we present the dynamics of  $|1\rangle_A|1\rangle_B$  (brown circles), which oscillates with near full contrast. (c) shows the behaviour of  $P_{20} + P_{02}$  (violet circles), which oscillates exactly out of phase compared to  $P_{11}$ . The grey dashed lines are simulated behaviour of distinguishable particles undergoing HOM interference

The hallmark of indistinguishable bosonic modes interacting through a BS is the HOM interference. Here we demonstrate that HOM interference can be achieved using the engineered frequency-converting BS between two photons at different frequencies. We start by preparing  $|1\rangle_A|1\rangle_B$  and monitor the population across the two memories after the application

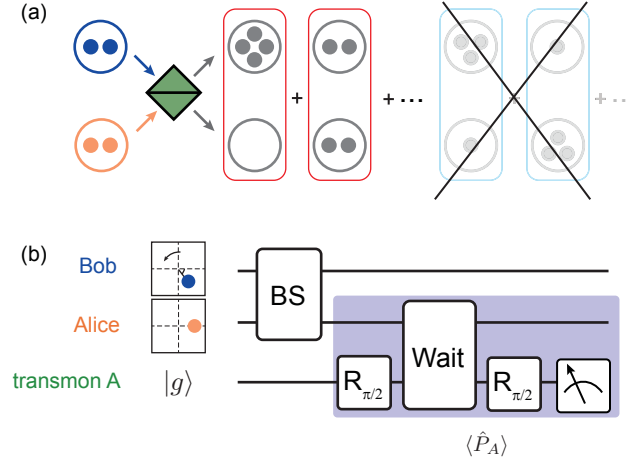


Figure 6.10: **Statistics of bosonic interference.** (a) Quantum statistic of bosonic interference that only allows even outcomes when the input states are identical since the odd probability amplitudes fully destructively interfere. Using this fundamental feature of quantum interference, we extract the overlap between two arbitrary quantum states by measuring the parity of one of the output ports of a 50:50 BS. (b) We use a simple experimental protocol to demonstrate this capability with coherent states in Alice and Bob. We prepare the two states with equal amplitude and a variable relative phase, then allow them to interfere through the frequency-converting BS and finally measure the photon number parity of Alice using the standard protocol.

of the drive tones. We observe the near complete destruction of the  $|1\rangle_A|1\rangle_B$  signal after the BS. At this point, we measure an equal probability of finding the system in the state  $|2\rangle_A|0\rangle_B$  and  $|0\rangle_A|2\rangle_B$ . This is an intrinsically quantum mechanical phenomena that relies on the two incident photons being fully indistinguishable such that probability amplitudes of being in  $|1\rangle_A|1\rangle_B$  after the BS destructively interfere. If the two photons are distinguishable, classical interference would be observed and the measured  $P_{11}$  would not fall below  $\simeq 0.5$ . Here, we measure a contrast of  $98 \pm 1\%$  in the oscillations of  $P_{11}$ , indicating that the engineered frequency conversion process fully compensates the energy difference between the two initial photons and allows them to interact as indistinguishable particles.

Further, the near complete refocusing of  $P_{11}$  and the full extinction of  $P_{\text{superposition}} = P_{20} \pm P_{02}$  at  $\theta = \pi/2$  also implies that there is a well-defined phase between  $|2\rangle_A|0\rangle_B$  and  $|0\rangle_A|2\rangle_B$ . The exact relative phase between the two states is determined by the relative phase of the two drives used to realise  $\hat{U}_{\text{BS}}$ . In this study, the exact phase is unimportant as

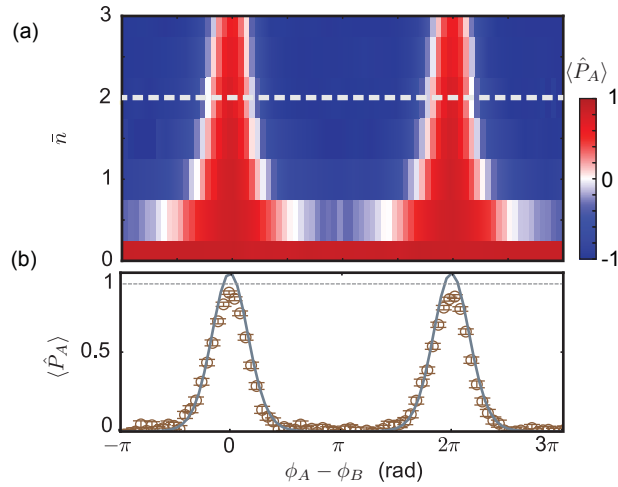


Figure 6.11: **Overlap measurement of two coherent states.** (a) Measured quantum state overlap between two cavity states  $|\psi\rangle_A = e^{i\phi_A}|\alpha\rangle$  and  $|\psi\rangle_B = e^{i\phi_B}|\alpha\rangle$ . The measurement is done as a function of the relative phase as well as the displacement amplitudes in both cavities. The vertical axis is the averaged parity of Alice. (b) The average parity of Alice at  $\bar{n} = 2$  as a function of the relative phase. The data (brown dashed line) show excellent agreement with the overlap computed for the ideal states (solid grey line) except an overall reduction in contrast. The expected contrast with the decoherence of the cavities and the ancilla taken into account is given by the dashed grey line.

long as it remains constant over the course of the experiment. The HOM experiment verifies this since a statistical mixture consisting of these two states would only partially interfere at the next BS and results in a contrast of 0.5 for both  $P_{\text{superposition}}$  and  $P_{11}$ .

The HOM experiment also reveals an intrinsic property of bosonic systems: when the two identical Fock states interfere through a 50:50 BS, the photon number parities of the output ports are always even because all the odd outcomes interfere destructively as illustrated in Fig. 6.10(a). In fact, the average parity measured on one of the output ports of a BS is a direct probe of the overlap between the two incident states, i.e.  $\langle \hat{P} \rangle = \text{Tr}(\rho_A \rho_B)$  [120, 133, 134]. This establishes a connection between the state overlap and a single observable that is the photon number parity of one of the output modes regardless of the input states. An alternative method to obtain the overlap information is to perform full tomography on the two states, which is significantly more resource-intensive. Therefore, this property of quantum interference provides us with a very efficient probe to compare two complex quantum states.

As discussed in Chapter 3, we can perform robust parity measurements by simply using the dispersive coupling between the transmon ancilla and the memory mode. Combining it with the engineered BS, we perform the overlap measurement between two states  $|\psi\rangle_A = e^{i\phi_A}|\alpha\rangle$  and  $|\psi\rangle_B = e^{i\phi_B}|\alpha\rangle$  (Fig. 6.10(b)). With  $\phi_A$  fixed, we measure the parity of mode A as a function of  $\phi_B$  for different displacements in both modes. The parity of Alice is measured in this experiment because of the slightly more favourable parameters of ancilla qA, which permits a higher overall contrast. As expected, the maximum overlap is measured when  $\phi_A = \phi_B \pmod{2\pi}$ . As the displacement increases, the overlap becomes more sharply peaked. Here, we observe a reduction in the overall contrast at higher photon numbers due to the imperfections of the parity measurement. It mainly arises from the incomplete spectral unselectivity of the  $\pi/2$  pulse in presence of high photon number states in the cavities. This can be mitigated with a spectrally broader ancilla pulse in future measurement. This type of efficient comparison of quantum states is a very useful tool since full tomography becomes increasingly demanding with larger, more complex states.

In addition to the engineered BS operation, we can also implement on-demand DPS to Alice via its natural dispersive coupling ( $\chi_1$ ) to qA. This is governed by the unitary  $\hat{U}_{\text{DPS}}(t) = |g\rangle\langle g| \otimes \hat{I} + |e\rangle\langle e| \otimes e^{i\phi\hat{a}^\dagger\hat{a}}$ , where  $\phi = \chi_1 t$ . This implementation has two major advantages. First, it is fully programmable: the resulting differential phase,  $\phi \in [0, 2\pi]$ , is simply controlled by the evolution time,  $t$ , which can be tuned on the fly. Furthermore, it is photon-number independent.  $\hat{U}_{\text{DPS}}$  allows us to impart the same phase to each individual photon in Alice. Therefore, it is naturally compatible with more complex interference experiments involving multi-photon states.

Combining the BS and DPS capabilities, we construct cascaded MZ interferometers and program them to perform different interference experiments on the fly (Fig. 6.12(a)). As a simple example, we initialise the system in  $|1\rangle_A|1\rangle_B$ . After a single BS, the system reaches the superposition state  $|\Psi\rangle = \frac{1}{\sqrt{2}}(|0\rangle_A|2\rangle_B + e^{i\varphi}|2\rangle_A|0\rangle_B)$ . Subsequently, we impart a phase on Alice by exciting qA for a time  $\pi/\chi_1 \sim 600$  ns. This operation changes the relative phase between Alice and Bob, leaving the system in the state  $|\Phi\rangle = \frac{1}{\sqrt{2}}(|0\rangle_A|2\rangle_B + e^{i(\varphi+\pi)}|2\rangle_A|0\rangle_B)$ . This is now a ‘dark state’ of  $U_{\text{BS}}$  because the probability amplitudes

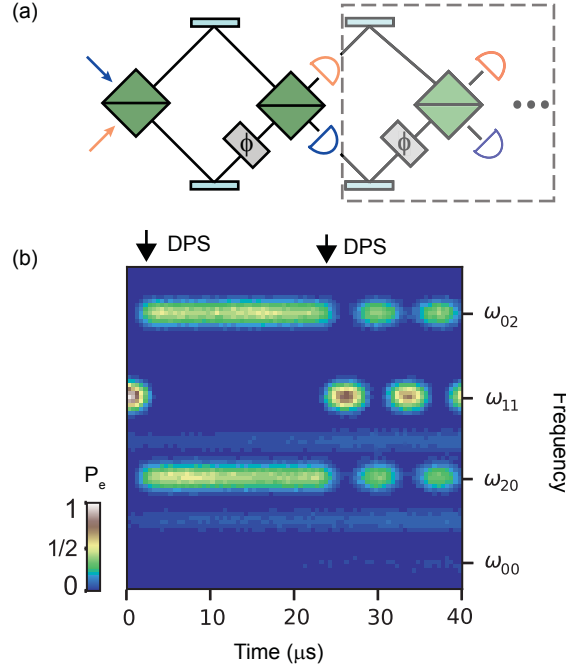


Figure 6.12: **Cascaded microwave Mach-Zehnder interferometers.** (a) Conceptual depiction of cascaded Mach-Zehnder (MZ) interferometers composed of 50:50 beamsplitters and differential phase shifters. Since the engineered BS operation allows frequency-conversion, we implement this on two modes (orange and blue) that are detuned from each other. (b) The spectroscopy measurement of joint photon distribution after each BS in the cascaded MZ interferometer, starting with the system in  $|1\rangle_A|1\rangle_B$ . A different phase of  $\phi = \pi$  is imparted after the first BS to change the relative phase of the two paths. This results in a complete destructive interference of all subsequent probability amplitudes of  $|1\rangle_A|1\rangle_B$ . An additional  $\pi$  phase is introduced after 8 beamsplitters, reversing the relative phase of  $|0\rangle_A|2\rangle_B$  and  $|2\rangle_A|0\rangle_B$  to allow the refocusing to  $|1\rangle_A|1\rangle_B$ .

of  $|1\rangle_A|1\rangle_B$  always interfere destructively, forcing the system to remain in  $|\Psi\rangle$  through all subsequent beamsplitters. We recover the HOM-type interference by implementing a second DPS of  $\pi$  on Alice. This experiment provides a great illustration of our ability to program the system to generate different types of bosonic interference. We can manipulate the signatures of interference on-the-fly with in-situ DPS performed by the transmon ancillae. Such cascaded interferometers, similar to the optical implementation in [135], can be scaled up to simulate complex bosonic interference in cQED.

Since the engineered BS is agnostic to the photon number in the memories, we extend these interference studies to multi-photon states. As a simple example, we show the evolution

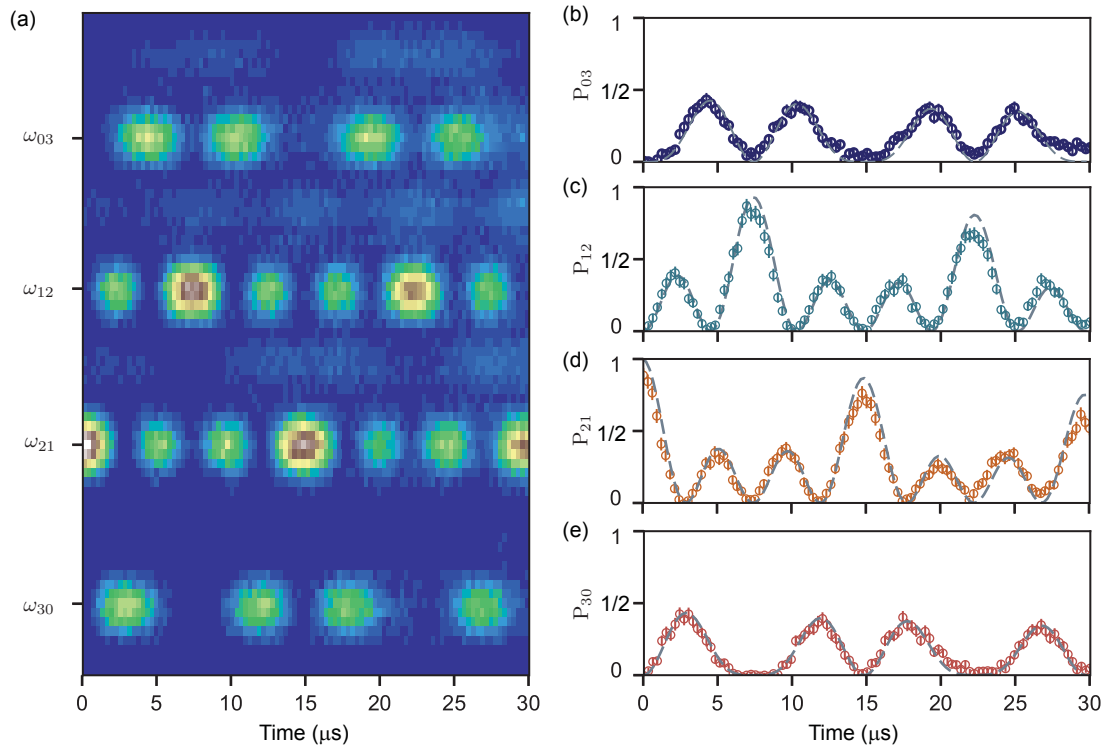


Figure 6.13: **Interference of multiphoton states.** (a) Spectroscopy measurement of joint photon distributions in Alice and Bob after a series of beamsplitters with the system initialised  $|2\rangle_A|1\rangle_B$ . (b) 1D cuts along the time axis for each outcome. Data (circles) show good agreement with simulation, which takes into account of the decoherence of both the cavities and the transmon ancilla.

of  $|2\rangle_A|1\rangle_B$  going through a series of beamsplitters in Fig. 6.13. Due to the absence of an independent ancilla that couples to Bob, it is rather cumbersome to prepare a Fock state in it directly using OCT pulses. To overcome this, we instead first initialise the system in  $|1\rangle_A|0\rangle_B$ . Subsequently, we use the engineered bilinear coupling to perform a SWAP operation and transfer this excitation from Alice to Bob. Finally, we complete the preparation by putting two photons in Alice using another numerically optimized OCT pulse. The entire process takes  $\sim 5 \mu\text{s}$  and produces the desired state with  $\sim 85\%$  fidelity with some spurious populations in  $|0\rangle_A|0\rangle_B$ ,  $|1\rangle_A|0\rangle_B$ , and  $|2\rangle_A|0\rangle_B$ . However, since the interference conserves the total photon number and the joint parity, the spurious populations do not change the statistics of the outcomes of  $|2\rangle_A|1\rangle_B$  undergoing  $\hat{U}(\theta)$ . Instead, they will result in a deterministic reduction in the measurement contrast. The measured interference

pattern is in good agreement with the simulated behaviour, indicating that the operation is robust irrespective of the state stored in Alice and Bob. As shown by this measurement, the number of possible outcomes increases quickly with the photon number in the system even with just two modes. With this implementation, we can efficiently probe the resulting quantum statistics despite the increasing complexity. It opens up a wide range of possibilities to perform bosonic sampling in this type of cQED architecture, which can be scaled up to more than two modes relatively easily.

## 6.4 Alternative drive configurations

Our ability to scale up towards more complex interferometers between multiple modes with potentially multiple excitations depends directly on the quality of the beamsplitter operations. Ideally, we would like to realise the beamsplitter quickly so that the operation is fast compare to both decoherence mechanisms and higher order nonlinearities such as Kerr. Furthermore, it is also crucial to ensure that the BS does not introduce additional noise to the system and degrade the coherence of the bosonic states stored in the high-Q modes. This requires us to implement a strong and yet precise bilinear coupling, with minimal participation of the transmon excited states. In order to do so, we must choose the frequencies and powers of the drives with caution.

We have chosen to drive the bilinear coupling with two separate microwave drives in order to have more flexibility in frequency configurations. Since only the detuning between the two tones must be fixed, the frequency matching condition can be satisfied with different spectral arrangements. Broadly speaking, we can separate them into three categories according to their detunings to the transition frequencies of qC as depicted in Fig. 6.14. The side ancillae are omitted in this discussion as their frequencies are placed far below Alice, Bob, and qC. Further, the spatial separation between the side ancillae and the drive modes, which are coupled to the system through a drive port above qC, also suppresses their sensitivity to the drives. We verify this by measuring the Stark shift on qA and qB in presence of the pump tones. Our measurements show that there is no measurable shift of their resonance

frequencies. Thus, we will omit the ancilla modes in this discussion.

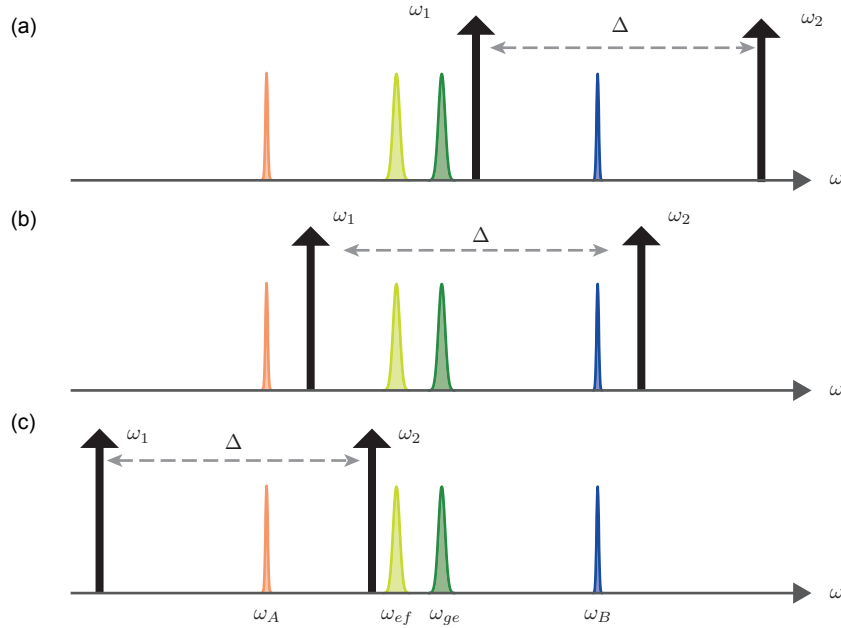


Figure 6.14: **Different frequency configurations of pumps** Three choices of drive frequencies relative to both the  $|g\rangle - |e\rangle$  (green) and  $|e\rangle - |f\rangle$  (yellow) frequencies of qC. In our designs, the resonance frequencies of Alice (orange) and Bob (blue) are roughly symmetric around  $\omega_{ge}$ . (a) Both drives are positioned at higher frequencies compared to the transition frequencies of qC. (b) The drives are placed above and below qC frequency. (c) Both drives are below the transition frequencies of qC

In our designs, the frequencies of Alice and Bob are typically placed to be roughly symmetric around  $\omega_{ge}$  such that  $\chi_{ac}$  and  $\chi_{bc}$  are similar in magnitude (200 - 400 kHz). Apart from the  $|g\rangle - |e\rangle$  transition, at  $\omega_{ge}$ , there are also higher order resonances at frequencies below it at  $\omega_{ef} = \omega_{ge} - \alpha$ ,  $\omega_{fh} \approx \omega_{ge} - 2\alpha$  etc. In the first drive configuration, we place both tones above  $\omega_{ge}$ . This allows us to avoid spectrally overlapping with any transitions of qC. The trade-off for this choice is the large detuning ( $\gtrsim 1.5$  GHz) between one of the drive tones  $\omega_2$  and our non-linear mode. As a result, the effective strength of this drive is diminished and a large amount of RF power is required to drive the desired coupling. We can typically achieve a relatively clean BS operation, with minimal qC participation and additional decoherence with a coupling strength on the order of 50 kHz.

It is important to note that the quality of the operation can be highly dependent on

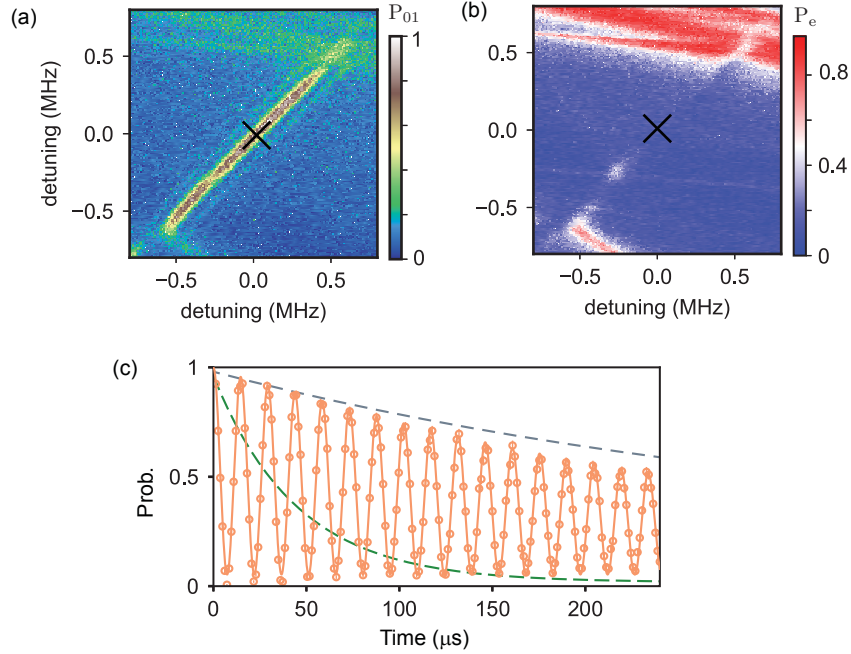


Figure 6.15: **Drives above the nonlinear mode** (a) Measurement of the probability of successfully transferring a single excitation from Alice to Bob using the driven bilinear coupling as a function of the frequencies of both drives. The black cross indicated the chosen set of frequencies at which the experiments in the earlier sections are implemented. (b) Corresponding independent measurement of qC population. (c) Measured decay a single excitation (orange) oscillating back and forth between Alice and Bob using this configuration. It is in good agreement with the natural decay timescale (grey dashed line) of a single photon in absence of the operation. The oscillation persists far beyond the transmon relaxation (green dashed line) timescale.

the exact frequencies of the drives. To demonstrate this, we monitor the probability of successfully transferring a single photon from Alice to Bob while simultaneously sweeping the detunings of both drive tones from a certain set of matched frequencies at moderate drive powers. We show in Fig. 6.15(a) that in general, the operation is successfully implemented when the frequency matching condition is satisfied, i.e. along the diagonal line. However, within  $\pm 0.5$  MHz from the initial frequencies we do observe regions where the operation fails, as indicated by the spurious features and the loss of contrast. We also independently measure the population of qC over the same range of detunings (Fig. 6.15(b)). Ideally, qC should remain in its ground state during the operation. However, we observe that the probability of it being excited to a higher level increases in the same regions where the operation fails. Our

data demonstrate that there is a strong correlation between the rising qC population and the degradation of the BS operation, both of which are extremely sensitive to the frequency of the drives. The interference experiments described above are performed in this drive configuration with the operation frequency indicated by the black cross, where qC remains predominantly in  $|g\rangle$  ( $>98\%$ ). This allows us to realise a high quality BS with its coherence limited by the intrinsic energy decay of the cavities, as shown in Fig. 6.15(c).

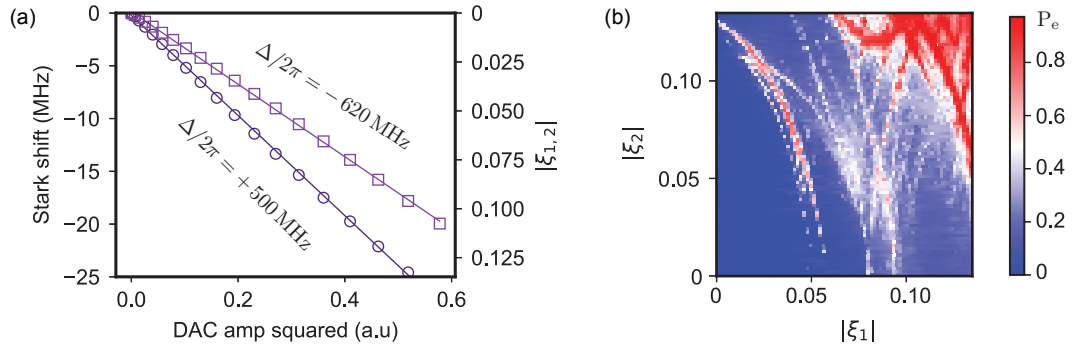


Figure 6.16: **Effects of the drives when placed symmetrically around nonlinear mode** In this configuration, the two drive tones are detuned by a similar amount above and below  $\omega_{ge}$ . (a) The resulting Stark shift due to each drive tone. This can be mapped to an effective drive power as shown in the secondary y-axis. The two drives now have a comparable impact on  $\omega_{ge}$ , in contrast to the case shown in Fig. 6.3. (b) We also monitor the population of qC as a function of the powers of each drive in this frequency configuration. We observe significant heating of the nonlinear mode at higher drive powers.

An alternative configuration is to shift both drives down in frequency such that they are placed roughly symmetrically around qC. This has the advantage of having more balanced effective drive strength from each tone and permits a potentially stronger coupling. We show in Fig. 6.16(a) that when the drives are arranged this way, we indeed observe a similar amount of Stark shift on qC. However, as shown in Fig. 6.16(b), we are more likely to excite the transmon to its higher levels with this configuration. In particular, the power of drive 1, which is below  $\omega_{ge}$  causes significant transmon heating and must be kept at a relatively low power. The presence of these spurious features are likely to be due to higher order transitions of qC. Tracking down the exact causes for them is not a trivial task as they tend to be multi-photon effects. An additional complication is the Stark shift of each mode. As a result, the frequencies and powers of the drives are no longer independent from each

other, making it even more challenging to compute all the possible multi-photon processes. One potential culprit that we have managed to identify is a process that takes one of each drive photons and converts them into a double excitation of qC, i.e.  $\omega_1 + \omega_2 = \tilde{\omega}_{gf}$ , where  $\tilde{\omega}_{gf}(\omega_1, \omega_2, \xi_1, \xi_2)$  is the Stark shifted frequencies of the  $|g\rangle - |f\rangle$  transition. In order to avoid this, we must sweep the frequencies of each drive carefully at the chosen amplitude. In practice, we typically operate at  $\xi_1 \sim 0.3$ ,  $\xi_2 \sim 0.6$  in order to achieve a relatively coherent and fast BS operation with  $g \sim 100$  kHz.

These two examples suggest that strong drive tones placed below the frequencies of the nonlinear mode is generally not undesirable due to the presence of higher order transitions. Indeed, when we attempted to implement the third drive configuration (Fig. 6.14(c)) we find that the qC is highly susceptible to heating even at relatively low drive powers. Therefore, we have generally avoided operating in this regime.

## 6.5 Discussion

To the best of our knowledge, the three experiments presented in this chapter are the first examples of interference between long-lived, stationary bosonic states in cQED. The engineered BS provides the advantage of allowing such interference between two detuned modes, enabling low cross-talk and good intrinsic coherence of each mode. More importantly, they also pave the way for a large variety of interference-based experiments in cQED systems. For example, with the robust BS and the simple different phase shifters, we now have a complete set of tools to implement LOQC with microwave photons. [136]. This approach has a competitive edge over the linear optical implementations since we can easily prepare single photon states with high fidelity and probe them in quantum non-demolition (QND) measurements.

Additionally, this ability to prepare and measure complex bosonic states, together with the robust BS operation, also makes cQED systems attractive for boson sampling. Boson statistics arising from multimode interference process have been studied extensively theoretically [137, 138] and become increasingly complex with more larger number of excitations, or

---

modes. In this system, we can quite easily increase both the number of interfering photons and the participating modes to realistically simulate the problem. In fact, a device consisting of four such 3D stub cavities has recently been tested in our group [55] and exhibits good coherence properties on par with single-cavity system. Four transmon ancillae (Y-mons) are used in this system to provide pair-wise couplings between the cavity modes. Such systems can be easily adapted (with slight changes in design parameters) to implement a multimode boson sampling experiment in the future.

Most importantly though, the implementation of this type of engineered BS operation between the two cavities is a crucial step towards constructing universal entangling operations between two logical qubits in the cavity-based quantum computing scheme. The calibrations and decoherence analysis described in this chapter provide a great foundation for establishing the more complex quantum operations that we are going to discuss in the following chapter.

## Chapter 7

# Building a universal entangler in cQED

The cavity-based quantum computing scheme has shown tremendous promise, with rapid progress in many different key aspects. In the previous chapters, we have looked at how some of the recent experiments have pushed beyond the control and measurement of single logical qubits encoded in multi-photon states of superconducting microwave cavities. With the multi-cavity architecture introduced in chapter 3, we have successfully demonstrated that we can efficiently manipulate and faithfully characterise complex joint cavity states. Moreover, we have also performed a CNOT gate between two multi-photon states, a first display our capability to implement robust inter-cavity gates without sacrificing favourable coherence properties of superconducting cavities.

In this final set of experiments, we will continue to develop the necessary components in our cQED toolbox and work towards realising a universal entangling operation between logical qubits encoded in two superconducting cavities. In particular, we aim to implement this operation in a way that is compatible with established error-correction schemes. The unitary that is capable of realising such a gate between two logical qubits, regardless of their encoding, is the exponential-SWAP (eSWAP) operation [139]. It operates on two bosonic modes with the evolution  $U_{\text{eSWAP}}(\theta) = \cos \theta \cdot \hat{I} + i \sin \theta \cdot \text{SWAP}$ , where  $\theta$  is a variable angle controlled by a third ancillary mode. When  $\theta = \pi/4$ ,  $U_{\text{eSWAP}} = \frac{1}{\sqrt{2}}(\hat{I} + i\text{SWAP})$  is a coherent combination of the identity and SWAP operator. It is sometimes denoted as the  $\sqrt{\text{SWAP}}$  gate, which together with single qubit rotations forms a set of universal quantum gate [140]. In general, the eSWAP unitary enables us to achieve universal computing with any bosonic

systems, compatible with all single-mode bosonic encodings. It can also be extended to higher-order QEC in a more complex quad-rail logical schemes [139]. In addition, it is a key component in quantum machine learning and quantum principal component analysis [141, 142]. However, due to the complexity of the operation, such a unitary has so far only been studied theoretically [139, 143] but has not demonstrated experimentally at the time of this writing.

In this chapter, we will look into the essential ingredients required for the realisation of this operation in the cQED setting. In the previous chapter, I have introduced the concept of engineering inter-cavity operations without explicitly involving the higher excited levels of the transmon ancilla. I have also highlighted that one particular type of such two-cavity interactions that is fully tunable and can effectively implement a beamsplitter operation between two stationary cavity states. This provides an essential tool for performing the eSWAP unitary between two high-Q bosonic modes. We will explore the details of how to implement it based on the protocol proposed by L. Jiang and S. M. Girvin in section 7.1. Here, we again utilise the double-cavity device with three separate transmon ancillae and three independent readouts as described in section 3.4. With this system, I will show the first realisation of the eSWAP unitary using cQED systems in a single Fock encoding in section 7.2. Further, I will present in section 7.3 some recent data on the generation of a parityless two-mode cat state through the unitary  $U_{\text{eSWAP}}(\frac{\pi}{4})$ . At the time of this writing, we have also performed the operation using the Binomial encoding but have yet implemented full quantum process tomography to quantify the fidelity of the operation. Finally, I will conclude this chapter by outlining the potential improvements we aim accomplish in the near future using the same set tools developed in this work.

## 7.1 The exponential-SWAP unitary operation

The eSWAP unitary has been studied theoretically by Lau and collaborators [139, 143]. In their proposal, it is performed between two continuous-variable quantum modes using a two-level ancilla.

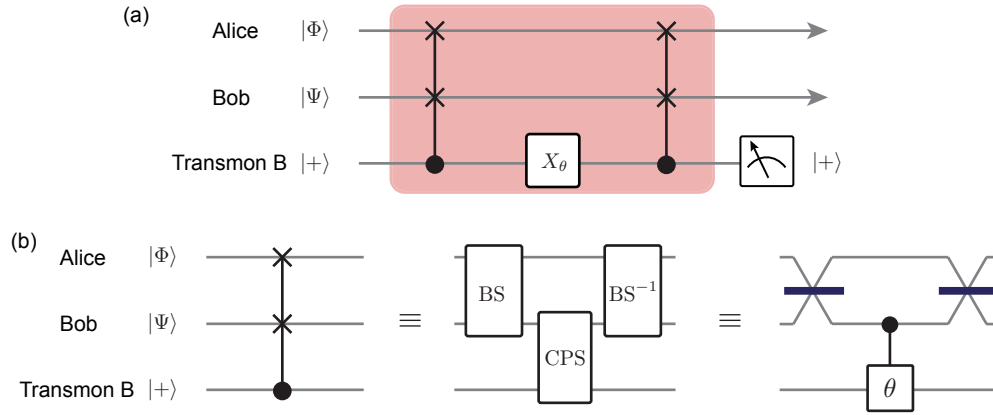


Figure 7.1: **Proposed circuit to implement  $U_{\text{eSWA}}(\theta)$**  (a) Proposed implementation consisting of single transmon rotations and the controlled-SWAP operation. (b) Decomposition of the controlled-SWAP gate into two 50:50 beamsplitters and controlled phase shift (CPS). It can be viewed as Mach-Zehnder interferometer with the phase shift on one arm, controlled by the transmon ancilla [144].

The proposed scheme is by design capable of having logical qubits with different encodings interact with one another without decoding; thus, the strength of different encodings can be utilized in the same computation. The physical implementation consists of the following operations in a protocol shown in Fig. 7.1(a):

1. prepare the ancilla in the superposition state  $|+\rangle = \frac{1}{\sqrt{2}}(|g\rangle + |e\rangle)$
2. perform an X-rotation by an angle  $2\theta$  ( $X_\theta = e^{\theta\sigma_x}$ )
3. implement a controlled-SWAP (cSWAP) gate described by the unitary:

$$U_{\text{cSWAP}} = |g\rangle\langle g| \cdot \hat{I} + |e\rangle\langle e| \cdot \text{SWAP} \quad (7.1)$$

The cSWAP operation also referred to as the Fredkin gate, which is a reversible three-bit quantum operation.

In this scheme, the cSWAP is the only missing piece of the puzzle in our double-cavity cQED systems. In Fig. 7.1(b), we show that it can be decomposed into two 50:50 beamsplitter operations with opposite phases separated by a CPS [144]. In the previous chapter, we introduced the frequency-converting bilinear coupling that allows us to perform a robust

beamsplitter between two detuned cavity modes. We also have full amplitude and phase control of the RF drives used to activate the operation. Therefore, it is straightforward to realise the two beamsplitters with opposite phases. The CPS can be interpreted as a phase accumulation on each cavity photon conditioned on the state of the ancilla, which is performed using the dispersive coupling between the ancilla and the cavity.

However, this proposed circuit has a crippling flaw in practice. This is because of the requirement of the ancilla remaining in coherent superpositions state through the entire routine. This makes it susceptible to both  $T_1$  and  $T_2$  errors of the ancilla. While the CPS can be completed in  $\sim 1/\chi \lesssim 1 \mu\text{s}$ , the BS operations typically requires 2-5  $\mu\text{s}$  in our system. This means a total gate time of several microseconds, which is not a negligible timescale compared to the  $T_2$  of the ancilla. In a typical 3D cQED system, the transmon's  $T_2$  tends to be more vulnerable to external perturbations such as mechanical vibrations or thermal noise. Hence, we expect significant imperfections to arise in this eSWAP implementation due to ancilla's  $T_2$  limitations.

To overcome this problem, it would be desirable to construct a protocol that will only require the ancilla to be in  $|+\rangle$  for short periods of time. Fortunately, due to the properties of the beamsplitter operations, we can indeed devise an alternative circuit. Two crucial simplifications make this possible:

1. The ancilla rotations (Hadamard and  $X_\theta$ ) both commute with the BS operations.
2. Two sequential beamsplitters effectively produce the identify operation

Based on this, we can reduce the decomposed eSWAP circuit (Fig. 7.2(a)) by first exchanging the order of  $X_\theta$  and the subsequent BS. This puts two beamsplitters in sequence and thus, allows us to remove them from the protocol. Furthermore, instead of preparing the ancilla in the superposition state at the very beginning of the experiment, we now perform a Hadamard gate after the first BS. As a results, we arrive at the simplified protocol depicted in Fig. 7.2(b) where the ancilla is only in  $|+\rangle$  for a short duration of  $\sim 1/\chi$  (red box).

With these modifications, we now have a more robust circuit for the eSWAP operation in cQED. These changes are highly advantageous because the beamsplitter operations are

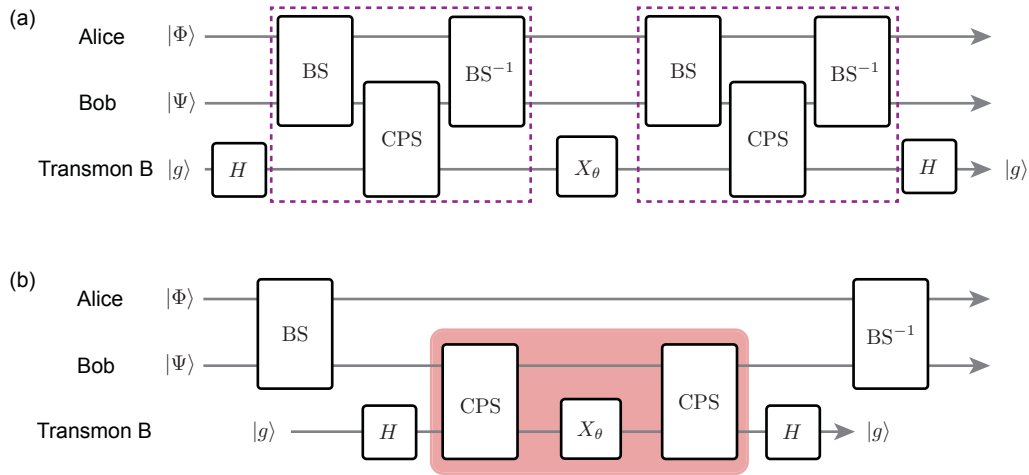


Figure 7.2: (a) The decomposed circuit describing the implementation of eSWAP with ancilla rotation, beamsplitter and CPS gates. (b) Simplified quantum circuit to a more robust eSWAP. The ancilla now remains in  $|g\rangle$  during the relatively slow BS operations and the system is only susceptible to its  $T_1, T_2$  errors over a short duration indicated by the red box.

relatively slow compared to the other gates. By eliminating two of them, the total gate time for the new protocol is now appreciably shorter. This reduces the probability of errors due to cavity decoherence as well as higher order terms such as the Kerr nonlinearity. More importantly, it significantly shortens the time over which the ancilla is in its excited state to only the CPS and  $X_\theta$  operations. Since the CPS is implemented via the dispersive coupling, i.e.  $CPS = |g\rangle\langle g| \otimes \hat{I} + |e\rangle\langle e| \otimes (-1)^{\hat{n}}$ , its duration is relatively short ( $\sim \pi/\chi$ ). The single transmon rotations are also typically fast ( $\sim 20$  ns). Therefore, we can suppress the transmon's  $T_1$  and  $T_2$  effects since it now remains in the ground state during the relatively slow BS operations.

## 7.2 eSWAP operation in single photon encoding

In order to see the eSWAP unitary in action, we first use the simplest encoding as an illustration. We initialise Alice and Bob in the four basis states of the  $\{|0\rangle, |1\rangle\}$  encoding and probe the outcomes after the operation using a spectroscopy measurement. In this particular example, we realise a 50:50 beamsplitter in  $\approx 2\ \mu\text{s}$  with every transmon rotations

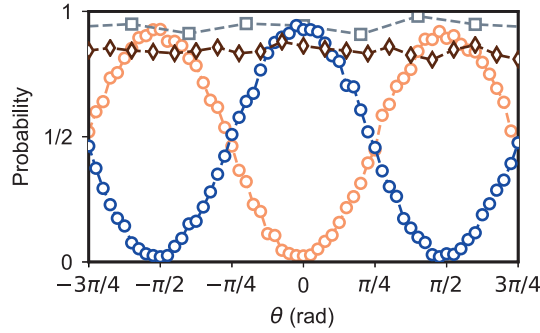


Figure 7.3: **eSWAP in single photon encoding.** The probabilities of measuring each basis state in  $\{|0\rangle, |1\rangle\}$  encoding after eSWAP with a variable control angle,  $\theta$ .  $P_{00}$  (grey square) and  $P_{11}$  (brown diamond) remain unchanged as a function of  $\theta$ . When starting from  $|0\rangle_A|1\rangle_B$ , we observe a periodic oscillation of  $P_{01}$  (blue circle). It is exactly out of phase with  $P_{10}$  (orange circle). They have equal amplitudes at  $\theta = \pi/4$  which corresponds to the entangling gate where a single excitation is equally split between Alice and Bob. All data shown in here are normalised by the selective  $\pi$ -pulse contrast of qA and qB.

taking 24-40 ns and CPS  $\sim 320$  ns each. This results in a total gate time of  $\approx 4 \mu\text{s}$ , roughly 1% of the cavity coherence times and at least an order of magnitude faster than the timescales associated with higher order non-linearities such as self-Kerr and cross-Kerr.

As shown in Fig. 7.3, we implement the experiment as a continuous function of the control angle. This allows us to explore the different gates performed by the eSWAP unitary. Using joint spectroscopy of qA and qB, we measure a near unity probability of being in  $|0\rangle_A|0\rangle_B$  regardless of  $\theta$ . When starting from  $|0\rangle_A|1\rangle_B$ , we observe periodic oscillations of  $P_{01}$  with high contrast while  $P_{10}$  oscillates exactly out of phase. In particular, the result indicates that at  $\theta = \pm\pi/2$ , the excitation is fully transferred from Bob to Alice. Moreover, at  $\theta = \pi/4$ , both probabilities have the same amplitude, indicating an even split of the excitation between the two cavities as a result of the entangling operation. The measurement outcome with the initial state  $|1\rangle_A|0\rangle_B$  is not shown in Fig. 7.3 since it is identical to that of  $|0\rangle_A|1\rangle_B$ , as expected. Another key observation is that  $P_{11}$  remains constant over all  $\theta$  with a slightly diminished contrast compared to  $P_{00}$ . This reduction ( $\sim 5\%$ ) is primarily due to the imperfect preparation of  $|1\rangle_A|1\rangle_B$ , as shown by independent calibrations of the state preparation process. The lack of oscillations in  $P_{11}$  attests to the preservation of the code space under the eSWAP unitary. We can contrast this with the simple beamsplitter

operation, under which the same initial state evolves out of the code space to a superposition of  $|2\rangle_A|0\rangle_B$  and  $|0\rangle_A|2\rangle_B$ . We can characterise the leakage by independently probing the probabilities of occupying Fock state  $|2\rangle$  in Alice and Bob. Here, our measurement shows a constant value of  $P_{20} \approx 2\%$  and  $P_{02} \approx 1\%$  respectively.

This simple measurement provides an intuitive illustration of the behaviour of the system under the eSWAP unitary. Further, it is also a useful calibration procedure to tune up the full sequence. Since the protocol is compatible with any bosonic encodings, the calibrated parameters can be directly applied to more complex code words. It is important to minimise non-idealities from each individual step to avoid compounded errors in the full sequence. Here, let us discuss a few details related to the tune-up process that are crucial to the faithful construction of the operation.

Transmon rotations are the most straightforward to calibrate since it only involves a single two-level system. We use established techniques to tune the precise pulse amplitudes to perform  $\pi/2$  pulses using a pulse train experiment. By repeating the pulse, the effects of small imperfections in the amplitudes can be exaggerated and hence corrected. In practice, we can perform  $\pi/2$  pulses with  $> 99\%$  fidelity using such calibration procedure.

The effective mixing angle of the two beamsplitters are tuned independently by adjusting the pump duration. In this experiment, we aim to perform a robust 50:50 BS. To do so, we adopt a similar strategy as in the pulse train experiment where we repeatedly apply the beamsplitters to amplify the sensitivity to small mis-calibrations in the pump length. With this, we can precisely tune the duration, up to the 4 ns resolution of the FPGA, to perform a balanced beamsplitter with fidelity  $\gtrsim 98\%$ .

CPS can typically be tuned using standard Ramsey revival experiments. However, in the presence of the additional  $X_\theta$  gate separating the two CPS gates and its finite pulse duration, additional care must be taken to ensure a precise  $\pi$  phase is imparted to each photon if the ancilla is excited, regardless of  $\theta$ . The exact CPS times are tuned using the interference of a single photon in a Mach-Zehnder interferometer at different control angles. We initialise the system in  $|0\rangle_A|1\rangle_B$  and implement the eSWAP protocol while sweeping the delay times used to realise the two CPS operations. We measure the probability of both  $P_{10}$

and  $P_{01}$  after the protocol at a  $\theta = 0, \pi/4, \pi/2$  respectively. This provides us with a easy way to fine-tune the CPS gates and impart the appropriate phase to the cavity state with the effects of finite pulse durations taken in account.

### 7.3 Generating a two-mode cat state using eSWAP

Using these calibration tools, we apply the eSWAP unitary to more complex cavity states. In this section, we will revisit the two-mode cat state first introduced in Chapter 4. However, rather than creating it using the qcMAP protocol, we now can generate the highly entangled state using a eSWAP quantum gate with the control angle tuned to  $\pi/4$ . To demonstrate this capability, let us consider an initially separable state  $|\psi\rangle_0 = \frac{1}{\mathcal{N}}(|\alpha\rangle_A - |\alpha\rangle_B)$ , where  $\mathcal{N} = \sqrt{2}\alpha$  is the normalisation constant (omitted in the subsequent description).

With the control angle adjusted to  $\theta = \pi/4$ , we can implement the entangling gate to  $|\psi\rangle_0$  and perform joint Wigner tomography to characterise the output state. Since  $U_{\text{eSWAP}}(\theta = \frac{\pi}{4})$  is simply a coherent superposition of swapping the cavity states or identity, we expect the outcome of the experiment to be:

$$|\psi\rangle = \mathcal{N}(|\alpha\rangle_A - |\alpha\rangle_B + i|-\alpha\rangle_A|\alpha\rangle_B) \quad (7.2)$$

where  $\mathcal{N}$  is the normalisation constant and will be omitted in the subsequent discussions.

This is an entangled state of Alice and Bob but without joint parity, i.e  $\langle \hat{P}_A \hat{P}_B \rangle = 0$ . This is not surprising as the initial state does not have a joint parity either and the operation preserves the joint photon number parity. We can capture the features of this parity-less two-mode cat state by considering the joint Wigner function in selected 2D planes in the 4D phase space it resides in.

With this new experimental flexibilities provided by this multi-ancillae device, we can now measure the joint Wigner without relying on the Y-mon. Rather, we can monitor the joint Wigner function of Alice and Bob individually using their respective transmon ancilla and their independent single shot readout. The joint parity is inferred from the shot-to-shot correlated single Wigner measurements since  $P_{AB}(\beta_1, \beta_2) = P_A(\beta_1, \beta_2)P_B(\beta_1, \beta_2)$ . In prac-

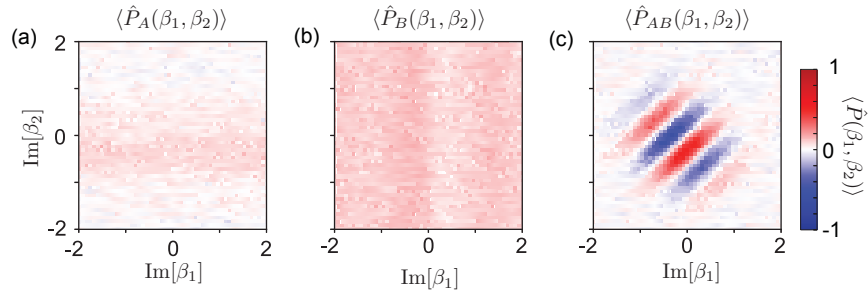


Figure 7.4: **Joint Wigner measurement from correlated single Wigner functions.** (a), (b) The individual averaged Wigner tomography of Alice and Bob in  $\text{Im}[\beta_1]$  -  $\text{Im}[\beta_2]$  plane. They do not exhibit any negativity as the subsystems of an entangled state do not contain any quantum coherence. However, when we correlate the two measurement shot by shot by taking a product of the measured parities at a particular point in phase space, the coherence of the entangled state is recovered.

tice, we perform single-shot displaced parity measurement on Alice and Bob simultaneously and compute the resulting joint displaced parity by multiplying the two outcomes. Just as we discussed in section 4.2, the average single Wigner functions do not contain any quantum coherence since the other subsystem of the entangled state has been traced out as shown in Fig. 7.4 (a) and (b). In contrast, the joint Wigner averaged over all the measurement contains the fringes that indicate the presence of non-classical correlations (Fig. 7.4(c)). This method of measuring the joint Wigner function is in principle more robust than that presented in section 4.2 since we no longer need to manipulate superpositions of the transmons  $|g\rangle$ ,  $|e\rangle$ , and  $|f\rangle$  state to achieve the effectively matched  $\chi$ . This reduces the errors due to imperfect transmon manipulations and imprecise joint parity mapping time. However, by doing two individual measurements, we are now susceptible to the decoherence effects and readout errors of both transmons. In this particular device, the transmon  $T_2$ s are embarrassingly low and rather unstable (5-20  $\mu$ s). As a result, the individual parity contrast of Alice and Bob are each  $\sim 90\%$ . This means that the maximum contrast we are able to obtain in the joint Wigner functions, assuming perfect state preparation, is roughly 80%, which is experimentally verified by the joint Wigner tomography of  $|0\rangle_A|0\rangle_B$ .

Having introduced our method to measure the joint Wigner function of Alice and Bob in this set-up, we now proceed to present the data taken on two plane cuts that contains

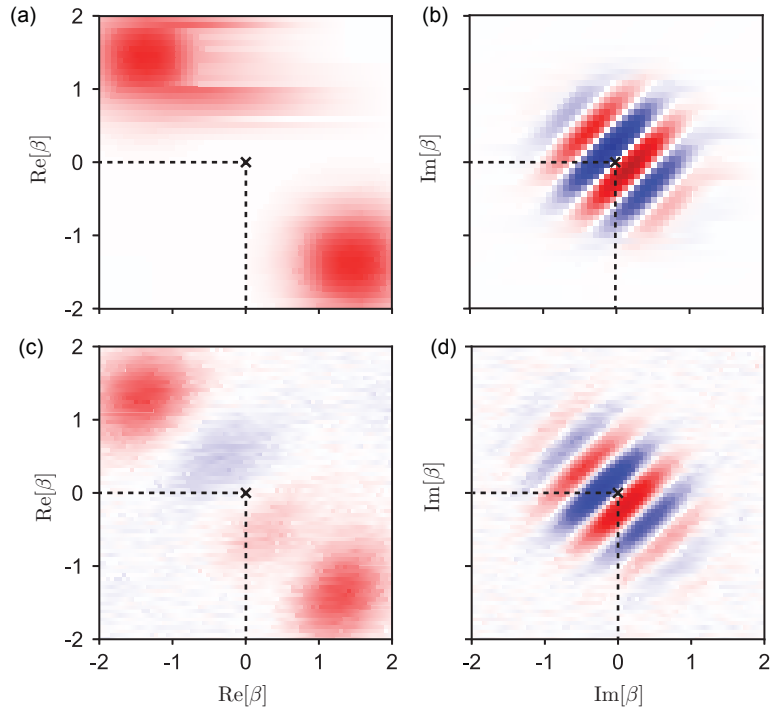


Figure 7.5: **Joint Wigner tomography of a two-mode cat state.** Data are taken along the Re – Re (a) and Im – Im (b) axes of Alice and Bob respectively. Each point corresponds to a displaced joint parity in a four-dimensional phase space. The features in (a) indicates the probability distribution of the two coherent state components in both cavities. The quantum coherence is shown by the interference fringes in (b). The origin in both planes corresponds to the measured joint parity. In this case, the state has zero joint parity.

the main features of this parityless entangled cat state. In Fig. 7.5(a)-(b), we show the calculated ideal Wigners on two selected planes defined by the real (imaginary) axis of Alice and Bob respectively with both the two orthogonal axes fixed at the origin. The measured joint Wigners on the same planes are shown in (c) and (d). They show remarkable qualitative agreement with the ideal state. In the Re-Re plane, we observe two positively-valued Gaussian hyperspheres, at  $\beta = [\sqrt{2}, -\sqrt{2}]$  and  $\beta = [-\sqrt{2}, \sqrt{2}]$ . They correspond to the probability distributions of the two coherent state components of  $|\psi\rangle$ . The origin, which corresponds to the joint parity of Alice and Bob, is very close to zero. It is consistent with the expected outcome as the initial state has  $\langle \hat{P}_A \hat{P}_B \rangle = 0$ . Therefore, the output must remain parity-less since the entangling operation preserves joint parity. In the orthogonal

plane defined by the two imaginary axes, we observe an interference structure with no joint parity. This is in good agreement with the simulated behaviour. The raw data show an overall  $\approx 72\%$  contrast of the ideal Wigner function.

The additional features on the Re-Re plane (Fig. 7.5(c)) can be accounted for by the self-Kerr nonlinearities of Alice and Bob. In the absence of the microwave drives, we have independently measured them to be small ( $\lesssim 4$  kHz) and have negligible effects on the joint Wigner tomography. However, due to the application of strong pump tones during the eSWAP protocol, Kerr effects can be enhanced. This is because the strong drive tones are likely exciting higher order terms in addition to enabling the bilinear coupling that performs the beamsplitters, and result in a larger non-linearity in the cavity. We can verify this by calculating the ideal Wigners with the enhanced Kerr taken into account. Indeed, with Kerr  $\approx 10$  kHz the calculated joint Wigner functions exhibit the same features as the data. Additionally, if the stronger self-Kerr stems from higher order terms from the cosine expansion, the effect must be frequency-dependently. We verify this by moving the two drive frequencies together while maintaining the same effective coupling strength. We have found that indeed, the effects of pump-induced self-Kerr can be further magnified or suppressed depending on the exact frequencies of the two drives.

We compare this with the action of a simple beamsplitter on coherent states, which are semi-classical. The engineered unitary  $\hat{U}_{\text{BS}}$  we presented in section 6.1 is a linear operation. It does not generate any entanglement between Alice and Bob when they are encoded in the coherent basis. This is shown in Fig. 7.6 where we have performed a simple BS operation on the initial state  $|0\rangle_A|\alpha\rangle_B$ , with  $\alpha \approx \sqrt{3.5}$ . The output remains a separable state with no quantum correlations between Alice and Bob. Non-classical states can be created, such as the familiar NOON states, using simple beamsplitters. However, that relies on the quantum nature of the input states, i.e. Fock states, rather than the operation itself. When a cat state,  $|\alpha\rangle \pm |-\alpha\rangle$ , is prepared in Alice or Bob, an entangled state can be generated simply by the action of  $\hat{U}_{\text{BS}}$ . However, this brings the system out of its initial code space to a two-mode cat with  $\alpha' = \alpha/\sqrt{2}$ . Based on Ref. [50], the encoding can be preserved if we combine the beamsplitter operation with a two-photon dissipation process that stabilises the manifold of

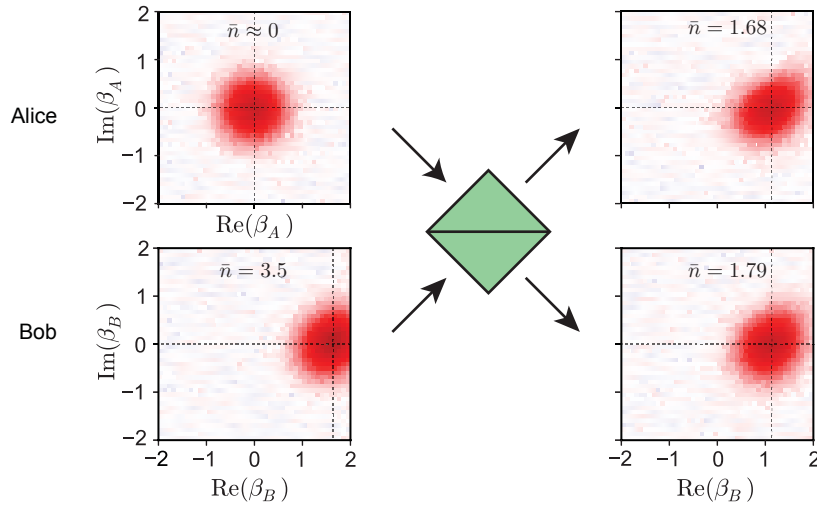


Figure 7.6: **Coherent state under  $U_{BS}$ .** We initialise the system in  $|0\rangle_A|\alpha\rangle_B$ , with  $\alpha \approx \sqrt{3.5}$ . After a simple BS operation, we measure the Wigner function of Alice and Bob independently. The resulting result is a separable state of two smaller coherent states each with amplitude  $\alpha' \approx \alpha/\sqrt{2}$ . This is in stark contrast to the action of the eSWAP gate, which creates an entangled two-mode cat state.

the initial code words [132]. However, this requires additional drives that could introduce other types of imperfections. The eSWAP unitary, on the other hand, only requires the beamsplitter operation and the intrinsic dispersive coupling.

Another way to characterise this entangled state is to consider it as an entangled pair of qubits encoded in the coherent state basis. In this picture, we can probe the full set of two-qubit joint Pauli operations effectively without doing full tomography over the entire 4D phase space. The 16 two-qubit correlators are mapped out directly by performing 16 independent measurements of  $\langle \hat{P}_J(\beta_1, \beta_2) \rangle$  as described in section 4.3.

The measured outcomes for state  $|\psi\rangle$ , created by the universal entangling gate, is shown in Fig. 7.7. It is in excellent agreement with the ideal case with an overall reduction in contrast but no significant spurious correlations. It is important to note that with  $\alpha = \sqrt{2}$ , the two coherent state components are not fully orthogonal. Therefore, the calculated outcomes for the ideal states also contains some non-zero elements which would vanish as we increase the size of the coherent states. This provides a direct fidelity estimation [86] of  $\frac{1}{4}(\langle II \rangle - \langle XY \rangle + \langle YX \rangle + \langle ZZ \rangle) \approx 70\%$  compared to the ideal Bell state. This comfortably

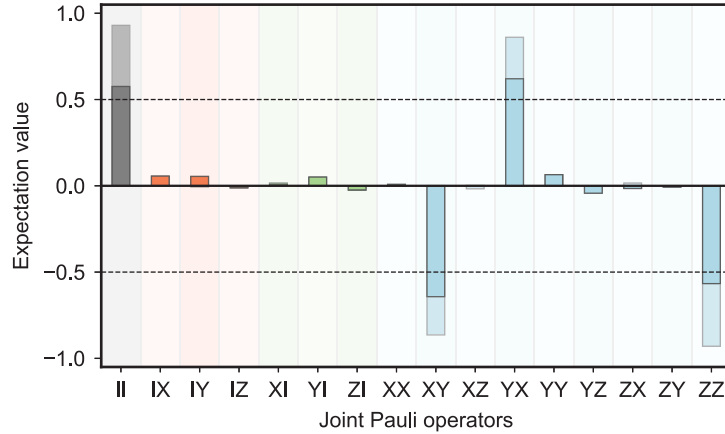


Figure 7.7: **Joint Pauli correlators after  $U_{\text{eSWAP}}(\theta = \frac{\pi}{4})$ .** Tomography of a parityless two-mode cat state generated by the universal entangling operation with  $\alpha = \sqrt{2}$ . The raw data is overlaid on top of simulated outcomes (translucent) from an ideal state with the same excitation. The ideal bars do not fully reach unity due to presence of Kerr nonlinearities in each cavity and the small overlap due to the relatively small value of  $\alpha$ . The measured outcomes show good agreement with prediction except some overall reduction in amplitude due to inefficiencies in the joint Wigner tomography. Despite these non-idealities, the result shows clear indication of entanglement.

surpasses the 50% bound for classical correlations. It is also consistent with the contrast of the joint Wigner measurements, indicating that the reduced contrast is most likely due to the imperfections in the measurement rather than the entangling operation itself.

We also verify that the eSWAP unitary performs as expected at other control angles. While we have the capability to continuously tune the control angle as shown in Fig. 7.3, two of these angles are particularly illustrative:  $\text{eSWAP}(\theta = 0) \equiv \hat{I}$  and  $\text{eSWAP}(\theta = \frac{\pi}{2}) \equiv \text{SWAP}$ . They are tested in the coherent basis using the same joint Wigner measurement as shown in Fig. 7.8. We initialise the system in  $|-\alpha\rangle_{\text{A}}|\alpha\rangle_{\text{B}}$  and perform the same eSWAP protocol at these two chosen control angles. Despite the rather coarse sampling, it is clear that the final states are  $|-\alpha\rangle_{\text{A}}|\alpha\rangle_{\text{B}}$  and  $|\alpha\rangle_{\text{A}}|-\alpha\rangle_{\text{B}}$  respectively with no spurious features, except a small distortion due to Kerr. These results show that the engineered eSWAP unitary indeed performs the identity and SWAP operation at  $\theta = 0, \pi/2$  respectively.

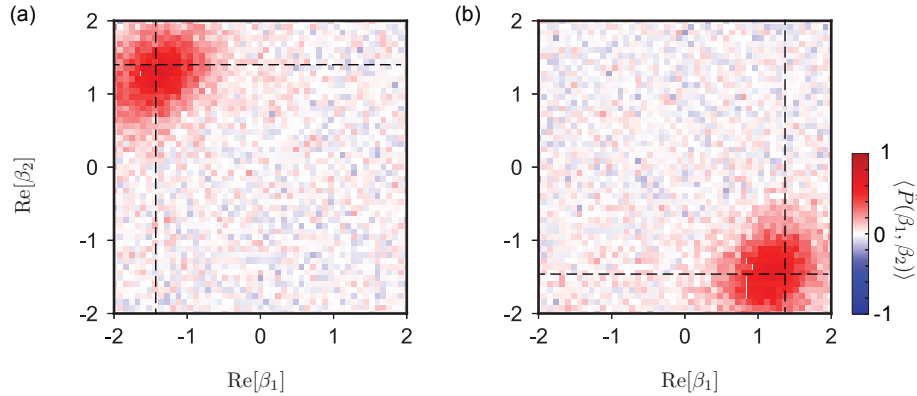


Figure 7.8: **Joint Wigner function after eSWAP unitary** Data taken on the plane defined by the  $\text{Re} - \text{Re}$  axes for an initial state of  $|- \alpha\rangle_{\text{A}}|\alpha\rangle_{\text{B}}$ . (a) The final state after  $\text{eSWAP}(\theta = 0)$ . (b) The final state after  $\text{eSWAP}(\theta = \frac{\pi}{2})$ . The distortion of the blob is again due to self Kerr effect of the cavities.

## 7.4 Discussion

The joint Wigner tomography and the Pauli correlator measurements show conclusively that we have successfully engineered the eSWAP unitary between two microwave cavity modes. Its action on both the Fock and coherent state encoding further shows that this unitary is capable of performing an entangling operation between the two modes irrespective of the code words used. These results are still fairly preliminary and yet, it is indisputable that highly non-classical correlations are present in the final state after the entangling gate. In order to more precisely and quantitatively characterise the performance of the gate, we need to implement full quantum process tomography. This can be done using the same techniques described in section 5.3. The experimental implementation of full process tomography is underway at the time of this writing. We intend to perform it on several different encodings to verify that the operation is truly compatible with different types of bosonic codes.

As we move towards applying this universal entangler between logical qubits encoded in multi-photon states, we must pay more attention to the effects of higher order terms. Our preliminary results indicate that the effective Kerr nonlinearity, and potentially other 6th order terms, tend to increase due to the presence of strong pumps used in the beamsplitter

operation. It would be desirable to explore other possibilities to enable the beamsplitter between two cavities which do not introduce additional higher order effects. For example, a three-wave mixing process through a SNAIL-type device [145] can potentially alleviate this problem. Experimental work is in progress to integrate such devices with 3D cavities in a way that does not limit their intrinsic coherence properties.

The unitary operation implemented in the scope of this work is not yet fault-tolerant: errors in the gate can propagate and degrade the information encoded in the cavities. This is mainly due to the entanglement of the transmon ancilla and the cavity state during the sequence, which makes the system susceptible to both transmon decay and dephasing errors. It can, however, be made fault-tolerant by using multiple levels of the transmon [144] to perform the CPS and  $X_\theta$  operations. This is, of course, more challenging experimentally but with the continual improvements of the coherence times of the devices and the control capabilities of each individual component, such fault-tolerant entangling operations can be realised in the foreseeable future. Combining this gate with active error tracking and error correction will allow us to perform universal quantum computing between two error-protected bosonic qubits [139]. The eSWAP gate is an extremely powerful tool because its action does not depend on the details of the choice of orthogonal basis  $|0\rangle_L$  and  $|1\rangle_L$ . Therefore, it can be used as a robust entangling gate on any single-mode bosonic encoding, such as cat code [146, 50], binomial code [51], GKP code [99], etc.

In summary, the results shown in this chapter are a proof-of-principle demonstration of an universal entangling gate between states stored in two high-Q superconducting cavities. Together with single qubit rotations, it forms a universal set of quantum gates for the cavity-based quantum computing framework. Its potential to be made fault-tolerant and compatibility with bosonic QEC schemes also makes it a crucial ingredient in the future implementation of more complex quantum algorithms on a network of logical qubits.



## Chapter 8

### Conclusion and future directions

It is a truly amazing time to be in the field of quantum computing and quantum information science. With the profound scientific and technological impacts it entails, this subject has become not only the focal point of academic research, but also the interest of tech giants such as Google and IBM. Instead of focusing on the integration of large numbers of two-level systems, our team at Yale have chosen to pursue a more modular architecture where each individual module can be error-corrected. The results shown by N. Ofek and A. Petrenko [49] mark the first time that quantum information has been preserved for a longer time than the coherence of the best physical component through QEC. Furthermore, recent experimental progress in the coherent transfer of multi-photon quantum states, compatible with existing QEC schemes, between two separate modules [54] now allows us to effectively connect distant quantum modules and eventually form a larger quantum network. The experimental work described in this thesis is an integral part of this effort. The results we have highlighted have far-reaching implications in the future design and control of more complex quantum modules. Moreover, the various techniques developed during these experiments, such as joint Wigner tomography and the engineered beamsplitter operation between high-Q modes, are valuable and versatile tools for the ensuing experimental endeavors in superconducting circuits.

In the final chapter of this thesis, I would like to look ahead and highlight some of the exciting new scientific pursuits that are now within reach. I will also briefly discuss my personal take on the key challenges ahead in our efforts of building a robust superconducting quantum computer. I would also like to emphasise that although realising a quantum

---

computer is the ultimate goal of many of the research efforts, we must not forget to revel in the spectacular scientific discoveries we are making along the way.

The design and full characterisation of the first double-cavity system used to create the two-mode cat state (chapter 4) has convincingly demonstrated the potential of such devices where two or more high-Q modes can be jointly manipulated. It has also introduced a viable strategy towards effectively harnessing a larger Hilbert space without sacrificing the favourable coherence characteristics or drastically increasing the error channels. The device has since inspired a variety of other multi-cavity designs, such as the four-cylinder quantum machine, shown in Fig. 8.1, which enabled the recent demonstration of a teleported gate between two logical qubits [55]. In this device, each pair of high-Q cavities are coupled through Y-jos which can be used for both individual and joint cavity manipulations. Using the same design strategies, we can in principle continue to increase the power of these modules by incorporating even more cavities in the system. Such multi-cavity, multi-ancilla systems provide an excellent platform for future experimental explorations in cQED.

Another development showcased in this work is the driven bilinear coupling between two cavities. While the four-wave mixing process through the Josephson junction has long been a staple of cQED experiments, we have demonstrated that it can be used as a robust frequency-converting, bilinear coupling between two high-Q modes in chapter 6. This is a valuable tool for implementing both bosonic interference experiments, as well as engineering new inter-cavity quantum gates. In particular, this type of driven operation only virtually involves the nonlinear element. In other words, the excited levels of the transmon ancilla are not populated during the operation, making the system immune to decoherence mechanisms of the transmon which are typically far less favourable than that of the cavities.

Combining this capability with the multi-cavity modules, we now have a playground for a large variety of interesting experiments. For example, the four-cylinder device where pairs of cavities modes can interact through the driven bilinear coupling will allow us to implement more nested quantum interferometers and simulate the highly non-trivial boson statistics in a generalised HOM experiment [147]. This type of boson sampling problems become quickly intractable for classical machines as we scale up to more modes and more

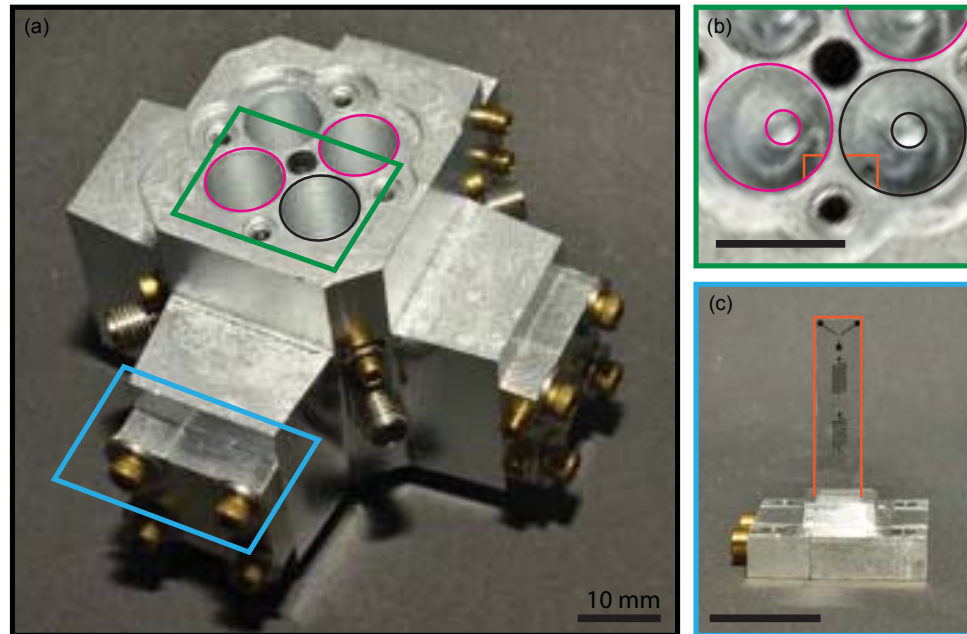


Figure 8.1: **Photograph of a quantum module consisting of 4 high-Q cavities.** (a) The machined Al package contains four coaxial  $\lambda/4$  3D cavities, three of which are used in this work. The cavities that serve as data qubits and bus are outlined in pink and black, respectively. A detailed photograph of the cavities is shown in (b). Two clamps anchor each sapphire chip, one is highlighted in blue and is detailed in (c). The visible connectors are input ports for each cavity; the input/output ports for the transmon and readout resonators are on the underside of the device and thus not visible. (b) Top-down photograph of cavities. We illustrate the three cavities using the same colour scheme in a; the inner circle represents the inner conductor that defines the cavity mode. The orange outline shows the sapphire chip inserted into the device package. Also visible are the antenna pads of the transmon that enable the coupling to each cavity. (c) Photograph of sapphire chip on which the transmon and readout resonators are fabricated. The sapphire chip is outlined in orange and contains several elements: from the top of the figure moving down, the Y-mon, the readout resonator, and the Purcell filter. Figure reproduced from Ref. [55] with permission

excitations. There have been many theoretical studies [138, 137, 148] but experimental realisations remain challenging due to practical challenges such as difficulty in preparing coherent multi-photon quantum states. In cQED systems, we can more easily scale up to several bosonic modes while still maintaining precise quantum control over each of them in this multi-cavity architecture. Facilitated by the large nonlinearity of transmons, we can also efficiently prepare quantum states with larger number of excitations. Therefore, it would be extremely advantageous to realise multi-mode and multi-excitation interference between stationary bosonic modes in cQED architecture.

Additionally, with more cavities and the ability to implement entangling operations between them at our disposal, we can also realise higher-order encoding schemes. One protocol for level-two encoding between logical qubits using a quad-rail scheme has been proposed in Ref. [139], where four logical qubits can be error-corrected and all logical gates between them can be implemented coherently in a fault-tolerant manner. The schematic for realising the proposed scheme using cQED systems is shown in Fig. 8.2. This provides a hardware efficient platform to implement robust logical operations between protected logical qubits.

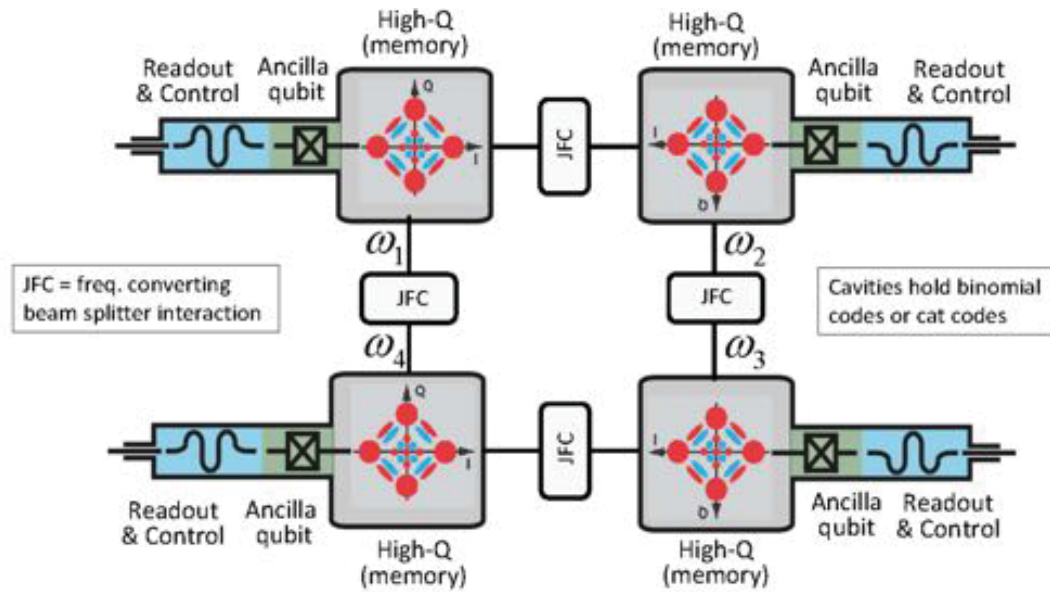


Figure 8.2: **Quad-rail encoding in cQED using a four-cavity architecture.** Logical qubits are encoded in the multiphoton states in each superconducting cavity. The cavities are coupled through some general non-linear elements, which we call the Josephson Frequency Converters (JFC), that can be driven to introduce either three or four wave mixing processes. Each memories mode can have its independent ancilla and readout resonator for the purpose of robust single-cavity manipulations and tomography. Figure reproduced from Liang Jiang's presentation with permission.

While there is no fundamental limit on scaling up to larger number of modes in this type of 3D structures, we fairly quickly run into a number of practical challenges in realising it experimentally. Although the modules, even with several mode cavities incorporated, do not themselves have a particularly large volume, the accompanying filtering and microwave drive lines do take up a significant portion of the available fridge space. Furthermore,

as we introduce more modes in the system, it becomes increasingly crucial to achieve the target design parameters precisely and reliably. These are the challenges that we hope to overcome by developing micro-machined cQED components, each of which is more compact and defined with lithographic precision. Such micro-machined quantum elements are part of the multilayer microwave integrated quantum circuit (MMIQC) architecture developed at Yale. Recent progress on MMIQC has shown that the quality factor of such micro-machined cavities have exceeded  $\sim 10^6$  [149] and can be readily integrated with a standard transmon ancilla [150]. I personally find these developments extremely exciting as this architecture combines the scalability of 2D structures and the coherence properties of 3D systems. With the rapid progress shown in this area in the recent years, it will not be long before we can perform these complex multi-cavity operations on a compact stack of integrated micro-machined resonators.

Another aspect of superconducting circuits that I find immensely exciting is its potential to be integrated with other types of quantum elements in hybrid systems. In particular, the marriage between atoms and spins to superconducting circuits is quickly emerging as a strong candidate for implementing scalable quantum information processing machines [151]. Recent experimental progress has shown that by coupling a spin ensemble to a superconducting resonator, it is now possible to control the relaxation of the spin systems on-demand through Purcell effects [152]. This provides a useful tool for the efficient initialisation and measurement of the spin systems. These types of hybrid devices combine the outstanding coherence properties, scalability, and compactness of the spin system and the controllability of superconducting circuits. I think that such hybrid devices which harness the advantages and strengths of the different systems hold tremendous promise for the exploration of new quantum phenomena and bring about novel technologies for quantum information processing.

Although there are still numerous challenges ahead, the rapid progress in quantum computing in the cQED framework certainly inspires a strong sense of optimism. In less than two decades since the first demonstration of a Rabi oscillation of a Cooper pair box [23], there has been an abundance of incredible developments in superconducting circuits. The

storage time of quantum information in cQED components have increased by near 6 orders of magnitude from ns to ms. Moreover, the infidelities of quantum operations on one or two registers have been pushed to a fraction of a percent over the recent years. We have not only successfully constructed an error-corrected logical qubit but also developed means to implement robust quantum operations between several of them. With the tremendous momentum it has garnered, superconducting circuits are undoubtedly one of most promising systems to ultimately realise a practical quantum computer. I am truly fortunate to be part of this effort during these exciting times.

## List of publications

The results presented in this thesis are based on the following publications:

1. C. Wang, **Y. Y. Gao**, I. M. Pop, U. Vool, C. J. Axline, T. Brecht, R. W. Heeres, L. Frunzio, M. H. Devoret, G. Catelani, L. I. Glazman, R. J. Schoelkopf, “Measurement and Control of Quasiparticle Dynamics in a Superconducting Qubit”, [Nature Communications 5, 5836 \(2014\)](#)
2. C. Wang, **Y. Y. Gao**, P. Reinhold, R. W. Heeres, N. Ofek, K. Chou, C. Axline, M. Reagor, J. Blumoff, K. M. Sliwa, L. Frunzio, S. M. Girvin, L. Jiang, M. Mirrahimi, M. H. Devoret, and R. J. Schoelkopf, “A schrodinger cat living in two boxes”, [Science, vol. 352, no. 6289, pp. 1087-91, \(2016\)](#)
3. S. Rosenblum and **Y. Y. Gao**, P. Reinhold, C. Wang, C. J. Axline, L. Frunzio, S. M. Girvin, Liang Jiang, M. Mirrahimi, M. H. Devoret, R. J. Schoelkopf, “A CNOT gate between multiphoton qubits encoded in two cavities”, [Nature Communications 9, 652 \(2018\)](#)
4. **Y. Y. Gao**, B. J. Lester, Yaxing Zhang, S. Rosenblum, C. Wang, L. Frunzio, Liang Jiang, S. M. Girvin, M. H. Devoret and R. J. Schoelkopf, “Programmable interference between two microwave quantum memories”, [to appear in PRX \(2018\)](#)
5. **Y. Y. Gao** and B. J. Lester, L. Frunzio, Liang Jiang, S. M. Girvin, M. H. Devoret and R. J. Schoelkopf, “A universal entangling operation between two logicals”, [preprint \(2018\)](#)

## References

- [1] R. P. Feynman, “Simulating physics with computers,” *International Journal of Theoretical Physics*, vol. 21, no. 6-7, pp. 467–488, 1982.
- [2] D. Deutsch and R. Jozsa, “Rapid solution of problems by quantum computation,” *Proceedings of the Royal Society A: Mathematical, Physical and Engineering Sciences*, vol. 439, no. 1907, pp. 553–558, 1992.
- [3] R. Cleve, A. Ekert, C. Macchiavello, and M. Mosca, “Quantum algorithms revisited,” *Proceedings of the Royal Society A: Mathematical, Physical and Engineering Sciences*, vol. 454, no. 1969, pp. 339–354, 1998.
- [4] M. H. Devoret and R. J. Schoelkopf, “Superconducting circuits for quantum information: an outlook,” *Science*, vol. 339, no. 6124, pp. 1169–74, 2013.
- [5] M. A. Nielsen and I. L. Chuang, *Quantum Computation and Quantum Information*. Cambridge University Press, 2001.
- [6] A. Blais, R.-S. Huang, A. Wallraff, S. M. Girvin, and R. J. Schoelkopf, “Cavity quantum electrodynamics for superconducting electrical circuits: An architecture for quantum computation,” *Physical Review A*, vol. 69, no. 6, 2004.
- [7] A. Wallraff, D. I. Schuster, A. Blais, L. Frunzio, R. Huang, J. Majer, S. Kumar, S. M. Girvin, and R. J. Schoelkopf, “Strong coupling of a single photon to a superconducting qubit using circuit quantum electrodynamics,” *Nature*, vol. 431, no. 7005, pp. 162–7, 2004.

- 
- [8] A. Blais, J. Gambetta, A. Wallraff, D. I. Schuster, S. M. Girvin, M. H. Devoret, and R. J. Schoelkopf, “Quantum-information processing with circuit quantum electrodynamics,” *Physical Review A*, vol. 75, no. 3, 2007.
- [9] D. Schuster, *Circuit Quantum Electrodynamics*. Ph.D Thesis, Yale University, 2007.
- [10] L. V. Bishop, *Circuit Quantum Electrodynamics*. Ph.D Thesis, Yale University, 2010.
- [11] S. Girvin, *Circuit QED: Superconducting Qubits Coupled to Microwave Photons*. Oxford University Press, 2014.
- [12] H. Paik, D. I. Schuster, L. S. Bishop, G. Kirchmair, G. Catelani, A. P. Sears, B. R. Johnson, M. J. Reagor, L. Frunzio, L. I. Glazman, S. M. Girvin, M. H. Devoret, and R. J. Schoelkopf, “Observation of high coherence in josephson junction qubits measured in a three-dimensional circuit qed architecture,” *Phys Rev Lett*, vol. 107, no. 24, p. 240501, 2011.
- [13] D. I. Schuster, A. A. Houck, J. A. Schreier, A. Wallraff, J. M. Gambetta, A. Blais, L. Frunzio, J. Majer, B. Johnson, M. H. Devoret, S. M. Girvin, and R. J. Schoelkopf, “Resolving photon number states in a superconducting circuit,” *Nature*, vol. 445, no. 7127, pp. 515–8, 2007.
- [14] A. Megrant, C. Neill, R. Barends, B. Chiaro, Y. Chen, L. Feigl, J. Kelly, E. Lucero, M. Mariantoni, P. J. J. O’Malley, D. Sank, A. Vainsencher, J. Wenner, T. C. White, Y. Yin, J. Zhao, C. J. Palmström, J. M. Martinis, and A. N. Cleland, “Planar superconducting resonators with internal quality factors above one million,” *Applied Physics Letters*, vol. 100, no. 11, p. 113510, 2012.
- [15] M. Reagor, W. Pfaff, C. Axline, R. W. Heeres, N. Ofek, K. Sliwa, E. Holland, C. Wang, J. Blumoff, K. Chou, M. J. Hatridge, L. Frunzio, M. H. Devoret, L. Jiang, and R. J. Schoelkopf, “Quantum memory with millisecond coherence in circuit qed,” *Physical Review B*, vol. 94, no. 1, 2016.

- 
- [16] B. D. Josephson, "Possible new effects in superconductive tunnelling," *Physics Letters*, vol. 1, no. 7, pp. 251–253, 1962.
- [17] B. D. Josephson, "The discovery of tunneling supercurrents," *Science*, vol. 184, no. 4136, pp. 527–30, 1974.
- [18] J. E. Mooij, "Josephson persistent-current qubit," *Science*, vol. 285, no. 5430, pp. 1036–1039, 1999.
- [19] J. R. Friedman, V. V. Patel, W. Chen, S. K. Tolpygo, and J. E. Lukens, "Quantum superposition of distinct macroscopic states," *Nature*, vol. 406, no. 6791, pp. 43–6, 2000.
- [20] I. Chiorescu, Y. Nakamura, C. J. Harmans, and J. E. Mooij, "Coherent quantum dynamics of a superconducting flux qubit," *Science*, vol. 299, no. 5614, pp. 1869–71, 2003.
- [21] Y. Yu, S. Han, X. Chu, S. I. Chu, and Z. Wang, "Coherent temporal oscillations of macroscopic quantum states in a josephson junction," *Science*, vol. 296, no. 5569, pp. 889–92, 2002.
- [22] J. M. Martinis, S. Nam, J. Aumentado, and C. Urbina, "Rabi oscillations in a large josephson-junction qubit," *Phys Rev Lett*, vol. 89, no. 11, p. 117901, 2002.
- [23] Y. Nakamura, Y. A. Pashkin, and J. S. Tsai, "Coherent control of macroscopic quantum states in a single-cooper-pair box," *Nature*, vol. 398, no. 6730, pp. 786–788, 1999.
- [24] K. W. Lehnert, K. Bladh, L. F. Spietz, D. Gunnarsson, D. I. Schuster, P. Delsing, and R. J. Schoelkopf, "Measurement of the excited-state lifetime of a microelectronic circuit," *Phys Rev Lett*, vol. 90, no. 2, p. 027002, 2003.
- [25] L. Dicarlo, M. D. Reed, L. Sun, B. R. Johnson, J. M. Chow, J. M. Gambetta, L. Frunzio, S. M. Girvin, M. H. Devoret, and R. J. Schoelkopf, "Preparation and measurement of three-qubit entanglement in a superconducting circuit," *Nature*, vol. 467, no. 7315, pp. 574–8, 2010.

- 
- [26] J. Koch, T. M. Yu, J. Gambetta, A. A. Houck, D. I. Schuster, J. Majer, A. Blais, M. H. Devoret, S. M. Girvin, and R. J. Schoelkopf, “Charge-insensitive qubit design derived from the cooper pair box,” *Physical Review A*, vol. 76, no. 4, 2007.
- [27] M. H. Devoret, *Quantum fluctuations (Les Houches session LXIII)*. Elsevier, New York, p351-386, 1997.
- [28] M. Reed, *Entanglement and Quantum Error Correction with Superconducting Qubits*. Ph.D Thesis, Yale University, 2013.
- [29] S. Haroche and J.-M. Raimond, *Exploring the Quantum: Atoms, Cavities, and Photons*. Oxford Graduate Texts, 2006.
- [30] B. R. Johnson, M. D. Reed, A. A. Houck, D. I. Schuster, L. S. Bishop, E. Ginossar, J. M. Gambetta, L. DiCarlo, L. Frunzio, S. M. Girvin, and R. J. Schoelkopf, “Quantum non-demolition detection of single microwave photons in a circuit,” *Nature Physics*, vol. 6, no. 9, pp. 663–667, 2010.
- [31] A. Kamal, A. Marblestone, and M. Devoret, “Signal-to-pump back action and self-oscillation in double-pump josephson parametric amplifier,” *Physical Review B*, vol. 79, no. 18, 2009.
- [32] N. Bergeal, F. Schackert, M. Metcalfe, R. Vijay, V. E. Manucharyan, L. Frunzio, D. E. Prober, R. J. Schoelkopf, S. M. Girvin, and M. H. Devoret, “Phase-preserving amplification near the quantum limit with a josephson ring modulator,” *Nature*, vol. 465, no. 7294, pp. 64–8, 2010.
- [33] L. G. Lutterbach and L. Davidovich, “Method for direct measurement of the wigner function in cavity qed and ion traps,” *Physical Review Letters*, vol. 78, no. 13, pp. 2547–2550, 1997.
- [34] S. Haroche and J.-M. Raimond, “Exploring the quantum: Atoms, cavities, and photons,” *Oxford Graduate Texts*, 2006.

- [35] G. Kirchmair, B. Vlastakis, Z. Leghtas, S. E. Nigg, H. Paik, E. Ginossar, M. Mirrahimi, L. Frunzio, S. M. Girvin, and R. J. Schoelkopf, “Observation of quantum state collapse and revival due to the single-photon kerr effect,” *Nature*, vol. 495, no. 7440, pp. 205–9, 2013.
- [36] R. W. Heeres, P. Reinhold, N. Ofek, L. Frunzio, L. Jiang, M. H. Devoret, and R. J. Schoelkopf, “Implementing a universal gate set on a logical qubit encoded in an oscillator,” *Nat Commun*, vol. 8, no. 1, p. 94, 2017.
- [37] N. Khaneja, T. Reiss, C. Kehlet, T. Schulte-Herbruggen, and S. J. Glaser, “Optimal control of coupled spin dynamics: design of nmr pulse sequences by gradient ascent algorithms,” *J Magn Reson*, vol. 172, no. 2, pp. 296–305, 2005.
- [38] C. Axline, M. Reagor, R. Heeres, P. Reinhold, C. Wang, K. Shain, W. Pfaff, Y. Chu, L. Frunzio, and R. J. Schoelkopf, “An architecture for integrating planar and 3d cqed devices,” *Applied Physics Letters*, vol. 109, no. 4, p. 042601, 2016.
- [39] A. D. Corcoles, E. Magesan, S. J. Srinivasan, A. W. Cross, M. Steffen, J. M. Gambetta, and J. M. Chow, “Demonstration of a quantum error detection code using a square lattice of four superconducting qubits,” *Nat Commun*, vol. 6, p. 6979, 2015.
- [40] J. Kelly, R. Barends, A. G. Fowler, A. Megrant, E. Jeffrey, T. C. White, D. Sank, J. Y. Mutus, B. Campbell, Y. Chen, Z. Chen, B. Chiaro, A. Dunsworth, I. C. Hoi, C. Neill, P. J. O’Malley, C. Quintana, P. Roushan, A. Vainsencher, J. Wenner, A. N. Cleland, and J. M. Martinis, “State preservation by repetitive error detection in a superconducting quantum circuit,” *Nature*, vol. 519, no. 7541, pp. 66–9, 2015.
- [41] M. D. Reed, L. DiCarlo, S. E. Nigg, L. Sun, L. Frunzio, S. M. Girvin, and R. J. Schoelkopf, “Realization of three-qubit quantum error correction with superconducting circuits,” *Nature*, vol. 482, no. 7385, pp. 382–5, 2012.
- [42] D. Riste, S. Poletto, M. Z. Huang, A. Bruno, V. Vesterinen, O. P. Saira, and L. DiCarlo, “Detecting bit-flip errors in a logical qubit using stabilizer measurements,” *Nat Commun*, vol. 6, p. 6983, 2015.

- 
- [43] D. G. Cory, M. D. Price, W. Maas, E. Knill, R. Laflamme, W. H. Zurek, T. F. Havel, and S. S. Somaroo, “Experimental quantum error correction,” *Physical Review Letters*, vol. 81, no. 10, pp. 2152–2155, 1998.
- [44] O. Moussa, J. Baugh, C. A. Ryan, and R. Laflamme, “Demonstration of sufficient control for two rounds of quantum error correction in a solid state ensemble quantum information processor,” *Phys Rev Lett*, vol. 107, no. 16, p. 160501, 2011.
- [45] J. Cramer, N. Kalb, M. A. Rol, B. Hensen, M. S. Blok, M. Markham, D. J. Twitchen, R. Hanson, and T. H. Taminiau, “Repeated quantum error correction on a continuously encoded qubit by real-time feedback,” *Nat Commun*, vol. 7, p. 11526, 2016.
- [46] G. Waldherr, Y. Wang, S. Zaiser, M. Jamali, T. Schulte-Herbruggen, H. Abe, T. Ohshima, J. Isoya, J. F. Du, P. Neumann, and J. Wrachtrup, “Quantum error correction in a solid-state hybrid spin register,” *Nature*, vol. 506, no. 7487, pp. 204–7, 2014.
- [47] T. Aoki, G. Takahashi, T. Kajiya, J.-i. Yoshikawa, S. L. Braunstein, P. van Loock, and A. Furusawa, “Quantum error correction beyond qubits,” *Nature Physics*, vol. 5, no. 8, pp. 541–546, 2009.
- [48] T. B. Pittman, B. C. Jacobs, and J. D. Franson, “Demonstration of quantum error correction using linear optics,” *Physical Review A*, vol. 71, no. 5, 2005.
- [49] N. Ofek, A. Petrenko, R. Heeres, P. Reinhold, Z. Leghtas, B. Vlastakis, Y. Liu, L. Frunzio, S. M. Girvin, L. Jiang, M. Mirrahimi, M. H. Devoret, and R. J. Schoelkopf, “Extending the lifetime of a quantum bit with error correction in superconducting circuits,” *Nature*, vol. 536, no. 7617, pp. 441–5, 2016.
- [50] M. Mirrahimi, Z. Leghtas, V. V. Albert, S. Touzard, R. J. Schoelkopf, L. Jiang, and M. H. Devoret, “Dynamically protected cat-qubits: a new paradigm for universal quantum computation,” *New Journal of Physics*, vol. 16, no. 4, p. 045014, 2014.

- 
- [51] M. H. Michael, M. Silveri, R. Brierley, V. V. Albert, J. Salmilehto, L. Jiang, and S. Girvin, “New class of quantum error-correcting codes for a bosonic mode,” *Physical Review X*, vol. 6, no. 3, 2016.
- [52] C. Shen, K. Noh, V. V. Albert, S. Krastanov, M. H. Devoret, R. J. Schoelkopf, S. M. Girvin, and L. Jiang, “Quantum channel construction with circuit quantum electrodynamics,” *Physical Review B*, vol. 95, no. 13, 2017.
- [53] S. Touzard, A. Grimm, Z. Leghtas, S. Mundhaba, P. Reinhold, R. Heeres, C. J. Axline, Reagor.M, K. Chou, J. Blumoff, K. Sliwa, S. Shankar, L. Frunzio, R. J. Schoelkopf, M. Mirrahimi, and M. H. Devoret, “Coherent oscillations inside a quantum manifold stabilized by dissipation,” *arXiv:1705.02401*, 2018.
- [54] C. J. Axline, L. Burkhardt, W. Pfaff, M. Zhang, K. C. Chou, P. Campagne-Ibarcq, P. Reinhold, L. Frunzio, S. M. Girvin, L. Jiang, M. Devoret, and R. J. Schoelkopf, “Deterministic remote entanglement of superconducting circuits through microwave two-photon transitions,” *arXiv:1712.05854*, 2018.
- [55] K. C. Chou, J. Z. Blumoff, C. Wang, P. Reinhold, C. J. Axline, Y. Y. Gao, L. Frunzio, M. Devoret, L. Jiang, and R. J. Schoelkopf, “Deterministic teleportation of a quantum gate between two logical qubits,” *arXiv:1801.05283*, 2018.
- [56] S. Haroche, “Nobel lecture: Controlling photons in a box and exploring the quantum to classical boundary,” *Reviews of Modern Physics*, vol. 85, no. 3, pp. 1083–1102, 2013.
- [57] D. J. Wineland, “Nobel lecture: Superposition, entanglement, and raising schrödinger’s cat,” *Reviews of Modern Physics*, vol. 85, no. 3, pp. 1103–1114, 2013.
- [58] I. L. Chuang and M. A. Nielsen, “Prescription for experimental determination of the dynamics of a quantum black box,” *Journal of Modern Optics*, vol. 44, no. 11-12, pp. 2455–2467, 1997.

- [59] M. Reagor, H. Paik, G. Catelani, L. Sun, C. Axline, E. Holland, I. M. Pop, N. A. Masluk, T. Brecht, L. Frunzio, M. H. Devoret, L. Glazman, and R. J. Schoelkopf, "Reaching 10 $\mu$ s single photon lifetimes for superconducting aluminum cavities," *Applied Physics Letters*, vol. 102, no. 19, p. 192604, 2013.
- [60] C. Wang, Y. Y. Gao, I. M. Pop, U. Vool, C. Axline, T. Brecht, R. W. Heeres, L. Frunzio, M. H. Devoret, G. Catelani, L. I. Glazman, and R. J. Schoelkopf, "Measurement and control of quasiparticle dynamics in a superconducting qubit," *Nat Commun*, vol. 5, p. 5836, 2014.
- [61] C. Wang, C. Axline, Y. Y. Gao, T. Brecht, Y. Chu, L. Frunzio, M. H. Devoret, and R. J. Schoelkopf, "Surface participation and dielectric loss in superconducting qubits," *Applied Physics Letters*, vol. 107, no. 16, p. 162601, 2015.
- [62] S. E. Nigg, H. Paik, B. Vlastakis, G. Kirchmair, S. Shankar, L. Frunzio, M. H. Devoret, R. J. Schoelkopf, and S. M. Girvin, "Black-box superconducting circuit quantization," *Phys Rev Lett*, vol. 108, no. 24, p. 240502, 2012.
- [63] B. Vlastakis, G. Kirchmair, Z. Leghtas, S. E. Nigg, L. Frunzio, S. M. Girvin, M. Mirrahimi, M. H. Devoret, and R. J. Schoelkopf, "Deterministically encoding quantum information using 100-photon schrodinger cat states," *Science*, vol. 342, no. 6158, pp. 607–10, 2013.
- [64] R. W. Heeres, B. Vlastakis, E. Holland, S. Krastanov, V. V. Albert, L. Frunzio, L. Jiang, and R. J. Schoelkopf, "Cavity state manipulation using photon-number selective phase gates," *Phys Rev Lett*, vol. 115, no. 13, p. 137002, 2015.
- [65] A. Ourjoumtsev, H. Jeong, R. Tualle-Brouri, and P. Grangier, "Generation of optical 'schrodinger cats' from photon number states," *Nature*, vol. 448, no. 7155, pp. 784–6, 2007.
- [66] M. Brune, E. Hagley, J. Dreyer, X. Maitre, A. Maali, C. Wunderlich, J. M. Raimond, and S. Haroche, "Observing the progressive decoherence of the "meter" in a quantum measurement," *Phys Rev Lett*, vol. 77, no. 24, pp. 4887–4890, 1996.

- 
- [67] J. P. Dowling and G. J. Milburn, “Quantum technology: the second quantum revolution,” *Philos Trans A Math Phys Eng Sci*, vol. 361, no. 1809, pp. 1655–74, 2003.
- [68] Z. Leghtas, G. Kirchmair, B. Vlastakis, M. H. Devoret, R. J. Schoelkopf, and M. Mirrahimi, “Deterministic protocol for mapping a qubit to coherent state superpositions in a cavity,” *Physical Review A*, vol. 87, no. 4, 2013.
- [69] A. Ourjoumtsev, F. Ferreyrol, R. Tualle-Brouri, and P. Grangier, “Preparation of non-local superpositions of quasi-classical light states,” *Nature Physics*, vol. 5, no. 3, pp. 189–192, 2009.
- [70] B. C. Sanders, “Review of entangled coherent states,” *Journal of Physics A: Mathematical and Theoretical*, vol. 45, no. 24, p. 244002, 2012.
- [71] P. Bertet, A. Auffeves, P. Maioli, S. Osnaghi, T. Meunier, M. Brune, J. M. Raimond, and S. Haroche, “Direct measurement of the wigner function of a one-photon fock state in a cavity,” *Physical Review Letters*, vol. 89, no. 20, 2002.
- [72] S. Deleglise, I. Dotsenko, C. Sayrin, J. Bernu, M. Brune, J. M. Raimond, and S. Haroche, “Reconstruction of non-classical cavity field states with snapshots of their decoherence,” *Nature*, vol. 455, no. 7212, pp. 510–4, 2008.
- [73] C. Schmid, N. Kiesel, W. Wieczorek, H. Weinfurter, F. Mintert, and A. Buchleitner, “Experimental direct observation of mixed state entanglement,” *Phys Rev Lett*, vol. 101, no. 26, p. 260505, 2008.
- [74] L. Sun, A. Petrenko, Z. Leghtas, B. Vlastakis, G. Kirchmair, K. M. Sliwa, A. Narla, M. Hatridge, S. Shankar, J. Blumoff, L. Frunzio, M. Mirrahimi, M. H. Devoret, and R. J. Schoelkopf, “Tracking photon jumps with repeated quantum non-demolition parity measurements,” *Nature*, vol. 511, no. 7510, pp. 444–8, 2014.
- [75] P. Milman, A. Auffeves, F. Yamaguchi, M. Brune, J. M. Raimond, and S. Haroche, “A proposal to test bell’s inequalities with mesoscopic non-local states in cavity qed,” *The European Physical Journal D*, vol. 32, no. 2, pp. 233–239, 2004.

- 
- [76] Z. Y. Ou, S. F. Pereira, H. J. Kimble, and K. C. Peng, “Realization of the einstein-podolsky-rosen paradox for continuous variables,” *Phys Rev Lett*, vol. 68, no. 25, pp. 3663–3666, 1992.
- [77] B. Julsgaard, A. Kozhekin, and E. S. Polzik, “Experimental long-lived entanglement of two macroscopic objects,” *Nature*, vol. 413, no. 6854, pp. 400–3, 2001.
- [78] C. Eichler, D. Bozyigit, C. Lang, M. Baur, L. Steffen, J. M. Fink, S. Filipp, and A. Wallraff, “Observation of two-mode squeezing in the microwave frequency domain,” *Phys Rev Lett*, vol. 107, no. 11, p. 113601, 2011.
- [79] E. Flurin, N. Roch, F. Mallet, M. H. Devoret, and B. Huard, “Generating entangled microwave radiation over two transmission lines,” *Phys Rev Lett*, vol. 109, no. 18, p. 183901, 2012.
- [80] I. Afek, O. Ambar, and Y. Silberberg, “High-noon states by mixing quantum and classical light,” *Science*, vol. 328, no. 5980, pp. 879–81, 2010.
- [81] H. Wang, M. Mariani, R. C. Bialczak, M. Lenander, E. Lucero, M. Neeley, A. D. O’Connell, D. Sank, M. Weides, J. Wenner, T. Yamamoto, Y. Yin, J. Zhao, J. M. Martinis, and A. N. Cleland, “Deterministic entanglement of photons in two superconducting microwave resonators,” *Phys Rev Lett*, vol. 106, no. 6, p. 060401, 2011.
- [82] T. Monz, P. Schindler, J. T. Barreiro, M. Chwalla, D. Nigg, W. A. Coish, M. Harlander, W. Hansel, M. Hennrich, and R. Blatt, “14-qubit entanglement: creation and coherence,” *Phys Rev Lett*, vol. 106, no. 13, p. 130506, 2011.
- [83] P. T. Cochrane, G. J. Milburn, and W. J. Munro, “Macroscopically distinct quantum-superposition states as a bosonic code for amplitude damping,” *Physical Review A*, vol. 59, no. 4, pp. 2631–2634, 1999.
- [84] B. Vlastakis, A. Petrenko, N. Ofek, L. Sun, Z. Leghtas, K. Sliwa, Y. Liu, M. Hatridge, J. Blumoff, L. Frunzio, M. Mirrahimi, L. Jiang, M. H. Devoret, and R. J. Schoelkopf,

- “Characterizing entanglement of an artificial atom and a cavity cat state with bell’s inequality,” *Nat Commun*, vol. 6, p. 8970, 2015.
- [85] M. P. da Silva, O. Landon-Cardinal, and D. Poulin, “Practical characterization of quantum devices without tomography,” *Phys Rev Lett*, vol. 107, no. 21, p. 210404, 2011.
- [86] S. T. Flammia and Y. K. Liu, “Direct fidelity estimation from few pauli measurements,” *Phys Rev Lett*, vol. 106, no. 23, p. 230501, 2011.
- [87] K. Banaszek and K. Wodkiewicz, “Testing quantum nonlocality in phase space,” *Physical Review Letters*, vol. 82, no. 10, pp. 2009–2013, 1999.
- [88] R. W. Andrews, A. P. Reed, K. Cicak, J. D. Teufel, and K. W. Lehnert, “Quantum-enabled temporal and spectral mode conversion of microwave signals,” *Nat Commun*, vol. 6, p. 10021, 2015.
- [89] U. Leonhardt, “Measuring the quantum state of light,” *Cambridge University Press*, 1997.
- [90] F. Motzoi, J. M. Gambetta, P. Rebentrost, and F. K. Wilhelm, “Simple pulses for elimination of leakage in weakly nonlinear qubits,” *Phys Rev Lett*, vol. 103, no. 11, p. 110501, 2009.
- [91] J. Joo, W. J. Munro, and T. P. Spiller, “Quantum metrology with entangled coherent states,” *Phys Rev Lett*, vol. 107, no. 8, p. 083601, 2011.
- [92] S. van Enk and O. Hirota, “Entangled coherent states: Teleportation and decoherence,” *Physical Review A*, vol. 64, no. 2, 2001.
- [93] A. Roy, L. Jiang, A. D. Stone, and M. Devoret, “Remote entanglement by coherent multiplication of concurrent quantum signals,” *Phys Rev Lett*, vol. 115, no. 15, p. 150503, 2015.
- [94] P. W. Shor, “Scheme for reducing decoherence in quantum computer memory,” *Physical Review A*, vol. 52, no. 4, pp. R2493–R2496, 1995.

- 
- [95] A. M. Steane, “Error correcting codes in quantum theory,” *Phys Rev Lett*, vol. 77, no. 5, pp. 793–797, 1996.
- [96] J. Chiaverini, D. Leibfried, T. Schaetz, M. D. Barrett, R. B. Blakestad, J. Britton, W. M. Itano, J. D. Jost, E. Knill, C. Langer, R. Ozeri, and D. J. Wineland, “Realization of quantum error correction,” *Nature*, vol. 432, no. 7017, pp. 602–5, 2004.
- [97] D. Nigg, M. Muller, E. A. Martinez, P. Schindler, M. Hennrich, T. Monz, M. A. Martin-Delgado, and R. Blatt, “Quantum computations on a topologically encoded qubit,” *Science*, vol. 345, no. 6194, pp. 302–5, 2014.
- [98] T. Monz, K. Kim, A. S. Villar, P. Schindler, M. Chwalla, M. Riebe, C. F. Roos, H. Haffner, W. Hansel, M. Hennrich, and R. Blatt, “Realization of universal ion-trap quantum computation with decoherence-free qubits,” *Phys Rev Lett*, vol. 103, no. 20, p. 200503, 2009.
- [99] D. Gottesman, A. Kitaev, and J. Preskill, “Encoding a qubit in an oscillator,” *Physical Review A*, vol. 64, no. 1, 2001.
- [100] C. Wang, Y. Y. Gao, P. Reinhold, R. W. Heeres, N. Ofek, K. Chou, C. Axline, M. Reagor, J. Blumoff, K. M. Sliwa, L. Frunzio, S. M. Girvin, L. Jiang, M. Mirrahimi, M. H. Devoret, and R. J. Schoelkopf, “A schrodinger cat living in two boxes,” *Science*, vol. 352, no. 6289, pp. 1087–91, 2016.
- [101] J. Majer, J. M. Chow, J. M. Gambetta, J. Koch, B. R. Johnson, J. A. Schreier, L. Frunzio, D. I. Schuster, A. A. Houck, A. Wallraff, A. Blais, M. H. Devoret, S. M. Girvin, and R. J. Schoelkopf, “Coupling superconducting qubits via a cavity bus,” *Nature*, vol. 449, no. 7161, pp. 443–7, 2007.
- [102] P. J. Leek, S. Filipp, P. Maurer, M. Baur, R. Bianchetti, J. M. Fink, M. GÃ¼ppl, L. Steffen, and A. Wallraff, “Using sideband transitions for two-qubit operations in superconducting circuits,” *Physical Review B*, vol. 79, no. 18, 2009.

- 
- [103] S. Zeytinoğlu, M. Pechal, S. Berger, A. A. Abdumalikov, A. Wallraff, and S. Filipp, “Microwave-induced amplitude- and phase-tunable qubit-resonator coupling in circuit quantum electrodynamics,” *Physical Review A*, vol. 91, no. 4, 2015.
- [104] M. Pechal, L. Huthmacher, C. Eichler, S. Zeytinoğlu, A. Abdumalikov, S. Berger, A. Wallraff, and S. Filipp, “Microwave-controlled generation of shaped single photons in circuit quantum electrodynamics,” *Physical Review X*, vol. 4, no. 4, 2014.
- [105] S. Gasparinetti, S. Berger, A. A. Abdumalikov, M. Pechal, S. Filipp, and A. J. Wallraff, “Measurement of a vacuum-induced geometric phase,” *Sci Adv*, vol. 2, no. 5, p. e1501732, 2016.
- [106] B. Hacker, S. Welte, G. Rempe, and S. Ritter, “A photon-photon quantum gate based on a single atom in an optical resonator,” *Nature*, vol. 536, no. 7615, pp. 193–6, 2016.
- [107] S. Krastanov, V. V. Albert, C. Shen, C.-L. Zou, R. W. Heeres, B. Vlastakis, R. J. Schoelkopf, and L. Jiang, “Universal control of an oscillator with dispersive coupling to a qubit,” *Physical Review A*, vol. 92, no. 4, 2015.
- [108] W. K. Wootters, “Entanglement of formation of an arbitrary state of two qubits,” *Physical Review Letters*, vol. 80, no. 10, pp. 2245–2248, 1998.
- [109] E. Magesan, J. M. Gambetta, B. R. Johnson, C. A. Ryan, J. M. Chow, S. T. Merkel, M. P. da Silva, G. A. Keefe, M. B. Rothwell, T. A. Ohki, M. B. Ketchen, and M. Steffen, “Efficient measurement of quantum gate error by interleaved randomized benchmarking,” *Phys Rev Lett*, vol. 109, no. 8, p. 080505, 2012.
- [110] N. H. Nickerson, Y. Li, and S. C. Benjamin, “Topological quantum computing with a very noisy network and local error rates approaching one percent,” *Nat Commun*, vol. 4, p. 1756, 2013.
- [111] R. Barends, J. Kelly, A. Megrant, A. Veitia, D. Sank, E. Jeffrey, T. C. White, J. Mutus, A. G. Fowler, B. Campbell, Y. Chen, Z. Chen, B. Chiaro, A. Dunsworth, C. Neill, P. O’Malley, P. Roushan, A. Vainsencher, J. Wenner, A. N. Korotkov, A. N. Cleland,

- and J. M. Martinis, “Superconducting quantum circuits at the surface code threshold for fault tolerance,” *Nature*, vol. 508, no. 7497, pp. 500–3, 2014.
- [112] L. DiCarlo, J. M. Chow, J. M. Gambetta, L. S. Bishop, B. R. Johnson, D. I. Schuster, J. Majer, A. Blais, L. Frunzio, S. M. Girvin, and R. J. Schoelkopf, “Demonstration of two-qubit algorithms with a superconducting quantum processor,” *Nature*, vol. 460, no. 7252, pp. 240–4, 2009.
- [113] R. C. Bialczak, M. Ansmann, M. Hofheinz, E. Lucero, M. Neeley, A. D. O’Connell, D. Sank, H. Wang, J. Wenner, M. Steffen, A. N. Cleland, and J. M. Martinis, “Quantum process tomography of a universal entangling gate implemented with josephson phase qubits,” *Nature Physics*, vol. 6, no. 6, pp. 409–413, 2010.
- [114] C. K. Hong, Z. Y. Ou, and L. Mandel, “Measurement of subpicosecond time intervals between two photons by interference,” *Phys Rev Lett*, vol. 59, no. 18, pp. 2044–2046, 1987.
- [115] A. M. Kaufman, B. J. Lester, C. M. Reynolds, M. L. Wall, M. Foss-Feig, K. R. Hazzard, A. M. Rey, and C. A. Regal, “Two-particle quantum interference in tunnel-coupled optical tweezers,” *Science*, vol. 345, no. 6194, pp. 306–9, 2014.
- [116] E. Bocquillon, V. Freulon, J. M. Berroir, P. Degiovanni, B. Placais, A. Cavanna, Y. Jin, and G. Feve, “Coherence and indistinguishability of single electrons emitted by independent sources,” *Science*, vol. 339, no. 6123, pp. 1054–7, 2013.
- [117] R. Lopes, A. Imanaliev, A. Aspect, M. Cheneau, D. Boiron, and C. I. Westbrook, “Atomic hong-ou-mandel experiment,” *Nature*, vol. 520, no. 7545, pp. 66–8, 2015.
- [118] K. Toyoda, R. Hiji, A. Noguchi, and S. Urabe, “Hong-ou-mandel interference of two phonons in trapped ions,” *Nature*, vol. 527, no. 7576, pp. 74–7, 2015.
- [119] M. C. Tichy, “Interference of identical particles from entanglement to boson-sampling,” *Journal of Physics B: Atomic, Molecular and Optical Physics*, vol. 47, no. 10, p. 103001, 2014.

- 
- [120] R. Islam, R. Ma, P. M. Preiss, M. E. Tai, A. Lukin, M. Rispoli, and M. Greiner, “Measuring entanglement entropy in a quantum many-body system,” *Nature*, vol. 528, no. 7580, pp. 77–83, 2015.
- [121] A. Aspect, “Bell’s inequality test: more ideal than ever,” *Nature*, vol. 398, no. 6724, pp. 189–190, 1999.
- [122] H. J. Kimble, Y. Levin, A. B. Matsko, K. S. Thorne, and S. P. Vyatchanin, “Conversion of conventional gravitational-wave interferometers into quantum nondemolition interferometers by modifying their input and/or output optics,” *Physical Review D*, vol. 65, no. 2, 2001.
- [123] D. Leibfried, B. DeMarco, V. Meyer, M. Rowe, A. Ben-Kish, J. Britton, W. M. Itano, B. Jelenkovic, C. Langer, T. Rosenband, and D. J. Wineland, “Trapped-ion quantum simulator: experimental application to nonlinear interferometers,” *Phys Rev Lett*, vol. 89, no. 24, p. 247901, 2002.
- [124] E. Knill, R. Laflamme, and G. J. Milburn, “A scheme for efficient quantum computation with linear optics,” *Nature*, vol. 409, no. 6816, pp. 46–52, 2001.
- [125] P. Kok, W. J. Munro, K. Nemoto, T. C. Ralph, J. P. Dowling, and G. J. Milburn, “Linear optical quantum computing with photonic qubits,” *Reviews of Modern Physics*, vol. 79, no. 1, pp. 135–174, 2007.
- [126] B. Peropadre, G. G. Guerreschi, J. Huh, and A. Aspuru-Guzik, “Proposal for microwave boson sampling,” *Phys Rev Lett*, vol. 117, no. 14, p. 140505, 2016.
- [127] C. Lang, C. Eichler, L. Steffen, J. M. Fink, M. J. Woolley, A. Blais, and A. Wallraff, “Correlations, indistinguishability and entanglement in hongâĂŞouâĂŞmandel experiments at microwave frequencies,” *Nature Physics*, vol. 9, no. 6, pp. 345–348, 2013.
- [128] F. Nguyen, E. Zakka-Bajjani, R. W. Simmonds, and J. Aumentado, “Quantum interference between two single photons of different microwave frequencies,” *Phys Rev Lett*, vol. 108, no. 16, p. 163602, 2012.

- 
- [129] M. Mariani, H. Wang, R. C. Bialczak, M. Lenander, E. Lucero, M. Neeley, A. D. O'Connell, D. Sank, M. Weides, J. Wenner, T. Yamamoto, Y. Yin, J. Zhao, J. M. Martinis, and A. N. Cleland, "Photon shell game in three-resonator circuit quantum electrodynamics," *Nature Physics*, vol. 7, no. 4, pp. 287–293, 2011.
- [130] W. Pfaff, C. J. Axline, L. D. Burkhardt, U. Vool, P. Reinhold, L. Frunzio, L. Jiang, M. H. Devoret, and R. J. Schoelkopf, "Controlled release of multiphoton quantum states from a microwave cavity memory," *Nature Physics*, 2017.
- [131] Y. Zhang and S. Girvin *In preparation*, 2018.
- [132] Z. Leghtas, S. Touzard, I. M. Pop, A. Kou, B. Vlastakis, A. Petrenko, K. M. Sliwa, A. Narla, S. Shankar, M. J. Hatridge, M. Reagor, L. Frunzio, R. J. Schoelkopf, M. Mirrahimi, and M. H. Devoret, "Quantum engineering. confining the state of light to a quantum manifold by engineered two-photon loss," *Science*, vol. 347, no. 6224, pp. 853–7, 2015.
- [133] A. J. Daley, H. Pichler, J. Schachenmayer, and P. Zoller, "Measuring entanglement growth in quench dynamics of bosons in an optical lattice," *Phys Rev Lett*, vol. 109, no. 2, p. 020505, 2012.
- [134] R. Filip, "Overlap and entanglement-witness measurements," *Physical Review A*, vol. 65, no. 6, 2002.
- [135] A. Crespi, R. Osellame, R. Ramponi, D. J. Brod, E. F. Galvao, N. Spagnolo, C. Vitelli, E. Maiorino, P. Mataloni, and F. Sciarrino, "Integrated multimode interferometers with arbitrary designs for photonic boson sampling," *Nature Photonics*, vol. 7, no. 7, pp. 545–549, 2013.
- [136] L. Chirulli, G. Burkard, S. Kumar, and D. P. Divincenzo, "Superconducting resonators as beam splitters for linear-optics quantum computation," *Phys Rev Lett*, vol. 104, no. 23, p. 230502, 2010.

- 
- [137] S. H. Tan, Y. Y. Gao, H. de Guise, and B. C. Sanders, “ $Su(3)$  quantum interferometry with single-photon input pulses,” *Phys Rev Lett*, vol. 110, no. 11, p. 113603, 2013.
- [138] M. Tillmann, S.-H. Tan, S. E. Stoeckl, B. C. Sanders, H. de Guise, R. Heilmann, S. Nolte, A. Szameit, and P. Walther, “Generalized multiphoton quantum interference,” *Physical Review X*, vol. 5, no. 4, 2015.
- [139] H. K. Lau and M. B. Plenio, “Universal quantum computing with arbitrary continuous-variable encoding,” *Phys Rev Lett*, vol. 117, no. 10, p. 100501, 2016.
- [140] D. Loss and D. P. DiVincenzo, “Quantum computation with quantum dots,” *Physical Review A*, vol. 57, no. 1, pp. 120–126, 1998.
- [141] V. Giovannetti, S. Lloyd, and L. Maccone, “Quantum random access memory,” *Phys Rev Lett*, vol. 100, no. 16, p. 160501, 2008.
- [142] S. Lloyd, M. Mohseni, and P. Rebentrost, “Quantum principal component analysis,” *Nature Physics*, vol. 10, no. 9, pp. 631–633, 2014.
- [143] H. K. Lau, R. Pooser, G. Siopsis, and C. Weedbrook, “Quantum machine learning over infinite dimensions,” *Phys Rev Lett*, vol. 118, no. 8, p. 080501, 2017.
- [144] L. Jiang, S. M. Girvin, Y. Y. Gao, B. J. Lester, and R. J. Schoelkopf, “Robust quantum logical gates,” *US patents application number 62/613,937*, 2018.
- [145] N. E. Frattini, U. Vool, S. Shankar, A. Narla, K. M. Sliwa, and M. H. Devoret, “3-wave mixing josephson dipole element,” *Applied Physics Letters*, vol. 110, no. 22, p. 222603, 2017.
- [146] Z. Leghtas, G. Kirchmair, B. Vlastakis, R. J. Schoelkopf, M. H. Devoret, and M. Mirrahimi, “Hardware-efficient autonomous quantum memory protection,” *Phys Rev Lett*, vol. 111, no. 12, p. 120501, 2013.
- [147] Y. L. Lim and A. Beige, “Generalized hongoumandel experiments with bosons and fermions,” *New Journal of Physics*, vol. 7, pp. 155–155, 2005.

- 
- [148] M. C. Tichy, M. Tiersch, F. de Melo, F. Mintert, and A. Buchleitner, “Zero-transmission law for multiport beam splitters,” *Phys Rev Lett*, vol. 104, no. 22, p. 220405, 2010.
- [149] T. Brecht, W. Pfaff, C. Wang, Y. Chu, L. Frunzio, M. H. Devoret, and R. J. Schoelkopf, “Multilayer microwave integrated quantum circuits for scalable quantum computing,” *npj Quantum Information*, vol. 2, no. 1, 2016.
- [150] T. Brecht, Y. Chu, C. Axline, W. Pfaff, J. â. Blumoff, K. Chou, L. Krayzman, L. Frunzio, and R. â. Schoelkopf, “Erratum: Micromachined integrated quantum circuit containing a superconducting qubit [phys. rev. applied 7 , 044018 (2017)],” *Physical Review Applied*, vol. 8, no. 3, 2017.
- [151] Z.-L. Xiang, S. Ashhab, J. Q. You, and F. Nori, “Hybrid quantum circuits: Superconducting circuits interacting with other quantum systems,” *Reviews of Modern Physics*, vol. 85, no. 2, pp. 623–653, 2013.
- [152] A. Bienfait, J. J. Pla, Y. Kubo, X. Zhou, M. Stern, C. C. Lo, C. D. Weis, T. Schenkel, D. Vion, D. Esteve, J. J. Morton, and P. Bertet, “Controlling spin relaxation with a cavity,” *Nature*, vol. 531, no. 7592, pp. 74–7, 2016.